MICRO AND NANO FLOWS

# BOOK OF ABSTRACTS

## MNF2K23

## MICRO and NANO FLOWS CONFERENCE

**Padova 18-20 September 2023**

**University of Padova**
**Department of Management and Engineering**
**@Palazzo della Salute**
**Via San Francesco 90, 35121 Padova**

**https://www.micronanoflows.com/mnf2023**

UNIVERSITÀ DEGLI STUDI DI PADOVA

dtg

## GOLD SPONSORS



**In collaboration with**

**DII Department of Industrial Engineering, University of Padova**

**ICEA Civil, Environmental and Architectural Engineering, University of Padova**

## Conference Chair

Prof. Simone Mancin, DTG, Dept. of Management and Engineering

## Co-Chair

Prof. Luca Doretti, ICEA, Civil, Environmental and Architectural Engineering

Prof. Elisa Cimetta, DII Department of Industrial Engineering

## Local Organizing Committee

Prof. Claudio Zilio
Prof. Giulia Righetti
Dr. Carolina Mira-Hernández
Eng. Dario Guarda
Eng. Giacomo Favero
Dr. Wagd Ajeeb
Eng. Gianluca Slaviero
Ms. Ernesta Baaba Mensah

## Conference Committee

Prof. Tassos Karayiannis (Chair), Brunel University London, UK
Prof. Stavroula Balabani, University College London, UK
Prof. Juergen J. Brandner, Karlsruhe Institute of Technology, Germany
Dr. Francesco Coletti, Brunel University London, UK
Prof. Srinivas Garimella Georgia Institute of Technology, USA
Prof. Marc Hodes, Tufts University, USA
Prof. Demetrios Papageorgiou, Imperial College London, UK
Prof. Gherhardt Ribatski, University of Sao Paulo, Brazil
Prof. Gabriele Angelo Dubini, Politecnico di Milano, Italy
Prof. Koji Takahashi, Kyushu University, Japan
Prof. Bing-Yang Cao Tsinghua University, China

## International Scientific Committee

A. Al-Jumaily, Auckland University of Technology, New Zealand
P. Angeli, University College London, UK
D. Attinger, Iowa State University, USA
S. Balabani, University College London, UK
C. Baroud, Laboratoire d'Hydrodynamique de l'École Polytechnique, France
A. Betz, Kansas State University, USA
B. Bai, Xi'an Jiaotong University, China
L. Cheng, Sheffield Hallam University, UK
C. Y. Ching, McMaster University, Canada
E. Cimetta, University of Padova, Italy
S. Colin, University of Toulouse, France
A. A. Darhuber, Eindhoven University of Technology, The Netherlands
D. Del Col, University of Padova, Italy

# Contents

## SESSION 1a
## Nanofluids and Applications
Chair: **R. Rhiel**

# Research on thermal management of micro-electronics based on microfluidics

Xuefeng LIN [1,#], Gan ZHANG [1,#], M. Elena NAVARRO[1,*] and Yulong DING[1]

1: Birmingham Centre for Energy Storage & School of Chemical Engineering, University of Birmingham, Birmingham, UK

* Corresponding author: Tel.: +44 7511 932912; Email:h.navarro@bham.ac.uk
#: Contribute equally to this work

**Abstract:** The rapid development of electronic communication, supercomputing and other fields has move forward the need of high power densities and the miniaturization of devices, which requires more advanced microchip heat flow management technology. Gallium nitride (GaN) high-electron-mobility-transistor device (HEMT) can generate radio frequency (RF) power densities of 6 W/mm at high breakdown voltage. The purpose of this study is to achieve more efficient high-density, non-uniform heat management of microelectronic devices by developing high-performance heat transfer fluid (HTF) and compact cooling devices, such as study GaN based transistors. Through the performance characterization of nano heat transfer fluid and their performance simulation studies in micro-jet-channels, it was found that boron nitride water nanofluids (0.5 wt.%,) at room temperature increases 5.2 % thermal conductivity compared to the base fluid. Besides, reduced graphene oxide (rGO) in EG/rGO, for temperatures up to -50 °C achieved 17 % and 11% thermal conductivity increase with 2.0 wt.% rGO. The result of the performance of the designed microfluidic system suggests that with a microchip target power density of 5 W/mm ($1\times10^7$ W/mm$^2$), the peak temperature in the devices was far below 200 °C with the thermal resistance of jetting channel accounting for 20-41% of the total thermal resistance.

**Keywords:** Thermal management, Microfluidic channel, GaN transistors, Nanofluids, Heat transfer coefficient, Thermal resistance

## 1. Introduction

Recent development trends of Electronic Science and Technology in recent decades, moved gradually to high-power and miniaturized microchips. In order to ensure safe and stable operation, power consumption has to be automatically limited in electronic devices to prevent high heat flux density and uneven heat flux distribution, which makes a large amount of heat accumulate locally in electronic equipment, resulting in the continuous rise of equipment temperature and the increase of equipment failure rate. According to literature [1], with the increase of working temperature, the possibility of equipment failure increases almost exponentially. Good thermal management technology is the key to ensure the safe and stable operation of electronic equipment. Generally, enhanced heat transfer technology includes the development of efficient heat transfer fluid (HTF) [2-6] and the improvement of comprehensive heat transfer coefficient through the optimal design of internal heat transfer surface structure [7-10]. The low thermal conductivity and low convective heat transfer coefficient of air cannot meet the heat dissipation requirements of microelectronics. Liquid forced convection is the mainstream heat transfer scheme at present. Traditional HTFs include water, oil, EG, and/or their mixtures etc. Studies have shown that the use of nanofluids with nanoparticles added to the basic HTF has the effect of enhancing heat transfer. In addition, as an excellent heat transfer design method, the application of

micro jet impingement array in the cooling of microelectronics can obtain good external surface heat dissipation effect. Compared with other cooling channels such as microchannels and metal foam based channels, micro jet impingement has the highest heat transfer coefficient.

## References

1. Murshed S M S, De Castro C A N. A critical review of traditional and emerging techniques and fluids for electronics cooling[J]. Renewable and Sustainable Energy Reviews, 2017, 78: 821-833.
2. Chabi A R, Zarrinabadi S, Peyghambarzadeh S M, et al. Local convective heat transfer coefficient and friction factor of CuO/water nanofluid in a microchannel heat sink[J]. Heat and Mass Transfer, 2017, 53(2): 661-671.
3. Zheng L, Xie Y, Zhang D. Numerical investigation on heat transfer performance and flow characteristics in circular tubes with dimpled twisted tapes using Al2O3- water nanofluid[J]. International Journal of Heat and Mass Transfer, 2017, 111: 962-981.
4. Sun B, Qu Y, Yang D. Heat transfer of single impinging jet with Cu nanofluids[J]. Applied Thermal Engineering, 2016, 102: 701-707.
5. Ghanbarpour M, Nikkam N, Khodabandeh R, et al. Improvement of heat transfer characteristics of cylindrical heat pipe by using SiC nanofluids[J]. Applied thermal engineering, 2015, 90: 127-135.
6. Ghanbarpour M, Khodabandeh R, Vafai K. An investigation of thermal performance improvement of a cylindrical heat pipe using Al2O3 nanofluid[J]. Heat and Mass Transfer, 2017, 53(3): 973-983.
7. Bayomy A M, Saghir M Z. Experimental study of using γ-Al2O3–water nanofluid flow through aluminum foam heat sink: comparison with numerical approach[J]. International Journal of Heat and Mass Transfer, 2017, 107: 181-203.
8. Bayomy A M, Saghir M Z. Experimental Investigation of Using γ-Al2O3–Water Nanofluid Flow in Aluminum Foam Heat Sink[C]//ICTEA: International Conference on Thermal Engineering. 2017, 2017.
9. Dyga R, Płaczek M. Heat transfer through metal foam–fluid system[J]. Experimental thermal and fluid science, 2015, 65: 1-12.
10. Lu T J, Stone H A, Ashby M F. Heat transfer in open-cell metal foams[J]. Acta materialia, 1998, 46(10): 3619-3635.

# Experimental study of magnetic convection in a lab-scale direct absorption solar collector

Boris V. BALAKIN[1,*], Mattias STAVA[2], Anna KOSINSKA[1]

1: Western Norway University of Applied Sciences, Bergen, Norway
2: University of Bergen, Bergen, Norway

* Corresponding author: Tel.: +47 55 58 56 38; Email: boris.balakin@hvl.no

**Abstract** Nanofluids can be used for gathering and transporting heat in direct absorption solar collectors (DASC). In this study, we experimentally demonstrate that an aqueous nanofluid of $Fe_2O_3$ can flow in a pump-free DASC through photomagnetic convection. The flow was established for particle concentrations of 1-2% wt. under the simultaneous influence of radiated heat and a permanent magnetic field of up to 28 mT. To achieve this, we developed a theoretical model to calculate the velocity of convection and the thermal efficiency of the DASC.

**Keywords:** nanofluid, ferrofluid, direct absorption solar collector, magnetic convection

## 1. Introduction

There are multiple studies of nanofluid-based direct absorption solar collectors in the literature. DASCs based on nanofluids of CuO [1] demonstrated better thermal performance if compared to solar collectors with equivalent geometry but with surface absorption. However, commercial collectors with surface absorption outperform DASCs [2]. Therefore, the thermal performance of DASC can be improved through photomagnetic convection. In this case, a magnetic nanofluid is used in the collector together with an external source of magnetic field.

In this research, we developed a laboratory-scale experimental system to study the phenomenon, presented schematically in Fig. 1.

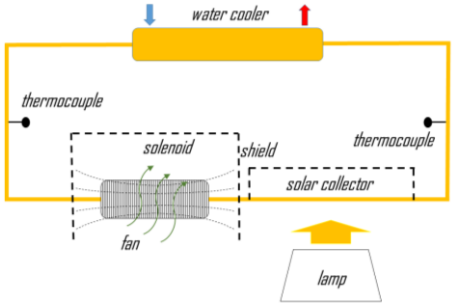


**Fig.1**. Scheme of the experiment.

The system consisted of a closed-loop of 4-mm glass tubes with a total length of 1.2 m. One side of the loop included a spiral heat exchanger, which was used to cool down the nanofluid with tap water at 12°C. A DASC region was located 100-mm from the opposite side of the loop, and was irradiated by a 2.8-W halogen lamp. Two K-type thermocouples were placed at the sides of the loop.

The magnetic field was established at the entrance to the DASC zone using FC-5818 solenoid from APW. The solenoid operated at 6 V and 0-1.3 A. The produced magnetic field was up to 28 mT. The solenoid and the rest of the rig were protected from the thermal radiation of the lamp using the reflective shields. The solenoid was cooled by an air fan whose power was adjusted to maintain the solenoid at ambient temperature equal to 23 °C.

We produced nanofluid dispersing 50-nm nanoparticles of $Fe_2O_3$ in distilled water using an ultrasound cleaner at 130 W. The concentration of the particles was 2% wt. The particle size, as measured by static light scattering, remained around 50 nm in fresh samples but increased to 110 nm after experiments due to aggregation.

The experimental procedure consisted of the following steps: filling up the nanofluid in the loop, connecting tap water to the cooling heat

exchanger, switching on the lamp and solenoid, and recording the temperatures at the thermocouples until a steady-state was achieved.

## 2. Results and discussion

In Fig. 2, we present the temperature difference in the flow loop over time for different particle concentrations with and without the magnetic field. With no magnetic field, there is a low temperature gradient in the DASC, indicating incipient flow and temperature distribution mainly due to thermal conduction. When the magnetic field was on, a temperature difference of 12 °C was established in the system for the concentration of 1% wt. The temperature difference reduced when the concentration of particles increased. The increase in the number of nanoparticles increases the driving force for photomagnetic convection, causing the temperature profile to narrow in the loop..

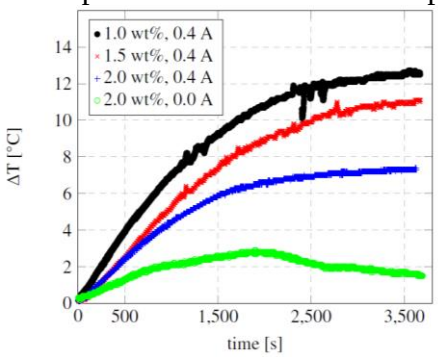


**Fig.2.** Temperature difference as a function of concentration and solenoid current.

The velocity of convection can be estimated by assuming that hydraulic flow resistance balances the flow-driving forces in the loop. This means that the frictional pressure drop is balanced by the magnetic and thermophoretic forces [3]:

$$\xi \rho_{nf} \frac{v^2}{2} \sim \phi_p \mu_0 M_m H^{max} + \frac{-6 n_p \pi \mu_l \nu_l d C_s}{1 + 6 C_m \mathrm{Kn}} \frac{k_l/k_p + 2 C_t \mathrm{Kn}}{1 + 2 k_l/k_p + 4 C_t \mathrm{Kn}} \frac{\Delta T}{T},$$

where $\xi$ is the hydraulic resistance of the system, $\rho_{nf}$ is the density of the nanofluid, v is the mean flow velocity, $\phi_p$ is the volume fraction of particles, $M_m$ is the magnetization, $H_{max}$ is the magnetic field, $n_p$ is the number density of particles, $\mu_l$, $\nu_l$ are the dynamic and the kinematic viscosities of the base fluid, $k$ is the thermal conductivity, $Kn$ is the Knudsen number of the particles, $T$ is the temperature, and the constants are $C_s$=1.17, $C_m$=1.14, $C_t$=2.18.

The calculation revealed that the mean flow velocity increases to an asymptotic value with the current. The asymptotic value rose from 2 mm/s to 5 mm/s when the particle concentration increased from 0.5% wt. to 2% wt. Using the computed flow velocity, we calculated the thermal efficiency of the DASC. The maximum thermal efficiency was 65% for the 2-% nanofluid at 28 mT.

## 3. Conclusions

In this work, we examine the impact of magnetic field on the convection of nanofluid in the laboratory-scale DASC. The nanofluid was produced using 50-nm particles of $Fe_2O_3$ and distilled water without surfactant. The collector's temperature difference was dependent on particle concentration and magnetic field. The thermal efficiency of the collector was 65%,which was lower than the efficiency of the third-party DASCs from the literature. Further optimization of the system is required to achieve better performance.

## Acknowledgments

This study was supported by the Norwegian Research Council (project No. 300286).

## References

[1] Karami, M., Akhavan-Bahabadi, M.A., Delfani, Sh., Raisee, M., 2015. Experimental investigation of CuO nanofluid-based direct absorption solar collector for residential applications, Ren.&Sust.Energy Rev. 52, 793-801.

[2] Goel, N., Taylor, R.A., Otanicar, T., 2020. A review of nanofluid-based direct absorption solar collectors: design considerations and experiments with hybrid PV/Thermal and direct steam generation collectors. Ren.Energy. 145, 903-913.

[3] Balakin, B. V., Stava, M., Kosinska, A., 2022. Photothermal convection of a magnetic nanofluid in a direct absorption solar collector. Solar Energy, 239, 33-39.

# Selection of hybrid or mono nanofluids for one-phase heat exchangers: common features in experimental research

Javier P. VALLEJO[1,*], Jose I. PRADO[2], Luis LUGO[2]

1: Centro Universitario de la Defensa en la Escuela Naval Militar, Marín, ES
2: CINBIO, Universidade de Vigo, Grupo GAME, Departamento de Física Aplicada, Vigo, ES

* Corresponding author: Tel.: +34 986 804975; Email: jvallejo@cud.uvigo.es

**Abstract:** Hybrid nanofluids show increasing attention in convective heat transfer applications. Numerous experimental studies independently analyse the convective heat transfer for mono or hybrid nanofluids in single-phase convective heat transfer applications. However, there are still no general conclusions about which nanofluids, mono or hybrid, performs better. This work analyses the experimental studies that jointly evaluate both hybrid and mono nanofluids and the main outcomes are classified according to the heat transfer device (tubular, plate and minichannel heat exchangers). The results from the literature mainly support that there is no synergistic effect for hybrid nanofluids on convective heat transfer in laminar flow.

**Keywords:** Nanofluids, Hybrids, Heat exchangers, Convection

## 1. Introduction

Based on the heat transfer mechanism, heat exchangers are classified into single-phase and two-phase. In terms of construction features, tubular heat exchangers (double tube, shell and tube, flexible tube) and plate heat exchangers (gasketed, brazed, welded) are the most common. Miniature heat exchangers are increasingly required in technological applications [1]. Research on the efficiency optimization of systems involving exchangers has led to the development of several passive and active techniques. Among the former, nanofluids have been a noticeable field of research in last decades. In addition, interest in hybrid nanofluids has grown due to the chance of further improving heat transfer. [2].

This article reflects on whether hybrid or mono nanofluids are the best candidates for single-phase convection based on experimental results from the literature. Consequently, the experimental studies (up to early 2022) that jointly analyse hybrid nanofluids and the corresponding mono nanofluids in single-phase convective heat exchangers have been critically summarized, classifying them into three groups: tubular, plate and mini-channel heat exchangers.

## 2. Discussion and Results:

### 2.1 Tubular heat exchangers

Two experimental studies [2, 3] analyse hybrid nanofluids and all corresponding mono nanofluids (Figure 1). Gupta et al. [2] studied a silver:multi-walled carbon nanotubes (Ag:MWCNT) hybrid nanoadditive, and the corresponding Ag and MWCNT mono nanoadditives. The MWCNT/water mono nanofluid obtained the higher heat transfer coefficient ($h$) rise, 67.5%.

Naddaf et al. [3] considered MWCNT:graphene nanoplatelet (MWCNT:GNP) hybrid nanoadditive at 1:1 ratio, and the corresponding MWCNT and GNP mono nanoadditives. Nanofluids based on a diesel oil were designed and tested in laminar flow. The GNP/water mono nanofluid reached the highest $h$ increase.

In addition, fourteen experimental research papers examining hybrid nanofluids and only one of the mono options were found [1]. Water is the base fluid in all cases. Some of these studies show that the mono nanofluid obtains the greatest $h$ or Nusselt number ($Nu$) improvement, while others revealed that the hybrid nanofluid performs better. However, the mono nanofluid with the best thermal performance could not have been included in the analysis.

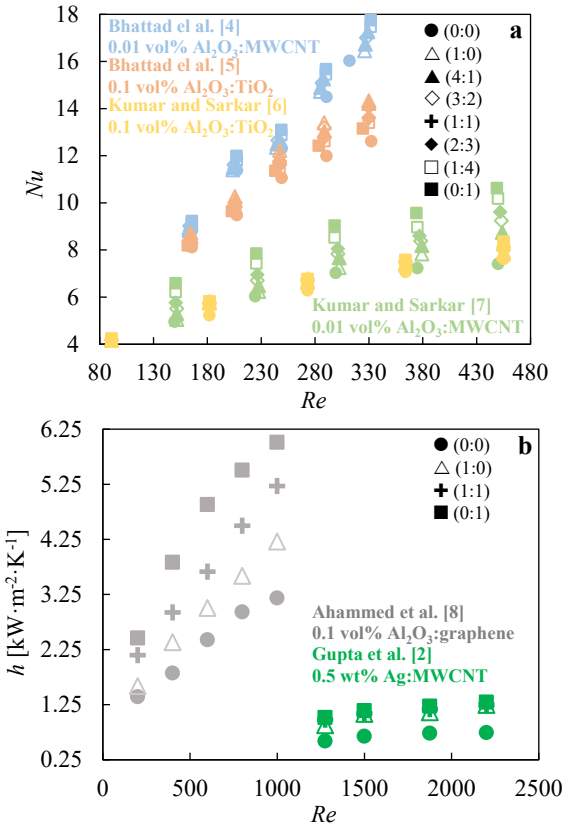


**Fig. 1.** *Nu* (a) and *h* (b) versus *Re* for aqueous nanofluids from experimental studies [3-8].

### 2.2 Plate heat exchangers

Two experimental studies [4, 5] investigate hybrid nanofluids and all corresponding mono nanofluid (Figure 1). Bhattad et al. [4] studied $Al_2O_3$:MWCNT hybrid nanoadditives and the corresponding $Al_2O_3$ and MWCNT mono nanoadditives. Aqueous nanofluids were analysed in laminar flow. The mono nanofluid MWCNT/water achieved the greatest *h* improvement, 15.2%. The higher thermal conductivity (TC) of MWCNT plays a key role. Bhattad et al. [5] analysed $Al_2O_3$:$TiO_2$ hybrid nanoadditives and the analogous $Al_2O_3$ and $TiO_2$ mono nanoadditives. Aqueous nanofluids were evaluated in laminar flow. The maximum *h* enhancement was noticed for the $Al_2O_3$/water mono nanofluid, 16.9%. The highest pumping power was noted for the $TiO_2$/water nanofluid. In addition, three experimental articles examine hybrid nanofluids and only one of the mono options [1]. They show that one of the hybrids presents the best performance, but the mono nanofluid with higher TC may not be included (MWCNT).

### 2.3 Minichannel heat exchangers

Six experimental studies [1, 6-8] explore hybrid nanofluids and both mono nanofluids (Figure 1). As an example, one of them is summarized. Kumar and Sarkar [6] synthetized $Al_2O_3$:$TiO_2$ hybrid and the equivalent $Al_2O_3$ and $TiO_2$ mono nanoadditives. Water-based nanofluids were analysed in laminar regime. Maximum *h* and *Nu* improvements (12.8% and 11.8%, respectively) are described for the $Al_2O_3$/water mono nanofluid.
Furthermore, two experimental works were found that examine hybrid nanofluids and one of the mono options [1]. Similar conclusions can be drawn as for the previous.

## 3. Conclusions

The experimental works that jointly examine hybrid and mono nanofluids for single-phase convection show these common characteristics:

- The base fluid is mostly water and the nanoadditives are carbon-based nanoparticles, metals and oxides up to a 0.5 % concentration.
- The hybrid nanoadditives are mixtures among mono nanomaterials and not composites.
- The evaluated flow regime is laminar.
- One of the mono nanofluids achieve higher *h* or *Nu* improvements than the hybrids.

The results from the literature mainly support that there is no synergistic effect for hybrid nanofluids on convection in laminar flow.

## Acknowledgements:

Grant PID2020-112846RB-C21 funded by MCIN/AEI/10.13039/501100011033. Grant PDC2021-121225-C21 funded by MCIN/AEI/10.13039/501100011033 and "European Union NextGenerationEU/PRTR". J.P.V. thanks CUD-ENM. J.I.P. thanks the Margarita Salas postdoctoral fellowship (NextGenerationEU).

## References

[1] J.P. Vallejo, J.I. Prado, L. Lugo, Appl. Therm. Eng. 203 (2022) 117926.
[2] M. Gupta, V. Singh, S. Kumar, N. Dilbaghi, J. Therm. Anal. Calorim. 142 (2020) 1545-1559.
[3] A. Naddaf, S.Z. Heris, B. Pouladi, Powder Technol. 352 (2019) 369-380.
[4] A. Bhattad, J. Sarkar, P. Ghosh, Appl. Therm. Eng. 162 (2019) 114309.
[5] A. Bhattad, J. Sarkar, P. Ghosh, Heat Mass Transf. 56 (2020) 2457-2472.
[6] V. Kumar, J. Sarkar, Powder Technol. 345 (2019) 717-727.
[7] V. Kumar, J. Sarkar, Appl. Therm. Eng. 165 (2020) 114546.
[8] N. Ahammed, L.G. Asirvatham, S. Wongwises, Int. J. Heat Mass Transf. 103 (2016) 1084-1097.

# Pd-PDMS nanofluids, a future alternative to be applied in concentration solar plants

Juan Jesús GALLARDO[1,*], Desireé M. DE LOS SANTOS[1], Rodrigo ALCÁNTARA[1], Iván CARRILLO-BERDUGO[1], Javier NAVAS[1]

1: Departamento de Química Física, Facultad de Ciencias, Universidad de Cádiz, 11510 Puerto Real (Cádiz), Spain

[*] Corresponding author. Email: jj.gallardo@uca.es

**Abstract:** In this work, nanofluids with different concentration of palladium nanoparticles have been prepared, and characterized, using polydimethylsiloxane (PDMS) as base fluid and 1-octadecanethiol as surfactant with the aim of obtain stables nanofluids and enhance thermal properties with respect to the base fluid. Helisol 5A®, a commercial PDMS, has been selected as base fluid due to its properties as heat transfer fluid (HTF) for concentrating solar power plants with no hazard classifications. Palladium nanoparticles have been used due to their demonstrated properties to form stable nanofluids by using other HTF with enhanced thermal properties. This fact has been proven in this work by the study of stability, particle size, specific heat, thermal conductivity, viscosity and density. These results reveal the potential capability of using Pd-PDMS nanofluids to enhance the yield of a concentrating solar plant with a more sustainable nanofluid.

**Keywords:** Concentrating solar power, nanofluids, palladium, polydimethylsiloxane, thermal properties.

## 1. Introduction

When combined with thermal energy storage, concentrating solar power (CSP) makes solar energy dispatchable and allows to align supply and demand, thus making more reliable energy conversion systems combined with other renewable technologies. The main limitation of CSP is the low achievable energy density under operation, due to the physical properties of the heat transfer fluid (HTF) that participates in solar-to-thermal energy conversion in parabolic- trough collectors. The currently most used HTF is the eutectic and azeotropic mixture of diphenyl ether and biphenyl, commercially available as Dowtherm A®, which is suitable for liquid phase operation up to 673 K, with low vapour pressure and dynamic viscosity, and non-corrosive nature. Its specific heat and thermal conductivity are suboptimal. Besides, the manipulation of this mixture can cause skin, eye and respiratory irritation to human beings, and an accidental release to the environment can cause severe and long-lasting effects on aquatic life [1]. Polydimethylsiloxane (PDMS) has been recently introduced as an outstanding alternative HTF for CSP technology. This linear silicone-based fluid, commercially available as Helisol 5A®, has similar thermal and rheological properties compared to Dowtherm A®, is thermally stable up to 698 K, and has no hazard classification [2].

The later endorses PDMS as an alternative HTF to better comply with sustainability principles in this application Specific heat and thermal conductivity of the new PDMS-based HTF can be improved by dispersing nanomaterials into it, as Pd, generating a colloidal suspension that is typically named nanofluid. Nanofluids as HTF for CSP plants, using the Dowtherm A® as base fluid, and Pd as nanoparticle in suspension has been previously studied by us [3]. In this way, the main objective of this work is to prepare stable Pd-PDMS nanofluids and their characterization through the measurement of different properties as viscosity, density, particle size and their capability to enhance thermal properties by measuring the specific heat a thermal conductivity of the nanofluids and comparing these results with the corresponding with the base fluid.

## 2. Methods

Pd containing nanofluids were prepared by sonication Pd solid in the host fluid. The host fluid was a 1 wt% ODT solution in the base fluid (Helisol 5A). An initial nanofluid was prepared using 100 ml of the host fluid and the

required amount of Pd to obtain a nanofluid with a mass fraction of Pd equal to 0.01 wt%. The mixture was sonicated using an ultrasound probe (model GM4200, supplied by Bandelin Electronics®) at 50% amplitude for 4 h with a 2:4s on: off pulsation, in a thermostatic bath at 293 K to prevent overheating. After that, aliquots were taken from the stock nanofluid to prepare nanofluids with mass fractions of Pd nanoparticles equal to 0.001 wt% and 0.002 wt% by addition of host fluid up to 50 ml. Dilutions were sonicated using a bath Elmasonic Select 30 50/60Hz for 5 min. After that, the nanofluids were characterized by the following techniques: density was measured with a portable densimeter with temperature compensation system (Model DMA 35 supplied by Anton Paar®), dynamic viscosity was determined with a rheometer at different temperature within the range 25-175 ºC (model HR-10, supplied by TA instruments®); the size of the nanoparticles in the nanofluid was measured by DLS with a Nano-Zs system (Malvern Instruments®); Changes in the extinction coefficient at $\lambda$ = 450 nm were registered using the OceanOptics DH2000-Bal halogen lamp and the USB-2000 + spectrometer. Finally, the thermal properties were measured with a DSC214-Polyma (Netzsch®) from 25 ºC to 200 ºC and a THB-100 (Linseis®) for specific heat and thermal conductivity, respectively.

## 3. Results and discussion

The colloidal stability of the nanofluid samples was analyzed as an aggregation rate using UV–visible spectroscopy. All measurements were performed in triplicate, on a daily basis, for 25 days. The spectral extinction coefficient is a good indicator for colloidal stability [4]. Fig. 1 shows the extinction coefficient at a wavelength of 450 nm for both nanofluids. A slight decrease in the extinction coefficient values is observed during the first week after preparation, and it remains stable onwards. Such a decrease is attributed to the aggregation of Pd nanoparticles. Absorbed and scattered radiation is directly proportional to the species in suspension, so that time invariant values of the spectral extinction coefficient indicate good stability of nanofluids prepared. Regarding thermal properties of the nanofluids, as an example, Fig. 2 shows the values of the isobaric specific heat of the nanofluids prepared in function of temperature. The addition of Pd nanoparticles induces an enhancement in specific heat, up to 2.93 ± 0.02% with 1·10-3 % wt. Pd and 5.17 ± 0.04 % with 2·10-3 % wt. Pd, in the range of temperatures of characterization.

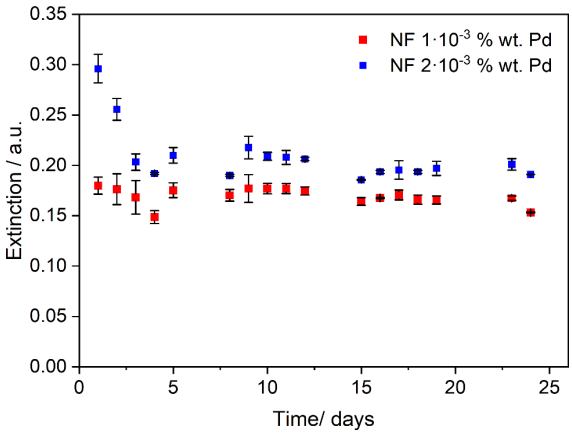


**Figure 1.** Extinction values measured for the nanofluid samples prepared as a function of time.

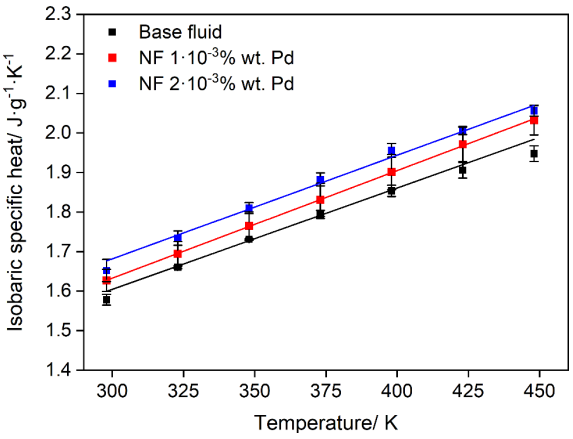


**Figure 2.** Isobaric specific heat values for nanofluid prepared as a function of temperature.

## Acknowledgements

We acknowledge *Ministerio de Ciencia e Innovación del Gobierno de España* for funding under grant TED2021-132518B-I00.

## References

[1] Dowtherm A® MSDS.
[2] Helisol 5A ® MSDS.
[3] I. Carrillo-Berdugo et al. *Sustainable Chemistry & Engineering.* 9(11), 4194-4205 (2021).
[4] W. Mäntele et al. Spectrochim. Acta Part A Mol. Biomol. Spectrosc. 173 (2017)

# Nanofluids based on transition metal dichalcogenides for application in concentrating solar power plants.

Paloma MARTÍNEZ-MERINO[1,*], Rodrigo ALCÁNTARA[1], Javier NAVAS[1]

1: Department of Physical Chemistry, University of Cádiz, Puerto Real, ES

* Corresponding author: Tel.: +34 956 016328; Email: paloma.martinez@uca.es

**Abstract**: Nanofluids based on spherical nanoparticles, nanosheets and nanowires of transition metal dichalcogenides such as $MoS_2$, $WS_2$ or $WSe_2$ have been researched. The base fluid of these nanofluids is the eutectic mixture of biphenyl and diphenyl oxide, a thermal oil typically used as heat transfer fluid in concentrating solar power plants based on parabolic trough collectors. According to UV-Vis and particle size results, the studied nanofluids showed long-term colloidal stability. In addition, all nanofluids exhibited improved thermal properties with respect to the base fluid, although the most significant improvements were obtained with the nanofluids based on nanosheets. The nanofluid based on $MoS_2$ nanosheets and the one based on $WSe_2$ nanosheets showed an improvement in the heat transfer coefficient of 36% and 34% respectively. These results demonstrate the high potential of the explored nanofluids as heat transfer fluids in solar power plants.

**Keywords:** Nanofluids, stability, thermal conductivity, heat transfer, concentrating solar power.

## 1. Introduction

Concentrating solar power (CSP) is one of the renewable energies with a high potential to meet the growing global energy demand. Concentrating solar power plants are classified according to the kind of solar collectors used, being the most implemented technology the parabolic trough collectors. In CSP plants based on parabolic trough collectors, concave mirrors reflect sunlight onto an absorber tube located at the focal line of the collectors. The absorber tube, coated with a selective absorber material, contains a heat transfer fluid (HTF) that reaches high temperatures. The thermal energy absorbed by the HTF is transferred to the power block to produce electricity. However, one of the problems of CSP plants is their high cost compared to fossil fuel-based power plants. For this reason, in recent years some authors have proposed replacing the thermal fluid used in these plants (typically a eutectic mixture of biphenyl and diphenyl oxide) with nanofluids. The suspension of nanoparticles in a fluid, typically called nanofluid, usually has improved thermophysical properties compared to the base fluids. Therefore, substitution could lead to an improvement in thermal efficiency and thus to an overall improvement of the CSP plant. Generally, most works are based on nanofluids based on metal nanoparticles or metal oxides but few works are focused on nanofluids based on transition metal dichalcogenides (TMDCs) [1,2]. In this work, the colloidal stability and thermal properties of nanofluids based on 1D, 2D or 3D nanostructures of TMDCs are explored to determine their feasibility as HTFs in CSP plants.

## 2. Methodology

TMDC-based nanofluids have been prepared by different procedures such as liquid-phase exfoliation or the two-step method. In the latter, the nanomaterial was first synthesized with the desired morphology and in the second step it was sonicated by ultrasound. The colloidal stability of nanofluids was determined by monitoring the extinction coefficient by UV-Vis and particle size using the Dynamic Light Scattering technique. The isobaric specific heat

was determined by temperature-modulated differential scanning calorimetry and thermal conductivity by light flash and transient hot bridge techniques.

## 3. Results

TEM images (Figure 1) confirmed the expected 1D, 2D and 3D morphology of the nanostructures hosted in the different prepared nanofluids.

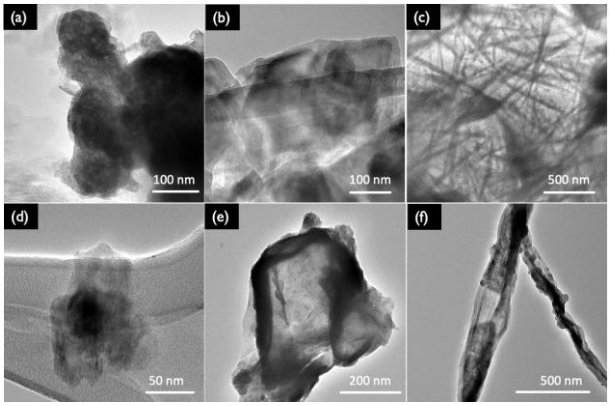


Figure 1. Nanostructures found in the prepared nanofluids. a) MoS2 spherical nanoparticles, b) MoS2 nanosheets, c) MoS2 nanowires, d) WS2 nanosheets, e) WSe2 nanosheets and f) WSe2 nanowires.

All TMDC-based nanofluids showed long-term colloidal stability. In some of them, a decrease in extinction coefficient and an increase in particle size were observed in the first days of characterisation. After the first few days, the extinction coefficient and particle size values remained constant, indicating that the nanofluids reached colloidal stability.
The efficiency of TMDC-based nanofluids as a heat transfer fluid in solar collectors is analysed through the Dittus-Boelter equation (1). This equation compares the heat transfer performance of the nanofluid to that of the base fluid and is defined as

$$\frac{h_{nf}}{h_{bf}} = \left(\frac{\rho_{nf}}{\rho_{bf}}\right)^{0.8} \left(\frac{k_{nf}}{k_{bf}}\right)^{0.6} \left(\frac{C_{P\,nf}}{C_{P\,bf}}\right)^{0.4} \left(\frac{\mu_{nf}}{\mu_{bf}}\right)^{-0.4}$$

where $h$ refers to the heat transfer coefficient, $\rho$ to the density, $k$ to the thermal conductivity, $C_P$ to the isobaric specific heat and $\mu$ to the viscosity of the fluid under consideration. Figure 2 shows that the $h_{nf}$ / $h_{bf}$ ratio is greater than 1 for all nanofluids, indicating that heat transfer is enhanced with the use of nanofluids compared to the base fluid. This ratio increases with increasing temperature and reveals that at 90°C an increase in heat transfer of up to 36% and 34% is achieved for nanofluids based on $MoS_2$ and $WSe_2$ nanosheets, respectively.

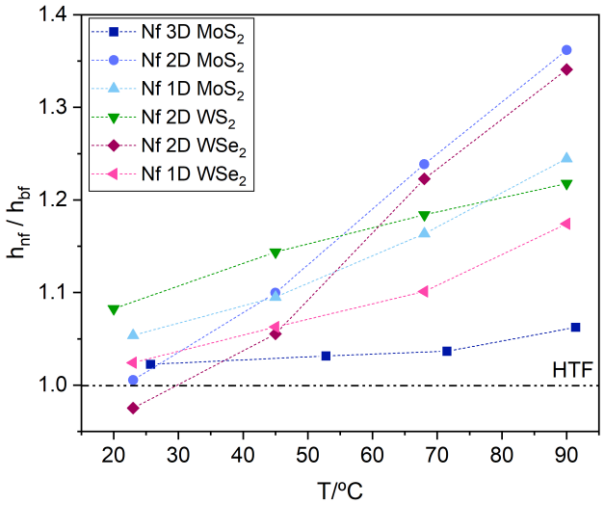


Figure 2. Variation of the ratio of the heat transfer coefficient of the nanofluids and the base fluid versus the increase in temperature.

## 4. Conclusions

This work reveals that TMDC-based nanofluids have a high potential to be used as heat transfer fluids in CSP plants. The nanofluids exhibited colloidal stability over time and thermal improvements with respect to the base fluid. The most significant improvements were found in nanofluids based on 2D morphology.

## 4. References

[1] J. Navas et al., On the enhancement of heat transfer fluid for concentrating solar power using Cu and Ni nanofluids: An experimental and molecular dynamics study, Nano Energy 27 (2016), 213-224
[2] T. Aguilar et al., Investigation of enhanced thermal properties in NiO-based nanofluids for concentrating solar power applications: A molecular dynamics and experimental analysis, Applied Energy 211 (2018) 677–688.

## SESSION 1b
## MINI-SIMPOSIUM
## Flows on micro- or nano- structured surfaces
Chair: **S. Cherubini**

# The effect of superhydrophobic surfaces on turbulent transition

Stefania CHERUBINI[1,*], Antoine JOUIN[1,2], Jean-Christophe ROBINET[2]

1: Department of Mechanics, Mathematics and Management, Polytechnical University of Bari, Italy, IT
2: Laboratoire Dynfluid, Arts et Metiers ParisTech, Paris, FR

* Corresponding author: Email: stefania.cherubini@poliba.it

**Abstract:** Superhydrophobic surfaces are known to reduce skin friction of overlying liquid flows. However, the effect of these surfaces on transition to turbulence is still not clear. This work investigates the effect of these micro- and nano-structured surfaces on transition to turbulence in a channel in order to evaluate the consequent drag reduction. In particular, the effect of the roughness anisotropy on turbulent transition is studied, showing that in these cases cross-flow effects dominate the flow dynamics, suggesting the need to consider these effects when modelling superhydrophobic surfaces.

**Keywords:** Nano-structured surfaces, Superhydrophobicity, transition to turbulence

## 1. Introduction

Superhydrophobic (SH) surfaces are composed by a hierarchical structure of micro-roughnesses able to trap the air underneath them, having the remarkable property of reducing the surface of contact with an overlying flow, which leads to a dramatic reduction of its drag [1]. This rough nanostructure, that can be found on many biological surfaces such as those of lotus leaves, butterfly wings or duck feathers, is rather complex, so that numerical simulations should rely on models for reducing this complexity. The computationally cheapest method is that of considering an equivalent boundary condition through a homogenisation procedure [2].
When this procedure is applied to isotropic roughness elements, it leads to a slip condition on the streamwise velocity only. Whereas, in the case of anysotropic roughnesses, it leads to the presence of spanwise component in the homogenized base flow velocity. This work aims at investigating the effect of these micro- and nano-roughnesses on turbulent transition, with special care to the influence of the three-dimensionality of the base flow on linear stability and transition.

## 2. Methodology

The flow of an incompressible fluid in a channel of height 2h covered with SH walls is tackled via numerical simulations. The Reynolds number is defined as $Re = U_r h/\nu$, where the reference velocity $U_r$ is 1.5 the wall-normal average of the base flow velocity, and $\nu$ is the kinematic viscosity. The dynamics of the flow is governed by the Navier-Stokes equations:

$$\frac{\partial U}{\partial t} = -(U\cdot\nabla)U - \nabla P + \frac{1}{Re}\nabla^2 U \qquad (1)$$

$$\nabla\cdot U = 0 \ . \qquad (2)$$

The flow is periodic in the streamwise and spanwise directions. The walls of the channel are covered either with SH isotropic square cubes or with SH riblets oriented with an angle $\theta=45°$ [3] with respect to the x direction. Both are modeled by means of an homogenised wall boundary conditions having a tensorial form:

$$\begin{bmatrix} U \\ W \end{bmatrix} = \pm L\,\partial_y \begin{bmatrix} U \\ W \end{bmatrix} \qquad (3)$$

the tensor L being defined as:

$$L = R\begin{pmatrix} l_{par} & 0 \\ 0 & l_{perp} \end{pmatrix} R^T \qquad (4)$$

where the rotation matrix R is a function of the angle $\theta$. For the anisotropic riblets, following [3] we set $l_{par}= 0.03$ yielding $L_{11} = L_{22} = 0.0225$ and $L_{12} = L_{21} = 0.0075$, whereas for

the isotropic cubes we consider L11 = L22 = 0.02. We have verified that these slip length values can be realistically obtained by microtextured SHS in wetting-stable conditions [4].
The flow field is decomposed as the sum of a steady base flow $Q_0(y) = [U_0,V_0,W_0,P_0]^T$ and an unsteady disturbance q(x,y,z,t) having small amplitude. The Navier-Stokes equations are then linearised with respect to the base flow, and normal-modes perturbations are considered. Modal and non-modal stability analysis are carried out [5], which are complemented by Direct Numerical Simulations in order to investigate the overall path to transition.

## 3. Results

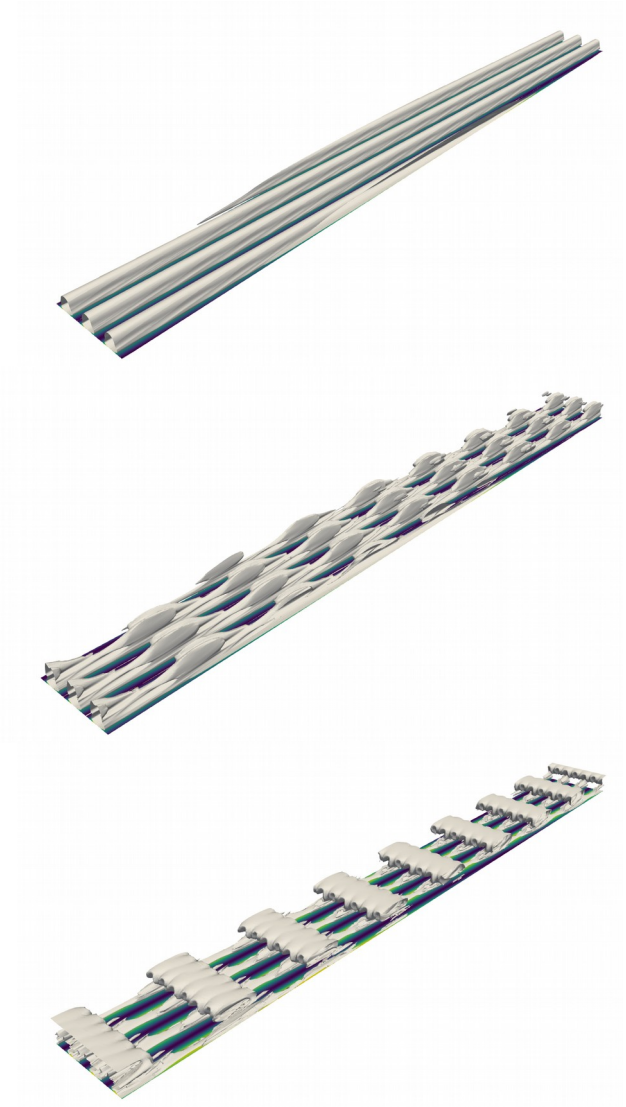

*Figure 1: Isosurfaces of the λ2 criterion extracted from the DNS at t=1000 (top) and 1050 (bottom), and contours of the streamwise velocity at the wall. The flow is from bottom to top, and left to right.*

In the case of isotropic roughnesses, SH surfaces are found to strongly influence transition induced by wall-close disturbances, such as Tollmien-Schlichting waves, even at subcritical Reynolds number. Whereas, they have a weak effect on the subcritical growth of coherent structures lying farther from the wall, such as streaks and streamwise vortices. In both cases, the spatial structure of these modal and non-modal disturbances and the consequent route to transition is not completely altered. On the other hand, in the case of anisotropic roughnesses, a new instability region linked to cross-flow effects is found (see figure 1, top frame). This mode is accompanied by a second unstable mode characterized by three-dimensional Tollmien-Schlichting waves. Optimal perturbations are also influenced by the cross-flow, becoming oblique streaks with non-zero streamwise wavenumber. Transition induced by Tollmien-Schlichting waves leads to streaky structures with large spanwise wavenumber. Whereas, unstable cross-flow vortices develop into large quasi spanwise-invariant structures before breaking down to turbulence (see figure 1, bottom frames). Secondary stability is finally used to sheds light on the last stage of transition in these two cases.

## 4. References

(1) Ou, J., Perot, B. & Rothstein, J. P. 2004 Laminar drag reduction in microchannels using ultrahydrophobic surfaces. Physics of Fluids 16, 4635–4643
(2) Bottaro, A. & Naqvi, S. 2020 Effective boundary conditions at a rough wall: a high-order homogenization approach. Meccanica 55.
(3) Pralits, J., Alinovi, E. & Bottaro, A. 2017 Stability of the flow in a plane microchannel with one or two superhydrophobic walls, Physical Review Fluids 2, 013901
(4) Seo, J. & Mani, A. 2016 On the scaling of the slip velocity in turbulent flows over superhydrophobic surfaces. Physics of Fluids 28, 025110.
(5) Schmid, P. J. & Brandt, L. 2014 Analysis of Fluid Systems: Stability, Receptivity, Sensitivity. Applied Mechanics Reviews 66, 024803

# Multiscale Analysis and Texture Design for Interfaces Hydrodynamically Lubricated by Variable Viscosity and Density Liquids

Sarp Ilgaz KOÇ[1,*], İlker TEMIZER[1], Luca BIANCOFIORE[1]

1: Department of Mechanical Engineering, Bilkent University, Ankara, TR

* Corresponding author: Tel.: +90 539 727 7733; Email: ilgaz.koc@bilkent.edu.tr

**Abstract:** Optimization is fundamental in lubrication as it is utilized to minimize the energy and durability loss due to friction. To be able to analyze such systems, efficient and accurate mathematical and numerical techniques are required during the modeling and the computation process. Although direct analyses of smooth surfaces for Newtonian flows are well documented in literature, analysis for rough surface textures can be challenging both in terms of modeling and solution. As roughness increases, the accuracy of the available models decreases while the necessary computational cost increases substantially. In this work, a model is developed for piezoviscous, compressible and shear-thinning lubricants using the modified viscosity approach [1] alongside homogenization [2] as a mathematical technique for the solution of the Reynolds equation to alleviate the inherent computational difficulties to model roughness. Figure 1 shows the pressure profile for two different geometries: a wedge (a) and a parabolic slider (b). The roughness in these cases is assumed to be sinusoidal. Our results demonstrate good agreement between rough and homogenized results. Furthermore, we use our model to optimize the topology of the interfaces lubricated by both variable density and viscosity to minimize the energy loss.

**Keywords:** Reynolds equation, Homogenization, Piezoviscosity, Compressibility, Shear-thinning, Optimization.

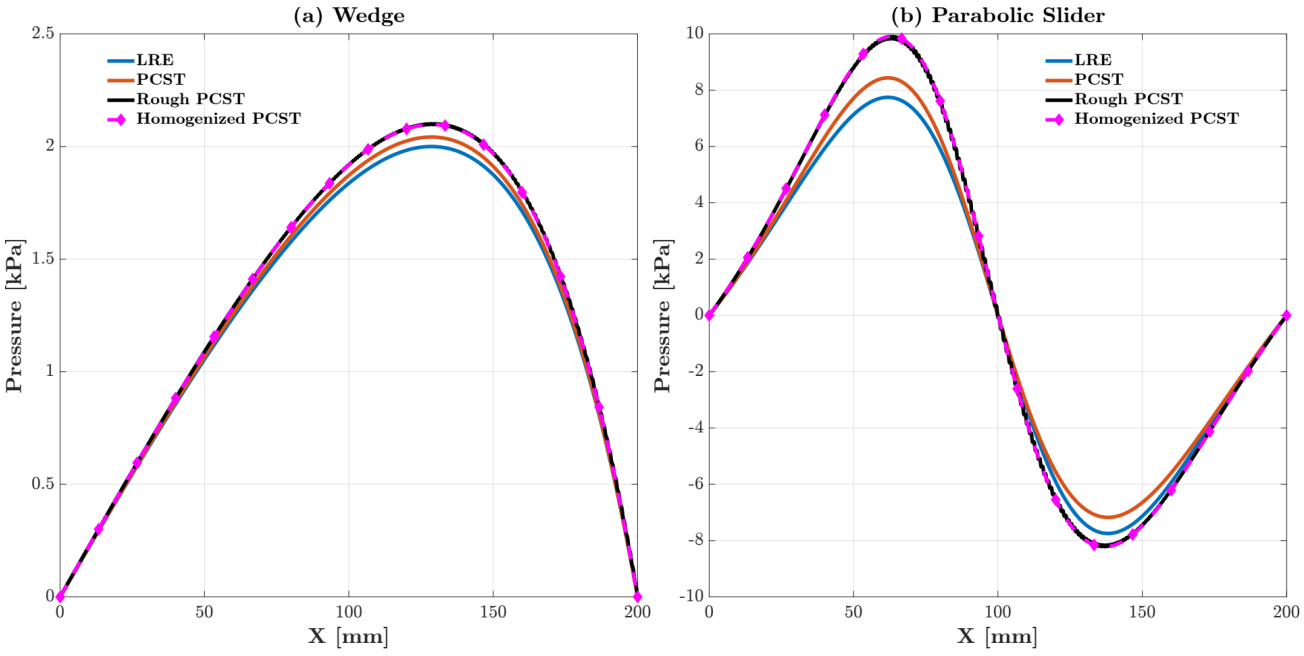


**Figure 1 Wedge and Parabolic Slider Pressure Results:** Pressure profile obtained for different models for (a) wedge and (b) parabolic slider. The basic linear Reynolds equation (LRE) is depicted by blue lines, while the piezoviscous, compressible and shear-thinning case (PCST) is depicted by red lines, rough PCST (black lines) indicates that the sinusoidal roughness is applied to the PCST case, and finally homogenized PCST (magenta lines) means that roughness is applied to the PCST case but the pressure profile is obtained using homogenization.

# References

[1] H. Ahmed and L. Biancofiore, "A modified viscosity approach for shear thinning lubricants," *Physics of Fluids, vol. 34, no. 10, p. 103103, Oct. 2022, doi: https://doi.org/10.1063/5.0108379.*

[2] B. A. Çakal, İ. Temizer, K. Terada, and J. Kato, "Microscopic design and optimization of hydrodynamically
interfaces," *International Journal for Numerical Methods in Engineering*, vol. 120, no. 2, pp. 153–178, Jun. 2019, doi: https://doi.org/10.1002/nme.6129.

# Linear Stability Of A Channel Flow Over a Superhydrophobic Surface

Antoine JOUIN[1,2,*], Stefania CHERUBINI[1], Jean-Christophe ROBINET[2]

1: DMMM, Politecnico di Bari, Bari, IT
2: DynFluid Laboratory, Arts et Métiers, Paris, FR

* Corresponding author: Tel.: +33 7 50 83 88 45; Email: antoine.jouin@ensam.eu

**Abstract:** The linear stability of superhydrophobic and liquid-infused surfaces is investigated in order to better understand interface failure mechanisms. Interface deformation is explicitly taken into account through a linearized Young-Laplace equation. The linear stability problem is solved with a Bloch wave formalism coupled with a two-dimensional stability problem. Two types of unstable modes could be found: modified Tollmien-Schlichting waves and capillary pressure waves.

**Keywords:** Superhydrophobic surfaces, Stability, Bloch waves, Capillary waves

## 1. Introduction

Superhydrophobic (SH) and liquid-infused surfaces present a considerable interest due to their drag-reducing properties. In these configurations, the flow over such a surface only sees a fraction of the solid rough surface and slips on the lubricant interfaces. However, this Cassie-Baxter state, in which the lubricant remains trapped, may not be durable as the interface between the two species becomes unstable and leads to the depletion of the superhydrophobic layer (the so-called *wetting* transition). Two failure mechanisms could be observed and identified: the development of capillary pressure waves, highly detrimental to the interface stability [1] and eventually inducing a roughness effect degrading the drag reduction [2], and mass diffusion of the trapped gas [3]. Most of this work is dedicated to the former and, in particular, how linear stability can help our understanding of the failure mechanisms of these surfaces.

## 2. Problem formulation

The influence of a SH wall on the channel flow stability is investigated. Grooves are now fully filled with gas and the liquid is assumed in a Cassie-Baxter state. The bottom wall consists in a flat wall alternating solid patches and trapped pockets of lubricant. The whole pattern has a half periodicity s. For simplicity, it is assumed that the solid and SH patches have the same size. No-slip boundary conditions are imposed on the solid part, while a shear-free boundary condition is assumed for the gas. The interface is also assumed to be pinned to the riblets' edges [1]. Navier-Stokes equations govern the flow dynamics while the interface deformation $\eta$ is dictated by a linearized Young-Laplace equation [1]:

$$\nabla^2\eta = \frac{p_1}{We}$$

where $p_1$ is the pressure disturbance above the interface and $We = \rho U^{*2} h^*/\gamma$ is the Weber number with $\rho$ the density of the fluid and $\gamma$ the surface tension. Finally, a kinematic condition ensures the coupling between the different variables:

$$v = \frac{\partial\eta}{\partial t} + u\frac{\partial\eta}{\partial x} + w\frac{\partial\eta}{\partial z}$$

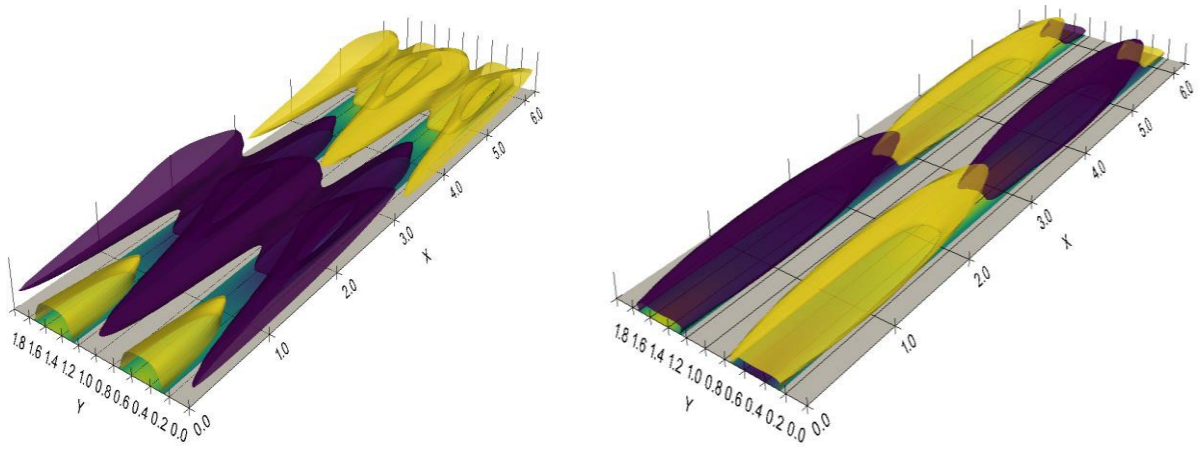


Figure 1: Streamwise velocity disturbance of the two unstable types of modes for $Re$ = 5000, $We$ = 12, $\alpha$ = 1 and $s$ = 0.3. Left: fundamental modified Tollmien-Schlichting wave. Right: subharmonic capillary pressure wave. Only the lower part of the channel for the sake of visualization.

Assuming viscous flow, a two-dimensional laminar base flow $U_0(y, z)$ can be found. The previous equations are linearised around this base flow and considering normal modes, a two-dimensional stability problem can be obtained. This problem quickly becomes too computationnally expensive to solve if the number of SH patches considered is large. To adress this issue, the framework based on a Bloch wave formalism and introduced in [4] is employed.

## 3. Results

The stability of the flow over a superhydrophobic wall is investigated for $Re = 5000$, $We = 10$, $\alpha = 1$ and several periodicities s. The most striking feature is the apparition of a new spatial branch associated with subharmonic capillary pressure waves competing with the fundamental Tollmien-Schlichting branch. Besides, the surface seems to have a limited influence on the growth rate: only larger periodicities s lead to unstable growth rates. Eigenfunctions corresponding to the two families of modes are displayed for $s = 0.3$ in figure 1. The first mode, which is the most unstable for small pattern periodicity, bears a strong resemblance with a Tollmien-Schlichting wave deformed by the presence of slip patches. Whereas, larger patterns tend to favour the subharmonic capillary mode, characterised by the propagation of a pressure disturbance on the interface. In this latter case, the streamwise velocity component assumes the largest values near the interface, while the cross-flow shows the development of large-scale vortices between two superhydrophobic patches.

## References

[1] J. Seo, R. García-Mayoral, and A. Mani, Pressure fluctuations and interfacial robustness in turbulent flows over superhydrophobic surfaces, Journal of Fluid Mechanics, vol. 783, pp. 448–473, 2015.

[2] J. Sundin, S. Zaleski, and S. Bagheri, Roughness on liquid-infused surfaces induced by capillary waves', J. Fluid Mech., vol. 915, p. R6, 2021.

[3] H. Ling, J. Katz, M. Fu, and M. Hultmark, Effect of Reynolds number and saturation level on gas diffusion in and out of a superhydrophobic surface, Phys. Rev. Fluids, vol. 2, no. 12, p. 124005, 2017.

[4] P. J. Schmid, M. F. de Pando, and N. Peake, Stability analysis for n-periodic arrays of fluid systems', Phys. Rev. Fluids, vol. 2, no. 11, p. 113902, 2017.

# A Homogenization-Based Analysis of Turbulent Channel Flows over Transversely Isotropic Porous Beds

Essam Nabil AHMED[1], Alessandro BOTTARO[1,*]

1: DICCA, Università degli Studi di Genova, Genova, IT

* Corresponding author: Email: alessandro.bottaro@unige.it

**Abstract:** The turbulent flow in a channel bounded from one side by a smooth, impermeable wall and from the other side by a transversely isotropic porous substrate (of porosity $\theta$ = 0.5) with either streamwise- or spanwise-preferential permeability is numerically studied; the velocity components at the fictitious interface between the permeable bed and the channel flow region are described by homogenization-based, effective boundary conditions, able to macroscopically mimic the influence of the porous medium on the overlying turbulent boundary layer. This procedure allows to bypass the numerical resolution of the flow within the pores of the substrate and thus to alleviate the mesh requirements and accelerate the direct numerical simulations (DNS). The mean velocity profiles and the turbulence statistics next to the different permeable walls are analyzed, and the consequent effects on the skin-friction drag are interpreted. Drag reduction (up to 5%) is achieved with substrates of streamwise-preferential permeability, capable to mitigate the intensity of turbulent fluctuations; however, in analogy to the behavior observed for the case of riblets, performance degradation is observed when the pattern periodicity exceeds a value of about 15 wall units.

**Keywords:** Permeable Walls, Turbulence, Drag Reduction, Homogenization, Effective Conditions

## 1. Introduction

Properly engineered surfaces/substrates can favorably interact with the overlying turbulent boundary layer, and thus be used as a passive drag reduction strategy. While porous media with either isotropic or spanwise-preferential permeability are known to increase skin-friction drag [1, 2], a favorable effect is obtainable with permeable beds of streamwise-preferential permeability [2, 3]. We employ here the same upscaling approach and effective boundary conditions described in [2] to study the turbulent flow in a channel bounded by a single permeable wall, considering four types of solid inclusions, and varying the pitch distance of the porous pattern.

## 2. Effective Boundary Conditions

The microscale problem within the pores of the substrate is first analyzed; the microscopic variables are asymptotically expanded in terms of a small parameter $\epsilon$ representing the ratio between the pitch distance of inclusions ($\ell$) and half the channel height ($H$). Applying continuity of the velocity and traction vectors at the matching interface with the macroscopic, channel flow domain, we obtain the following second-order accurate effective boundary conditions for the three velocity components:

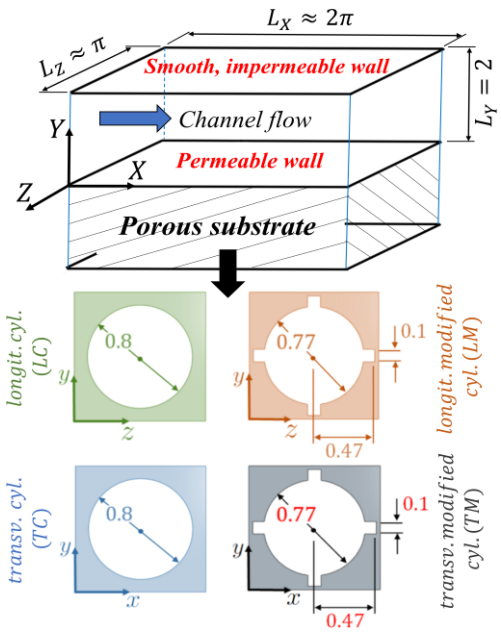


**Fig. 1.** (top) Sketch of the computational domain for the macroscale problem with the effective BCs imposed at $Y$= *0*; (bottom) geometries of the porous media under study with the dimensions shown on a 1×1 unit cell, yielding a porosity of 0.5.

$$U(X,0,Z,t) = \epsilon\lambda_x S_{12} + \epsilon^2 \mathcal{K}_{xy}^{itf} \frac{\partial S_{22}}{\partial X}, \quad (1)$$

$$V(X,0,Z,t) = -\epsilon^2 \left[\mathcal{K}_{xy}^{itf} \frac{\partial S_{12}}{\partial X} + \mathcal{K}_{zy}^{itf} \frac{\partial S_{32}}{\partial Z}\right] + \epsilon^2 \mathcal{K}_{yy} \frac{\partial S_{22}}{\partial Y}, \quad (2)$$

$$W(X,0,Z,t) = \epsilon\lambda_z S_{32} + \epsilon^2 \mathcal{K}_{zy}^{itf} \frac{\partial S_{22}}{\partial Z}, \quad (3)$$

with $X$, $Y$, and $Z$ the macroscopic coordinates (normalized by $H$) and $S_{12}$, $S_{22}$, and $S_{32}$ the components of the normalized macroscopic stress tensor. The dimensionless Navier-slip coefficients ($\lambda_x$ and $\lambda_z$), interface-permeability ($\mathcal{K}_{xy}^{itf}$ and $\mathcal{K}_{zy}^{itf}$), and medium permeability ($\mathcal{K}_{yy}$) are all dependent on the microscopic details of the porous pattern. Typical geometries of the solid inclusions under study, either longitudinal (*LC* and *LM*) or transverse (*TC* and *TM*), are sketched in Fig. 1; refer to [2] for values of the model coefficients.

## 3. Sample Results

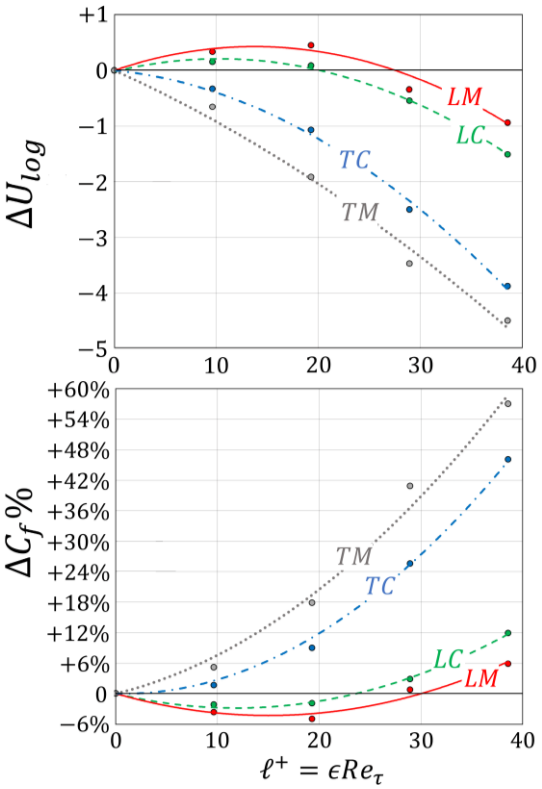


**Fig. 2.** Shift of the intercept of the logarithmic velocity profile due to the presence of the permeable wall ($\Delta U_{log}$) and consequent percentage change in skin-friction coefficient ($\Delta C_f$ %), plotted against the periodicity of different porous beds measured in wall units ($\ell^+$).

The mean velocity profiles above the porous structures under study are analyzed at a shear-velocity Reynolds number $Re_\tau \approx 190$, with $\epsilon$ varied between 0.05 ($\ell^+ \approx 10$) to 0.2 ($\ell^+ \approx 40$). A major parameter is the positive/negative shift of the velocity profile in the log-law region ($\Delta U_{log}$) relative to the reference impermeable-channel case ($\epsilon = 0$), which can be linked to the reduction/increase of skin-friction coefficient $C_f$, as shown in Fig. 2. A drag-reducing effect is attainable with the patterns *LC* and *LM*, having streamwise-preferential permeability/slip. An upper bound of drag reduction is found at $\ell^+ \approx 15$. Triggering of Kelvin–Helmholtz-like rollers [3] may be responsible for performance degradation beyond this limit. By contrast, $C_f$ increases monotonically with $\ell^+$ for transverse inclusions (*TC* and *TM*). The analysis of turbulent statistics provides interpretation of the aforementioned behaviors. Distributions of velocity fluctuations in the buffer layer are presented in Fig. 3; porous media with longitudinal inclusions yield a field with regular elongated streaks and mild near-wall vortical structures.

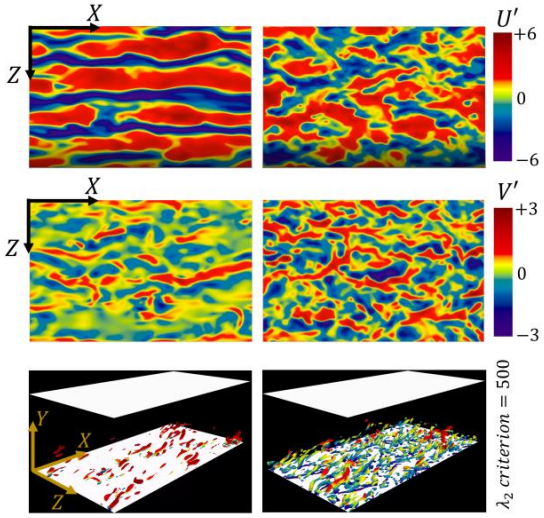


**Fig. 3.** Instantaneous distributions of (top) streamwise and (middle) wall-normal velocity fluctuations over a horizontal plane at $Y^+ = 20$, for the porous substrates (left) *LM*, $\ell^+ \approx 20$ and (right) *TM*, $\ell^+ \approx 40$. Corresponding vortical structures are shown in the bottom frame.

## 4. References

[1] Rosti, M.E., Cortelezzi, L., Quadrio, M., 2015. Direct numerical simulation of turbulent channel flow over porous walls. *J. Fluid Mech.* **784**, 396–442.

[2] Ahmed, E.N., Naqvi, S.B., Buda, L., Bottaro, A., 2022. A homogenization approach for turbulent channel flows over porous substrates: Formulation and implementation of effective boundary conditions. *Fluids* **7** (5), 178.

[3] Gómez-de Segura, G., García-Mayoral, R., 2019. Turbulent drag reduction by anisotropic permeable substrates–analysis and direct numerical simulations. *J. Fluid Mech.* **875**, 124–172.

## SESSION 1c
## Fluid flow in microchannels and porous media
Chair: **K. Hooman**



Eesha KULKARNI[1], Chayan DAS[1] , Shanmuganathan RAMAN[1] , Soumyadip SETT[1]
1: Department of Mechanical Engineering, Indian Institute of Technology Gandhinagar, Gujarat, India



Josiah JORDAN[1], Duncan A. LOCKERBY[1]
1: School of Engineering, University of Warwick, Coventry, CV5 7AL



Bernardo BUONOMO[1], Oronzio MANCA[1], Sergio NARDINI[1], Safa SABET[1]
1: Dipartimento di Ingegneria, Università degli Studi della Campania "Luigi Vanvitelli", Aversa (CE), IT


Pamela VOCALE[1], Gian Luca MORINI[2]

1: Department of Engineering and Architecture, University of Parma, Parma, IT
2: DIN, Alma Mater Studiorum - Università di Bologna, Bologna, IT

# Computer Vision Enabled Dropwise Condensation Heat Transfer Measurement

Eesha KULKARNI[1], Chayan DAS[1] , Shanmuganathan RAMAN[1] , Soumyadip SETT [1, *]

1: Department of Mechanical Engineering, Indian Institute of Technology Gandhinagar, Gujarat, India

* Corresponding author: Tel.: +91 9687987443; Email: soumyadipsett@iitgn.ac.in

**Abstract:** Vapour condensation is a ubiquitous process that is widely used in industrial applications for heat and energy transfer. Dropwise condensation, where the condensate forms discrete droplets on the condenser surface which are subsequently removed leading to continuous replenishment of nucleation sites, has been shown to have 5-7X higher heat transfer coefficients compared to its counterpart filmwise condensation. The rapid condensate droplet growth and departure during dropwise condensation often makes heat transfer quantification a major challenge. In this work, a computer-vision based framework is developed to quantify condensation mass flux by accurately identifying the non-planar near-spherical droplets as captured during condensation on a flat, hydrophobic copper surface. The condensate droplet sizes, distribution, growth rate and departure information are acquired from the time-lapsed images using a Mask RCNN network. A motion tracker is used to track a droplet's trajectory as it slides down a flat surface during condensation, and from the departure droplet sizes and frequencies, the condensation mass flux is calculated to compute the heat transfer coefficient. Our work applies computer vision techniques on large-scale condensers and paves the way to train machine learning models for predicting heat transfer coefficients in applications where imaging is not feasible.

**Keywords:** Dropwise condensation, Superhydrophobic, Heat transfer coefficient, Computer vision, Machine learning

## 1. Introduction

Industrial applications such as power plants, desalination, building heating-cooling (HVAC), and thermal management of electronics and batteries heavily rely on condensation for effective heat and energy transfer. Vapor can condense on a surface either in the form of discrete droplets, termed as dropwise condensation (DWC), or in the form of continuous film, termed as filmwise condensation (FWC). DWC involves rapid droplet growth, coalescence, and condensate droplets departing from the condenser surface. Due to the continuous replenishment of the nucleation sites, DWC has been shown to have 5-7X enhancement[1] in heat transfer performance as compared to its counterpart FWC. In many cases, it becomes difficult to measure the relevant temperatures and saturation pressure during the condensation process, and accurate quantification of heat transfer becomes a challenge[2]. More importantly, considering the large number of condensate droplets on a surface, measuring individual droplet growth rate, droplet size distribution and condensate droplet departure radius becomes challenging. To overcome this challenge, in this work, we employ computer vision techniques to capture the condensate droplet dynamics from time interval images taken during water vapor condensation on copper-based condenser surfaces. Utilizing simultaneous techniques of grayscaling, thresholding, edge detection, and contour detection, we measure the necessary droplet parameters (growth rate, droplet size distribution, departure radii, etc.) from the images which allows us to compute the condensation heat transfer coefficients.

## 2. Results & Discussion

Computer vision (CV) and machine learning (ML) are increasingly being applied to heat transfer applications[3]. In this study, we use the Mask RCNN model[4] to generate the necessary data set from the images captured during vapor condensation. Flat copper tabs (50 mm x 50 mm) are used as the condenser

surfaces, which are rendered hydrophobic by standard chemical vapor deposition of silane[5]. The copper surfaces are mounted on a Peltier element kept inside a chamber and the surface temperature maintained at 10 ºC. The chamber is maintained at ambient conditions ($T_{amb}$ = 28 ºC, RH = 75%), facilitating atmospheric water vapor condensation on the copper surface. Images of the condensation process are taken using a DSLR camera at regular time intervals, which are then processed using computer-vision algorithm. We use the Mask RCNN model, a deep learning model for instance segmentation, which identifies individual objects within an image and assigns a unique label to each object. In each image, individual droplets are identified and area calculated, from which the droplet size distribution is predicted (Fig. 2).

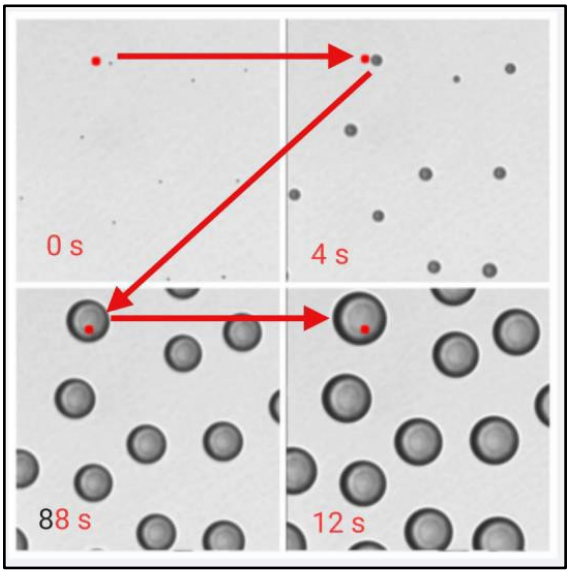


Figure 1.Tracking droplets as their size changes

Moreover, we study the trajectory of individual droplet as it slides down the non-wetting surface using a motion tracker from the images captured during experimentation. A motion tracker or object tracker primarily does two tasks - detecting the objects and linking them through different frames. Here, the motion tracker is built using the open CV function of Optical Flow which uses the Lucas-Kanade tracking algorithm. The tracking algorithm operates by estimating the motion between two consecutive frames of an image or video sequence by solving a system of linear equations using a set of sparse optical flow vectors. All in all, we use the deep learning network and motion tracking algorithm to understand and predict the relation between the droplet characteristics and eventually study its impact on the heat and mass transfer and analyze the heat transfer coefficient trends in the dropwise condensation process.

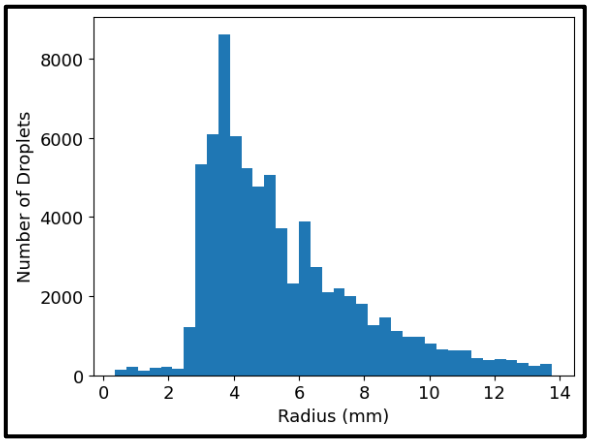


Figure 2. Typical droplet size distribution as captured from image processing during condensation on functionalized copper surface.

## References

[1] Enright, Ryan, Nenad Miljkovic, Jorge L. Alvarado, Kwang Kim, and John W. Rose. "Dropwise condensation on micro-and nanostructured surfaces." *Nanoscale and Microscale Thermophysical Engineering* 18, no. 3 (2014): 223-250.

[2] El Fil, Bachir, Girish Kini, and Srinivas Garimella. "A review of dropwise condensation: Theory, modeling, experiments, and applications." *International Journal of Heat and Mass Transfer* 160 (2020): 120172.

[3] Yang B, Zhu X, Wei B, Liu M, Li Y, Lv Z, Wang F. Computer Vision and Machine Learning Methods for Heat Transfer and Fluid Flow in Complex Structural Microchannels: A Review. *Energies*. 2023; 16(3):1500. https://doi.org/10.3390/en16031500

[4] He, Kaiming & Gkioxari, Georgia & Dollar, Piotr & Girshick, Ross. (2017). Mask R-CNN. 2980-2988. 10.1109/ICCV.2017.322.

[5] Chavan, Shreyas, et al. "Heat transfer through a condensate droplet on hydrophobic and nanostructured superhydrophobic surfaces." *Langmuir* 32.31 (2016): 7774-7787.

# Simulation of low-speed gas flows around fractal-like micro-scale particulate

Josiah JORDAN[1,*], Duncan A. LOCKERBY[1]

1: School of Engineering, University of Warwick, Coventry, CV5 7AL

* Corresponding author: Email: j.jordan.2@warwick.ac.uk

**Abstract:** We briefly outline the concept of the Method of Fundamental Solutions (MFS) applied to Grad's 13 moment (G13) equations originally developed by Grad (1949) to simulate low-speed flow around micro-scale particles of arbitrary geometry. We then apply the G13-MFS to soot particles – an omnipresent anthropogenic micro-scale particle – confirming the G13-MFS with previous results and use these to discuss the apparent systematic disparity between numeric and experimental results on soot particles (and similar particles). It was shown that the orientation of the soot particle, the most common explanation used for this disparity, can only be a partial explanation.

**Keywords:** Gas Particulate Flows, Method of Fundamental Solutions, Method of Reflections, Knudsen number, Fractal Aggregates, Soot

## 1. Introduction

Low-speed gas flow around micro-scale particles (e.g. soot and other pollutants), and through suspensions of particles, are surprisingly rich in physics and challenging to simulate. On top of the usual challenge of simulating low-Reynolds number flow around particles, their scale renders the conventional Stokes equations, and associated boundary conditions, inaccurate, and unable to capture rarefied effects such as thermophoresis and velocity slip [1, 2].

The problems are especially challenging for non-canonical geometries in the transitional Knudsen-number regime (the Knudsen number ($Kn$) is defined as the ratio of the molecular mean-free-path to the characteristic scale of the particle). In this paper we present an accurate and efficient framework for simulating micro-scale particulate flows in the transition regime to overcome the aforementioned challenges. This is by using the Method of Fundamental Solutions (MFS), applied to the linearised Grad's 13 moment (G13) equations [3], which provides a convenient and numerically efficient alternative to solving the full Boltzmann equation [4] for non-trivial geometries, such as soot particles.

## 2. Methodology

A fundamental solution to the linearised G13 equations can be viewed as the flow response to a point force ($\boldsymbol{f}$) and a point heat source ($g$) applied at a particular location in 3D space (a *singularity site)*. In the MFS, we use a superposition of these solutions, located at an array of $M$ singularity sites, to satisfy boundary conditions at $N$ locations on an interface (*boundary nodes*). Here, we restrict our attention to particles and the flows external to them; in this case the nodes are chosen to cover the particle's surface with the singularity sites located internally – see Figure 1 for illustration.

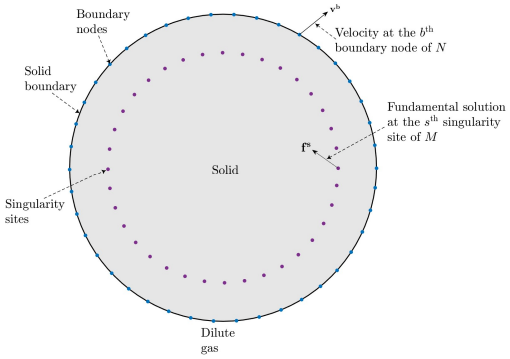


Figure 1 - Illustration of the MFS for a single particle, adapted from [5].

By superposition of these fundamental solutions, collectively satisfying the chosen boundary conditions, variables such as velocity and temperature can be found at any point in the

flow domain, and global properties such as total drag force can be obtained via a set of linear equations.

## 3. Application to Soot Particles

Soot particles are omnipresent in human environments and can be accurately modelled as fractal aggregates: an array of point contact spheres whose radius of gyration, $R_g$, scales with the number of spheres, $N$, according to the fractal scaling law [6]:

$$N = k_f \left(\frac{R_g}{R}\right)^{D_f} \quad (1)$$

where $k_f$ is the pre-factor that determines anistropy, $D_f$ is the fractal dimension that determines compactness, and $R$ is the radius of a single sphere. Soot particles formed via Brownian motion have, typically, $D_f \approx 1.8$ and $k_f \approx 1.3$ [6]. An example soot particle is shown in Figure 2 along with tracer particles of flow around the soot particle.

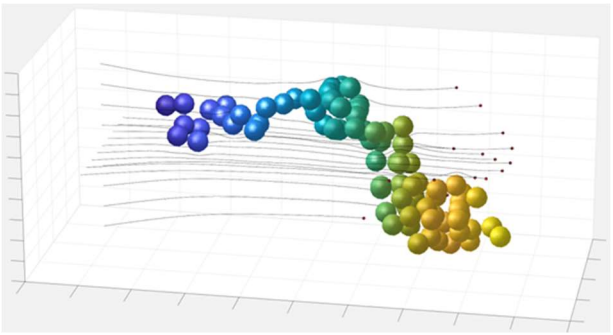

Figure 2 - Illustrative flow around a soot particle; individual carbon spheres coloured by surface temperature.

Using the MFS, we can efficiently calculate the drag on soot particles up to moderate Knudsen numbers. The drag on soot particles has been observed to scale with size in accordance with a power law [6], however there is a systematic disparity between numerical and experimental results as to the precise nature of this scaling in the transition regime.

To investigate this using the MFS, a $6 \times 6$ resistance tensor, $\mathcal{R}$, can be easily found relating the force ($\boldsymbol{f}$) and torque ($\boldsymbol{\tau}$) vectors, $\boldsymbol{F} = [\boldsymbol{f}, \boldsymbol{\tau}]$ to the velocity ($\boldsymbol{v}$) and angular velocity ($\boldsymbol{\omega}$) vectors $\boldsymbol{V} = [\boldsymbol{v}, \boldsymbol{\omega}]$ by [7]:

$$\boldsymbol{F} = \mathcal{R} \cdot \boldsymbol{V}. \quad (2)$$

From this tensor, calculated with the MFS, the effect of orientation on the drag on soot particles can be calculated, in an attempt to explain this disparity – the most common explanation used for this disparity (see, e.g. [8]). Figure 1 compares the scaling given in a review of experimental work [6] with results from the MFS for: the orientationally averaged drag, the hydrodynamically stable drag (zero torque), the drag when aligned with an external electric field, and the minimum possible drag.

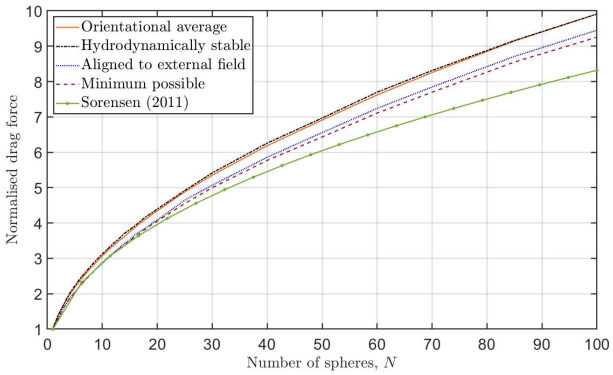


Figure 3 – comparison of the normalised drag force of different orientations, calculated by the MFS with the result from a review of experimental works [6].

Evidently, even the lowest possible drag in any orientation (the smallest eigenvalue of $\mathcal{R}$), as calculated by the MFS is still larger than the Sorensen result, meaning orientation is not the sole factor causing the disparity.

## References

[1] D. A. Lockerby and Reese J. M., "On the modelling of isothermal gas flows at the microscale," J. Fluid Mech., vol. 604, pp. 235-261, 2008.

[2] J. B. Young, "Thermophoresis of a Spherical Particle: Reassessment, Clarification, and New Analysis," Aerosol Science and Technology, vol. 45, pp. 927-948, 2011.

[3] H. Grad, "On the kinetic theory of rarefied gases," Commun. Pure Appl. Maths, vol. 2, pp. 331-407, 1949.

[4] D. A. Lockerby and B. Collyer, "Fundamental solutions to moment equations for the simulation of microscale gas flows," J. Fluid Mech., vol. 806, pp. 413-436, 2016.

[5] L. D. A. and B. Collyer, "Fundamental solutions to moment equations for the simulation of microscale gas flows," J. Fluid Mech., vol. 806, pp. 413-436, 2016.

[6] C. M. Sorensen, "The Mobility of Fractal Aggregates A Review," Aerosol Science and Technology, vol. 45, no. 7, pp. 765-779, 2011.

[7] J. Happel and H. Brenner, Low Reynolds number hydrodynamics: with special applications to, First ed., Springer Netherlands, 1967.

[8] J. Corson, G. W. Mulholland and M. R. Zachariah, "The effect of electric-field-induced alignment on the electrical mobility," Aerosol Science and Technology, vol. 52, p. 524, 2018.

# Local thermal equilibrium analysis of thermally developing forced convection in micro-channels with porous media and viscous dissipation

Bernardo BUONOMO[1,*], Oronzio MANCA[1], Sergio NARDINI[1], Safa SABET[1]

1: Dipartimento di Ingegneria, Università degli Studi della Campania "Luigi Vanvitelli", Aversa (CE), IT

* Corresponding author: Tel.: +39 0815010358; Email: bernardo.buonomo@unicampania.it

**Abstract:** The study investigates a dilute gas flowing through a parallel-plate microchannel filled with porous media, where the flow is hydrodynamically fully developed and thermally developing. Additionally, the viscous dissipation effect is taken into consideration while assuming local thermal equilibrium, or LTE. The study provides results for a Knudsen number range of 0 to 0.1, which includes dimensionless wall temperature profiles, Nusselt number, dimensionless fluid and solid phases, and entropy generation values.

**Keywords:** Micro-channel; Porous Media; Thermally developing flow; Local thermal equilibrium; Viscous dissipation

## 1. Introduction

The growing interest in miniaturized thermofluid systems due to the application in micro manufactured devices such as biomedical instrumentations, electronic packaging, micro-mechanics and avionics has determined an increasing development of research activity in fluid flow and heat transfer in microchannels. At these scales the phenomenon of rarefaction or Knudsen flow should be considered and the Navier-Stokes and energy equations in the continuum flow model could not be completely appropriated to describe the fluid flow and heat transfer [1,2]. The modeling in micro flow depends on the Knudsen number defined as the ratio of the fluid mean free path to the macroscopic length scale of the physical system. It allows to have a measure of the degree of rarefaction of gases which flow through very small channels and, consequently, of the degree of the validity of the continuum model [3]. A greater part of the investigations, both experimental and numerical, have been accomplished on forced convection gas flow in order to evaluate the pressure drop and the convective heat transfer in microchannels and microtubes [3]. Recently, research interest is developing on microchannels and microtubes filled with porous medium due to their applications in micro filtration, fractionation, catalysis and microbiology, as underlined in [2]. However, forced convection in porous channels and tubes in rarefied condition or in porous microchannels and microtubes have not been diffusely studied and analytical and/or numerical solutions on different geometrical and thermal conditions should be examined. Moreover, some phenomenological aspects related to porous microchannels and microtubes have received a small attention [2].

It seems that there is a lack of studies on thermally developing flow in microchannels or channels in rarefied gas filled with porous media, mainly for microchannels or channels with viscous dissipation [4]. In the present study a hydrodynamically fully developed and thermally developing flow of a dilute gas in a parallel-plate microchannel filled with porous media with viscous dissipation effect is carried out assuming the local thermal equilibrium, LTE. The forced convective flow through the porous matrix is assumed laminar and incompressible, with constant thermo-physical properties and the walls of the microchannel is assumed at assigned uniform temperature. The porous solid matrix is assumed isotropic and homogeneous. Solutions for Darcy extended

Brinkman model are evaluated and the heat transfer analysis is performed. Results, for Knudsen number range 0–0.1, in terms of dimensionless wall temperature profiles, Nusselt number, dimensionless fluid and solid phases and entropy generation values are given for various parameters values such as Darcy number and Brinkman number.
In Figure 1 the examined geometry is depicted.

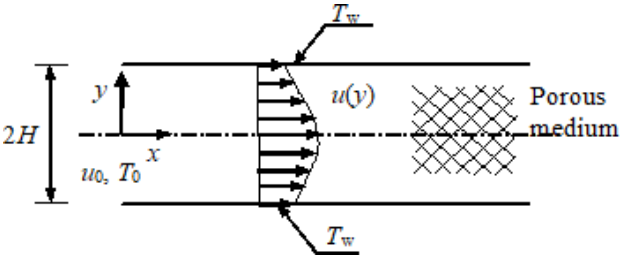


Figure 1. Sketch of the parallel-plate microchannel with porous medium.

Some results in terms of Nusselt number profiles along the microchannel are presented in Figure 2.

## Acknowledgements

This research was funded by Ministero dell'Istruzione, dell' Università e della Ricerca (MIUR), grant number PRIN-2017F7KZWS

## References

[1] Torabi, M., Karimi, N., Torabi, M., Peterson, G.P., Simonson, C.J., Generation of entropy in micro thermofluidic and thermochemical energy systems-A critical review, 2020 Int. J. Heat Mass Transfer 163,120471.

[2] Japar, W.M.A.A., Sidik, N.A.C., Saidur, R., Asako, Y., Nurul Akmal Yusof, S., A review of passive methods in microchannel heat sink application through advanced geometric structure and nanofluids: Current advancements and challenges, 2020 Nanotech. Rev. 9(1), pp. 1192-1216.

[3] Asadi, M., Xie, G., Sunden, B., A review of heat transfer and pressure drop characteristics of single and two-phase microchannels, 2014 Int. J. Heat Mass Transfer 79, pp. 34-53.

[4] Monsivais, I.G., Méndez, F., Lizardi, J.J., Ramos, E.A. Impact of viscous dissipation on the conjugate heat transfer between the walls of a porous microchannel, 2022 Physica Scripta 97(6), 065002.

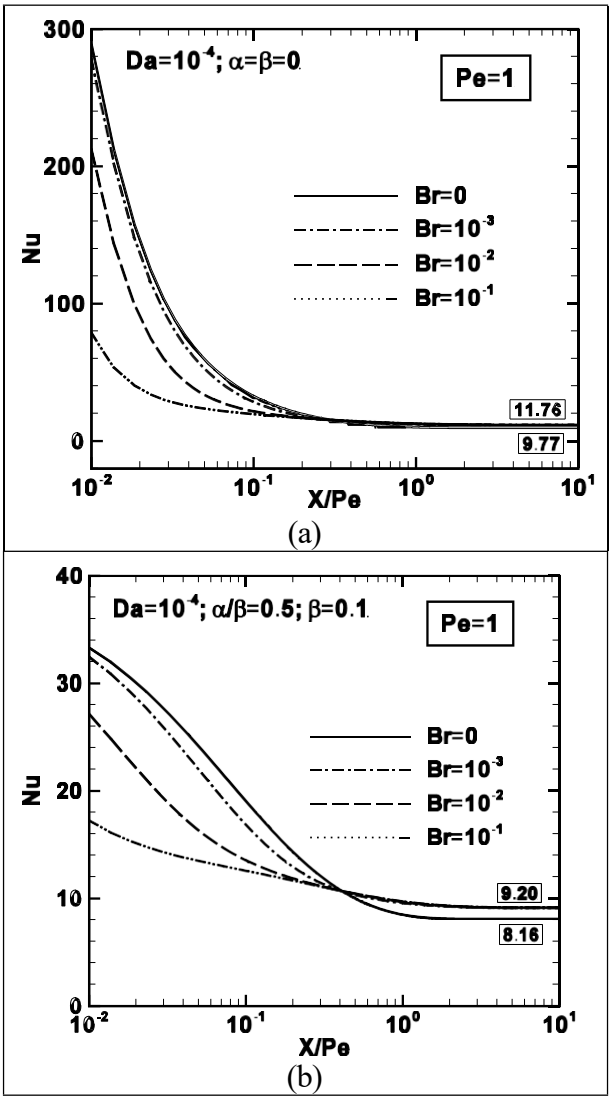


Figure 2. Nusselt number profiles as a function of X/Pe for Da=$10^{-4}$ and different Brinkman number: (a) Pe=1, α=β=0; (b) Pe=1, α/β=0.5 and with β=0.1.

# Rarefied Flows in Rhombic Microchannels under H2 Boundary Conditions

Pamela VOCALE[1,*], Gian Luca MORINI[2]

1: Department of Engineering and Architecture, University of Parma, Parma, IT
2: DIN, Alma Mater Studiorum - Università di Bologna, Bologna, IT

* Corresponding author: Tel.: +39 0521 905855; Email: pamela.vocale@unipr.it

**Abstract:** In this work, the influence of rarefied effects on fluid behavior in rhombic microchannels was numerically investigated. The analysis was carried out by considering a gaseous flow in laminar steady-state conditions and in hydrodynamically and thermally fully developed forced convection. The governing equations in the non-dimensional form were implemented and solved within the Comsol Multiphysics® environment, accounting for rarefaction and viscous dissipation effects. The data available in the literature were used to validate the numerical model. All comparisons showed perfect agreement. The numerical outcomes show that the Nusselt number decreases with increasing Brinkman number, while the influence of the rarefaction degree on the Nusselt number depends on the value of the acute angle and Brinkman number.

**Keywords:** Micro Flow, Rarefaction effects, viscous dissipation, noncircular cross-sections

## 1. Introduction

The combined effects of rarefaction and viscous dissipation were investigated in microchannels with circular, rectangular, trapezoidal, and elliptical cross-sections in microannulus and parallel plate microchannels [1].
However, other geometries need attention because of improvements in the microfabrication technique or the combination of simple geometries. Among these, rhombic microchannels can be found. They can be fabricated using a novel process [2] or can be obtained from triangular microchannels or from the etching of rectangular microchannels [3].
Therefore, only recently have the performance of microchannels featuring rhombic cross-sections been investigated. In particular, Saha et al. [3] presented a numerical investigation of the conjugate heat transfer of laminar water flows in rhombic microchannels by considering two different thermal boundary conditions. Their numerical outcomes highlighted that the effect of the acute angle on the Nusselt number is significant for acute angles greater than 10°.
However, to properly investigate the performance of microchannels, scaling effects should be accounted for.
In this work, the combined effects of rarefaction and viscous dissipation in microchannels with rhombic cross-sections are numerically investigated by considering a gaseous flow in laminar steady-state conditions in hydrodynamically and thermally fully developed forced convection.

## 2. Numerical procedure

### 2.1 Mathematical model

A Newtonian gas flowing in a rhombic microchannel was considered. By assuming a laminar fully developed flow and a fluid with constant properties, the Navier-Stokes equation in non-dimensional form was written as follows:

$$\frac{\partial^2 U}{\partial \xi^2} + \frac{\partial^2 U}{\partial \psi^2} = P \tag{1}$$

where $U$ and $P$ *are* the dimensionless velocity and pressure gradients, respectively. The compressibility effects were disregarded because of the low value of the Mach number [4].
The energy equation's non-dimensional form was written as follows:

$$\frac{\partial^2\theta}{\partial x^2}+\frac{\partial^2\theta}{\partial y^2}=\frac{U}{A^*}\left[L_P^*+Br\int_{A^*}\Phi^* dA^*\right]-Br\Phi^* \quad (2)$$

where $A^*$ is the dimensionless cross-sectional area ($A^*=A/D_h^2$), $L_P^*$ the dimensionless heated perimeter of the cross-section ($L_P^*=L_P/D_h$), and *Br is* the Brinkman number, which was defined as:

$$Br=\frac{\mu W^2}{qD_h} \quad (3)$$

being $\mu$ the fluid dynamic viscosity, $W$ the average fluid velocity, $q$ the wall heat flux, and $D_h$ the hydraulic diameter.

The rarefaction effects were accounted for by considering the first-order slip boundary condition and the temperature jump at the wall [5]:

$$U-U_w=\frac{2-\sigma_v}{\sigma_v}Kn\left(\frac{\partial U}{\partial n}\right)_w \quad (4)$$

$$\theta_w(x_w,y_w)=\theta(x_w,y_w)+\frac{2-\sigma_T}{\sigma_T}\frac{2k}{k+1}\frac{Kn}{\mathrm{Pr}} \quad (5)$$

where *Kn* is the Knudsen number and *Pr is* the Prandtl number.

The average Nusselt number was evaluated as follows:

$$Nu=\frac{h\,D_h}{\lambda}=\frac{1}{(\overline{\theta_w}-\theta_b)} \quad (6)$$

where $\overline{\theta_w}$ and $\theta_b$ were the average dimensionless wall temperature and the dimensionless bulk temperature, respectively.

### 2.2 Model validation and mesh independence analysis

The validation of the numerical model was carried out using the data available in the literature. In particular, closed-form solutions for fully developed slip flow [6] were used to validate the solution of the momentum equation, while the Nusselt numbers for no-slip flow [7] were used to validate the solution of both governing equations. A perfect agreement was found.

To obtain mesh-independent solutions, the results in terms of the Nusselt number obtained by adopting several grid resolutions were compared.

## 3. Main Results

Numerical outcomes reveal that the Nusselt number decreases with an increasing Brinkman number for all values of the Knudsen number and acute angle investigated here, as shown in Figure 1. Instead, the influence of the rarefaction degree on the Nusselt number depends on the value of the acute angle and the Brinkman number. The maximum reduction in the Nusselt number observed for an acute angle equal to 90° was 25%.

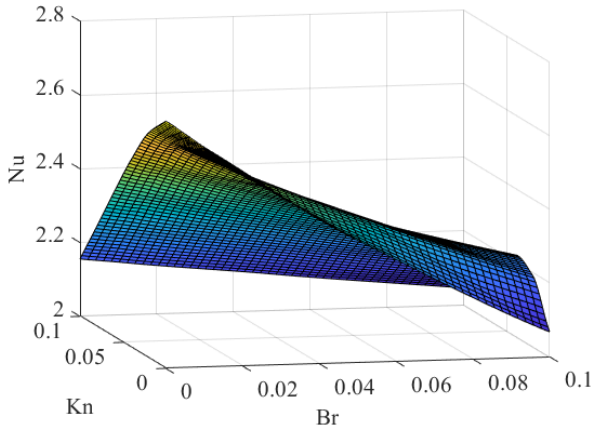


Figure 1. Nusselt number as a function of Knudsen and Brinkman numbers for $\varphi$=70.52°.

## 4. Conclusion

The results of the present study confirm that reducing channel size is not enough to enhance the convective heat transfer coefficient because of the presence of scaling effects.

## References

[1] Şen S., Darici S. 2017. https://doi.org/10.1016/j.applthermaleng.2016. 10.005
[2] Lee D.-K., Kwon J.Y., Cho Y.H. 2019. https://doi.org/10.1007/s00339-019-2600-2
[3] Saha S. K., Agrawal A., Soni Y. 2017. http://dx.doi.org/10.1016/j.ijthermalsci.2016.0 9.003
[4] Morini G.L., Spiga M. Tartarini P. 2004. https://doi.org/10.1016/j.spmi.2003.09.013
[5] Vocale P., Puccetti G., Morini G.L., Spiga M. 2014. https://doi.org/10.1088/1742-6596/547/1/012023
[6] Tamayol A., Hooman K. 2014. https://doi.org/10.1115/1.4004591
[7] Shah R.K., London A.L. 1978. Laminar flow forced convection in ducts.

## SESSION 2a
## Nanofluids and Applications
Chair: **B. Balakin**

**ELECTRICAL CONDUCTIVITY STUDIES ON IONIC LIQUIDS ENHANCED WITH NANOPARTICLES**

Elena Ionela CHERECHES[1], Alina Adriana MINEA[1]

1: Technical University ”Gheorghe Asachi” of Iasi, Romania, Faculty of Materials Science and Engineering, Bd. D. Mangeron, No. 63, 700050, Iasi, Romania

# Stability of a core-annular ferrofluid flow to axisymmetric and non-axisymmetric modes

Sarah FERGUSON BRIGGS[1,*], Mark BLYTH[2], Jonathan MESTEL[1]

1: Department of Mathematics, Imperial College London, UK
2: Department of Mathematics, University of East Anglia, UK

* Corresponding author: Email: sf218@ic.ac.uk

**Abstract:** The stability of a core-annular configuration of two concentric viscous ferrofluids in a straight, circular pipe is investigated, when an axial pressure gradient drives a base flow. In the absence of magnetic effects it is known that the base flow can inhibit capillary instabilities. A current-carrying, rigid wire runs along the axis of the pipe, producing an azimuthal magnetic field. Additionally, a constant axial field is applied across the domain. The two ferrofluids have different (constant) magnetic susceptibilities, producing a magnetic stress at the interface of the two fluids, which is stabilising or destabilising for different parameter regimes. The stability of both axisymmetric and non-axisymmetric modes is considered, in both linear and non-linear settings.

**Keywords:** Ferrofluids, Magnetic fluids, Core-annular flow, Stability.

## 1. Introduction

Ferrofluids are stable colloidal fluids, comprising of magnetic solids suspended in a carrier solution. Ordinarily, they behave as a Newtonian fluid, but in the presence of a magnetic field, the fluid becomes magnetised. They are therefore advantageous to many disciplines since they are easily manipulated by a field. For example, in magnetic drug targeting, a ferrofluid is bounded with the required drug, and directed to the target area using a magnetic field. From an engineering aspect, they are useful for heat dissipation and dynamic sealing since a magnetic field can be used in place of a structural support [1].

We develop on the work by [2], where a stationary ferrofluid column, centred on a current-carrying wire, surrounded by another ferrofluid of infinite domain, is investigated linearly. Here, we consider the effects of an outer-boundary, as well as the addition of a base-flow. These extensions prove relevant for oil transportation or magnetic drug targeting through arteries, where axial pressure driven flows in a pipe are utilised.

## 2. Formulation

A core-annular configuration is considered, where two concentric ferrofluids, with different constant magnetic susceptibilities, are within a solid, circular pipe. The flow is driven by an axial pressure gradient. A current-carrying wire runs along the axis of the pipe, producing an azimuthal field, and an axial constant field is applied across the domain.

Ferrofluids are treated as current-free with no free electric charge. They obey Maxwell's equations in the magneto-static limit, as well as an additional term in the stress-tensor, unique to ferro-hydrodynamics. For a colinear magnetisation and field, the stress-tensor for a ferrofluid is

$$\boldsymbol{T} = -\frac{\mu_0}{2}(1+\chi)H^2\boldsymbol{I} + (1+\chi)\boldsymbol{H}\boldsymbol{H}^T + \eta(\boldsymbol{\nabla u} + (\boldsymbol{\nabla u})^T),$$

where $\mu_0$ is the magnetic permeability of free space, $\chi$ is the magnetic susceptibility, $\boldsymbol{H}$ the magnetic field, $H = |\boldsymbol{H}|$, $\eta$ the viscosity, $\boldsymbol{u}$ the velocity, and $\boldsymbol{I}$ the identity matrix [3]. Since $\chi$ is piecewise constant, the magnetic forcing does not appear in the momentum equation. It does

however appear in the normal stress balance at the interface of the two fluids, namely,

$$[\boldsymbol{n} \cdot \boldsymbol{T} \cdot \boldsymbol{n}] = \sigma \boldsymbol{\nabla} \cdot \boldsymbol{n},$$

where **n** is the normal vector to the interface, $\sigma$ the surface tension, and the square bracket indicates the jump across the interface. Consequently, the magnetic forcing is confined to the interface of the two fluids, and not felt in the bulk of the fluids.

## 3. Stability

It has been well known since the work of Plateau [4] and Rayleigh [5], that capillary forcing acts to destabilise a cylindrical fluid column. Throughout the literature, it has been found that a static cylindrical system of two concentric fluids, with an outer boundary, still undergoes an instability due to surface tension [6].

Upon adding an axial flow, unstable modes can be dampened under certain conditions. Complete stabilisation can occur when the inner-fluid is more viscous than the outer-fluid. However, this requires a non-zero Reynolds number [6]. The addition of a wire or rod, running along the axis of the inner fluid, produces the same stability results for both a static and axial flow [6,7].

For magnetic fluids in the presence of a magnetic field, the magnetic forcing can act either to stabilise or destabilise the system, depending on the parameter values. Many works have studied a ferrofluid column in the presence of an azimuthal magnetic field, produced by a current-carrying wire positioned on the axis of the column. For a sufficiently strong current, the system is stable when the ferrofluid column is surrounded by a medium of lower magnetisation [8, 9, 10, 2]. However, [2] find that when the outer (unbounded) fluid is more magnetic than the inner fluid, increasing the current in the wire renders more modes unstable. In fact, non-axisymmetric modes are the most unstable. Nevertheless, it has been shown that applying an axial field can dampen all disturbances, apart from those in the long wave limit [2]. [2] postulate that an outer boundary would restrict these modes, and adding an axial field would then result in complete stabilisation, irrespective of which fluid is more magnetic.

Here, the effect of an outer boundary, base-flow, and magnetic field on the stability of the given system is explored, for zero and non-zero-Reynolds numbers. The influence of an azimuthal and axial field is investigated. Both $\chi_1 > \chi_2$ and $\chi_2 > \chi_1$ are considered, where $\chi_1$ is the magnetic susceptibility of the inner fluid and $\chi_2$ the outer fluid. The stability of the system is studied linearly and non-linearly, for both axisymmetric and non-axisymmetric modes.

## References

[1] *Scherer, C.; Figueiredo Neto, A.M.* (2005)
[2] *Ferguson Briggs, S.; Mestel, A.J.* (2022)
[3] *Rosensweig, R.E. (*1985)
[4] *Plateau, J. A. F. (*1873*)*
[5] *Rayleigh, L.* (1878)
[6] *Bassom, A.P. et. al.* (2012)
[7] *Dijkstra, H. A. (*1992*)*
[8] *Arkhipenko, V. I. et. al. (1980)*
[9] *Bashtovoi, V.; Kavkov, M. (1978)*
[10] *Canu, R. ; Renoult, M.-C. (2021)*

# Recent Research in Surface Coating for Anti-fouling

Wagd AJEEB[1], Simone MANCIN[1,*], Francesco COLETTI[2]

1: Department of Management and Engineering, University of Padova, Vicenza, IT
2: Department of Chemical Engineering, Brunel University London, UK

* Corresponding author: Tel.: +39 0444 998746; Email: simone.mancin@unipd.it

**Abstract:** With the development in industry applications and the requirements for higher energy efficiency, solving the fouling problem on heat transfer surfaces becomes an urgent need. The deposition of unwanted materials will limit the heat transfer performance and increase the pressure drops in the heat exchanger system. The coating was presented as an effective modification way of the surfaces' properties mainly towards the anti-fouling enhancement. Studies are still being conducted on advanced coating methods and materials to mitigate fouling. This study reviews the recent studies on antifouling coatings, and their results are presented and discussed.

**Keywords:** Fouling, Coating, surfaces

## 1. Introduction

Several challenges are facing the industry in the field of developing heat exchangers towards enhancing energy efficiency, decreasing the size and the costs [1]. In this, one of the greatest challenges in the heat transfer field is the fouling deposits of materials on the surfaces that can happen under various operation conditions [2]. The heat transfer is harmed and the pressure drops are increased, hence the energy efficiency and production in the application are reduced, causing large economic costs[3–5]. The latter will lead to extra fuel consumption and consequences on the rational use and saving of global energy (fossil fuel and renewable)and resources in the world. Besides the negative impact of fouling on the heat transfer performance, it also increases water consumption in cooling applications[6]. The extra usage of fossil fuels to overcome the energy losses by fouling has a significant impact on the environment [7], and the released carbon dioxide and greenhouse emissions affect the global warming problem [8,9]. In the world's current goals to protect the environment and natural resources management, it becomes important to resolve the fouling problem in heat exchangers.

## 2. Coating for Anti-fouling

The literature has presented several coating technologies that may be diverse in their advantages and limitations based on the operation conditions and the application, such as Physical Vapor Deposition (PVD), sputtering, Chemical Vapor Deposition (CVD), and Plasma processes [10]. Some surface coatings found in the literature are presented in Table 1. Some criteria are important when selecting the coating methods such as costs, surface geometry and material, deposition properties and operating temperature. Furthermore, the dip coating method can be *in situ* without costly machinery to apply the coatings to the surfaces of the active devices, as well as it provides the required thickness without waste[11,12].

Table 1. Types of some surface coatings

| Reference | Coating materials | Coating method | Remarks |
|---|---|---|---|
| Krumdieck et al. [13] | $Al_2O_3$ | PP-MOCVD | Uniform coating and amorphous. |
| Aggoun et al. [14] | Mg(OH)2/ CeO2 | Cathodic-electro | Uniform coating and compact. |
| Fengkun et al. [15] | $Al_2O_3$/WC-Co/epoxy | Air spraying process | Resistance to plastic deformation |
| Qiaolei et al. [16] | Al/316L-steel | Arc spraying | Resistance crack propagation |
| Ali et al. [17] | Mg-Si-O-N | Magnetron sputtering | Good chemical properties. |
| Han et al. [18] | C- YSZ | Plasma Spray | controlled thermal shock spits |

There was a specific interest in the advanced anti-fouling coating technologies and some were reported. In this, polymer materials have presented an essential role in organizing the reaction between colloid particles and surfaces, besides their hybrid forms that led to improved anti-fouling advantages [19–21]. Also, metallic coating materials with their ions e.g. $Ni^{2+}$, $Cu^{2+}$, $Al^{3+}$ have been used for anti-fouling on surfaces, such as Ni-PTFE [22], $Cu^{2+}$- $Zn^{2+}$ - [23] $Mg^{2+}$ mixture [23] and Ni-Cu-P [24]. On the other hand, other materials such as coating based-organic [25] and ceramic [26] can enhance the anti-fouling properties of surfaces. Some recently conducted research on antifouling coatings is presented in Table 2.

Table 2. Antifouling coatings based on different materials.

| **Ref.** | **Coating materials** | **Antifouling enhancement** |
|---|---|---|
| Ren et al. [27] | Ni-W-P | Enhanced by 67% |
| Liu et al. [28] | Ni-P- PTFE | Enhanced by 20% |
| Nie et al. [29] | SiO2-Ti3C2 | Good enhancement |
| Shang et al.[30] | MTMS-SiO2+ZnO | Good enhancement |
| Li et al. [31] | Nano-ZnO+PDMS | Good enhancement |
| Yin [32] | Cu-TiO2 | Long-term |
| Hu et al.[33] | Stearic acid-TiO2/Zn | Self-cleaning, anti-corrosion. |

## 3. Conclusions

The reviewed research presents various coating technologies for antifouling depending on the coating materials and using methods. Even though, it is still needed to develop those coating technologies mainly to be applied for large scales *in situ* and with low thermal resistance for industrial applications containing heat transfer. The latter can be achieved by taking advantage of the development in some scientific fields such as nanotechnology to produce advanced coating materials with advanced antifouling properties.

## References

[1] Ajeeb, W. & Murshed, S. M. S. *Therm. Sci. Eng. Prog.* (2022).
[2] Wen, D. *et al. Particuology* (2009).
[3] Coletti, F. & Hewitt, G. F. (Gulf Professional Publishing Elsevier, 2014).
[4] Al-Gailani, A. *et al. Int. J. Heat Mass Transf.* (2020).
[5] Al-Gailani, A. *et al. Therm. Sci. Eng. Prog.* (2021).
[6] CREMASCHI, L. & WU, X. *Heat Transf. Eng.* (2015).
[7] Bott, G. T. R. *Heat Exchanger Design Handbook* (Begell House Inc.). doi:10.1615/hedhme.a.000361.
[8] Müller-Steinhagen, H. *et al. Heat Transf. Eng.* (2009).
[9] Casanueva-Robles, T. & Bott, T. R. *Proc. 6th Int. Conf. Heat Exch. Fouling Cleaning, Challenges Oppor. RP2* (2005).
[10] Seshan, K. & Schepis, D. (Elsevier, 2018).
[11] Faustini, M. *et al. J. Phys. Chem. C* (2010).
[12] Zhang, J. X. *et al. J. Alloys Compd.* (2011).
[13] Krumdieck, S. *et al. Surf. Coatings Technol.* (2013).
[14] Aggoun, K. *et al. Surf. Coatings Technol.* (2019).
[15] Fengkun, L. *et al. Surf. Coat. Technol.* (2019).
[16] Li, Q. *et al. Surf. Coat. Technol.* (2019).
[17] Ali, S. *et al. Surf. Coat. Technol.* (2019).
[18] Han, Z. *et al. Surf. Coatings Technol.* (2007).
[19] Zhang, F. *et al. Langmuir* (2001).
[20] Zoppe, J. O. *et al.* (2017) doi:10.1021/acs.chemrev.6b00314.
[21] Wilson, D. I. *et al. Food Bioprod. Process.* (2014).
[22] Huang, K. & Goddard, J. M. *J. Food Eng.* (2015).
[23] Benslimane, S. *et al. Water Res. J.* (2020).
[24] Zuodong, L. *et al. Adv. Powder Technol.* (2023).
[25] Yao, Z. Q. *et al. Appl. Surf. Sci.* (2004).
[26] Wang, J. *et al. J. Energy Inst.* (2018).
[27] Ren, L. *et al.*
[28] Liu, Z. *et al. Heat Transf. Eng.* (2021).
[29] Nie, Y. *et al. Surf. Coat. Technol.* (2021).
[30] Shang, J. *et al. Polymers (Basel).* (2022).
[31] Li, X. *et al. Colloids Surfaces A Physicochem. Eng. Asp.* (2022).
[32] Yin, H. *et al. Vacuum* (2022).
[33] Hu, C. *et al. J. Alloys Compd.* (2021).

# Magnetic field influence on the ferronanofluid laminar pipe flow

Robert MULKA[1,*], Gabriela BĘBEN[1], Bartosz ZAJĄCZKOWSKI[1], Matthias H. BUSCHMANN[2]

1: Department of Thermal Sciences, Wrocław University of Science and Technology, Wrocław, PL
2: Institut für Luft- und Kältetechnik gGmbH Dresden, Dresden, DE

* Corresponding author: Tel.: +48 (71) 320 27 92; Email: robert.mulka@pwr.edu.pl

**Abstract:** The study presents the results of the investigation on the mixed-convection laminar flow of the MSG-W10 (FerroTec, USA) ferronanofluid under conditions of constant heat flux and radially directed magnetic field of various flux densities generated by permanent magnets. It is shown that depending on the magnetic flux density, it is possible to achieve a positive effect, as in the case of the low magnetic flux densities studied, but this result turns into a negative as the intensity of the magnetic field increases.

**Keywords:** heat transfer, laminar flow, mixed convection, ferronanofluid, magnetic field

## 1. Introduction

Nanofluids have received great scientific interest in single-phase and phase-change flow heat transfer applications due to the increased thermal conductivity of the medium caused by the presence of dispersed nanoparticles and accompanying phenomena (thermophoresis, Brownian motion, deposition on the evaporator surface) [1,2]. Ferronanofluid is a special type of nanofluid, containing nanoparticles that are susceptible to a magnetic field. Buschmann [3] in a review on the ferronanofluid flow under magnetic field presented three possible mechanisms that can be responsible for an improved heat transfer in laminar flow, and noted the need for further research to enable the derivation of relevant correlations for the Nusselt number and pressure drop. In this work, we present a study of the laminar flow of MSG-W10 (FerroTec, USA) ferronanofluid under conditions of constant heat flux and a radially directed magnetic field of different intensities generated by permanent magnets.

### 2.1 Experimental setup

The experiments were carried out on a setup allowing determination of local Nusselt number values and the effect of an external magnetic field. The main part of the setup consists of an entrance section that ensures the developed velocity profile, a test section with calibrated K-type thermocouples placed on the electrically heated copper pipe ($d_{in}$= 6 mm), and an exit section, which mixes the fluid. Inlet and outlet fluid temperature is measured using Pt100 thermometers. The magnetic field was provided by permanent magnets (NdFeB, N38) of different heights: 40x10x1/2/4/5/8 mm$^3$ placed on the top of a pipe, 28 mm from the pipe axis (2.1, 4.1, 7.5, 9.1, 13.1 mT, respectively). A commercial water based ferronanofluid MSG-W10 (FerroTec, USA) containing dispersed magnetite nanoparticles was used in the study. Measurements were taken for a constant Reynolds (Re = 163±3) and Prandtl number at the entrance to the test section.

## 2. Discussion and results

### 2.1 Effect of magnetic field intensity

Figure 1. presents a local Nusselt number distribution along the test pipe. Two regions of pure conduction (light orange) and mixed convection (orange) caused by a temperature gradient are highlighted on the plot. Black star markers represent the results for a ferrofluid flow absent magnetic field. Green triangles and

red crosses indicate the Nusselt number distribution for the 1 mm and 8 mm magnet, respectively.

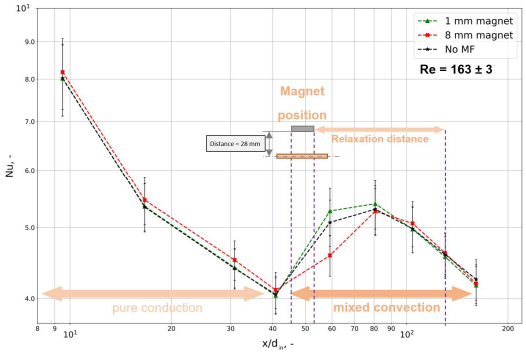


**Fig. 1.** Local Nusselt distribution along the pipe x axis.

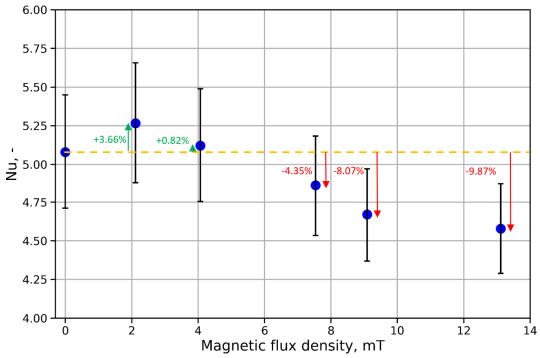


**Fig. 2.** Effect of the magnetic flux density on the local Nusselt number at the position of the 5$^{th}$ thermocouple.

The presence of the magnetic field caused a modification of the flow conditions and therefore a change of the Nusselt number downstream. Notably, this effect is dependent on the magnet size. We hypothesise that a change of magnetic field intensity caused a switch in the interaction mechanism of magnetic field with ferronanoparticles, and therefore in a position of the 5$^{th}$ thermocouple for the 1 mm magnet a 3.66% improvement of the Nusselt number is reported, while for the 8 mm magnet a deterioration of 9.87% is present. With a strong enough magnetic field the secondary motion can be weakened by the magnetic force acting on particles in a counter direction and be the cause of the local Nusselt number deterioration, as in the case of the 8 mm magnet. The explanation behind the enhanced heat transfer could be a formation of chain-like structures, which is possible under weak magnetic forces.

In Figure 2, the local Nusselt number is depicted at the position of the 5$^{th}$ thermocouple. It is clearly seen that for the two smallest magnets, an enhancement is present, but with increasing magnet size the effect is negative.

## 3. Summary

This study provides an insight into the interaction of various magnetic flux densities with a ferronanofluid flow on the local Nusselt number. It is shown that depending on the magnetic flux density, it is possible to achieve a positive effect, as in the case of the low magnetic field values studied, but this result turns into a negative as the intensity of the magnetic field increases. Responsibility for the switch is seen in an interaction mechanism change between the flowing ferronanofluid and the magnetic field. Further investigation on the critical ratio of viscous, magnetic and inertia forces that indicates a change of interaction mechanism of ferronanoparticles with magnetic field should be taken.

## Acknowledgements

This research was funded by National Science Centre, Poland, grant number: 2021/41/N/ST8/02120.

## References

[1] V. Bianco, O. Manca, S. Nardini, K. Vafai, Heat Transfer Enhancement with Nanofluids, CRC Press, 2015. https://doi.org/10.1201/b18324.

[2] A. Kujawska, R. Mulka, M.H. Buschmann, Z. Krolicki, B. Zajaczkowski, B., 2021. Impact of Silica Nanofluid Deposition on Thermosyphon Performance. Heat Transfer Engineering 42, 1702–1719. https://doi.org/10.1080/01457632.2020. 1818413

[3] M.H. Buschmann, Critical review of heat transfer experiments in ferrohydrodynamic pipe flow utilising ferronanofluids, International Journal of Thermal Sciences. (2020) 106426. https://doi.org/10.1016/j.ijthermalsci.20 20.106426.

# Polyvinyl Alcohol-Based Nanofibers with Improved Thermal Conductivity and Efficient Photothermal Response for Wearable Thermal Management

Lifei CHEN[1,2*], Qingyi MA[1,2], Xin WANG[1,2], Yanjie CHEN[1,2], Huaqing XIE[1,2]

1: School of Energy and Material Engineering, Shanghai Polytechnic University, Shanghai 201209, P. R. China
2: Shanghai Engineering Research Center of Advanced Thermal Functional Materials

[*] Corresponding author. Tel: +86 021 50214461; E-mail: lfchen@sspu.edu.cn

**Abstract:** The development and research of flexible and smart textiles have garnered significant attention in recent times. The incorporation of phase change materials into stimulus-responsive nanofibers has the potential to react to external stimuli and provide a comfortable microclimate for the human body. This approach holds promise for achieving instant energy conversion/storage and temperature regulation in smart clothing. However, the production of efficient and flexible intelligent thermoregulated nanofibers remains a challenge. In this study, we successfully prepared intelligent thermoregulated nanofibers with adjustable temperature, efficient thermal storage capacity, and excellent thermal conductivity using the emulsion electrostatic spinning method. By incorporating lauric acid as the phase change material and optimizing its addition ratio in the spinning emulsion, we obtained nanofibers with uniform diameter and eliminated the issue of material leakage. This resulted in outstanding phase change behavior and thermal storage capacity of the nanofibers, with an enthalpy value reaching 103.13 J/g, equivalent to 72% of pure lauric acid. Furthermore, the incorporation of carbon nanotubes and zinc oxide particles into the fibers provided UV resistance and a high thermal conductivity of 0.665 W·m-1·K-1. The use of a polyvinyl alcohol matrix ensured the flexibility of the nanofibers, with an elongation at break of approximately 25%, meeting international standards (10% ~ 30%). Additionally, the pollution-free polydimethylsiloxane coating not only protected the internal structure of the nanofibers but also imparted superior hydrophobicity and self-cleaning properties. Consequently, these intelligent thermoregulated nanofibers, with their comprehensive performance, offer an option for the development and application of wearable systems and protective fabrics.

**Keywords:** Phase change material; Emulsion electrostatic spinning; Intelligent thermoregulated nanofibers; Thermal energy storage; Self-cleaning

# Numerical analysis of hybrid nanofluid-cooled micro finned heat sinks for electronics cooling

Adeel ARSHAD[1,3,*], Muhammad IKHLAQ[2], Yuying YAN[3], Asif A. TAHIR[1]

1: Environment and Sustainability Institute (ESI), Faculty of Environment, Science and Economy, University of Exeter, Penryn Campus, Cornwall, TR10 9FE, UK
2: School of Engineering, Newcastle University, Newcastle Upon Tyne, NE1 7RU, UK
3: Fluids & Thermal Engineering (FLUTE) Research Group, Faculty of Engineering, University of Nottingham, Nottingham, NG7 2RD, UK

*Corresponding author: Email: a.arshad@exeter.ac.uk

**Abstract:** This study explores the thermohydraulic performance of a metallic-oxide based hybrid nanofluid-cooled micro pin-fin heat sink by adopting the multiphase Eulerian model. The circular configuration is adopted for micro pin-fins with the staggered arrangement and constant heat flux applied at the base of the heat sink. The mono and hybrid nanofluid are based on an aqueous solution of Ag and MgO nanoparticles and a pressure drop (ΔP) range is applied across the heat sink. The heat transfer and fluid flow performance are evaluated in terms of temperature difference, local heat transfer coefficient, thermal resistance, surface and average Nusselt number, whereas the velocity and flow streamline contours present the qualitative depiction of flow distributions across the heat sink. The results revealed that under certain ΔP conditions, the hybrid nanofluid showed optimum thermal performance of micro pin-fin heat sink compared to the water, as coolant, at constant nanoparticles loading at the perceptible margin. At an optimum ΔP, the higher average heat transfer coefficient, Nusselt number, and lower thermal resistance are achieved.

**Keywords:** Thermohydraulic Performance, Hybrid Nanofluid, Micro Pin-Fin, Heat Sink, Heat and Fluid Flow

## 1. Introduction

The new era of electronic industry is facing an exacerbation issue of cooling because of a compact space for circuitry which causes exorbitant heat generation. A 1.31% energy is consumed by data centers of total global electricity that account the 33% thermal management [1]. The reliability of integrated circuit (IC) silicon chips is decreasing 10% with a 2 °C rise in temperature. As reported, the major cause of failure of electronic components is the temperature rise which contributes of 55% [2]. The conventional cooling techniques are unable to remove the excessive heat because of lower thermal conductivity of coolant. Thus, the high-tech electronics need innovative cooling technology with advanced coolants, i.e., nanofluids, that possess the higher thermal conductivity and convective heat transfer rate. The dispersion high surface-to-volume ratio engineered nanoparticles into conventional fluids exhibit exceptional thermal conductance, suspension stability, higher solid-liquid interface that enhance the interphase heat exchange [3]. The utilizations of nanofluids, especially hybrid nanofluids, with micro pin-fin heat sink have been accessed by very few researchers. The present study investigates the thermohydraulic performance of aqueous solution mono and hybrid nanofluids flowing through a circular configured micro pin-fin heat sink under different pressure drop (ΔP) range. The numerical analysis is carried out by applying the multiphase Eulerian model for a constant volume fraction ($\phi$ = 1.0%).

## 2. Numerical formulation

An aluminum made and circular geometry having $d_f$ = 0.66 mm and $h_f$ = 2.5 mm of micro pin-fin heat sink with staggered arrangement was modelled, as shown in Fig. 1. A constant heat flux was applied at heat sink base and ΔP was applied of 570 Pa ≤ ΔP ≤ 2760 Pa. The nano and hybrid nanoparticles of Ag and MgO of $\phi$ = 0% and 1.0% were dispersed in water. The multiphase Eulerian approach is considered under laminar, steady-state, and incompressible flow conditions. The continuity, momentum and energy equations for $p^{th}$ phases ($p^{th}$ = *s* and *l*) are defined as follows:

$$\nabla.\left(\varphi_p \rho_p V_p\right) = 0 \quad (1)$$

$$\nabla.\left(\varphi_p \rho_p V_p V_p\right) = -\varphi_p \nabla P + \nabla.\left(\varphi_p \mu_p \nabla V_p\right) + S_{m_p} \quad (2)$$

$$\nabla.\left(\varphi_p \rho_p h_p V_p\right) = -\nabla.k_p \nabla T + \left[\nabla.\left(\varphi_p \mu_p \nabla V_p\right)\right]:\nabla V_p + q_p \quad (3)$$

The thermophysical properties of mono and hybrid Ag-MgO nanoparticles were calculated from Ref.

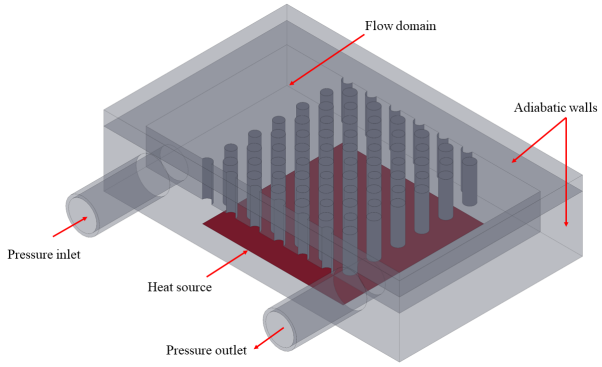


*Figure 1-Schematic heat sink with boundary conditions.*

[4]. At the inlet and outlet of heat sink, pressure inlet and pressure outlet boundary conditions were assigned, respectively. Steady-state 3D simulations were conducted using Ansys-FLUENT. The pressure-velocity coupling was formulated using SIMPLE algorithm and second-order-upwind scheme was applied. The convergence criteria were set of $10^{-4}$ for all transport equations.

## 2. Results and discussion

Fig. 1 shows the variations of thermal resistance ($R_{th}$) and average Nusselt number ($Nu_{avg}$) by varying different ΔP. The $R_{th}$ trend typically shows the inverse relation of heat transfer rate of a heat sink. A declining trend was observed with water, mono and hybrid nanofluids of Ag and MgO with escalating ΔP as result of augment flow velocity. At a constant ΔP, the effect of $R_{th}$ in case of nanofluid is lower than the water, used as coolants through the heat sink. Contrarily to the $R_{th}$, the increasing trend was obtained in $Nu_{avg}$ with the increase of ΔP because of enhanced heat transfer rate at higher flow rate. The reduction in $R_{th}$ is higher in Ag, Ag-MgO, and MgO based nanofluids compared to the water flowing across the heat sink at a certain ΔP. The improvement in $Nu_{avg}$ is significant higher either for both water or nanofluids cooled heat sinks at a higher ΔP. Compared to the water-cooled, Ag, Ag-MgO, and MgO dispersed mono and hybrid nanofluids depict the higher $Nu_{avg}$ enhancement, respectively. Fig. 2 represents the streamline flow of along the x-y plane by considering the Ag-MgO hybrid nanofluid case at maximum ΔP = 2760 Pa. A large recirculation zone is observed at top right corner at the inlet header however, a small zone is created along the bottom left corner before flowing through the pin-fin wetted area. This flow recirculation at inlet header is because of non-uniform distribution of local heat transfer coefficient ($h_l$) pattern at the upstream of pin-fin region.

## 2. Conclusion

The current numerical study presents the heat and

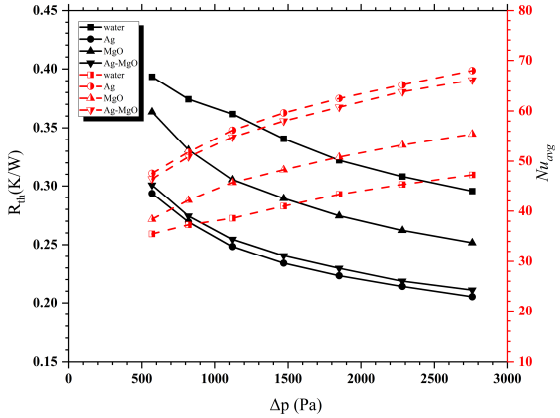


*Figure 2- Variations of $R_{th}$ and $Nu_{avg}$ vs Pa.*

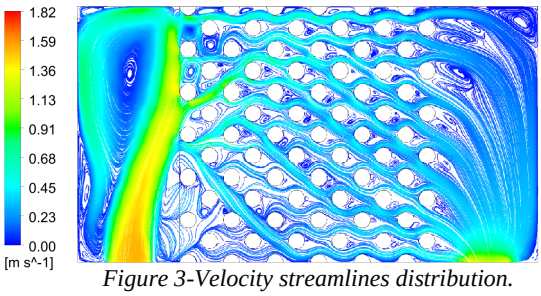


*Figure 3-Velocity streamlines distribution.*

fluid flow phenomenon of Ag and MgO dispersed mono and hybrid water based nanofluid-cooled micro pin-fin heat sink at constant ϕ and varying ΔP. The results revealed that the addition of Ag and MgO nanoparticles in base fluid enhance the heat transfer rate. The higher $Nu_{avg}$ and lower $R_{th}$ are achieved with the increase of ΔP. The highest $Nu_{avg}$ and lowest $R_{th}$ are obtained with Ag added water-based nanofluid because of the higher thermal conductivity of Ag, followed by Ag-MgO and MgO nanoparticles.

## References

1. Sharma, C.S., et al., *Energy efficient hotspot-targeted embedded liquid cooling of electronics.* Applied Energy, 2015. 138: p. 414-422.
2. Batunlu, C. and A. Albarbar, *Real-time system for monitoring the electro-thermal behaviour of power electronic devices used in boost converters.* Microelectronics Reliability, 2016. 62: p. 82-90.
3. Mahian, O., et al., *Recent advances in modeling and simulation of nanofluid flows-Part I: Fundamentals and theory.* Physics Reports, 2019. 790: p. 1-48.
4. Arshad, A., et al., *Thermal process enhancement of HNCPCM filled heat sink: Effect of hybrid nanoparticles ratio and shape.* International Communications in Heat and Mass Transfer, 2021. 125: p. 105323.

# Electrical conductivity studies on ionic liquids enhanced with nanoparticles

Elena Ionela CHERECHES[1], Alina Adriana MINEA[1,*]

1: Technical University "Gheorghe Asachi" of Iasi, Romania, Faculty of Materials Science and Engineering, Bd. D. Mangeron, No. 63, 700050, Iasi, Romania

* Corresponding author: Tel.: +40 723455071; Email: alina-adriana.minea@academic.tuiasi.ro

**Abstract:** Ionic liquids are a relative new class of materials and their special properties opens up new possibilities for obtaining new types of heat transfer fluids, prepared with the help of an ecological process, with the possibility of recycling and with wide applicability in industry. Ionanofluids are an innovative concept due to the growing need to identify non-polluting heat transfer fluids, while reducing energy consumption. Studies on the thermophysical properties determination of the ionanofluids are in its very first steps, as there are no complete approaches in the literature, thus the evaluation of the behavior of these fluids in practical applications is in its pioneering phase. This study aims to fill some gaps in the electrical conductivity of two ionic liquids as well as their suspensions with several nanoparticles.

**Keywords:** ionanofluids, electrical conductivity, ionic liquids, nanoparticles

## 1. Introduction

The idea of developing new fluids, with nanoparticles in suspension, appeared due to the exhaustion of all methods of heat transfer intensification. Initially, the idea of intensifying heat transfer was based on increasing the heat transfer surface, later, research was focused mainly on the heat transfer coefficient, which depends very much on the type of fluid (with reference to its thermophysical properties). Thus, the idea of fluid improvement and the development of new fluids with high thermal conductivity appeared. Studies on the determination of the thermophysical properties of ionanofluids must be deepened, as there are no complete approaches in the literature, making it impossible to evaluate the behavior of these fluids in practical applications. Several experimental studies are recently reported by Chereches et al. [1, 2] where the electrical conductivity experiments were performed at ambient temperature and heating in the range 293.15 - 333.15 K. The ionic liquid $[C_2mim][CH_3SO_3]$ has a high electrical conductivity (2520 μS/cm at 293.15 K), and the electrical conductivity of the mixture (ionic liquid plus water) is much higher (about 3 times higher) than that of each fluid (water or ionic liquid) as determined experimentally. The electrical conductivity clearly decreases by adding nanoparticles to the base mixture, the decrease being quantified up to 60 %, the higher values being recorded for the higher mass concentration. The experimental results on electrical conductivity are extremely few, there is no unitary theory regarding its variation with both the temperature and the concentration of nanoparticles or their type. This work consists of an comparative experimental study about the electrical conductivity of two types of ionanofluids with alumina nanoparticles, having as base liquid both the ionic liquid 1-ethyl-3-methylimidazolium methanesulfonate $[C_2mim][CH_3SO_3]$ and 1-butyl-3-methylimidazolium tetrafluoroborate $[C_4mim][BF_4]$.

## 2. Discussion and Results

The experimental results on the electrical conductivity of the new liquids were obtained with an Edge® Multiparameter HI 2030 (Hanna Instruments). The experiment was performed in two stages (at ambient temperature and heating in the range 293.15 - 333.15 K) the overall

accuracy being calculated at 3 %. The results will be discussed for ionanofluids with a mass concentration of 0.5 - 5.0 % wt nanoparticles of alumina, based on two ionic liquids: $[C_2mim][CH_3SO_3]$ and $[C_4mim][BF_4]$. The nanoparticles used are insulators, with a very low electrical conductivity (10 μS / cm [3]). The ionic liquid $[C_2mim][CH_3SO_3]$ (CAS 145022-45-3) with a purity ≥ 95 % and ≤ 0.5 % water content, was purchased from SIGMA-ALDRICH (St Louis, USA) and the ionic liquid $[C_4mim][BF_4]$ (CAS 174501-65-6), with a purity > 99 % and molecular weight 226.02 g / mol, was purchased from IoLiTec, Germany. Aluminum oxide nanoparticles were purchased from Sigma Aldrich (St. Louis, USA) under CAS number 1344-28-1. Information about manufacturing the new fluids and details about the metodology used see Chereches et al. [4]. We are inserting here several preliminary experimental results, since the experiment is ongoing.

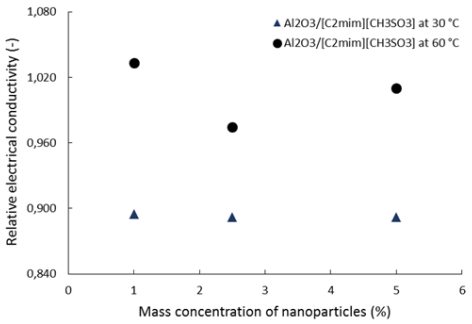


**Figure 1.** Comparation of experimental data at two temperature.

The relative electrical conductivity was evaluated for ionanofluids whose base fluid is ionic liquid $[C_2mim][CH_3SO_3]$ and different mass concentrations of alumina, the results for two temperatures being shown in Figure 1, where the decrease in electrical conductivity can be observed when the amount of added nanoparticles increase. This phenomenon is mainly attributed to the increase in the viscosity of the suspensions, but also to the addition of alumina nanoparticles which causes a slight decrease in ion mobility [4].

## 3. Conclusions

An experimental study on electrical conductivity for two types of ionic liquids enhanced with alumina nanoparticles was performed in this paper. The tests were collected at ambient temperature and at heating. As can be seen from the data presented, the electrical conductivity of an ionic liquid enhanced with nanoparticles depends very much on type of ionic liquid as well as the working temperature. As this study is in completion of this group research on $[C_2mim][CH_3SO_3]$ ionic liquid with alumina nanoparticles, it mat clearly affirm that ionic liquids behavior regard the electrical conductivity must be intensified.

## References

[1] E.I. Chereches and A.A. Minea, Electrical conductivity of new nanoparticle enhanced fluids: an experimental study, Nanomaterials 9 (2019) 190.

[2] I. Chereches, J.I. Prado, M. Chereches, A.A. Minea and L. Lugo, Experimental study on thermophysical properties of alumina Nanoparticle Enhanced Ionic Liquids, Journal of Molecular Liquids 291 (2019) 111332.

[3] E.I. Chereches and A.A. Minea, Experimental evaluation of electrical conductivity of ionanofluids based on water– [C2mim][CH3SO3] ionic liquids mixtures and alumina nanoparticles, Journal of Thermal Analysis and Calorimetry 145 (2021) 3151-3157.

[4] E.I. Chereches, D. Bejan, C. Ibanescu, M. Danu and A.A. Minea, Ionanofluids with $[C_2mim][CH_3SO_3]$ ionic liquid and alumina nanoparticles: an experimental study on viscosity, specific heat and electrical conductivity, Chemical Engineering Science, 229 (2021) 116140.

## Acknowledgments

This work was supported by a grant of the Romanian Ministry of Education and Research, CNCS-UEFISCDI, project number PD 36/2022, cod project PN-III-P1-1.1-PD-2021-0222, within PNCDI III.

## SESSION 2b
## MINI SYMPOSIUM
## Experimental techniques in phase change heat transfer
Chair: **M. Bucci**

# Understanding Accomplishments and Limitations of Infrared Thermometry for Boiling Heat Transfer Investigations

Artyom KOSSOLAPOV[1], Guanyu SU[1], Gustavo MATANA AGUIAR[1], Florian CHAVAGNAT[1], Jee Hyun SEONG[1], Chi WANG[1], Madhumitha RAVICHANDRAN[1], Matteo BUCCI[1,*]

1: Massachusset Institute of Technology, Cambridge, MA

*Corresponding author: Email: mbucci@mit.edu

**Abstract:** In every field of science, the possibility of discovering and understanding new phenomena, or testing new hypotheses, is strongly related to, and limited by the capability of observation. In this talk, we will discuss recent advances in experimental boiling heat transfer research made possible by high-speed infrared thermometry. We will discuss the potential of this technique in supporting the understanding of fundamental two-phase heat transfer problems. Examples are the growth and departure of bubbles from a heated surface, the distribution of the dry area fraction, the partitioning of heat flux, and the boiling crisis. We will also discuss its challenges and limitations, e.g., limited spatial and temporal resolution. However, while the use of infrared thermometry has been instrumental in providing an answer to some long-standing fundamental physical questions in boiling heat transfer, access to data is no longer sufficient. Nowadays, new understanding is hindered by our capability to analyze them. We can produce much more data than we can possibly analyze. This issue is critical for highly non-linear phenomena, e.g., boiling heat transfer, whose complexity is hidden beyond what a human eye can hardly see, or a human brain can timely analyze.

**Keywords:** Boiling, IR thermometry, Data analysis.

## 1. Introduction

In the past, most of the correlations and models used for the design and the safety analysis of two-phase heat transfer systems have been developed based on pointwise temperature and heat flux measurements. These data have been invaluable to narrow down first-order effects, e.g., the effect of forced convection or subcooling on the overall thermal performance of a heating element. However, as the need for validating mechanistic models has increased and different descriptions have produced comparable predictions, it has become clear that predicting these experiments is a necessary but not sufficient condition to validate modeling tools. Simply put, one can get the right overall values (e.g., of the heat transfer coefficient) for the wrong reason (e.g., overestimating the evaporation and underestimating other heat removal mechanisms or vice versa) [1].

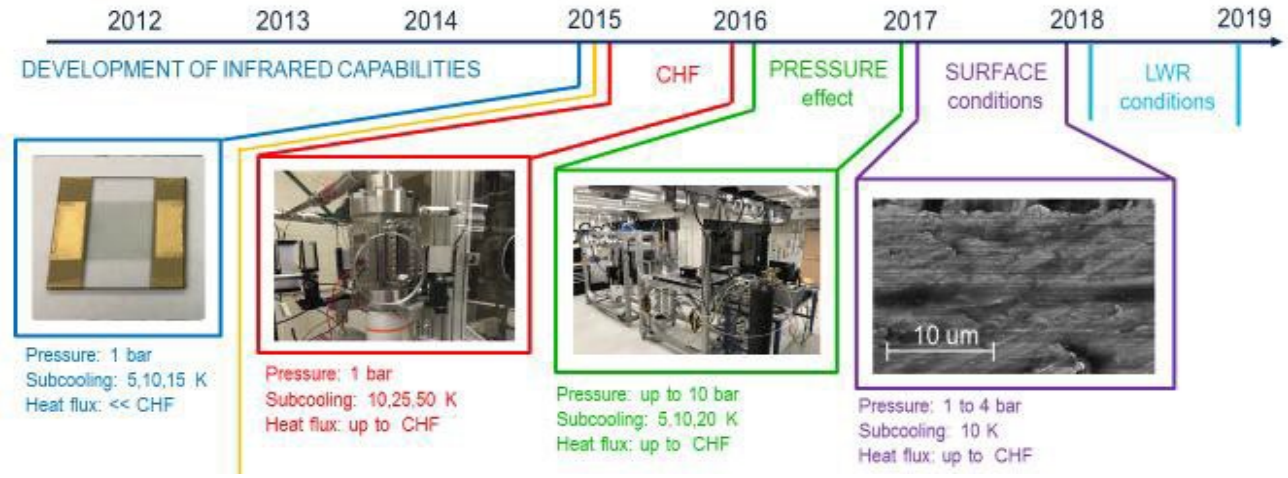


**Figure 1.** Timeline of boiling heat transfer experimental developments in our laboratory.

## 2. Infrared thermometry

Starting from early 2010, We have worked on developing a boiling platform featuring advanced, high-resolution, non-intrusive measurement techniques for boiling heat transfer investigations. Figure 1 provides an overview of the major milestones accomplished over the years, starting with the first implementation of infrared thermometry to study the flow boiling of water, and the development of a calibration technique to measure the time-dependent temperature and heat flux distributions on the boiling surface [2]. Based on these distributions, we developed post-processing algorithms to measure all the boiling parameters used as inputs in the mechanistic heat flux partitioning models, as well as quantify the contribution of the different heat transfer mechanisms [3]. In 2015, we have started the investigation of critical heat flux, first at ambient pressure, and then in high-pressure conditions (up to 10 bars). The tests performed before 2016 were all run with special infrared heaters made of sapphire, coated with a thin Indium Tin Oxide layer. This solution is the standard in infrared thermometry. However, as these surfaces are much different compared to commercial surface, in 2016, we have started developing a new type of heater where we can manipulate the surface conditions, including duplicating the morphology and wettability of boiler surfaces [4], and still make all the measurements enabled by our infrared diagnostics. With this kind of heater, we can nowadays investigate the effect of surface conditions on boiling heat transfer and the boiling crisis [5].

Despite the studies and discoveries made possible using infrared thermometry, such technique has crucial limitations. At high pressure and temperature, the characteristic bubble time and length scale are much smaller compared to low-pressure conditions. Infrared thermometry does have the spatial and temporal resolution necessary to capture the feature of the boiling process. Also, and importantly, when the thermal footprint of the bubble is not as strong as for low pressure water (e.g., with dielectric fluids), infrared measurements may become very noisy. To overcome this limitation, we have developed an optical technique based on light reflection, which allows detecting the presence of vapor bubbles attached to the boiling surface.

However, we are still in search of a thermometry technique that allows us measurement time-dependent temperature and heat flux distributions in such limiting cases. Infrared thermometry was brought to maturity during the last decade. The current decade will be the decade of post-processing and data analysis. Today we can produce much more data than we can possibly analyze using conventional image segmentation and data analysis. To overcome this limitation, we have started developing machine learning algorithms that can process the large amount of data recorded by infrared cameras online, almost in real-time [6,7]. Today we can measure boiling parameters and estimate margins to the boiling crisis as fast as we run experiments. This is another crucial step towards the development of autonomous experiments and learning, which we foresee may become a reality in the next decade.

## References

[1] Baglietto, E. and Christon, M., 2013. Demonstration & assessment of advanced modeling capabilities to multiphase flow with sub-cooled boiling. *CASL Internal Document*.

[2] Bucci, M., et al., 2016. “A mechanistic IR calibration technique for boiling heat transfer investigations”. *International Journal of Multiphase Flow*, 83, pp.115-127.

[3] Richenderfer, A., et al., 2018. Investigation of subcooled flow boiling and CHF using high-resolution diagnostics. *Experimental Thermal and Fluid Science*, *99*, pp.35-58.

[4] Su, G.Y., et al., 2020. “Investigation of flow boiling heat transfer and boiling crisis on a rough surface using infrared thermometry”. *International Journal of Heat and Mass Transfer*, 160, p.120134.

[5] Zhang, L., et al., 2023. A unifying criterion of

the boiling crisis. *Nature Communications*, *14*(1), p.2321.
[6] Ravichandran, M. and Bucci, M., 2019. Online, quasi-real-time analysis of high-resolution, infrared, boiling heat transfer investigations using artificial neural networks. *Applied Thermal Engineering*, *163*, p.114357.
[7] Ravichandran, M. et al., 2021. Decrypting the boiling crisis through data-driven exploration of high-resolution infrared thermometry measurements. *Applied Physics Letters*, *118*(25).

# A single-dye multispectral laser-induced fluorescence technique for thermographic measurements

Surya NARAYAN[1], Zengchao CHEN[1], Aleksei S. LOBASOV[1], Konstantin S. PERVUNIN[1], Christos N. MARKIDES[1,2,*]

1: Clean Energy Processes (CEP) Laboratory, Department of Chemical Engineering, Imperial College London, London SW7 2AZ, United Kingdom
2: Kutateladze Institute of Thermophysics, Siberian Branch of the Russian Academy of Sciences, Novosibirsk 630090, Russia

* Corresponding author: Email: c.markides@imperial.ac.uk

**Abstract:** We propose a new technique for temperature measurements based on single-dye multispectral laser-induced fluorescence. We demonstrate the technique by employing Nile Red, a temperature-sensitive fluorophore, dissolved in HFE-7100 fluid at concentrations from 0.3 to 30 mg/L. The absorbance and emission spectra of the Nile Red/HFE-7100 mixture were characterised using a spectrometer for an excitation wavelength of 527 nm, over a range of temperatures, from ambient conditions (298 K) up to the boiling point of HFE-7100 (333 K), to explore the mixture's temperature dependence. It was found that Nile Red in the presence of 1%-vol. ethanol has a sufficiently different temperature sensitivity in the wavelength band from 570 to 600 nm to that at wavelengths 620 nm, thus enabling ratiometric thermographic imaging with the proposed technique. Finally, temperature distributions inside a boiling flow in a vertical miniaturised channel were obtained to demonstrate the efficacy of the technique. The technique is also applicable other measurements (e.g., concentration) and in cases where a fluid can be directly excited by the light source, without the need for a dye additive.

**Keywords:** Fluorescence, spectral bands, Nile Red, LIF thermography, flow boiling, vapour bubble formation.

## 1. Introduction

Advanced laser-based techniques are among the most promising options for the simultaneous measurement of temperature and velocity fields in liquids under boiling conditions [1]. However, in the case of two-colour PLIF with two dyes, local changes in the relative concentration of the dyes may cause an increased errors in the temperature measurement. Using a single dye and recording fluorescent signals separately in two selected bands of the emission spectrum can overcome the problem of dye concentration non-uniformity [2]. To this end, a single-dye multispectral LIF (SDMS-LIF) technique has been developed to measure temperature in the whole field of a boiling flow. The technique was tested in the case of boiling flow in a miniaturised channel.

## 2. Experimental methods

The test facility is specifically designed to reproduce various flow boiling conditions in a miniaturised channel. The apparatus has a closed fluid loop and consists of a storage tank, peristaltic pump with a coarse inline particle filter, a high-accuracy mass-flow controller, test section, condenser, preheaters and a bypass circuit where a pressure controller is installed. The experiments were performed at nearly ambient pressure for mass fluxes ($G$) ranging from 33 to 100 kg/m$^2$·s. The inlet subcooling temperature $\Delta T_{sub} = T_{sat}(P_i) - T_i$ was varied from 5 to 25 K and the heat flux ($q$) supplied to the test substrate from 1.8 to 10 kW/m$^2$.

## 3. Working fluid mixture

Firstly, 300 mg of Nile Red was premixed in 100 mL of ethanol to form a buffer solution with a dye concentration of 3 g/L. The buffer solution was then added to a known volume of hydrofluoroether 7100 (HFE-7100), which is a 3M Nove 7100 engineered fluid, thus producing a Nile Red/HFE-7100 mixture with a dye concentration $C$ ranging from 0.3 to 30 mg/L. For the entire range of $C$, the ratio of ethanol to HFE-7100 did not exceed 1%-vol.

Finally, 4 mL of the dye mixture was poured into a quartz 10×10×50 mm cuvette (Hellma) that was placed in a Duetta spectrometer with a

built-in Peltier heating unit to measure its spectral characteristics as a function of $C$ and the mixture temperature $T$. The heating unit temperature was adjusted in steps of 5±0.1 °C with a holding time of 300 s before recording fluorescence signals at elevated $T$. The measured absorbance and emission spectra of the mixture (shown in Fig. 1) were used to identify two selective wavelength bands to enhance sensitivity of the ratiometric temperature measurements, so that Band 1 = 560–590 nm and Band 2 > 620 nm.

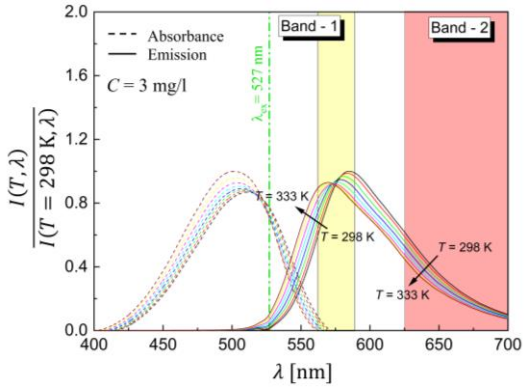


**Fig. 1:** Normalised absorbance and emission spectra for the Nile Red/HFE-7100 mixture with $C$ = 3 mg/L at different $T$.

## 4. Results and discussion

Figure 2 demonstrates that the selected bands of Nile Red in the presence of 1%-vol. ethanol allow ratiometric temperature measurements in HFE-7100. The effect of a vapour bubble on the thermal boundary layer (TBL) can be clearly observed.

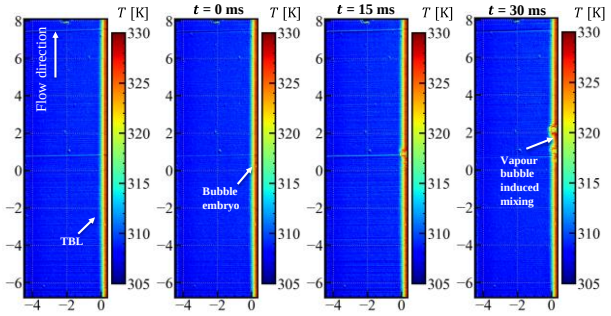


**Fig. 2:** Time evolution of the temperature field around a single vapour bubble formed at the wall of a vertical miniaturised channel for $C$ = 10 mg/L, $G$ = 33 kg/m$^2$s, $\Delta T_{sub}$ = 25 K and $q$ = 8.7 kW/m$^2$. All spatial dimensions are in mm.

Initially, a nucleation site is completely covered by the TBL. As the bubble grows and slides upwards along the wall, moving away from the nucleation site, a portion of the cold fluid from the bulk flow (i.e., from the central part of the channel) mixes with hot fluid near the heated substrate. This process can be referred to as bubble-induced mixing and is expected to lead to enhanced thermal transport, which is characteristic of the nucleate boiling regime.

## 5. Conclusions

Two distinct spectral bands (560–590 nm and >620 nm) were found for fluorescent dye Nile Red dissolved in HFE-7100, both of which are temperature sensitive. Spectrometric measurements of the absorbance and emission spectra were analysed for a range of dye concentrations from 0.3 to 30 mg/L and temperatures from 298 to 333 K. A novel single-dye multispectral laser-induced fluorescence (SDMS-LIF) technique was therefore proposed based on ratiometric quantitative imaging of these bands, and was demonstrated as being capable of whole-field temperature mapping as applied to single vapour bubble formation in a subcooled boiling flow in a vertical minichannel. The key features of bubble-induced mixing in a nucleate boiling regime were identified through of temperature fluctuation measurements in the thermal boundary layer. The technique is applicable other measurements (e.g., concentration) and in cases where a fluid can be excited by the light source, without the need for a dye additive.

## References

[1] Voulgaropoulos, V., Aguiar, G.M., Markides, C.N., Bucci, M., 2022. Simultaneous laser-induced fluorescence, particle image velocimetry and infrared thermography for the investigation of the flow and heat transfer characteristics of nucleating vapour bubbles. Int. J. Heat Mass Transf., 187, 122525.

[2] Lavieille, P., Lemoine, F., Lavergne, G., Lebouche, M., 2001. Evaporating and combusting droplet temperature measurements using two-color laser-induced fluorescence. Exp. Fluids, 31, 45–55.

# X-ray Computed Tomography for solid/liquid phase change: Challenges and Opportunities

Dario GUARDA[1, 2, *], Jorge MARTINEZ-GARCIA[2], Benjamin FENK[2], Damian GWERDER[2], Anastasia STAMATIOU[2], Jörg WORLITSCHEK[2], Simone MANCIN[1], Philipp SCHUETZ[2]

1: Department of Management and Engineering, University of Padova, Vicenza, IT
2: Competence Centre for Thermal Energy Storage, Lucerne University of Applied Sciences and Arts, Horw, CH

* Corresponding author: Tel.: +39 0444 998746; Email: dario.guarda@phd.unipd.it

**Abstract:** Latent Thermal Energy Storages (LTESs) are based on Phase Change Materials (PCMs), which exploit the phase transition, usually the solid-liquid one, to store heat. The use of these systems is a promising solution to boost the energy transition towards a sustainable future. Indeed, researchers and private companies are putting more and more efforts to deploy LTES in real world applications. X-ray Computed Tomography (XCT) is a technology that presents many opportunities to visualize the behaviour of PCMs. It allows to "see inside" the materials, meaning that it is possible to track the solid-liquid front while it evolves during the phase change, to assess new phases arising or void formation. Of course, XCT for PCMs analysis comes with some challenges because the solid/liquid phase change front moves as the process proceeds and thus, the scans must be quite fast to be able to catch the melting front evolution.

**Keywords:** Phase Change Material, Latent Thermal Energy Storage, X-ray computed tomography, volumetric liquid fraction

## 1. Introduction

PCMs bring innovation in many fields, e.g., waste heat recovery, battery thermal management, Heat Ventilation and Air Conditioning (HVAC) and buildings. The possibility to analyze PCMs behavior volumetrically with the XCT technology could lead to unprecedent advancement in the understanding of the solid-liquid phase-change process, which is of utmost importance for the future of LTES systems. Some researchers already started to go into this direction, analyzing ice/water system, eicosane, calcium chloride hexahydrate and magnesium chloride hexahydrate [1-4]. The aim of this work is to give an overview of the opportunities and the challenges that applying XCT technology to analyze PCMs brings.

## 2. Opportunities

Solid-liquid front, voids, shrinkage, crystal structure, segregation, secondary phases can be observed via XCT. From 4D images (3 space dimensions and time) it is possible to follow the melting or solidification process of PCMs, observing the evolution of the interior structures in the materials. In Figure 1, some features of 3 PCMs are reported.

In eicosane, it is possible to observe the liquid phase in the middle of the samples and the solid on the walls of the container. During the solidification, eicosane shrinks, generating voids inside the solid phase and a big conical crater at the interface with air. When observing calcium chloride hexahydrate, the solidification behaviour is similar for the fact that it starts from the walls but disparate since crystals are forming. The liquid phase is rendered with a blue slightly opaque volume, making it easier to see big crystals forming on the bottom. The third PCM discussed is sodium acetate trihydrate. The image shows smaller needles generated during the phase change, which are favoured due to the cooling rate. These results proof that XCT can be a very effective tool to analyse the PCMs phase change process.

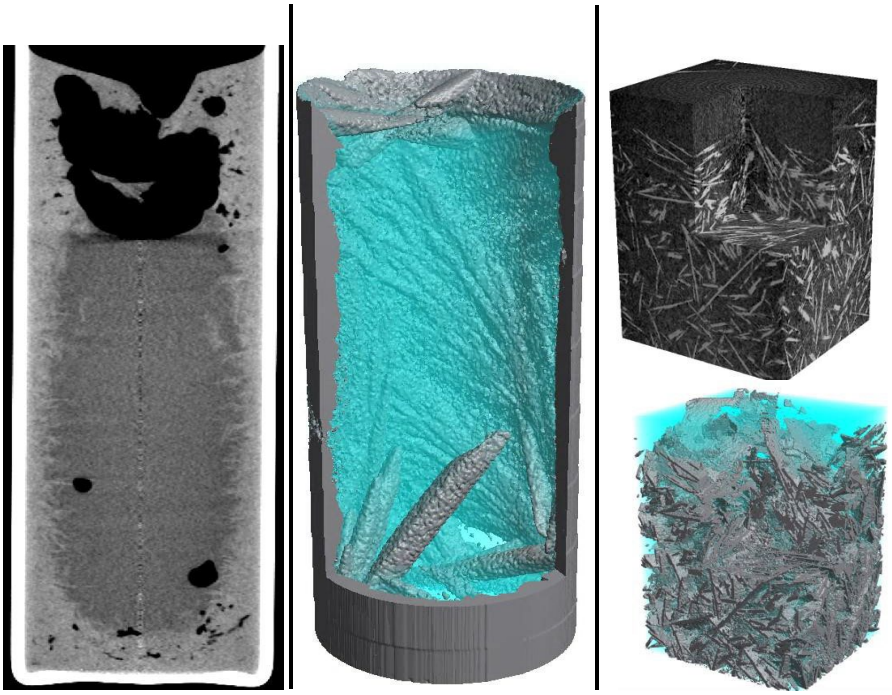

Figure 1. Post-processed images from XCT scan of 3 PCMs: eicosane, calcium chloride hexahydrate ($CaCl_2 \cdot 6H_2O$) and sodium acetate trihydrate (SAT).

## 3. Challenges

As every technology, also XCT has shortcomings. Among others, time is a fundamental factor in transient processes, but laboratory XCT can be considered slow for high resolution images. So, the faster the melting or cooling rate, the lower the achievable resolution. Furthermore, the material under test has to be selected correctly: XCT is based on the attenuation of X-rays from the materials and is sensitive to density. This means that solid and liquid state need to have a resolvable density difference and metallic (high density with respect to PCMs) temperature sensors could generate artefacts. It is also important to find a proper way to heat or cool inside the XCT chamber, which could not always be simple and straightforward.

## 4. Conclusions

XCT opens many possibilities in the PCMs research field, of course with some cautions needed.

## Acknowledgements

The authors want to acknowledge the support of the Swiss National Science Foundation made available by grant 200021_201088 ("Investigation of Salt Hydrates Segregation with XCT") and grant 206021_189608 ("FaCTES: Fast in-situ Computed Tomography for Energy Research and Space Biology").

## References

[1] Guarda, D.,Wahli, F., Gwerder, D., Martinez-Garcia, J., Stamatiou, A., Worlitschek, J., Mancin, S. and Schuetz, P., 2022. Phase change material numerical simulation: enthalpy-porosity model validation against liquid fraction data from an X-ray computed tomography measurement/system. Nondestruct. Test. Eval., 37.

[2] Guarda, D., Martinez-Garcia, J., Fenk, B., Schiffmann, D., Gwerder, D., , Stamatiou, A., Worlitschek, J., Mancin, S. and Schuetz, P., 2023. Under review.

[3] Martinez-Garcia, J., Gwerder, D., Wahli, F., Guarda, D., Stamatiou, A., Worlitschek, J., Schuetz, P., 2023. Volumetric quantification of melting and solidification of phase change materials by in-situ X-ray computed tomography., J. Energy Storage, 61, 106726.

[4] Kohler, T., Kögl, T., Müller, K., 2018. Study of the crystallization and melting behavior of a latent heat storage by computed tomography. Chem. Ing. Tech., 902018.

# Characterizing Multiphase Flows through Radiation-Based and Fluid Electrical Properties-Based Measurement Techniques

Victo PETROV[1,2,3,*], Annalisa MANERA[2,1,3]

1: Paul Scherrer Institut, 5232 Villigen PSI, Switzerland
2: ETH Zurich, 8092, Zurich, Switzerland
3: University of Michigan, 48109 Ann Arbor, USA

* Corresponding author: Email: victor.petrov@psi.ch

**Abstract:** The presented work constitutes an in-depth exploration of measurement methodologies that excel in capturing the intricate nature of multiphase flows. This investigation encompasses two distinct yet complementary approaches: radiation-based techniques (including x-ray, gamma-ray, and neutrons) and fluid electrical properties- based techniques (involving conductivity and capacitance). Through the utilization of these advanced methods and discussing them with attending researchers, our objective is to provide a comprehensive understanding of modern multiphase flow measurement techniques and their capabilities. All of the techniques presented have undergone rigorous testing across an extensive range of pressure and temperature conditions, thus offering valuable insights into their applicability within diverse scenarios. The adaptability of these techniques is further underscored by their successful implementation across various test section configurations and their efficacy with a wide array of fluids. These fluids encompass water, chloroform, refrigerants, oils, and organic liquids, often in combination with various gases or their corresponding vapors. Importantly, due to the inherent characteristics of these methods, as will be expounded upon in the talk, they do not necessitate optical access to the test section. Consequently, these techniques can be effectively employed across a broad spectrum of flow regimes, ranging from bubbly flow characterized by very low void fractions to droplet flow featuring very high void fractions, including transitions between regimes.
**Keywords:** Micro Flow, Microcirculation, Boiling, Pumps

## 1. Introduction

There is no need to reveal the significance of acquiring high-fidelity experimental data on two-phase flow. Specific facets may marginally vary based on the research domain, yet ultimately, all fields derive diverse benefits from it. At present, two-phase flow measurement techniques can be categorized as follows: **optic-based methods**[1] - hinge on diverse light reflection and propagation techniques, typically employing laser or LED light sources in conjunction with high-speed CMOS, sCMOS, or CCD cameras. In certain instances, supplementary insights can be gleaned through the utilization of IR or near-IR spectrum cameras; **differential Pressure measurement methods**[2] - boast a historical lineage and, as implied by the name, are rooted in gauging pressure disparities between two or more points, enabling flow characterization; **optic probe and fiber optic methods**[3] - facilitate point or 1D measurements by analyzing scattered light within thin, optically transparent mediums; other more **exotic techniques** like microwaves, acoustic, MRI, etc. While this work will focus on **radiation-based techniques**[4], including x-ray, gamma-ray, or neutron measurements, which harness ionizing radiation Interactions with the medium and radiation detectors to characterize two-phase or multi-phase flows, additionally, we will delve into **conductivity and capacitance-based techniques**[5] that exploit variations in the electrical properties of the medium for flow characterization.

## 2. Radiation-based techniques

The fundamental concept of radiation-based imaging methods centers around determining the linear attenuation coefficient of the medium, closely linked with its density. This coefficient can be computed for each measured beam using the Beer-Lambert Law, and then converted into the medium's density along the path of the beam. In a straightforward scenario, like an adiabatic air-water mixture in a test section, where the densities of each phase remain constant, the attenuation coefficient hinges solely on the air and water ratio along the beam's trajectory.

However, when imaging a heated test section, additional factors include thermal expansion and density variation with temperature for all involved phases. Despite these complexities, it's still possible to estimate the phase ratio. If a detector array is utilized instead of a point detector, projections of the phase ratio onto this array can be acquired, revealing a density distribution across the detector array. There are fundamental differences between X-ray and gamma-ray radiation sources, yet both can be effectively utilized for multi-phase imaging of different media. For example, X-ray sources can offer a substantial photon flux, enabling imaging with minimal exposure time. However, they are typically less energetic and can, therefore, penetrate through a lesser amount of material. If one can capture images of the same area from various angles, often referred to as projections, these acquired projections can be amalgamated into a sonogram.

These sonograms can be reconstructed by employing a Radon transformation or its variations, offering a 2D (for linear detectors) or 3D (for detector arrays) density distribution across the image area or volume, as shown in Figure 1.

## 3. Electrical property-based techniques

Among the various electric property-based techniques, this presentation will focus on two that utilize distinct principles. The first technique leverages electrical conductivity, making it suitable for highly conductive fluids like water. The second technique utilizes capacitance and is well-suited for purely conductive liquids such as refrigerants or oils. Both methods involve an array of transmitting and receiving conductive electrodes, often composed of stainless steel wires, positioned at specific distance. Measurements are taken at the intersection points of these electrodes. This is achieved through specially designed circuitry that generates a voltage spike at a single transmitter electrode and concurrently measures the associated currents at each intersection point with receiving electrodes. The transmitters are activated in rapid succession, enabling an almost immediate snapshot of the flow's cross- section. The circuitry for the receivers varies significantly depends on the property of interest and the method employed, whether it is resistance-based or capacitance-based.

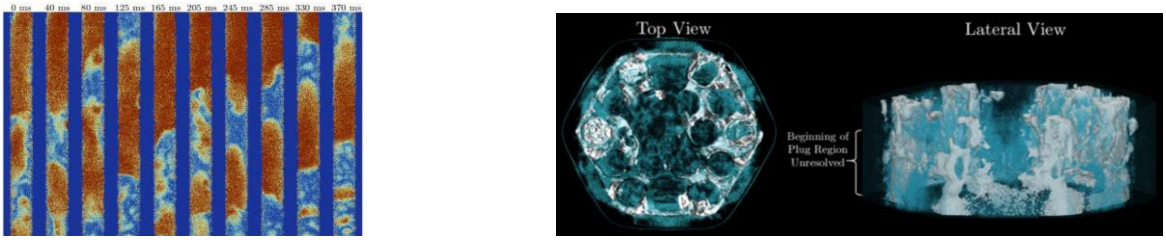


Figure 1. In-house examples: 2D bubble time evolution in the heated tube captured using X-ray radiography (left) and 3D distribution of resolidified metal structure in the fuel bundle captured using gamma-ray tomography

Some measurement examples taken with the conductivity-based system are shown in Figure 2. The same approach could be employed to measure concentrations (since electric properties depend on concentration) or a combination of void fractions and concentrations. If, instead of using a wire mesh, sensors are arranged in a pattern of surface-mounted electrodes, the electronics could be utilized for high-speed and high-resolution measurements of liquid films.

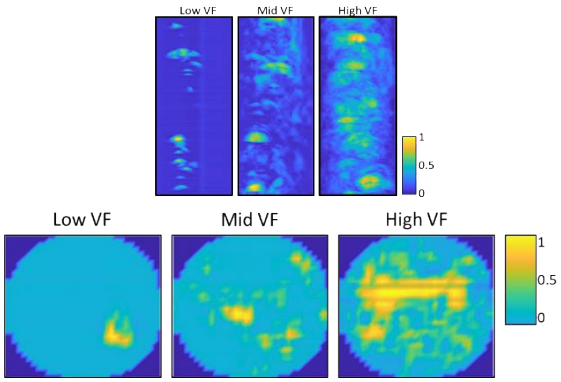


Figure 2. In-house examples of Bubble column measurements for three gas flow rates vertical cross-section (top) and horizontal cross-section (bottom).

## 4. Conclusions

Several measurement techniques for multiphase flows have been briefly discussed here, while detailed information will be provided during the presentation, along with various examples obtained in the ECMF lab.

## References

1. Williams, C. L., & Peterson Jr, A. C. (1978). Two-phase flow patterns with high-pressure water in a heated four-rod bundle. Nuclear Science and Engineering, 68(2), 155-169.
2. Jia, J, Babatunde, A and Wang, M (2015) Void Fraction Measurement of Gas-Liquid Two-Phase Flow from Differential Pressure. Flow Measurement and Instrumentation, 41. 75 - 80. ISSN 0955-5986
3. Baroncini, V.H.V.; Martelli, C.; Da Silva, M.J.; Morales, R.E.M. Single- and Two-Phase Flow Characterization Using Optical Fiber Bragg Gratings. Sensors 2015, 15, 6549-6559. https://doi.org/10.3390/s150306549
4. Adams R., Petrov, V., Manera, A., “Advanced high-resolution radiation-based measurement techniques for detailed void-fraction measurements in fuel bundles and high-pressure test sections”, (NURETH-17), Xi’an, China, Sep 3 – Sept 9 (2017).
5. Prasser, H. M., Böttger, A., & Zschau, J. (1998). A new electrode-mesh tomograph for gas–liquid flows. Flow Measurement and Instrumentation, 9(2), 111-119.
6. J. Diaz, Radiation Transmission Imaging Applications for Nuclear Reactor Systems, 2022 PhD thesis.

## SESSION 2c
## Mathematical and computational approaches
Chair: **S. Poncet**

Jody ALBERTAZZI[1], Renato ROTA[1], Valentina BUSINI[1]
1: Department of Chemistry, Materials and Chemical Engineering “Giulio Natta”, Politecnico di Milano, Milano, IT

# Non-isothermal evaporation

Eugene BENILOV[1, *]

1: Department of Mathematics and Statistics, University of Limerick, Limerick, IE

*Corresponding author: Email: eugene.benilov@ul.ie

**Abstract:** Evaporation of a liquid layer on a substrate is examined without the often-used isothermality assumption – i.e., temperature variations are accounted for. Qualitative estimates show that non-isothermality makes the evaporation rate depend on the conditions the substrate is maintained at. If it is thermally insulated, evaporative cooling dramatically slows evaporation down; the evaporation rate tends to zero with time and cannot be determined by measuring the external parameters only. If, however, the substrate is maintained at a fixed temperature, the heat flux coming from below sustains evaporation at a finite rate – deducible from the fluid's characteristics, relative humidity, and the layer's depth (whose importance has not been recognized before). The qualitative predictions are quantified using the diffuse- interface model applied to evaporation of a liquid into its own vapor.

**Keywords:** Interfaces, Evaporation, Non-Isothermal Effects, Diffuse-Interface Model

## 1. Introduction

Evaporation of liquids has been studied for over a century, since the pioneering work of James Clerk Maxwell, and it is still being studied now, as numerous issues have yet to be resolved.

Consider, for example, a flat liquid layer. It is generally believed that it evaporates at a steady rate depending on the liquid's parameters (temperature, heat of vaporization, etc.) and the humidity of air. There are numerous measurements of evaporation rates; a recent review of this work in application to water can be found in Refs. [1–2].

Fig. 1 shows a selection of measurements of the evaporation rate E, for water evaporating into still air, as a function of the temperature $T$ within a "room temperature" range. There is evident disagreement in these results, suggesting that important factors vary from experiment to experiment.

The present paper identifies at least some of these factors. It is shown that non-isothermal effects – e.g., the heat exchange between the liquid and substrate (and side walls, if any) – can make E depend on the distance between the interface and substrate, and the material the latter is made of.

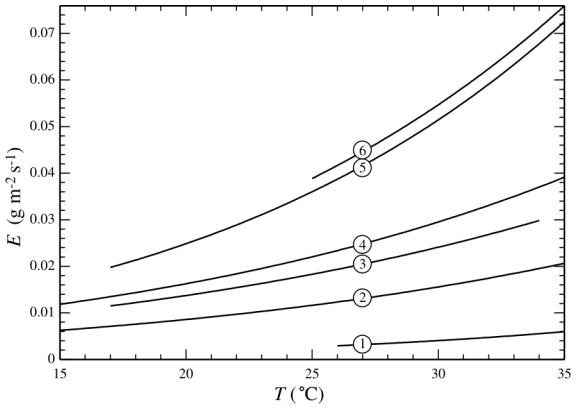


Fig. 1. Evaporation rate vs. temperature, according to the empiric formulae listed in Table 1 of Ref. [2]. In all cases, the relative humidity is 50%.

To illustrate the importance of heat exchange with the boundaries, consider an amount of liquid in a thermally insulated vessel – and let half of the liquid evaporate. The temperature of the remaining half decreases due to evaporative cooling – and the size of the decrease is easy to estimate. Assuming for simplicity that vaporization heat $\Delta h$ and the heat capacity $c_P^{(l)}$ of the liquid do not change significantly with $T$, one can

approximate the temperature decrease by

$$\Delta T = \frac{\Delta h}{c_P} \qquad (1)$$

For $\Delta h = 2.4417$ J kg$^{-1}$ and $cP = 4.1816 \times 10^{-3}$ J kg$^{-1}$ K$^{-1}$ (which correspond to water at 25°C), estimate (1) yields a somewhat unexpected result:

$$\Delta T \approx 584^{\circ}\,\mathrm{K}.$$

In reality, however, evaporation of liquid in an insulated vessel slows down to a virtual standstill well before it half-evaporates. Since the dependence of $E$ on $T$ at normal conditions is typically exponential, even a moderate temperature decrease can reduce the evaporation rate by an order of magnitude.

Alternatively, let the vessel's bottom and walls be kept at a fixed temperature (which seems to be a more realistic model in terms of applications). In this case, the energy lost to vaporization is replenished by the incoming heat flux, which can be readily calculated,

$$-\kappa^{(l)} T' = E\Delta h, \qquad (2)$$

where $\kappa^{(l)}$ is the liquid's thermal conductivity and the temperature gradient $T'$ can be expressed through the temperature difference $\Delta T$ between the interface and the nearest boundary and the corresponding distance $D$,

$$T' = \frac{\Delta T}{D}, \qquad (3)$$

To determine ΔT for water at 25°C, set $\kappa^{(l)}$=0.6065Wm$^{-1}$K$^{-1}$ and E = 0.025361g m$^{-2}$s$^{-1}$ which is the average of empiric curves 2–6 in Fig. 1 (curve 1 cannot be used, as 25°C is not in its range). With these values, expressions (1)–(3) yield

$$\Delta T = \frac{E\Delta h}{\kappa^{(l)}}\, D \approx \frac{1\ K}{1\ cm} \times D$$

Evidently, this estimate is both qualitatively and quantitatively different from that for insulated substrates.

The difference between fixed-$T$ and insulated vessels demonstrates the importance of heat fluxes from boundaries and, generally, non-isothermal effects. There are more of these to be mentioned: conductive and radiative heat exchange with air (which are often small, but can be important), convective heat transfer in liquid (which can be very important), etc.

In this work, non-isothermal effects are explored using the simplest setting: evaporation of a liquid into its own undersaturated vapor. It is described by a relatively simple model which does not include the diffusive mass flux (pure fluids do not diffuse). Evaporation in this case occurs via advection [3], but heat conduction is similar to that in mixtures.

The dynamics of the setting described is examined using the so-called diffuse interface model (DIM). It was proposed in 1901 by Diederik Korteweg and has been used since then in thousands of papers and for tens of applications (see a review of some of this work in Ref. [4]). The DIM is particularly suited to the problem at hand: it describes both liquid and vapor, as well as the interfacial dynamics – as opposed to models built of 'blocks' describing
one item each. The use of the DIM is convenient but not crucial, however, as non-nonisothermal effects can be introduced into any good model of evaporation.

## References

[1] T. Poós and E. Varju 2020 Mass transfer coefficient for water evaporation by theoretical and empirical correlations. Int. J. Heat Mass Transf. 153, 119500.

[2] E. Varju and T. Poós 2022 New dimensionless correlation for mass transfer at evaporation of open liquid surface in natural convection. Int. Commun. Heat Mass Transf. 136, 106102.

[3] E. S. Benilov 2022 Dynamics of a drop floating in vapor of the same fluid. Phys. Fluids 34, 042104.

[4] E. S. Benilov 2023 The multicomponent diffuse-interface model and its application to water/air interfaces. J. Fluid Mech. 954, A41.

# Thermal Distinction in Advancing and Receding Contact Lines: Insight from MD simulation

Hiroki KUSUDO[1,*], Takeshi OMORI[2], Laurent JOLY[3], Yasutaka YAMAGUCHI[1]

1: Department of Mechanical Engineering, Osaka University, Osaka, JP
2: Department of Mechanical Engineering, Osaka Metropolitan University, Osaka, JP
3: Institut Lumière Matière, Université Lyon 1, Villeurbanne, FR

* Corresponding author: Tel.: +81-6-6879-7329; Email: hiroki@nnfm.mech.eng.osaka-u.ac.jp

**Abstract:** In this study, we calculated the heat flux distribution in a quasi-2D Couette-type flow system of a Lennard-Jones liquid confined between two sliding solid walls, which reproduced steadily moving dynamic contact lines (DCLs). We found that the difference between the advancing and receding CLs are distinct not only in the apparent contact angle but also in the temperature. The heat transport analysis revealed that heat was produced and reduced around the advancing and receding CLs, respectively while in liquid bulk heat was only produced due to viscous dissipation. Based on the energy conservation law applied for control volumes set in the system, we quantitatively showed that the heat production and reduction originated not only from the stress work term due to viscous dissipation in the bulk, but also from the internal energy change along the pathline, and revealed that the heat production/reduction around the DCLs were induced mainly by the latter. This is analogous to latent heat, meaning that the interface change along the pathline induces the heat production/reduction in the same manner as the phase change in latent heat.

**Keywords:** Dynamic Contact Line, Wetting, Heat Transport, Molecular Dynamics

## 1. Introduction

Wetting is ubiquitous in our daily life, in nature and in various scientific and engineering fields. In particular, the behavior of the contact line (CL), where a liquid-vapor interface meets a solid surface, has long been a topic of interest because it plays a key role in wetting properties.

For the dynamic wetting, the dynamic contact angle (CA) is distinct for the advancing and receding ones unlike static wetting. Indeed, for modeling the dynamic CA difference, a number of theoretical simulations and experimental studies about the dynamic CL (DCL) have been conducted[1]; however, the governing principle of the CL motion still remains unclear due to the lack of the detailed information of the nanoscale thermal and fluid fields around the DCL to be connected to the macroscopic flow, and it is considered to be one of the long-standing unsolved problems of the fluid dynamics.

In this study, we analyzed the heat transport via the Method-of-Plane[2] around the DCLs of a quasi-2D NEMD system of a Lennard-Jones (LJ) fluid between parallel solid walls moving in the opposite directions tangential to the wall surfaces as shown in Fig.1.

## 2. System

We employed a NEMD simulation system of a quasi-2D Couette-type flow system with liquid–solid–vapor contact lines consisted of LJ fluid[3]. The 12-6 LJ potential was adopted between fluid-fluid and fluid-solid interactions and the parameters were set so that the static CA at 85 K is 57 degrees. In addition, the temperature in the second outermost layers of the solid walls was controlled at a control temperature 85 K by using the standard Langevin thermostat so that the steady-state was achieved with removing the generated viscous heat in the present study.

## 3. Results and Discussions

The top panel of Fig. 2 shows the temperature distribution and the heat flux field. The thermal distinction in the DCLs is clearly shown, *i.e.*, temperature rise and drop around the advancing and receding CLs, respectively. To quantitatively evaluate the heat production and reduction around the DCLs, we set three control volumes (CVs) shown with magenta in Fig. 2. We integrated the divergence of the heat flux in each CV as the surface integral of the heat flux on the enclosed surface of each CV, *i.e.*, $\int \mathrm{d}V \boldsymbol{\nabla} \cdot \boldsymbol{J}_\mathrm{Q} = \int \mathrm{d}\boldsymbol{S} \cdot \boldsymbol{J}_\mathrm{Q}$. The integration results are shown inside the CVs in the top panel of Fig. 2; heat is produced and reduced at the CVs surrounding the advancing (97 mW/m) and receding (–88 mW/m) CLs, respectively.

To elucidate this mechanism of the heat production and reduction around the dynamic CLs, we start from the energy conservation:

$$\boldsymbol{\nabla} \cdot \boldsymbol{J}_\mathrm{Q} = \boldsymbol{\tau} : \boldsymbol{\nabla} \boldsymbol{u} - \rho \frac{\mathrm{D}e_\mathrm{int}}{\mathrm{D}t}, \qquad (1)$$

where $\boldsymbol{J}_\mathrm{Q}$, $\boldsymbol{\tau}$, $\boldsymbol{u}$, $\rho$ and $e_\mathrm{int}$ denote the heat flux vector, stress tensor, velocity vector, density and the specific internal energy of fluid, whereas : and D/D$t$ denote the inner product of the second order tensor and the Lagrangian derivative. The bottom panel of Fig. 2 shows the fluid specific internal energy distribution with velocity field. Through the investigation of the second term on the right-hand side in Eq. (1) for each CV as shown in the bottom panel of Fig.2, it was shown that this internal energy change was the main cause of the heat production/reduction around the dynamic CLs.

## 4. Conclusion

We analyzed the heat transport around the dynamic contact lines in a quasi-2D NEMD system. The heat transport analysis revealed that heat was produced and reduced around the advancing and receding CLs, respectively while in liquid bulk heat was only produced due to viscosity dissipation. We found that this heat production/reduction around the dynamic CLs were mainly due to the internal energy change along the path line.

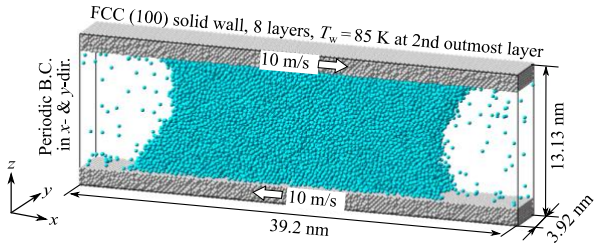


Fig. 1. Quasi-2D NEMD system of the dynamic contact lines of Lennar-Jones fluid.

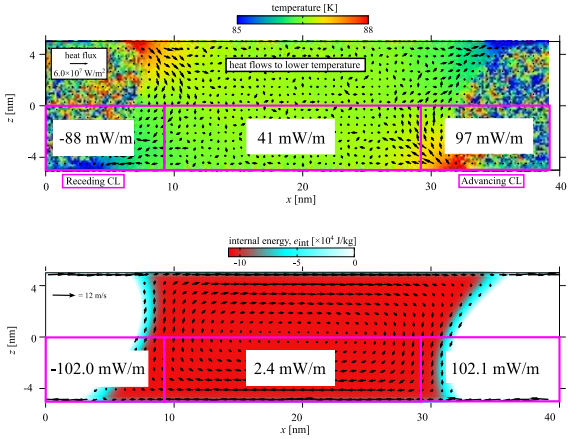


Fig. 2. Top: temperature distribution and heat flux field. Bottom: specific internal energy distribution and velocity field. The volume integral values of (top) the divergence of heat flux, and (bottom) the Lagrangian derivative of the internal energy in three control volumes were also shown.

## Acknowledgements

This work was supported by the JSPS KAKENHI grant (Nos. JP20J20251 and 22H01400), Japan and the JST CREST grant (No. JPMJCR18I1), Japan.

## References

[1] Snoeijer, J., Andreotti, B., 2013. Moving contact lines: Scales, regimes, and dynamical transitions. Annu. Rev. of Fluid Mech. 45, 269-292.

[2] Todd, B., Daivis, P., Evans, D., 1995. Heat flux vector in highly inhomogeneous nonequilibrium fluids. Phys. Rev. E 5 (51), 4362-4368.

[3] Kusudo, H., Omori, T., Yamaguchi, Y., 2021. Local stress tensor calculation by the method-of-plane in microscopic systems with macroscopic flow: A formulation based on the velocity distribution function. J. Chem. Phys. 18 (155), 184103.

# Dynamic Leidenfrost Effects: Computational Modelling to Predict Transitions in Drop Impact

Peter LEWIN-JONES[1*], James SPRITTLES[1], Duncan LOCKERBY[1]

1: University of Warwick, Coventry, UK
* Corresponding author: Email: peter.lewin-jones@warwick.ac.uk

**Abstract:** When a liquid drop is placed gently on a sufficiently hot surface it can levitate on its own evaporative vapour cushion. This 'Leidenfrost effect' is important for numerous industrial applications including spray cooling, where the dramatic decrease in thermal conductivity is detrimental. Conversely, moving drops in a low-friction manner is appealing for transport in microfluidic devices.
Recently, experimental studies have probed the *dynamic* Leidenfrost effect, where droplets approach the hot surface with a given speed. These have uncovered several interesting contact modes and unexpected effects including an oscillating film height in certain regimes. To provide new insight into the physical mechanisms involved and as an important predictive tool, we have developed a novel computational model for the dynamic Leidenfrost process. As now recognised for isothermal conditions, this requires gas kinetic effects to describe contact modes. This uses a lubrication framework, now including evaporation.
Our simulations are benchmarked against experiments and simulations of isothermal impacts and drop-drop collisions. Our model enables us to explore the parameter space of impacting velocity and solid surface temperature, probe different regimes of contact and vapour film behaviour, with the aim of predicting the minimum film thickness and the critical impact speed for contact to occur.

**Keywords:** Fluid Dynamics, Free Surface Flows, Drop Impact, Computation, Leidenfrost Effect

## 1. Introduction

When a liquid drop is placed gently on a sufficiently hot surface it can levitate on its own evaporative vapour cushion. This 'Leidenfrost effect' is important for numerous industrial applications such as spray cooling, where the dramatic decrease in thermal conductivity is detrimental. Conversely, moving drops around in a low-friction manner is appealing as a mode of transport in microfluidic devices.
Recently, experimental studies [1-2] have probed the dynamic Leidenfrost effect, where droplets can be forced into contact when impact speeds are large enough, uncovering several interesting modes of contact and discovering new unexpected effects, such as an oscillating film height in certain regimes.

## 2. Model and Numerical Method

To provide new insight into the physical mechanisms involved in such phenomena and as an important predictive tool, we have developed a novel computational model for the dynamic Leidenfrost process, building on previous work [3-4] for isothermal and quasi-static Leidenfrost drops. We solve the axisymmetric Navier-Stokes equations in the drop, implemented in the open-source finite element library oomph-lib.
This is coupled to a lubrication equation (1) on the surface of the drop for the vapour pressure $P$, given film height $h$ and radial velocity $u$ and the effect of evaporation due to the linear temperature profile in the film.

$$\frac{\partial h}{\partial t} - \frac{k_v \Delta T}{\rho_v L h} = \nabla \cdot \left( \frac{\Delta_P^{\Phi} h^3}{12 \mu_v} \nabla P - \frac{hu}{2} \right) \quad (1)$$

As now recognised for isothermal conditions, this requires gas kinetic effects to describe contact modes.
The gas kinetic factor $\Delta\Phi$ $(Kn)$ can incorporate a variety of slip models and interface conditions, and depends on the

Knudsen number $Kn = \lambda/h$ defined as the ratio of the vapour's mean free path to the film thickness.
We use adaptive time-stepping and adaptive re-meshing. The mesh is moved using a pseudo-solid arbitrary Lagrangian-Eulerian framework, which keeps the moving surface of the drop as the boundary of the domain.

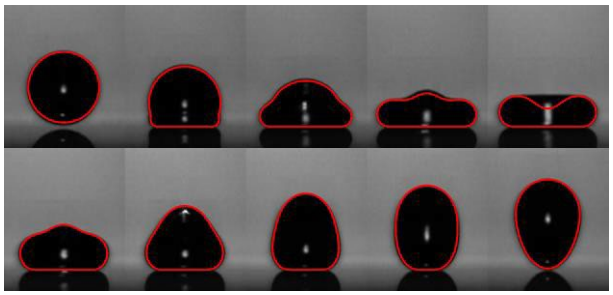

Figure 1: Comparison of our simulation (red) with isothermal experiment from [5], showing drops can bounce off wettable solids, due to an intervening air cushion.

## 3. Benchmarking

Our simulations have been benchmarked against experiments and simulations of isothermal impacts (fig 1), and our methodology has been used to predict the bouncing-merging transitions in drop-drop collisions.

## 4. Future Work

Our model enables us to explore the parameter space of impacting velocity and solid surface temperature, and probe different regimes of contact and vapour film behaviour, with the aim of predicting the minimum film thickness reached and the critical impact speed at which contact will occur.
The model will be extended to include heat flow within the drop, incorporating buoyancy and the thermal Marangoni effect, which are predicted to be of critical importance in determining the Leidenfrost temperature.

## References

[1] Shirota, M., van Limbeek, M.A.J., Sun, C., Prosperetti, A., Lohse, D., 2016. Dynamic Leidenfrost Effect: Relevant Time and Length Scales. Phys. Rev. Lett. 116, 064501. https://doi.org/10.1103/PhysRevLett.116.064501

[2] Chantelot, P., Lohse, D., 2021. Drop impact on superheated surfaces: short-time dynamics and transition to contact. Journal of Fluid Mechanics 928. https://doi.org/10.1017/jfm.2021.843

[3] Chubynsky, M.V., Belousov, K.I., Lockerby, D.A., Sprittles, J.E., 2020. Bouncing off the Walls: The Influence of Gas-Kinetic and van der Waals Effects in Drop Impact. Phys. Rev. Lett. 124, 084501. https://doi.org/10.1103/PhysRevLett.124.084501

[4] Chakraborty, I., Chubynsky, M.V., Sprittles, J.E., 2022. Computational modelling of Leidenfrost drops. Journal of Fluid Mechanics 936. https://doi.org/10.1017/jfm.2022.66

[5] de Ruiter, J., Lagraauw, R., van den Ende, D., Mugele, F., 2015. Wettability-independent bouncing on flat surfaces mediated by thin air films. Nature Phys 11, 48–53. https://doi.org/10.1038/nphys3145

# Numerical and experimental analysis of forced convection for compressible micro gas flow in turbulent regime

Danish REHMAN[1], J.D. MOYA-RICO[2], Chungpyo HONG[3], Gian Luca MORINI[1,*]

1: DepaMicrofluidics Laboratory, Dept. of Industrial Eng. Via del Lazzaretto 15/5, University of Bologna, Bologna 41031, Italy
2: Renewable Energy Research Institute, Section of Solar and Energy Efficiency, C/ de la Investigacion 1, 02071, Albacete, Spain
3: Department of Mechanical Engineering, Kagoshima University, 1-21-40 Korimoto, Kagoshima 890-8580, Japan

* Corresponding author: Email: gianluca.morini3@unibo.it

**Abstract:** Experimental results of heat transfer characteristics for compressible gas flows through microtubes are far from being unequivocal in the turbulent flow regime. Due to a limited number of flow sensors that can be employed in microdevices, it becomes essential to couple numerical models with experiments to understand the fluid behavior inside the microtube. In addition, in many cases, the thermal boundary condition of the real case is different from the theoretical one (i.e. constant heat flux (CHF) or constant wall temperature (CWT)). Thus, a combined experimental and numerical study on the forced convection of compressible gas through a microtube is performed in this paper. Experimental results of Nitrogen gas flow through a 173 μm microtube are used to validate the employed numerical model by varying Reynolds number (Re) from 3,500 to 7,500. Using a hybrid thermal boundary condition, numerical Nusselt number showed an excellent agreement with the experimentally deduced values. The validated numerical model was used to evaluate the Nusselt number for 2,500< Re <20,000 under the ideal CHF boundary condition. It was shown that for the values of Re where the temperature difference between the wall of the microtube and bulk temperature of the Nitrogen gas becomes zero or negative, the Nusselt number loses its meaning. It is further demonstrated that the Nusselt numbers, in the range of the investigated Re, are higher than the predictions of the conventional Gnielinski correlation in which the compressibility effects are not accounted for.

**Keywords:** Micro Flow, Microcirculation, Boiling, Pumps

## 1. Introduction

A great interest in the investigations of gas flows inside very narrow channels is due to pioneering studies of Wu and Little. Numerous research works have been carried out later studying different microtubes (MTs) and microchannels, circulating different fluids and under wide operating conditions. From the literature review [1–8], it can be seen that heat transfer characteristics of gas microflows are still not fully explored. Experimental results of a few studies predict significantly higher $Nu$ for smaller diameter MTs (e.g. [2, 8]) whereas it is found to be following the conventional correlations as in [4]. Therefore, further research in the field of forced convection in MTs when gas flows are used is needed. In this work, heat transfer characteristics of gas microflows in the turbulent regime are analyzed using numerical modeling. The numerical model is first validated with the experimental results and later used to understand the evolution of heat transfer characteristics under different thermal boundary conditions and their effects on the evaluation of the average $Nu$ for the MT.

## 2. Numerical and experimental setup

A MT having the Dh of 173 μm and length (L) of 100 mm, is simulated for the current study. Test section schematic representing the simulated MT and the inlet manifold is designed in Workbench Design Modeler and is meshed using ANSYS meshing software.

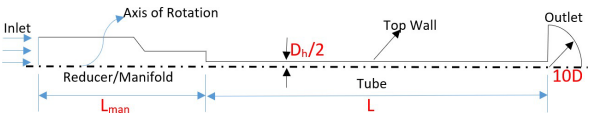


Figure 1. Computational domain for MT cross section.

A structured mesh of 40 × 200 is used in the MT. The number of divisions along the radial direction is the same for inlet reducer/manifold and outlet whereas 15 meshing nodes are used along the length of reducer and outlet respectively. Steady state RANS simulations are performed for all turbulent cases where SST $k$-$\omega$ turbulence model is used. A modified formulation of $\gamma$-$Re_\theta$ transition turbulence model for internal flows is applied [9]. The value of turbulence intensity at the inlet is 5% for all considered $Re$. A convergence criterion of $10^{-6}$ for RMS residuals of governing equations is chosen while monitor points for pressure and velocity at the MC/MT inlet and outlet are also observed during successive iterations. The reference pressure of 101 kPa was used.

To validate the adopted numerical model, experimental tests have been carried out. The testing apparatus with relevant instruments used to test the MT is shown in figure 2. The desired volume flow of the Nitrogen gas is imposed using a suitable mass flow controller. A commercial stainless steel MT

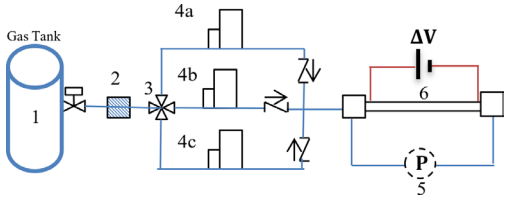


Figure 2. Schematic representation of the experimental test bench; Gas tank (1), particle filter (2), switch valve (3), mass flow meters (4), differential pressure sensor (5), MT (6).

from Upchurch® was used in the current experimental campaign for the evaluation of the thermal behavior of gas flows. The MT was heated using the Joule heating effect. A total of 7 K-type thermocouples were attached along the length of the MT to measure the wall temperature. To measure the total temperature at the outlet, Yamada et al. [10] used alternate baffles in the outlet chamber to reduce the speed of exiting gas flows avoiding the kinetic component of the temperature. A similar outlet chamber is also fabricated in the current study by micromachining a PMMA plastic sheet. A schematic diagram of the proposed device to measure the outlet temperature of the gas is shown in Figure 3a. The gas exits from the tube outlet and enters the outlet chamber where its temperature is measured at the red points (see Figure 3a).

Figure 3. Outlet chamber for total temperature measurement; design (a), and realized (b).

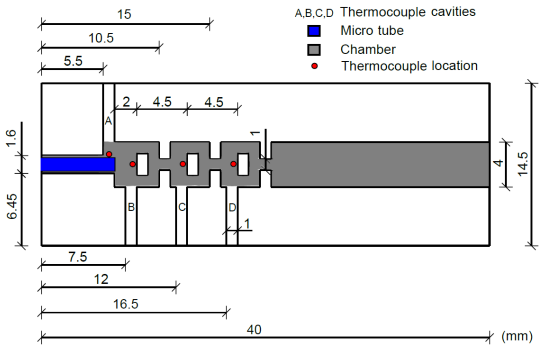


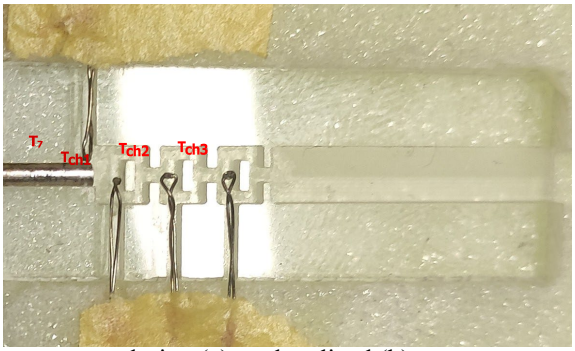


The thermocouple located in channel A is for measuring the wall temperature right at the outlet of the MT. The whole outlet chamber, as shown in figure 3b is then placed in a Styrofoam housing to avoid any possible heat loss to the surroundings. Under the applied H-boundary condition (CHF) the mean Nusselt number can be calculated as follows:

$$Nu_{av} = \frac{hD_h}{k_f} = \frac{D_h q_w}{k_f(\overline{T}_w - \overline{T}_b)} \qquad (1)$$

where Dh is the hydraulic diameter of the MT, h is convective heat transfer coefficient and kf is the fluid thermal conductivity calculated at average bulk temperature. Tw is the average wall temperature along the length of the MT and Tb is the average bulk temperature of the

gas between inlet and outlet. Heat flux at the inner wall of the MT can be calculated by making energy balance between inlet and outlet of the MT as follows:

$$q_w = \frac{\dot{Q}}{A_{ht}} = \frac{\dot{m} c_p \left(T_{out} - T_{in}\right)}{\pi D_h \Delta x} \qquad (2)$$

where $c_p$ is the gas specific heat at $T_b$, $\dot{m}$ is the mass flow rate of the gas, $T_{in}$ and $T_{out}$ are the gas temperature at the inlet and outlet of the MT, and $\Delta x$ represents the heated length of the tube. $\dot{Q}$ is the thermal power and $A_{ht}$ represents the heat transfer area.

## 3. Results and discussions

Instead of applying a CHF boundary condition in the numerical model, a temperature function based on the measured wall temperature profiles is evaluated using regression analysis in MATLAB. This function is then used as a wall thermal boundary condition for the validation of experimental results. It is well established that gas in MTs undergoes strong compressibility and hence experiences a significant decrease in static temperature close to the outlet [11–13]. Therefore, numerical $T_{out}$ is taken as the total temperature of the gas at the outlet instead of static temperature. This is also close to the experimental settings where gas is forced to stagnate on the baffle within the outlet chamber, providing a measure of the gas total temperature. The measured temperature of the gas in the outlet chamber is compared with the numerical results in figure 4a. The numerically evaluated gas outlet temperature is close to the value measured by the first thermocouple in the chamber. The numerical values of Nu are

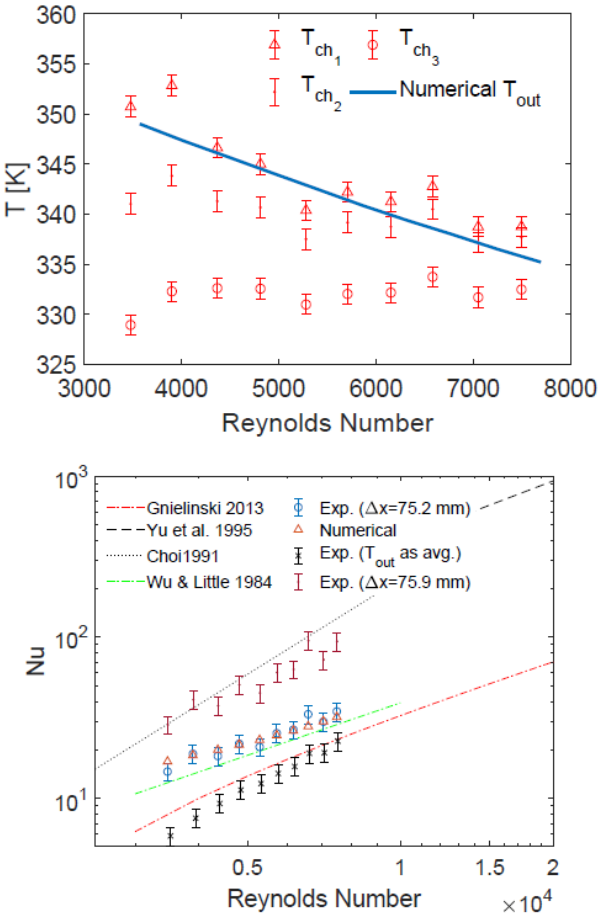


Figure 4. Comparison of experimental and numerical; outlet total temperature (a), Nusselt number (b).

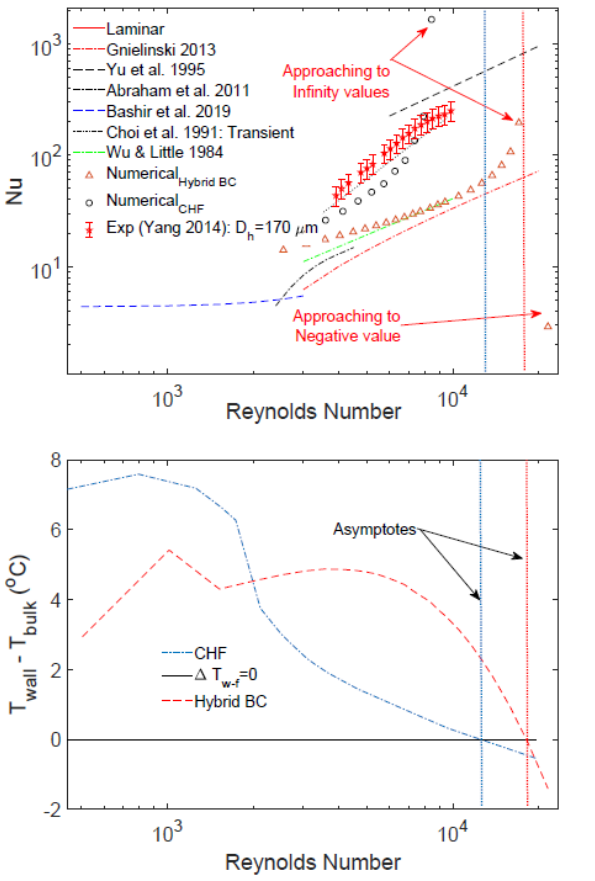


Figure 5. Comparison of *Nu* evaluated using hybrid and pure CHF boundary conditions (a), and the difference between wall temperature and bulk fluid total temperature (b).

compared with the experimental results in figure 4b. Three different evaluations of experimental Nu are plotted. If an average of the three thermocouples placed in the outlet chamber is used to represent $T_{out}$ as it was done by [10], the experimental $Nu$ is lower than the conventional Gnielinski's estimations. Evaluated *Nu* follows the trend predicted by Choi [2] in the case when $\Delta x$ is varied only by 0.7% of L. When the $\Delta x$ is 75.2 mm instead of 75.9 mm, the experimental results show an excellent agreement with the numerical results. Both experimental, as well as numerical values, are higher than Gnielinski's predictions. The difference between current results and Gnielinski's correlation is 89% at *Re* of ∼3,900 and reduces to 50% at Re of ∼7,500. Instead, the trend of the present numerical results closely follows the correlation proposed by Wu & Little [1]. Computations are further performed by applying a CHF boundary condition on the wall of the MT. For the comparison, simulations with experimental hybrid boundary condition are also extended to a higher Re. The comparison of computed *Nu* is shown in figure 5a. It is evident that when CHF boundary condition is applied at the entire length of the MT, the resulting *Nu* is much higher than what was observed for the experimental case (hybrid boundary condition). In the lower range of *Re*, numerical results are in agreement with the correlation proposed by Choi [2] but for *Re* > 4,000, these stay lower. However, there is a sharp increase in the value of *Nu* close to *Re* of ∼10,000 where it reaches significantly higher asymptotic values and then becomes negative. A similar trend can also be seen for the hybrid boundary condition case but at a higher *Re.* To underline the reason for such anomaly in the *Nu* for highly turbulent gas microflows, the temperature difference between wall and fluid bulk temperature is analyzed in figure 5b. When the gas velocity becomes too high along the length of the channel, $T_b$ (evaluated from total temperature) becomes almost equals to the integrated wall temperature and hence denominator of the average Nusselt number (see equation 1) approaches to zero.

## 4. Conclusions

A combined experimental and numerical campaign is carried out to investigate the forced convection of Nitrogen gas flow in a MT of 173 $\mu$m. For the thermal boundary condition encountered in the experimental settings, computed *Nu* from the numerical model is 89% higher than Gnielinki's correlation in the early turbulent regime and becomes 50% at the *Re* of ∼7,500. For a pure CHF boundary condition along the complete length of the MT, *Nu* from the numerical model is significantly higher than Gnielinski and is close to the trend predicted by Choi [2]. Furthermore, for the high speed gas flows (*Re* > 10, 000 in case of the current study), the bulk temperature of the gas becomes higher than the wall temperature of the MT, determining a vertical asymptote of *Nu*. Finally, the comparison between the numerical and the experimental data confirms how even the small variation of the thermal boundary conditions, adopted in the numeri- cal model, strongly affects the Nusselt numbers in the presence of strong compressibility effects within the turbulent flow regime.

## Acknowledgements

This research received funding from the European Union's Framework Programme for Research and Innovation Horizon 2020 (2014–2020) under the Marie Sklodowska-Curie Grant Agreement No. 643095 (MIGRATE Project).

## References

[1] Wu P and Little W 1984 *Cryogenics* 24 415 – 420 ISSN 0011-2275 URL http://www.sciencedirect.com/science/article/pii/0011227584900158

[2] Choi S 1991 *Micromechanical Sensors, Actuators, and Systems, ASME* 123–134

[3] Yu D, Warrington R, Barron R and Ameel T 1995 *ASME/JSME Thermal Engineering Conference* 1 523–530

[4] Yang C Y, Chen C W, Lin T Y and Kand- likar S G 2012 *Experimental Thermal and Fluid Science* 37 12 – 18 ISSN 0894-1777 URL http://www.sciencedirect.com/science/article/pii/S0894177711001725

[5] Hong C, Yamamoto T, Asako Y and Suzuki K 2012 *Journal of Heat Transfer* 134 ISSN 0022-1481 011602 URL https://doi.org/10.1115/1.4004645

[6] Hong C, Asako Y and Lee J H 2008 *J. Phy. D Apll. Phy.* 41

[7] Yang Y, Chalabi H, Lorenzini M and Morini G

L 2014 *Heat Transfer Engineering* 35 159–170 (*Preprint* https://doi.org/10.1080/01457632.2013.812489) URL https://doi.org/10.1080/01457632.2013.812489

[8] Yang Y, Hong C, Morini G L and Asako Y 2014 *International Journal of Heat and Mass Transfer* 78 732 – 740 ISSN 0017-9310 URL http://www.sciencedirect.com/science/article/pii/S001793101400595X

# Thermocapillary Bubble migration in very small-scale containers in Normal gravity environment

Yousuf ALHENDAL[1,*], Sara TOUZANI[2]

1: Mechanical Power and Refrigeration Department (MPR), College of Technological Studies (CTS), Public Authority for Applied Education and Training (PAAET), Kuwait.
2: Research team, Energy Systems, Mechanical Materials and Structures, and Industrial Processes Modeling (MOSEM2PI), Mohammadia School of Engineers, Mohammed V University in Rabat, P.O. Box 765 Agdal, Rabat, Morocco

*Corresponding author: Tel.: +965 66764000; Email: Ya.alhendal@paaet.edu.kw

**Abstract**: Bubble migration in normal gravity environment is numerically investigated using ANSYS-FLUENT software. The volume-of-liquid (VOF) method and geometric reconstruction scheme were used to track the gas-liquid interface. The appearance of thermocapillary flow in normal gravity can cause a decrease or increase in bubble migration depending on the geometry dimension. These results are difficult to obtain experimentally, which indicates the importance of this numerical study to understand the behavior of bubbles in the Earth with very small dimensions and in the presence of the Marangoni phenomenon.

**Keywords:** Thermocapillary, Gravity force, Bubble migration, Marangoni flow, Two-phase

## 1. Introduction

For different industrial applications, bubbles formation can be harmful to equipment [1]. Therefore, understanding the bubble dynamic is very important. It can help in designing new machines to either eliminate or manage those bubbles impact. With gravity, bubbles can deform and even break up, which makes their motion complex [2]. In this paper, an isolated Nitrogen bubble motion under gravity inside a container filled with Ethanol, is investigated (figure 1). The upper and lower walls are held at $T_{hot}$ = 325 K and $T_{cold}$ =300 K respectively. The lateral walls are adiabatic. Non-slip condition is applied on all walls. The thermocapillary bubble velocity is small and the flow is laminar. The thermophysical properties of the host liquid, which is incompressible and Newtonian, are assumed constant except for surface tension, σ. This later is varying according to temperature by the following expression:

$$\sigma = \sigma_0 + \sigma_T(T_0 - T) \qquad (1)$$

Before releasing the bubble into the unsteady motion, a steady state temperature field is established. The continuum surface force (CSF) model proposed by [3] is used to compute the surface tension force for the cells containing the gas-liquid interface. Ansys-Fluent is used to solve the governing equations by employing the VOF method.

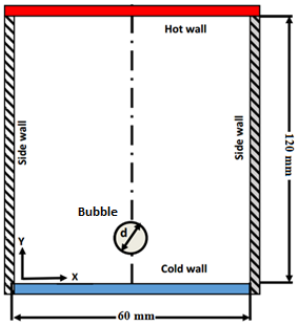


Fig 1. Schematic of the computed field for the 2D axis

## 2. Results and Discussion

In this work, three heights (h) of the container are considered: 10, 15 and 20 mm, and the bubble migration under normal gravity is studied for three bubble diameters (d): 0.64, 0.98 and 1.28 mm, respectively.

When d=0.64mm and h=10 mm, the bubble motion under gravity alone is slower than the

case where thermocapillary is presented (figure 2. a). However, for d=0.98mm and h=15 mm, the impact of the thermocapillary force decreases. The bubble begins to exceed under gravity alone (figure 2.b). The same thing is observed for d=1.28mm and h=20 mm (figure 2.c). In figure 3, the flow patterns of the bubble under gravity alone and with the addition of thermocapillary force are plotted. For both cases, the bubble shape is deformed. The deformation is enhanced with thermocapillary force existence.

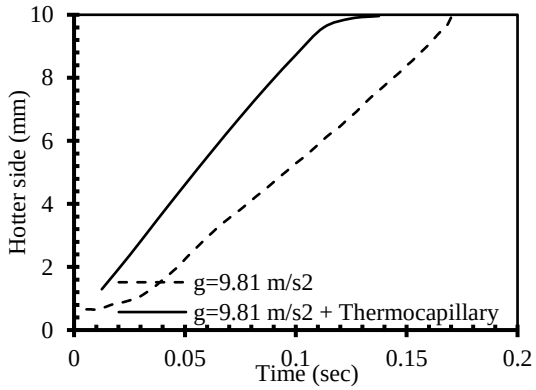


(a)

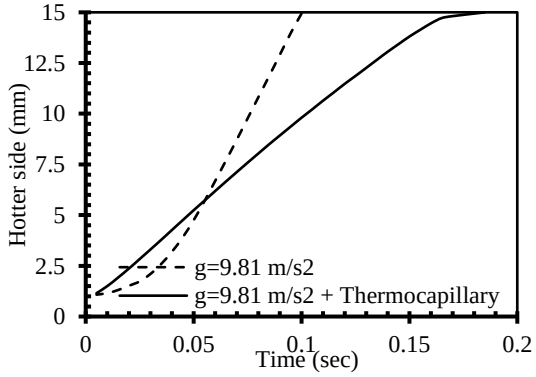


(b)

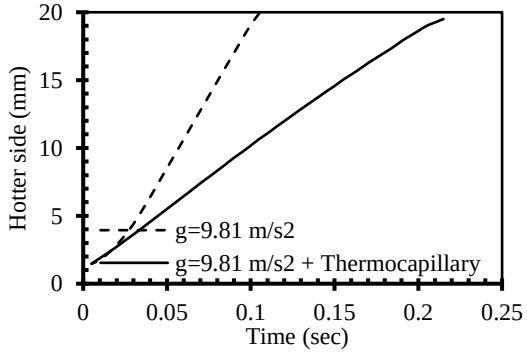


(c)

Figure 2: Trajectory of bubble under Normal gravity alone and under gravity + Thermocapillary for:
a: Bubble diameter = 0.64mm, height = 10mm.
b: Bubble diameter = 0.98mm, height =15mm.
c: Bubble diameter = 1.28mm, height =20mm.

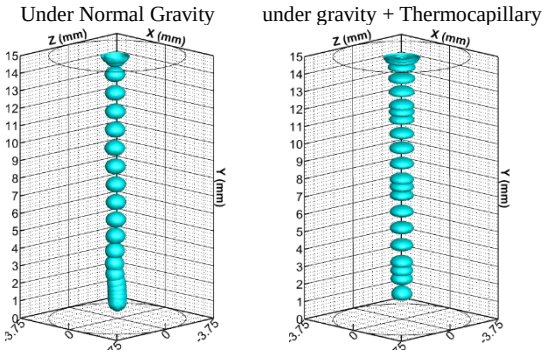


(a)

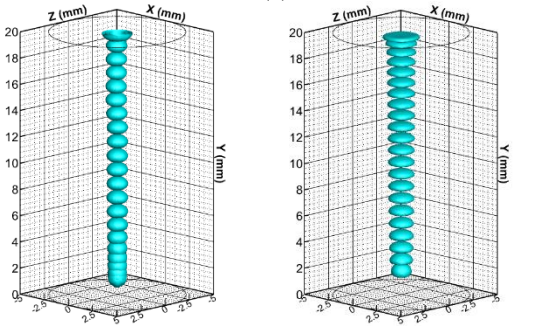

(b)

Figure 3: Flow patterns for:
a: Bubble diameter =0.98mm, height = 15 mm.
b: Bubble diameter =1.28 mm, height = 20 mm.

## 3. Conclusion

A CFD model, using ANSYS/FLUENT, is developed to study nitrogen bubble migration in a normal gravity environment in the presence of the Marangoni phenomenon. In general, for small scall of less than 10 mm in height, the driving force for movement is the thermocapillary force, which plays an important role in either accelerating or slowing down the migration of bubbles at a higher scale.

## References

[1] Nie, D. M., Qui, L. M., Zhang, X. B., 2015. Bubble Motion under gravity through Lattice Boltzmann Method. Proceedings of the 2015 International Conference on Artificial Intelligence and Industrial Engineering, 123, 531-533.
[2] Filella A., Ern, P., Roig, V., 2015. Oscillatory motion and wake of a bubble rising in a thin-gap cell. J. Fluid Mech., 778,60-88.
[3] Brackbill, J. U., Kothe, D. B., Zemach, C. 1992. A continuum method for modeling surface tension. J. Comput. Phys. 100, pp. 335–354.

# Computational Fluid Dynamics comparison of static mixers in emulsification processes

Jody ALBERTAZZI[1], Renato ROTA[1], Valentina BUSINI[1,*]

1: Department of Chemistry, Materials and Chemical Engineering "Giulio Natta", Politecnico di Milano, Milano, IT

* Corresponding author: Tel.: +; Email: valentina.busini@polimi.it

**Abstract:** Emulsions are droplet dispersions of immiscible liquids in a continuous phase, which find applications in many industry sectors such as cosmetics, pharmaceuticals, chemicals, and the food industry. The energy required for the breakage of droplets can be obtained through mechanical agitators in stirred tanks or through active mixers such as pulse-flow mixers and ultrasonic mixers; however, instruments such as static mixers represent a good alternative, since they usually require lower maintenance costs and they are less susceptible to failures. Static mixers are commercialized in a wide range of shapes and dimensions; two of the most commonly employed static mixers are represented by the Kenics Static Mixers and the Sulzer Static Mixers. The study of the mixing process inside these two types of static mixers have been already been treated; however, to the best of the authors' knowledge, these two static mixers have not been compared in emulsification processes. The goal of this work is to compare, through a Computational Fluid Dynamics approach, the performance of the Sulzer Static Mixers and the Kenics Static Mixers for the production of emulsions considering different values of Reynolds number.

**Keywords:** CFD, emulsions, static mixers

## 1. Introduction

Emulsions are dispersions of one fluid into another immiscible one [1]; they are used in many different industrial fields, from the chemical to pharma and food [2]. Emulsions can be produced in batch mode; however, continuous emulsification can ensure reduced volumes and a constant quality of the final product. Static mixers represent an increasingly adopted tool for producing emulsions in a continuous mode; indeed, they can offer a more homogeneous distribution of the field of breakage than other tools such as stirred-tanks or rotor-stators [3], while requiring low operation costs and maintenance. Among static mixers, two of the most common ones are the Kenics Static Mixers (KSM) and the Sulzer Static Mixers (SMX). Even if these mixers have already been studied in other works, in terms of pressure drop and mixing efficiency, to the best of the authors' knowledge they have not been compared in emulsification processes with different range of fluid dynamic conditions and fluid properties. The goal of this work is to compare, through a Computational Fluid Dynamics approach the performance of the Sulzer Static Mixers and the Kenics Static Mixers for the production of emulsions, considering different values of Reynolds number. The modelled geometries are reported in Fig. 1 and consist in two pipes equipped with 10 KSM (Fig 1a) and 10 SMX (Fig 1b).

## 2. Methods

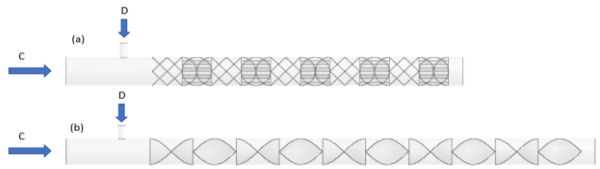


**Fig. 1.** Pipe equipped with Kenics Static Mixers (a) ; Pipe equipped with Sulzer Static Mixers (b)

The continuous phase, named C, enters the pipe, which has a diameter equal to $d_{ax} = 0.04$ $m$ while the dispersed phase, named D, enters through a lateral tube with a diameter equal to $d_{lat} = 0.01$ $m$. Since the aspect ratio of the KSM is equal to 1.5, the pipe equipped with KSM is longer than the pipe equipped with SMX. The geometries were discretized into

meshes composed of cells with a dimension equal to 3 mm in the whole domain except for the areas in proximity of the mixing elements, where cell sizes equal to 0.4 mm were applied. The simulations were conducted by means of the Ansys Fluent 19.1 software; the turbulence was modelled through the realizable k-ε model, which can reproduce complex flow with strong streamline curvature [3].

## 3. Results

The continuous phase is an aqueous solution of high-fructose corn syrup, with density equal to $\rho_C = 1268\ kg/m^3$ and viscosity equal to $\mu_C = 0.022\ Pa \cdot s$, while the dispersed phase is silicon oil, with density equal to $\rho_D = 978\ kg/m^3$ and viscosity equal to $\mu_D = 0.978\ Pa \cdot s$. The interfacial tension between the two fluids is equal to $\sigma = 0.0385\ 1/N$ [4]. Simulations were carried varying the spatial velocity inside the pipe, to obtain different values of Reynolds number (Re), defined as $Re = \frac{\rho_C \cdot v \cdot D}{\mu_C}$, where v is the spatial velocity inside the pipe and D is the diameter of the pipe. Fig 2 shows the values of the Sauter diameter (defined as $d_{32} = \frac{\sum N_i d_i^3}{\sum N_i d_i^2}$) monitored at the outlet of the pipe as a function of Re; we can see that the Sauter diameters obtained tend to decrease with the Re number. Moreover, the droplet diameters obtained with the SMX are considerably lower than the ones obtained with the KSM.

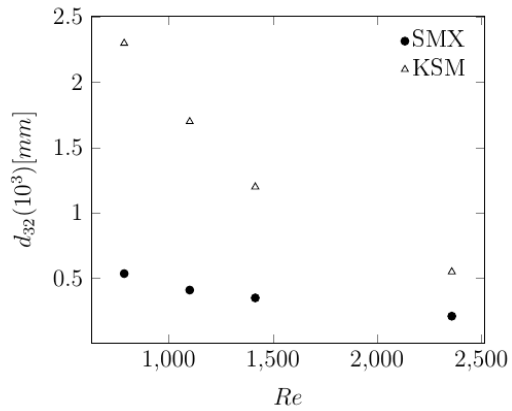


**Fig. 2** Sauter diameters as function of the Re number

This result can be understood by looking at the contours of turbulence eddy dissipation obtained with the two static mixers. This parameter is a measure of the turbulence reached in the pipe and is responsible for the breakage of droplets; the higher the turbulence eddy dissipation, the smaller the diameter of droplets. It is possible to see in Fig. 3 that the SMX can reach higher values of turbulence eddy dissipation, thus justifying the difference obtained in the droplet diameters.

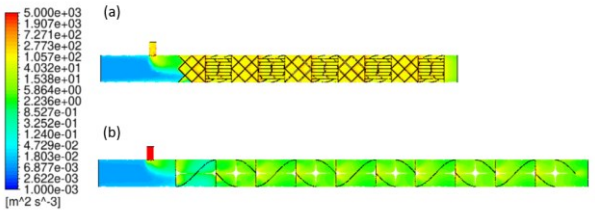


**Fig. 2** Turbulence eddy dissipation with SMX (a) and KSM (b) for $Re = 2358c$

## 4. Conclusions

In this work, the performance of SMX and KSM were compared; it was found that the droplet diameters obtained with SMX are smaller than the ones obtained with the KSM. With this type of static mixer, it is possible to obtain higher values of turbulence eddy dissipation (i.e., smaller droplet diameters) in a shorter pipe length.

## References

[1] Madhavan, N.; Yalla, E.; Pushpavanam, S.; Renganathan, T.; Mukherjee, M.; Basavaraj, M. G. Semi-batch and continuous production of Pickering emulsion via direct contact steam condensation. Soft Matter, 2021, 17, 9636.

[2] Coroneo, M.; Montante, G.; Paglianti, A.; Computational Fluid Dynamics Modeling of Corrugated Static Mixers for Turbulent Applications. Industrial & Engineering Chemistry Research, 2012, 51, 15986-15996.

[3] Lebaz, N.; Aziz, F.; Sheibat-Othman, N. Modeling Droplet Breakage in Continuous Emulsification Using Static Mixers in the Framework of the Entire Spectrum of Turbulent Energy. Industrial & Engineering Chemistry Research, 2022, 61, 541–553.

[4] Rama Rao, N.V.; Baird, M.H.I.; Hrymak, A.N.; Wood, P.E. Dispersion of high-viscosity liquid–liquid systems by flow through SMX static mixer elements. Chemical Engineering Science, 2007, 62, 6885-6896.

## SESSION 3a
## MINI SYMPOSIUM
## Nanofluids: beyond NANOconVEX
Chair: **Prof. L. Hernández López**



Jorge BURGOS[1], Rosa MONDRAGÓN[1], Simona BARISON[2], Filippo AGRESTI[2], Simone MANCIN[3], Giulia RIGHETTI[3], Stefano ROSSI[4], Leonor HERNANDEZ[1]
1: Department of Mechanical Engineering and Construction, Universitat Jaume I, Castellón de la Plana, Spain
2: CNR ICMATE, Padova, Italy
3: Department of Management and Engineering, University of Padova, Vicenza, IT 4: CNR ITC, Padova, Italy



Hazhir FATAHI[1], Kevin DAOUST[2], Hamid AKBARZADEH[3,4], Simone MANCIN[5], Jérôme CLAVERIE[2], Sébastien PONCET[1]
1: Department of Mechanical Engineering, Université de Sherbrooke, Sherbrooke, Canada
2: Department of Chemistry, Université de Sherbrooke, Sherbrooke, Canada
3: Department of Bioresource Engineering, McGill University, Montreal, Canada
4: Department of Mechanical Engineering, McGill University, Montreal, Canada
5: Department of Management and Engineering, University of Padova, Vicenza, Italy



Aswin RAGUNATHAN[1], Alexander KOROBKO[1], Sana FATEH[1]
1: SYNANO, Molengraaffsingel 10, 2629 JD, Delft, NL



Shunsuke HASHIMOTO[1], Satoshi YAMAGUCHI[2], Masashi HARADA[2], Kenji NAKAJIMA[3], Tatsuya KIKUCHI[3], Kazuki OHISHI[4]
1: Energy Management Research-Domain, Emerging Technology Div., Toyota Central R&D Labs., Inc., JP
2: Analysis Research-Domain, Emerging Technology Div., Toyota Central R&D Labs., Inc., JP
3: Materials & Life Science Div., J-PARC Center, JP 4: Neutron Science and Technology Center, CROSS, JP

# Paraffin/water nanoemulsions with reduced supercooling for thermal management systems

Jorge BURGOS[1], Rosa MONDRAGÓN[1], Simona BARISON[2], Filippo AGRESTI[2], Simone MANCIN[3], Giulia RIGHETTI[3], Stefano ROSSI[4], Leonor HERNANDEZ[1,*]

1: Department of Mechanical Engineering and Construction, Universitat Jaume I, Castellón de la Plana, Spain
2: CNR ICMATE, Padova, Italy
3: Department of Management and Engineering, University of Padova, Vicenza, IT
4: CNR ITC, Padova, Italy

* Corresponding author: Email: lhernand@uji.es

**Abstract**: Phase change material nanoemulsions were synthesised and characterised to be used as possible storage and heat transfers fluids in low temperature thermal management. Thermal energy storage densities of different paraffin / water nanoemulsions were studied, and RT44HC was selected as the optimized PCM. Seven different nucleating agents, including paraffin waxes with higher melting point, nanoparticles and other organic materials, have been experimentally tested. It was found that 5% paraffin nanoemulsions with 1-octadecanol as nucleating agent (weight fraction 1:10 with respect to PCM), reduced supercooling up to 32 % over samples without nucleating agent, while maintaining the thermal properties of the sample under thermal cycling. Good stability (for both high temperatures and thermal cycling) of the nanoemulsions were observed, while an increase in the viscosity was measured.

**Keywords:** Paraffin/water nanoemulsion, supercooling, thermal management systems

## 1. Introduction

Thermal management systems (TMS) are crucial in the present context of heating and cooling energy demands. TMS with water as working fluid is one of the most commonly used. However, water can only use sensible heat to store thermal energy. Latent heat from phase change materials (PCM) can improve this thermal energy storage density, so different paraffin/water nanoemulsions have been previously studied. Some practical applications of these nanoemulsions could be for electronic cooling or for solar thermal systems. Nevertheless, three important challenges for the applications of these nanoemulsions are high supercooling, poor stability and increased viscosity. The addition of nucleating agents (NA) is the most common approach to reduce supercooling. In this study, different NA have been used when synthesizing paraffin/water nanoemulsions (PCMEs) with 5% of optimized PCM. Stability and viscosity measurements have been performed for the sample with the best supercooling behaviour.

## 2. Materials and synthesis

Three commercial paraffin waxes in the temperature range of water applications, RT35HC, RT44HC and RT54HC (Rubitherm Technologies GmbH) were evaluated as PCMs for the PCME. Sodium dodecyl sulphate (SDS) was used as surfactant, as provided the highest nanoemulsion stability in previous studies [1]. Seven NA were tested to reduce supercooling: RT70HC, palmitic acid, functionalized $TiO_2$, myristic acid, 1-octadecanol, 1-hexadecanol and docosanol.

The paraffin and the NA were pre-melted in a temperature controlled oil bath under magnetic stirring, while SDS was dissolved in deionised water and then mixed with the melted paraffin/NA mixture. This mixture was dispersed with the ultrasound probe (Sonics VCX130, Sonics and Material, Inc., operating at 20 kHz and 130 W), firstly at 50% power for 5 minutes in on-off steps of 5 seconds in the oil bath between 50-60 ºC, and then the same process was carried out at room temperature at 75% power. To prepare 20 g of sample the

concentrations were set to 5 wt.% for the paraffin, 1:8 weight fraction for SDS:PCM and 1:10 for NA:PCM, except for functionalized $TiO_2$ nanoparticles, where 0.5:10 was used. These values were also used in previous studies [1].

## 2. Results

The first step was to select the paraffin to be used in the nanoemulsion by maximizing their resulting thermal energy storage density (TESD). TESD was calculated as the addition of sensible heat storage of the emulsion (in a temperature step of 15ºC) and the latent heat storage due to the paraffin melting. Theoretical (provided by manufacturer) and experimental (measured in DSC3 Mettler Toledo) datasets were used for these calculations. The best result was obtained for the RT44HC nanoemulsion, for both theoretical and experimental data, with 14.9% and 16.1% of TESD increase with respect to water. Hence this paraffin was selected for the further stages of the research.
The supercooling of PCME using different types of NA was evaluated. It was remarkable the 32.4% supercooling improvement when using 1-octadecanol, reducing the initial supercooling of the nanoemulsion from 14.9 to 10.1 ºC. Figure 1 shows the DSC heat flow curves for the RT44HC paraffin, and the PCME without and with 1-Octadecanol as NA. The melting point is maintained for both nanoemulsions. However, while supercooling is low for pure paraffin, significantly increases for the nanoemulsion, although an important reduction is observed when using 1-octadecanol as NA.

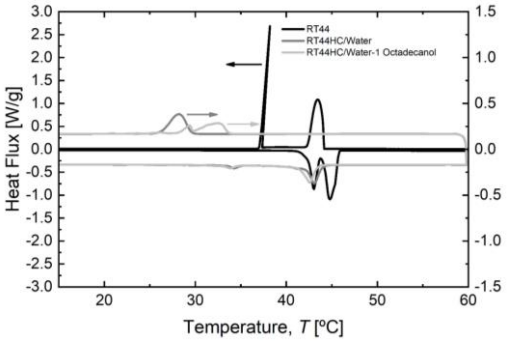

Fig 2. Heat flow curves of different samples.

Once the optimized nanoemulsions were developed (RT44HC/water-1 octadecanol), their colloidal stability and rheological behaviour was evaluated. High temperature colloidal stability of the sample was measured with DLS (Malvern Zetasizer Nano ZS) at different temperatures: first at 25ºC, then at 70ºC and then at 25ºC again. The resulting Z-average values for each of these temperatures were 189.2 nm, 180.5 nm and 202.1 nm respectively, showing a good stability with only small changes in the size distribution. Thermal cycling stability was evaluated applying ten temperature cycles between 0 and 60 ºC in DSC. Negligible changes in crystallization temperature (0.5%) and latent heat (0.6%) of the nanoemulsion were observed. The apparent viscosity of PCME at different temperatures was measured with a rotational rheometer (AR G2, TA Instruments) in the 0-1200 $s^{-1}$ shear rate range. Viscosities of 1.31 mPa·s and 0.57 mPa·s were obtained for 25 ºC and 70 ºC respectively, which represents an increase of about 44% with respect to water.

## 3. Conclusions

The use of 5 wt.% of RT44HC in PCME increased by 16% TESD while the addition of 1-octadecanol as NA reduced its supercooling by 32%. The resulting nanoemulsions showed good results for stability (both high temperature and thermal cycling), however an increase in the viscosity (around 44%) was observed.

## Acknowledgments:

This research was partially funded by projects UJI-B2020-32, PROMETEO/2020/029, PCM Cool Project@CNR and research stay CIBEFP/2021/10.

## References

[1] Burgos, J., Ayora-Fernández, M., Mondragón, R., Nithiyanantham, U., Fabregat-Santiago, F., Hernández, L., 2022 October. Characterization of hybrid carbon -paraffin/water nanoemulsions for DASC: stability, thermal energy storage and optical properties. In 6th Int. Symposium on IMPRES.

# Thermal conductivity improvement of adipic acid as a phase change material by boehmite-silica core-shell nanoparticles

Hazhir FATAHI[1], Kevin DAOUST[2], Hamid AKBARZADEH[3,4], Simone MANCIN[5], Jérôme CLAVERIE[2], Sébastien PONCET[1,*]

1: Department of Mechanical Engineering, Université de Sherbrooke, Sherbrooke, Canada
2: Department of Chemistry, Université de Sherbrooke, Sherbrooke, Canada
3: Department of Bioresource Engineering, McGill University, Montreal, Canada
4: Department of Mechanical Engineering, McGill University, Montreal, Canada
5: Department of Management and Engineering, University of Padova, Vicenza, Italy

* Corresponding author: Email: Sebastien.Poncet@usherbrooke.ca

**Abstract:** Phase change materials (PCMSs) can store and release a high amount of thermal energy at different operating temperatures. They can be integrated in both thermal management and thermal storage applications. However, the low thermal conductivity of PCMs is a challenge to overcome. The aim of this study is to improve the thermal conductivity of adipic acid, which is a non-hazardous organic PCM capable of storing 250 J/g of thermal energy at 150 °C. To do so, nanoparticles of boehmite-silica in the form of core-shell are dispersed in melted adipic acid at low amount (up to 0.2 wt%). The results show an increase of 9 % in the thermal conductivity without reducing the enthalpy.

**Keywords:** Phase change material, Nanoparticles, Thermal Conductivity, Enthalpy

## 1. Introduction

The application of Phase change materials is becoming more and more promising in both thermal management and storage applications because of their high capacity to store and release heat. The main challenge that hinders PCMs to be more integrated in the mentioned applications is their low thermal conductivity [1]. Therefore, one need to customize their thermal conductivity based on the potential application. There are several methods to improve the heat transfer phenomenon in PCMs such as inserting metallic fins or foams, using extended surfaces, and dispersing nanoparticles in PCMs [1,2]. For most PCM applications, the thermal conductivity enhancement should not reduce the high enthalpy of PCMs. Using nanoparticles and synthesizing a nano-structure enables us to develop a nano-PCM with multi-functional properties for different applications. When using nanoparticles, there are several challenges such as cost of nanoparticles, compatibility with host matrix, stability in the matrix. In this study, we synthesized a cost-effective boehmite-silica ($AlOOH@SiO_2$) core@shell nanoparticles to improve the thermal conductivity of PCMs.

## 2. Material and Methods

In this study adipic acid, which is an organic non-hazardous compound, is used as a PCM without further purification. Adipic acid can store and release around 250 J/g of thermal energy at 150 °C [3]. To improve thermal conductivity of adipic acid, core-shell nanoparticles ($AlOOH@SiO_2$) is synthesized via Stöber method that is based on sol-gel process. The boehmite nanoparticles with a blade like shape (an average length of 40 nm) used as a core for the formation of silica shell. Boehmite, which is an aluminum hydroxide, is a cost-effective additive that can be synthesized from aluminum industries wastewater. The TEM image of ($AlOOH@SiO_2$) core-shell nanoparticles is presented in Figure *1*.

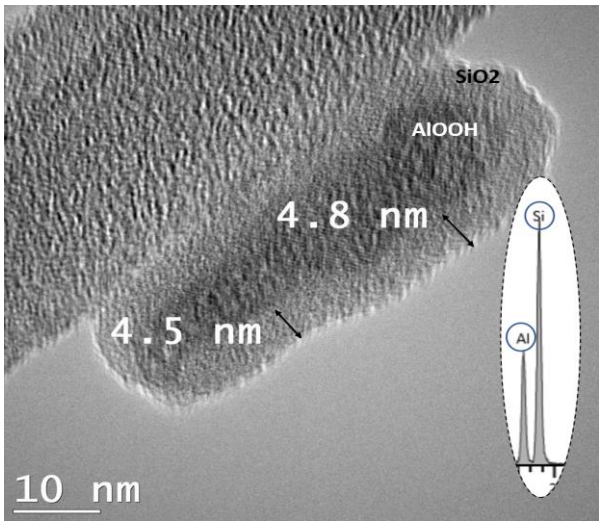


Figure 1 TEM image of a single AlOOH@$SiO_2$ particle.

Different weight percentages of the nanoparticles (0.05, 0.1 and 0.2 wt%) is dispersed in melted adipic acid under continuous stirring and non-continuous sonication. Disk shape samples of nano-PCMs with a diameter of 20 mm and a thickness of 6 mm are prepared for measuring thermal conductivity. using modified transient plane source technique (MTPS). The effect of adding nanoparticles on the enthalpy of adipic acid is analyzed by differential scanning calorimetry (DSC, TA Q20P) test in nitrogen atmosphere with a heating rate of 2˚C/min.

## 3. Results

Figure *2* (left y axis) presents the thermal conductivity enhancement of nano-PCM as a function of weight percentage of nanoparticles. The results show an increase of 9% in the thermal conductivity of the nano-PCM by adding 0.05 wt% of boehmite-silica core@shell nanoparticles. However, this enhancement drops to 6.5% and stabilizes by increasing the weight percentage of the added nanoparticles to 0.1 and 0.2 wt%. It is also observed on Figure *2* (right y axis) that adding the nanoparticles leads to a maximum 3% decrease in the enthalpy of adipic acid at 0.2 wt% of AlOOH@ $SiO_2$.

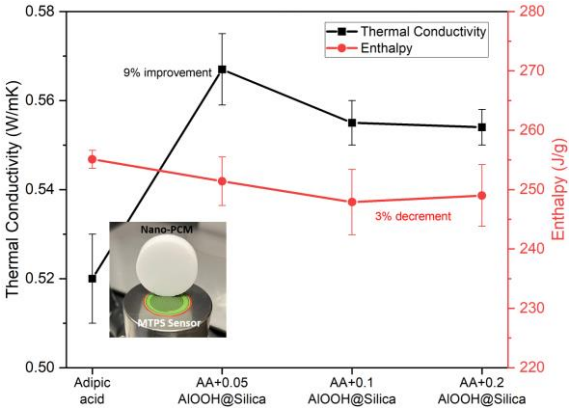


Figure 2 Thermal conductivity and enthalpy change of the nano-PCM as a function of wt%.

## 4. Conclusion

A maximum 9% thermal conductivity improvement of an organic PCM (adipic acid) is achieved adding AlOOH@$SiO_2$ nanoparticles at 0.05 wt% without decreasing its enthalpy.

## References

[1] G. Righetti, G. Savio, R. Meneghello, L. Doretti, S. Mancin, Experimental study of phase change material (PCM) embedded in 3D periodic structures realized via additive manufacturing, Int. J. Therm. Sci. 153 (2020) 106376. https://doi.org/10.1016/J.IJTHERMALSCI.2020.106376.

[2] S. Motahar, N. Nikkam, A.A. Alemrajabi, R. Khodabandeh, M.S. Toprak, M. Muhammed, A novel phase change material containing mesoporous silica nanoparticles for thermal storage: A study on thermal conductivity and viscosity, Int. Commun. Heat Mass Transf. 56 (2014) 114–120. https://doi.org/10.1016/J.ICHEATMASSTRANSFER.2014.06.005.

[3] H. Fatahi, J. Claverie, S. Poncet, Experimental investigation of the rheological and phase change behavior of adipic acid as a phase change material (PCM) for thermal energy storage at 150 °C, Thermochim. Acta. (2022) 179206. https://doi.org/10.1016/J.TCA.2022.179206.

# Comparative Analysis of Heat Transfer Enhancement in Nucleate Pool Boiling: Nanofluids vs Micro Surface Modifications

Aswin RAGUNATHAN[1], Alexander KOROBKO[1], Sana FATEH[1, *]

1: SYNANO, Molengraaffsingel 10, 2629 JD, Delft, NL

* Corresponding author: Tel.: +31 06 26247115; Email: s.fateh@synano.eu

**Abstract:** The pool boiling of nanofluids and base fluids on structured surfaces has been investigated for quite a long time. Significant effort has been made in studying and understanding the effect of such features on the heat transfer performance of the two-phase cooling solutions. In addition to previous research, the present experimental study shows significantly positive effect of the engineered surfaces with various structures and mild effect of $Al_2O_3$ nanoparticles on the boiling curve of water at atmospheric pressure.

**Keywords:** Pool Boiling, Micro-Structured Surfaces, $Al_2O_3$ Nanofluids, Heat Transfer

## 1. Introduction

Efficiency and control of the two-phase heat transfer through a solid-liquid interface are of great value in various industrial, scientific, and engineering applications [1]. Improving such processes offers substantial benefits for thermal management systems, the performance of electronic devices, and advancing energy conversion technologies, among other pivotal applications. In recent decades, the surface modification and employment of nanofluids have collected substantial attention for their capacity to enhance the nucleate heat transfer and to govern the maximum (Critical) Heat Flux that a surface can accommodate before a transition from nucleate boiling to film boiling occurs [2, 3].

The synergy between fluid properties and surface features significantly governs the pool boiling heat transfer on a large scale, controlling the formation and dynamics of bubbles on a minor scale and their influence on the heat transfer coefficient. Despite the significant amount of research that has been done in this area, the complete understanding and prediction of the boiling process on all scales and conditions is still on the other side of the horizon.

The main objective of our study is to compare the effect of micro-structured surfaces and nanofluids on the efficiency of nucleate pool boiling heat transfer in the fixed experimental environment.

## 2. Nucleate Pool Boiling

The experimental research was aimed at pool boiling tests on non-modified and modified aluminium surfaces at atmospheric conditions. Three discrete types of modification (holes, pillars, and channels) were laser-fabricated on the sample surface, maintaining uniform feature dimensions across all variations, Fig. 1.

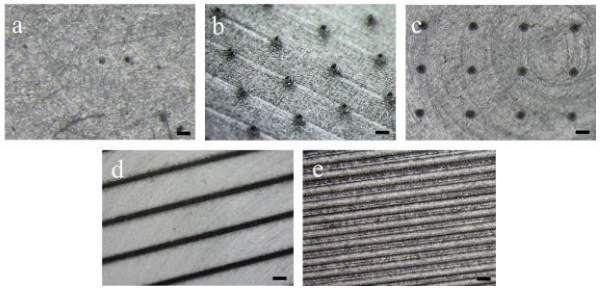


**Fig. 1.** Boiling surfaces of low (b, c, d; 1 mm pitch) and high (e; 0.3, mm pitch) structure density. Bar corresponds to 0.2 mm scale. (a) shows the unmodified surface.

Water and water-based $Al_2O_3$ nanofluid of various particle concentrations (0.01, 0.1, 1 wt%) and 100 nm of average particle size were employed to determine their heat transfer performance in relation to the boiling surface. An in-house pool boiling experimental setup was designed and constructed. The setup validation and baseline measurements were conducted using pool boiling of water on the unaltered aluminum surface (Fig. 1(a)) and results were compared with the ones presented

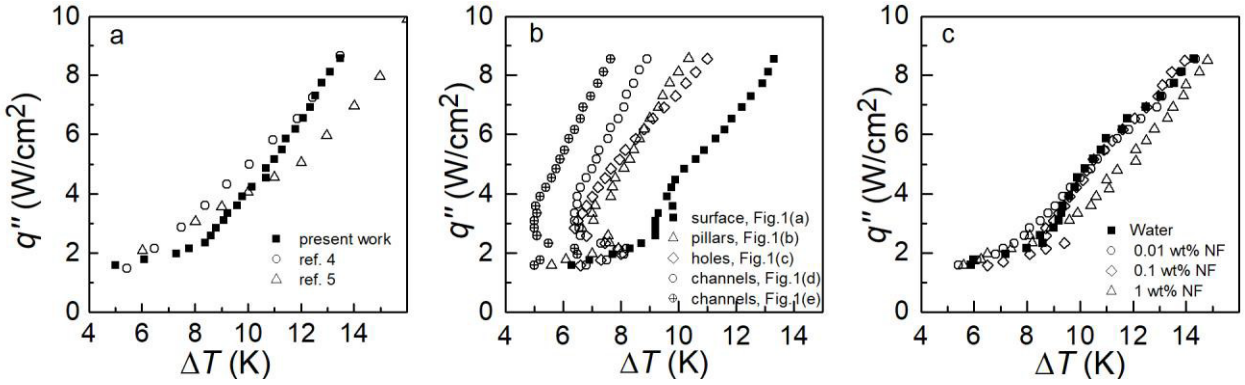


**Fig. 2.** (a) Comparison of pool boiling curve of water obtained in this study with data collected from the literature. (b) Pool boiling curves of water on unmodified (Fig. 1 (a)) and modified surfaces. (c) Experimental data for water-based $Al_2O_3$ nanofluid of various concentrations. Wall superheat temperature, $\Delta T$, is the difference between the surface temperature and the saturation temperature of fluid.

in the literature. Heat flux through the boiling surface was incrementally raised, ranging from 1.5 to 9 W/cm². Consistent outcomes were observed across multiple trials for each sample, exhibiting a nearly identical relation between heat flux and wall superheat temperature.

Figure 2 (a) shows validation curves for pool boiling of water on an unaltered surface. In general, the data are in line with the previously published results, but with the Onset of Nucleate Boiling (ONB) at $\Delta T \sim 8.5$ K. Above ONB, a nearly linear correlation between the heat flux and the excess temperature is established.

The structure of the boiling surface alters the boiling process significantly by shifting the ONB point to lower surface temperatures, Fig. 2(b). Although the surface with micro-channels shows the highest increase in heat transfer, all the pool boiling curves for structured surfaces obey S-shape behavior with almost linear dependency at high heat fluxes. With increasing the surface density of micro-channels, Fig. 1(e), the heat transfer intensifies, and the surface temperature decreases further, Fig. 2(b).

The effect of $Al_2O_3$ nanoparticles on the boiling process was investigated on unaltered surface as shown in Fig. 2(c). Results suggest that for the concentration scale of 0.01 and 0.1 wt%, nanoparticles have a slight effect on the boiling process. For nanofluids with 1 wt% particle concentration, the transition from convective to nucleate pool boiling regime occurs more smoothly delaying the boiling and thus degrading the heat transfer performance.

## 3. Conclusions

The boiling heat transfer coefficient increased by up to 50% for channels, 40% for holes, and 30% for pillars compared to original non-modified surfaces. Although the boiling curves hold almost the same scaling at high *q"*, the main cause of the heat transfer increase is the reduction of the boiling incipience temperatures, by 2-3° C. On the other hand, alumina nanofluids do not significantly increase the boiling process and even reduce the heat transfer performance at higher particle concentrations.

### References

[1] Murshed, S.M.S., De Castro, C.A.N., 2017. A critical review of traditional and emerging techniques and fluids for electronics cooling. Renew. Sust. Energ. Rev. 78, 821-833.

[2] Liang, G., Mudawar, I., 2019. Review of pool boiling enhancement by surface modification. Int. J. Heat Mass Transf. 128, 892-933.

[3] Liang, G., Mudawar, I., 2018. Review of pool boiling enhancement with additives and nanofluids. Int. J. Heat Mass Transf. 124, 423- 453.

[4] Kamel, M.S., Lezsovits, F., 2020. Enhancement of pool boiling heat transfer performance using dilute cerium oxide/water nanofluid: An experimental investigation. Int. Comm. Heat Mass Transf. 114, 104587.

[5] Wen, D. S., Wang, B. X., 2002. Effects of surface wettability on nucleate pool boiling heat transfer for surfactant solutions. Int. J. Heat Mass Transf. 45, 1739-1747.

# Mechanism of Thermal Conductivity Enhancement in Nanofluids

Shunsuke HASHIMOTO[1,*], Satoshi YAMAGUCHI[2], Masashi HARADA[2], Kenji NAKAJIMA[3], Tatsuya KIKUCHI[3], Kazuki OHISHI[4]

1: Energy Management Research-Domain, Emerging Technology Div., Toyota Central R&D Labs., Inc., JP
2: Analysis Research-Domain, Emerging Technology Div., Toyota Central R&D Labs., Inc., JP
3: Materials & Life Science Div., J-PARC Center, JP
4: Neutron Science and Technology Center, CROSS, JP

* Corresponding author: Tel.: +81 561 71 8008; Email: e1639@mosk.tytlabs.co.jp

**Abstract:** The behavior of liquid molecules in the nanofluids of $SiO_2$ particle with sizes exceeding 100 nm dispersed in a 50 wt% aqueous solution of ethylene glycol was investigated using several analytical methods that utilize neutrons and X-rays. The translational motion of liquid molecules around nanoparticles was restrained in nanofluids. Additionally, the presence of nanoparticles excites vibrations derived from intermolecular hydrogen bonds of liquid molecules extensively surrounding the particles, while limiting vibrations derived from intramolecular hydrophobic covalent bonds. The vibration of liquid molecules is equivalent to phonon conduction in solids, and the increase in thermal conductivity of the suspension due to the presence of nanoparticles is inferred to be derived from the limitation of the translational diffusion and the resulting solid-like behavior of the liquid molecules.

**Keywords:** $SiO_2$ nanofluid, Thermal conductivity, Liquid molecule, Hydrogen bond

## 1. Introduction

Recently, nanofluids, which contain nanometer size particles, have received remarkable attention as the next generation of coolant due to their brilliant thermal performance [1]. There are several interesting research about the anomalous enhancement of effective thermal conductivity, $\lambda$ in nanofluids [2]. The present study focused on the dynamics of liquid molecules around particles in nanofluids, which may be responsible for the increase in the $\lambda$ with nanofluids. Interestingly, our previous study [3] demonstrated that the $\lambda$ of the $SiO_2$-ethylene glycol (EG)/water nanofluid, which is from 100 to 1000 nm in diameter, becomes local maximum value at the particle diameter of 300 nm. In addition, the measured $\lambda$ of the nanofluid is higher than the estimated values from each property of particles and base fluid and their composition from "Effective Medium Theory (EMT)" [4]. In the present study, the dynamics of solution molecules surrounding $SiO_2$ particles in nanofluids were analyzed by means of various techniques; Quasi-Elastic Neutron Scattering (QENS), Small-Angle Neutron Scattering (SANS), Inelastic X-ray Scattering (IXS), Wide-Angle X-ray Scattering (WAXS). Finally, the enhancement mechanism of $\lambda$ in nanofluids was discussed based on the obtained findings.

## 2. Experimental

### 2.1 Materials

$SiO_2$ nanoparticles were obtained from Nippon Shokubai Co., Ltd. The average diameter of $SiO_2$ nanoparticles is 100, 300, 500, and 1000 nm. Special grade EG (99.9% purity) and purified water were obtained from FUJIFILM Wako Pure Chemical Co., Ltd. Finest grade EG-d4 (98% purity), EG-d6 (98% purity), and EG (O, O-d2) (98% purity) were obtained from Cambridge Isotope Laboratories, Inc. Research grade deuterium ($D_2O$, 99.9 at.%) was obtained from Sigma-Aldrich Co., Ltd. The homogeneous nanofluid was prepared by ultrasonic dispersion of the particles in 50 wt% EG solution at the solid fraction of 7-10 wt%.

### 2.2 Analyses

QENS and SANS measurements were performed at 298 and 333 K using a cold-

neutron disk-chopper spectrometer (BL14) and a small- and wide-angle neutron scattering instrument (BL15) installed at J-PARC in Japan. IXS measurements was performed at 353 K using the high-resolution IXS spectrometer installed at BL35XU of SPring-8 in Japan. WAXS measurements was performed at 298 K using a powder X-ray diffractometer system with semiconductor 2D detectors installed at BL5S2 of Aichi SR in Japan.

## 3. Results and Discussion

Figure 1 shows the correlation between $\lambda$ and self-diffusion coefficient ($D$), which can be obtained from QENS results. The $D$ of the nanofluids is smaller than that of EG solution. Additionally, the $D$ becomes small with the increase of $\lambda$. This indicates that the suppression of translational motion of liquid molecules around particles is one of key factors of $\lambda$ enhancement.

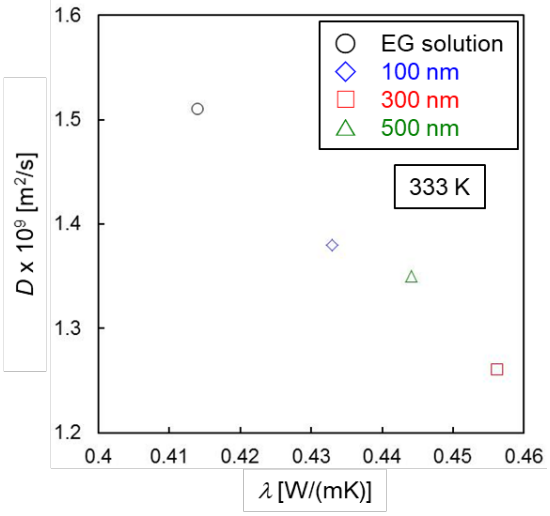


**Fig. 1.** Analytical results by QENS measurements; correlation between the $D$ and $\lambda$.

Figure 2 demonstrates the relaxation behavior of the vibration mode obtained from QENS measurements, where $Q$ represents the momentum transfer. Because the scattering cross-section of each H and D atom concerning the neutron differs greatly, it is possible to obtain motion information on each EG/water molecule and hydrogen bonds. The presence of $SiO_2$ particles in the $C_2D_4(OH)_2/H_2O$ system (red and green markers) increases the half-width at the same $Q$ value. Therefore, the presence of $SiO_2$ particles may increase the energy of the OH vibration of water and EG molecules and the vibrations derived from hydrogen bonds between those molecules. However, the presence of $SiO_2$ particles reduces the intensity and half-width at the same $Q$ value in the $C_2H_4(OD)_2/D_2O$ systems (blue and yellow markers in). Therefore, the presence of $SiO_2$ particles may significantly reduce the relaxation rate of the hydrophobic CH vibration of the EG molecule. Additionally, based on SANS, IXS and WAXS measurements, the presence of $SiO_2$ particles is thought to excite vibrations derived from hydrogen bonds of liquid molecules extensively surrounding the particles, while suppressing vibrations derived from hydrophobic covalent bonds. Because liquid molecule vibration is equivalent to phonon conduction in solids, the improvement in thermal conductivity of the solution due to the presence of nanoparticles appears to be due to the limitation of translational diffusion and the resulting solid-like behavior of the liquid molecules.

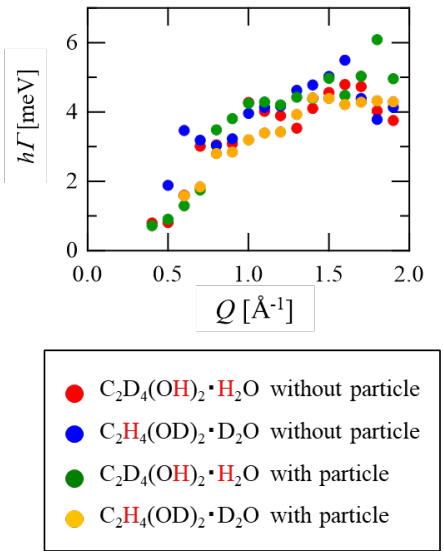


**Fig. 2.** Relaxation behavior in vibration mode (hΓ: half width at half maximum of the peak).

## References

[1] J. A. Eastman, et al., Ann. Rev. Mater. Res., 34, (2004) 219-246.
[2] B. Sahin, et al., Exp. Therm. Fluid Sci., 50,(2013) 21-28, etc.
[3] S. Hashimoto et al., Int. J. Heat Mass Transf., 150, (2020) 119302.
[4] S. K. Das, S. U. S. Choi, H. E. Patel, Heat Transf. Eng., 27, (2006) 3-19.

## SESSION 3b
## MINI SYMPOSIUM Part 1 of 2
## Near surface effects in two-phase flows
Chair: **M. Magnini**



Mirco MAGNINI[1], Gabriele GENNARI[1], Edward SMITH[2], Gavin PRINGLE[3]
1: Department of Mechanical, Materials and Manufacturing Engineering, University of Nottingham, Nottingham NG7 2RD, United Kingdom
2: Department of Mechanical and Aerospace Engineering, Brunel University London, Uxbridge UB8 3PH, United Kingdom
3: EPCC, University of Edinburgh, James Clerk Maxwell Building, Edinburgh, EH9 3FD, UK



Chi WANG[1], Md Mahamudur RAHMAN[2], Matteo BUCCI[1]
1: Massachusset Institute of Technology, Cambridge, MA
2: University of Texas at El Paso, El Paso, TX



Cassiano TECCHIO[1], Xiaolong ZHANG[2], Benjamin CARITEAU[1], Gilbert ZALCZER[2], Pere R. i CABARROCAS[3], Pavel BULKIN[3], Jérôme CHARLIAC[3], Corentin LE HOUEDEC[1], Loïc LOIGEROT[1], Simon VASSANT[2], Guillaume BOIS[1], Elie SAIKALI[1] and Vadim S. NIKOLAYEV[2]
1: Université Paris-Saclay, CEA, STMF, 91191 Gif-sur-Yvette Cedex, France
2: Université Paris-Saclay, CEA, SPEC, CNRS, 91191 Gif-sur-Yvette Cedex, France
3: Institut Polytechnique de Paris, Ecole Polytechnique, LPICM, CNRS, 91120 Palaiseau, France



Francis DENT[1], Sepideh KHODAPARAST[1]
1: School of Mechanical Engineering, University of Leeds, UK

# Coupled atomistic-continuum simulations of single- and two-phase flows

Mirco MAGNINI[1,*], Gabriele GENNARI[1], Edward SMITH[2], Gavin PRINGLE[3]

1: Department of Mechanical, Materials and Manufacturing Engineering, University of Nottingham, Nottingham NG7 2RD, United Kingdom
2: Department of Mechanical and Aerospace Engineering, Brunel University London, Uxbridge UB8 3PH, United Kingdom
3: EPCC, University of Edinburgh, James Clerk Maxwell Building, Edinburgh, EH9 3FD, UK

* Corresponding author: Email: mirco.magnini@nottingham.ac.uk

**Abstract:** Many fluidic processes in science and engineering are underpinned by the two-way interactions among physics happening at the micro-scale and the boundary conditions set by the outer system. One such example is the flow of a fluid over a rough surface, where the bulk fluid motion is set by an external force while the microscale surface topography determines the local shear stress, or boiling over typical metallic surfaces, where the boiling dynamics depend on near-surface molecular interactions that trigger nucleation, but also on external forces such as buoyancy and drag/lift forces determining the thickness of thermal boundary layers and the bubble detachment and departure from the heated surface. These are examples of multiscale problems and are very difficult to be studied at a fundamental level due to the separation of scales. We present a novel multiscale simulation method which merges molecular dynamics (MD) and continuum-scale (CS) descriptions into a single modelling framework, where MD resolves the near-wall region where molecular interactions are important, and a computational fluid dynamics solver resolves the bulk flow. We showcase the model capabilities by showing the results of two examples, a Couette flow and a pool boiling case.

**Keywords:** Multiscale, Boiling, Simulation, Molecular.

## 1. Introduction

The next generation of science depends on solving the problem of linking simulations at different scales. In many physical processes, phenomena happening at the molecular scale determine the large-scale dynamics of the system. For example, near-wall turbulence in fluid mechanics depends on the wall-fluid molecular interaction, bubble/droplet nucleation in heating/cooling processes depend on the thermal fluctuations at the nanoscale, the wear of interacting surfaces in tribology depends on the viscoelastic properties of materials at localised points of contact. These molecular-level physics are implemented via empirical closure models in state-of-art continuum-scale simulation methods, which often limit the reliability of simulation outputs. Coupled algorithms have the potential to revolutionise the simulation of engineering systems allowing them to retain the full molecular detail [1]. In domain decomposition coupling, Molecular Dynamics (MD) captures the near-wall region whereas a continuum-scale (CS) description based on the Navier-Stokes equations resolves the bulk flow; flux and/or state properties are directly exchanged in an overlap region, without intermediate models. While this technique is well established for wall-bounded single-phase flows, its adoption in multiphase flows is still in its infancy. In this work, we present our progress in developing a coupled MD-CS framework using a full open-source platform and show preliminary results for single- and two-phase flows.

## 2. Methods

Coupled atomistic-continuum simulations with domain decomposition require a MD solver, here we use LAMMPS, and a CS solver, here we use OpenFOAM and a Volume Of Fluid method with phase-change libraries validated in previous studies [2]. A schematic

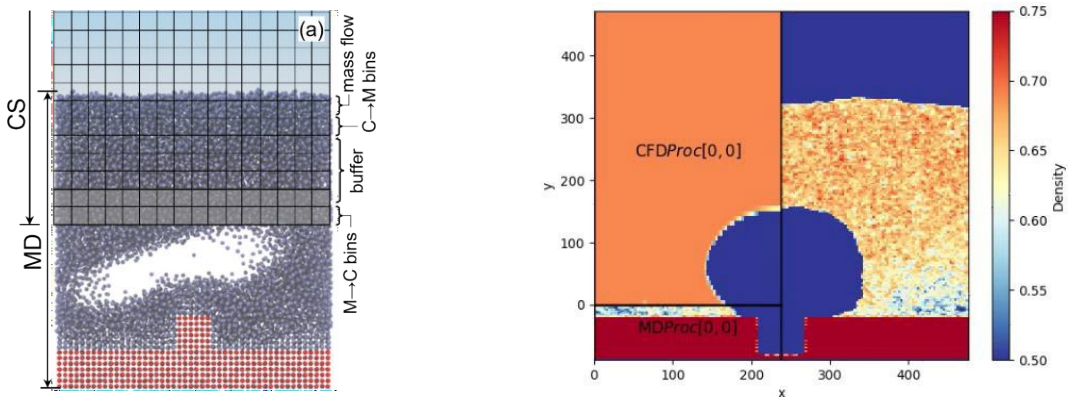


Figure 1: [left] Schematic of the domain decomposition coupling; M stands for Molecular, C for continuum. [right] Coupled simulation of pool boiling of Argon; the left-hand side displays the CS density field, the right- hand side the MD density field. The unit length is 0.34 nm; a MD density of 0.7 corresponds to 1160 kg/m$^3$.

of the domain decomposition coupling is shown in Fig. 1(left): the MD resolves the near-wall region where the bubble nucleates, the CS mesh resolves the far-field region. The two regions must communicate, since the MD fields must be imposed to the CS as boundary conditions, and the CS fields must be imposed to the MD using constrained dynamics algorithms. This occurs over an overlap region in the domain. The coupling is handled by the CPL library [1]. For the Couette flow, the coupling is two-way and complete [3]. For the boiling case, the coupling is still one-way from MD to CS, while the two-way coupling is work in progress [3].

## 3. Results

Here we show only the results of the boiling case. We simulate the pool boiling of Argon with a wall temperature of 125 K and a saturation temperature of about 115 K. The entire domain is a 2D box of 160x160 nm$^2$. At t=0, the domain is filled with liquid Argon. Since the coupling is still one-way, the MD simulation needs to be self-sustained and, since top and bottom MD boundaries are closed boundaries, a layer of vapour Argon is placed on top of the liquid to prevent an excessive increase of pressure while the bubble grows. In the CS model, the top boundary is an outflow, and the bottom boundary receives velocity, phase fraction and temperature data from the MD. In both models, the side boundaries are periodic. Figure 1(right) shows the simulation results at the last time instant before the simulation terminates. The bubble first nucleates in the MD region and then enters in the CS region, where it continues growing owing to the vapour inflow from the MD and the phase-change at the interface calculated by the CS model. Bubble dynamics, size and growth rates match seamlessly between the MD and CS model, provided that the saturation temperature and accommodation coefficients are carefully set in the CS model. All modelling framework and simulation setup are available open-access in Github [4].

## References

[1] E. R. Smith et al., CPL library - A minimal framework for coupled particle and continuum simulation, Comput. Phys. Commun. 250 (2020) 107068.
[2] F. Municchi, I. El Mellas, O. K. Matar, M. Magnini, Conjugate heat transfer effects on flow boiling in microchannels, Int. J. Heat Mass Transf. 195 (2022) 123166.
[3] M. Magnini, G. Gennari, E. Smith, G. Pringle, Coupling LAMMPS and OpenFOAM for Multi-Scale Models, EPCC-ARCHER2 webinar: https://www.archer2.ac.uk/training/courses/23 0719-openfoam-lammps-vt/.
[4] Github, CPL_APP_OPENFOAM: https://github.com/Crompulence/CPL_APP_O PENFOAM

## Acknowledgments

This project was funded by the 6$^{th}$ ARCHER2 eCSE call, project ARCHER2-eCSE06-1.

# Decrypting the Mechanisms of Wicking and Evaporation Heat Transfer on Micro-Pillars during the Pool Boiling of Water using High-Resolution Infrared Thermometry

Chi WANG[1], Md Mahamudur RAHMAN[2], Matteo BUCCI[1,*]

1: Massachusset Institute of Technology, Cambridge, MA
2: University of Texas at El Paso, El Paso, TX

*Corresponding author: Email: mbucci@mit.edu

**Abstract:** Surfaces featuring micron-scale pillars have demonstrated remarkable potential in delaying the boiling crisis and enhancing the critical heat flux (CHF). Despite these promising results, the underlying physical mechanisms responsible for this enhancement have remained unclear, primarily due to a lack of suitable diagnostics that can elucidate the impact of micro-pillars on thermal transport phenomena within the engineered surface. In this study, we present, for the first time, measurements of time-dependent temperature and heat flux distributions on a boiling surface with engineered micro-pillars using infrared thermometry. Our investigations have revealed the existence of an intra-pillar liquid layer formed through the nucleation of bubbles and partially replenished through capillary effects. However, the energy dissipated by the evaporation of this liquid layer alone cannot account for the observed CHF enhancement.

**Keywords:** Micro pillars, Boiling Crisis, Wicking, IR thermometry

## 1. Introduction

Boiling heat transfer is a vital process utilized in diverse technologies to achieve efficient thermal management. However, its effectiveness is limited by a phenomenon known as the boiling crisis. When the boiling crisis occurs, a vapor film develops on the boiling surface, effectively isolating it from the surrounding liquid. This isolation leads to a potentially hazardous increase in the temperature of the surface that needs to be cooled down. Consequently, delaying the boiling crisis and increasing the Critical Heat Flux (CHF), which represents the heat flux at which the boiling crisis occurs, are of paramount importance to the thermal transport community.

Surfaces featuring micron-scale pillars have demonstrated remarkable potential in delaying enhancing the critical heat flux (CHF). In a study by Rahman et al. (2014), they observed that CHF enhancement on such surfaces is closely tied to surface wickability. Subsequent research by Li and Huang (2017) attempted to explain this relationship by suggesting that the CHF enhancement is facilitated by the evaporation of the liquid flow wicked by these micro-pillars. However, the precise mechanism remains elusive. Despite the work by Yu et al. (2018), which confirmed the presence of a liquid layer within the pillar structures, it remains uncertain whether this liquid layer is formed primarily through wicking or if it already exists beforehand. Moreover, the extent to which its evaporation contributes to the CHF enhancement remains unclear.

Our study aims to close this knowledge gap. To this end, we have developed special infrared heaters and deployed high-resolution thermometry techniques. Thanks to these technical advances, we can discern the origins of the liquid layer and quantify the extent of its contribution to CHF enhancement. Our research endeavors to provide a deeper understanding of the underlying mechanisms driving CHF enhancement on surfaces with engineered micro-pillars, offering invaluable insights for the advancement of thermal transport techniques and safer, more efficient cooling applications.

We emphasize that, while IR thermometry have been successfully used to study boiling on multiple surfaces, e.g., by Bucci *et al.* (2016) and Su *et al.* (2020), technical and practical

limitations have prevented its application to the study of boiling on surfaces with micro pillars. In this study, we have developed a new heater, shown in Fig. 1 (A), that allow measuring time-dependent distributions of temperature (Fig. 1 (D)) and heat flux (Fig. 1 (E)) at the base of micro-pillar structures (Fig. 1 (B)). Our micro-pillars are square, with a side and a height of 10 µm, and are 10 µm spaced.

## 2. Results and Discussion

We have conducted pool boiling test in the facility shown in Fig. 1 (C) on the micro-pillar surface and, for comparison, on a plain surface. Boiling curves are plotted in Fig. 1 (F). From the heat flux map shown in Fig. 1 (E), we can detect the evaporation of a liquid layer (with very high heat flux) under the bubble footprints. This liquid layer only becomes dry very close to boiling crisis. For each pixel in the dry patch, we can calculate the amount (i.e., the equivalent thickness) of liquid that has been evaporated before the surfaces dries out. The result is plotted in Fig. 1 (G). We can see that the evaporated thickness varies from around 8 µm at the location where the surface dries out first (point a in Fig. 1 (G)) to 35 µm at the edge of the dry patch. These results suggest that the amount of liquid wicked by the pillars near the edge of the dry patch boundaries (i.e., the extra 20 µm of evaporated liquid) is from wicking.
We examine all the pixels in Fig. 1 (G) and ascertain that in all the liquid evaporated on the dry patch, 40% comes from wicking and 60% comes from the liquid that is trapped within the pillars when the bubble grows on top of them. By isolating surface region where this liquid evaporates from the other region, we reveal that evaporation accounts for about 30% of the total energy removed during boiling on the pillar surface. Converting the energy removed by each mechanism to equivalent heat flux on the whole surface, we get 0.22 MW/m$^2$ for evaporation of the wicking flow and 0.33 MW/m$^2$ for evaporation of the trapped liquid. The remaining 1.30 MW/m$^2$ is removed by convection and transient conduction heat transfer mechanisms. We perform a similar analysis for a plain surface and observe that energy removed by evaporation equivalents to 0.29 MW/m$^2$, whereas energy removed by convection and transient conduction equivalents to 0.82 MW/m$^2$.

## 3. Conclusions

The boiling process on the pillar surface involves the evaporation of a liquid layer underneath bubbles. This liquid layer can be either trapped within the pillars at the moment of bubble growth or resupplied by wicking flow phenomena. Both the evaporation of the trapped liquid and the wicking flow contribute to energy removal, but not enough to explain the CHF enhancement. By comparing the heat flux removed by the different heat transfer mechanism, we can see that the evaporation of

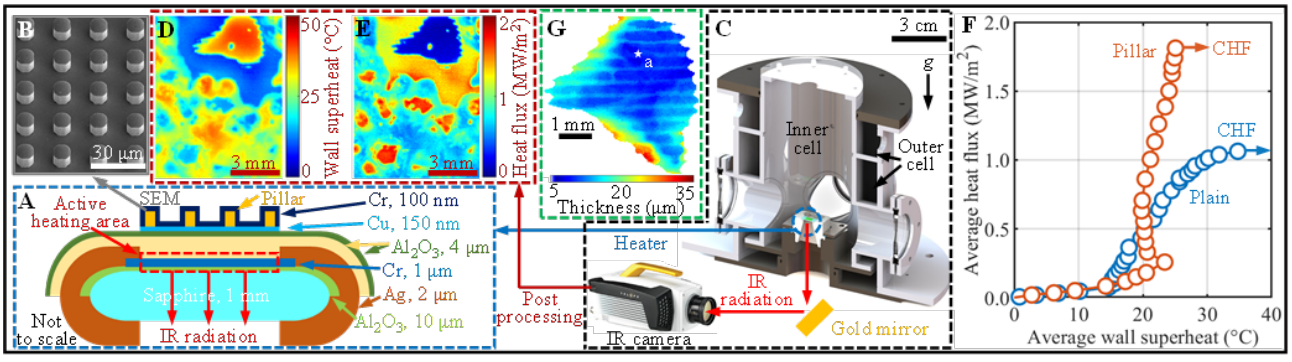


**Figure 1:** Schematic of the heater (A). SEM picture of the pillar structure (B). Pool boiling facility (C). Wall superheat (D) and heat flux (E) on the pillar surface at an average heat flux of 1.81 MW/m$^2$ obtained using infrared thermometry. Boiling curves of the pillar surface and a plain surface (F). Evaporated liquid thickness (G).

the wicking flow (corresponding to 0.22 $MW/m^2$) cannot explain, by itself, the CHF enhancement on
the pillar surface (i.e., 0.74 $MW/m^2$). In fact, most of the energy is removed by non-evaporative heat transfer mechanisms, e.g., transient conduction and convective effects. Thus, they must be modeled correctly to accurately predict the CHF enhancement.
In addition to these results, we will also discuss the development of a simple yet effective analytic model that shed light on the role of conduction effects in the boiling substrates and within the intra-pillar liquid layer itself. Remarkably, these conduction effects also govern the wicking flow rate and its penetration length. The boiling crisis emerges when, due to coalescence, the intra-pillar liquid layer's size grows excessively, making it impossible for the wicking flow to reach its innermost region.

## References

Bucci, M., Richenderfer, A., Su, G.Y., McKrell, T. and Buongiorno, J., 2016. “A mechanistic IR calibration technique for boiling heat transfer investigations”. *International Journal of Multiphase Flow*, 83, pp.115-127.

Li, R. and Huang, Z., 2017. “A new CHF model for enhanced pool boiling heat transfer on surfaces with micro-scale roughness”. *International Journal of Heat and Mass Transfer*, 109, pp.1084-1093.

Rahman, M.M., Olceroglu, E. and McCarthy, M., 2014. “Role of wickability on the critical heat flux of structured superhydrophilic surfaces”. *Langmuir*, 30(37), pp.11225-11234.

Su, G.Y., Wang, C., Zhang, L., Seong, J.H., Kommajosyula, R., Phillips, B. and Bucci, M., 2020. “Investigation of flow boiling heat transfer and boiling crisis on a rough surface using infrared thermometry”. *International Journal of Heat and Mass Transfer*, 160, p.120134.

Yu, D.I., Kwak, H.J., Noh, H., Park, H.S., Fezzaa, K. and Kim, M.H., 2018. “Synchrotron x-ray imaging visualization study of capillary-induced flow and critical heat flux on surfaces with engineered micropillars”. *Science advances*, 4(2), p.e1701571.

# Microscale Phenomena in Nucleate Boiling

Cassiano TECCHIO[1,*], Xiaolong ZHANG[2], Benjamin CARITEAU[1], Gilbert ZALCZER[2], Pere R. i CABARROCAS[3], Pavel BULKIN[3], Jérôme CHARLIAC[3], Corentin LE HOUEDEC[1], Loïc LOIGEROT[1], Simon VASSANT[2], Guillaume BOIS[1], Elie SAIKALI[1] and Vadim S. NIKOLAYEV[2]

1: Université Paris-Saclay, CEA, STMF, 91191 Gif-sur-Yvette Cedex, France
2: Université Paris-Saclay, CEA, SPEC, CNRS, 91191 Gif-sur-Yvette Cedex, France
3: Institut Polytechnique de Paris, Ecole Polytechnique, LPICM, CNRS, 91120 Palaiseau, France

* Corresponding author: Tel.: +33 0169084947; Email: cassiano.tecchio@cea.fr

**Abstract:** We report an experimental and theoretical study on the microscale physical phenomena occurring during the growth of a single bubble in saturated pool boiling. We focus on the liquid microlayer that can form between the heater and the liquid-vapor interface of a bubble. We describe microlayer as consisting of two regions: a ridge near the contact line followed by a wider and flatter profile. The microlayer thickness in the ridge increases over time due to the collection of liquid promoted by the dewetting phenomenon. The flatter part has a slightly bumped profile and thins over time. This bumped profile is a result of an interplay between viscous and surface tension forces acting at the bubble foot edge during its receding. Its thinning over time is due to its evaporation solely. We also show that the contact line receding is accelerated by the evaporation. At the liquid-vapor interface, the results indicate that the thermal resistance increases over time reaching a value up to 60 times higher than the kinetic theory result with the unity accommodation coefficient. The contribution of microlayer evaporation to the overall bubble growth is ~18%.

**Keywords:** Microlayer, Boiling, Bubble, Heat Transfer

## Extended Abstract

A microlayer of liquid can be formed underneath a growing boiling bubble at nucleate boiling under specific conditions of wettability, wall superheating and dewetting velocity [1]. Typically, it has a thickness of up to a few $\mu\mu$m and extents over a few mm horizontally [2]. Its formation, shape, evaporation and depletion are then of great importance to the overall bubble growth. In this work, we investigate it both experimentally and theoretically during the growth of a single bubble.

The experiment is performed in a boiling cell at atmospheric pressure that comprises a water liquid pool, its temperature homogenizer, and a boiling surface. A thermal bath provides continuous fluid flow to the homogenizer that surrounds the cell in order to minimize thermal gradients and to keep the pool at saturation temperature. The boiling surface consists of a ~850 nm thick indium-tin oxide (ITO) deposited on a magnesium fluoride (MgF2) optical porthole. MgF2 is transparent to visible and infrared (IR) light whereas ITO is transparent to visible but opaque to IR. The single bubble growth is triggered by localized heating using a continuous-wave IR laser with wavelength emission at 1.2 $\mu\mu$m. The ITO film is heated thanks to its high IR absorption.

High-speed and high-resolution optical diagnostics are used to characterize the

near- wall phenomena and bubble dynamics. From below the cell, white light interferometry and IR thermography give a measure of the microlayer thickness and the wall temperature distribution, respectively, whereas side-wise shadowgraphy provides the bubble macroscopic shape. The measurements are performed synchronously and simultaneously at 4000 fps.

The numerical simulation of microlayer dynamics is performed using the two-dimensional lubrication theory. The set of equations presented in [3] to study the dewetting by evaporation represent all the physical phenomena relevant to the experiment. The governing equation takes into account the triple contact line receding accelerated by evaporation and the decelerated motion of the bubble foot edge. Vapor recoil, Kelvin effect and interfacial thermal resistance are also taken into account. The boundary conditions are the following: At the contact line: the microlayer thickness is zero; the microscopic contact angle is fixed at $10^{o}$ (defining the wall wettability) and a finite liquid pressure is imposed. At the bubble foot edge, the meniscus curvature is imposed, which is proportional to the experimental bubble radius determined by the side-wise shadowgraphy. The numerical simulation gives as outputs the microlayer profile and contact line position over time. A homogeneous wall superheating that changes in time is used as input to reflect the experimental superheating at the contact line.

Figure 1 shows the numerical and experimental results on the microlayer profiles at selected time moments. The microlayer can be seen as the Landau-Levich film deposited by the bubble edge during its receding caused by the bubble growth. The microlayer consists of a growing in time dewetting ridge located near the contact line followed by a flatter and wider film. The ridge is a result of liquid collection due to the contact line receding and the high viscous stresses in the flatter part of the microlayer. As the interface slopes are steep over almost all the dewetting ridge, it cannot be detected by the interferometry methods. Both the thickness and the position of bump agree with the experiment. The microlayer thinning over time is a result of its evaporation. The rapid contact line receding is accelerated in our case due to the strong evaporation promoted by the localized laser heating.

We also determine the wall heat flux through the microlayer by solving numerically the transient heat conduction in the MgF2. The experimental temperature distribution on the ITO was used as a boundary condition. With the knowledge of microlayer thickness, wall superheating and the heat flux, one determines the interfacial thermal resistance. We show that it increases over time reaching up to 60 times its kinetic theory result (that assumes the unity accommodation coefficient). This result indicates that impurities, which are known to be collected at the liquid-vapor interface, accumulate there over time.

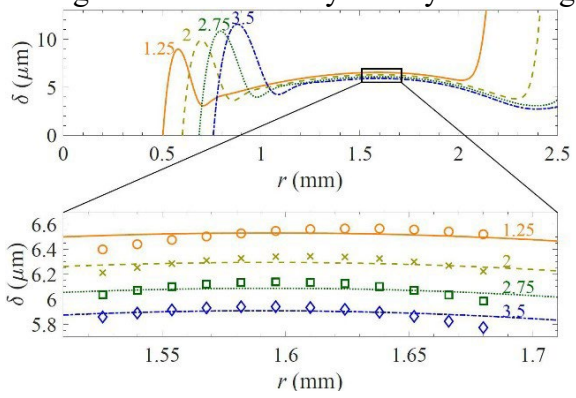


Figure 1. Top: Temporal evolution of the numerical microlayer profile. Bottom: comparison between numerical (lines) and experimental (characters) data. The corresponding times are labeled in ms.

The contribution of microlayer evaporation to the overall bubble growth of 18% was found. This result is in good agreement with other similar experiments [4].

# References

[1] Urbano, A., Tanguy, S., Huber, G., Colin, C., 2018. Direct numerical simulation of nucleate boiling in micro-layer regime, Int. J. Heat Mass Transfer, 123, 1128–1137.

[2] Tecchio, C., 2022. Experimental study of boiling: Characterization of near-wall phenomena and bubble dynamics. PhD thesis. Université Paris- Saclay.

[3] Zhang, X., Nikolayev, V., 2022. Dewetting acceleration by evaporation, J. Fluid Mech, 948, A49

[4] Jung, S., Kim, H., 2014. An experimental method to simultaneously measure the dynamics and heat transfer associated with a single bubble during nucleate boiling on a horizontal surface. Int. J. Heat Mass Transfer, 73, 365–375.

# Heterogeneous nucleation and growth of droplets on liquid films

Francis DENT[1], Sepideh KHODAPARAST[1,*]

1: School of Mechanical Engineering, University of Leeds, UK

* Corresponding author: Tel.: +44 07526984634; Email: s.khodaparast@leeds.ac.uk

**Abstract:** Micro/nano-patterned surfaces foster advantageous functionalities related to wetting, self-cleaning and adhesion, leading to growing applications in emerging technologies. Currently, most surface patterning approaches rely on top-down fabrication methods that are not only costly but suffer from limited scalability. Here, we introduce an alternative bottom-up approach for micro/nano-patterning of polymeric coatings, based on the breath figure technology. We create a self-assembled array of spherical water droplets on the surface of sub-cooled thin films of photo-sensitive polymers through inducing drop-wise condensation in humid environments. Droplet footprints are subsequently arrested at desired times by exposing the polymer film to curing UV illumination, generating circular micro/nano pores on the surface. We characterise the kinetics of drop-wise condensation through real-time optical microscopy analysis to generate a mechanistic model for design of such micro/nano-patterned surfaces. Finally, we demonstrate the capacity of the prediction models and the manufacturing technology by fabricating patterned polymeric coatings with pore dimensions ranging from 100's of nanometers to 10's of micrometers.

**Keywords:** Condensation, Liquid film, Heterogeneous nucleation, breath figure, micro droplets.

## 1. Introduction

Breath figure refers to the appearance of self-assembled water condensation droplets on sub-cooled substrates in humid environments. Conventionally, breath figure approach has been used to fabricate a variety of micro/nano patterned polymeric films and porous structures by sub-cooling liquid films of polymeric solutions through solvent evaporation (Widawski et al. 1994). However, as prediction of evaporation induced sub-cooling and transient properties of the polymeric solution during solidification remains unresolved, mechanistic design and control of the final pattern dimension and surface coverage has not yet been fully achieved. To eliminate the complexities associated with evaporation induced cooling and solidification processes, here we propose an alternative breath figure approach in which film cooling is induced by an external Peltier device while polymerisation is affected by UV curing. In order to provide a mechanistic model of the kinetics that control the surface coverage and dimensions of the final pattern, we will follow the kinetics of drop-wise condensation from initial nucleation to the growth and assembly of the droplets. The following sections will summarise the experimental procedure and results of the analyses. For more details, refer to our recent publication (Dent et al. 2022).

## 2. Experimental approach

Borosilicate glass coverslips were used as supporting substrates for the thin polymer films. Two single-component photocurable optical adhesives, NOA61 and NOA63 (NOA, Norland Products Inc.) were spin coated on the glass coverslips to obtain a thin film of approximately 30 μm thickness. Photopolymer surface tension (SFT) in air and interfacial tension (IFT) in de-ionised water (Milli-Q type 1) were measured based on pendant drop analysis using a tensiometer (Theta, Biolin Scientific). ForNOA61, these were calculated to be SFT 40.5 mN/m and IFT = 11.8 mN/m. NOA63 exhibited relatively lower IFT in both air and water, measured as SFT = 37.0 mN/m and IFT = 9.1 mN/m. Experimental analyses were performed at laboratory environmental

conditions of temperature ($T_0$) and relative humidity (RH). The patterned films were created by initiating condensation on the sub-cooled wet polymer films and curing them under a collimated 356 nm UV flood curing system (Dymax Redi-Cure550) to arrest the breath figure pattern at time $t_c$. The sub-cooling level, $\Delta T$, was set by placing the substrate on a thermoelectric Peltier cooling stage at the start of each experiment based on the saturation temperature at the corresponding RH and $T_0$. Real-time kinetics of condensation droplet growth was quantified using an optical microscope. The micro/nano patterned films were imaged using a laser scanning confocal microscopy and Scanning electron microscopy.

## 3. Results and discussion

Upon sub-cooling at constant relative humidity, NOA61 provided sparse condensation nucleation sites, thus the initial growth of the water droplets was in initial diffusion-limited regime. In contrast, the lower IFT of NOA63 makes it more thermodynamically favourable for water droplets to nucleate, relative to NOA61 (Nepomnyashchy et al. 2006). Therefore, higher density of condensation nucleation is observed on NOA63, demonstrating its suitability as the film material for generation of breath figure patterns with high pattern density (Fig. 1). The maximum observed packing corresponds to over 70% of the theoretical packing limit in a 2D plane (around $A_f$ =0.9), complimenting earlier studies and suggesting this is near optimal packing given the viscous liquid boundaries which stabilise/encapsulate the droplets.

Prior to any coalescence events, the temporal growth of individual droplets on NOA61 is well predicted by a power law with exponent of 1/3. Beyond this time, the growth rate increases in a transitional regime as the tighter droplet packing leads to more frequent coalescence events between neighbouring droplets. In this regime, the droplet growth follows a power law with exponent of unity with respect to time, demonstrating coalescent-dominating growth manifested by the large droplet number density as predicted by previous scaling analysis (Viovy et al. 1988). In contrast, droplet growth on NOA63 falls in the coalescence-dominated regime from early times, where the self-similarity of droplet packing results in an effectively constant area coverage of $A_f$ = 0:66. The diametric growth power law where the unity exponent is conserved throughout the analysis period (Fig. 1). Thanks to the larger number of condensation nucleation sites on NOA63, droplets are generally smaller than those observed on NOA61.

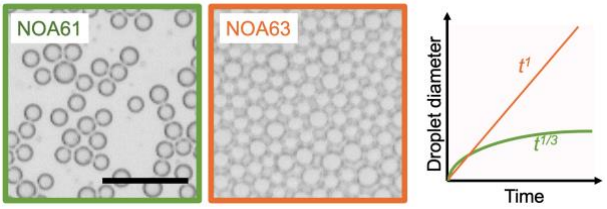


*Figure 1: Condensation droplets on two photocurable polymer films with different interfacial energies. Scale bar refers to 20 μm.*

Fast curing of the polymeric films joined with the deterministic knowledge of condensation droplet growth allows arresting the associated breath figure patterns at any point of time to achieve the desired pattern dimension (Fig. 2). Relative to other costly fabrication tools, the current fluid-based surface patterning technique is energy-efficient, scalable, and inexpensive, offering promising routes for patterning a variety of polymeric materials.

## References

[Widawski et al. 1994] Self-organised honeycomb morphology of star-polymer polystyrene films, Nature 369, 387–389 (1994).

[Dent et al. 2022] Temporally arrested breath figures. ACS Appl. Mater. Interfaces 14 (23), 27435– 27443 (2022).

[Nepomnyashchy et al. 2006] Nucleation and growth of droplets at a liquid-gas interface. Phys. Rev. E. 74, 021605 (2006).

[Viovy et al. 1988] Scaling description for the growth of condensation patterns on surfaces. Phys. Rev. A, 37, 4965 (1988).

## SESSION 3c
## Experimental approaches in single- and two- phase flow
Chair: Prof. **T. Karayiannis**

# Direct-contact condensation from vapour- inert gas mixture in a spray ejector condenser

Dariusz MIKIELEWICZ[1,*], Milad AMIRI[1], Michał KLUGMANN[1], Jarosław MIKIELEWICZ[2]

1: Institute of Energy, Gdańsk University of Technology, Gdańsk, PL
2: Institute of Fluid-Flow Machinery, 80-231 Gdansk, PL

* Corresponding author: Tel.: +48 347 2254; Email: dariusz.mikielewicz@pg.edu.pl

**Abstract:** The present study presents the analytical model of direct condensation in a spray ejector condenser (SEC) in the presence of inert gas, namely carbon dioxide. The model incorporates the continuity, momentum and energy equations to describe the phenomenon. In addition, impact of breakup of droplets has been considered, so that maximum droplet diameter after breakup has been obtained, which, in turn, leads to assume the best estimate for the diameter of droplet, on which steam is condensed.

**Keywords:** spray ejector condenser, breakup, direct-contact condensation, analytical modeling

## 1. Introduction

Direct-contact condensation plays a pivotal role for both engineering and natural sciences that has been exploited in many fields. Direct contact condensation (DCC) is found when a gas/vapour stream comes into contact with a subcooled liquid, and is associated with high heat transfer coefficients as there are no partitions as in conventional heat exchange procedures. Direct-contact condensation of vapour with inert gas on a spray of subcooled liquid exists in a number of technical applications such as for example in the nuclear industry (e.g. pressurize under normal operating conditions, in safety analyses) and in the chemical industry (e.g. mixing-type heat exchanger, degasser, sea water desalting). Another application is when the supersonic steam jet flows combines with cold water in the mixing nozzle in an emergency cooling system of nuclear reactor, causing direct-contact condensation. The condensing-injector is propounded a potential heat exchanger or energy-efficient pump due to its higher heat exchange coefficient, low-grade thermal energy utilization and ability to pressurize without rotating components.

## 2. The model

The theoretical analysis in the paper concerns the issue of direct-contact condensation of vapour with inert gas within ejector creating a subcooled water spray. The physical situation considered is shown in Fig. 1.

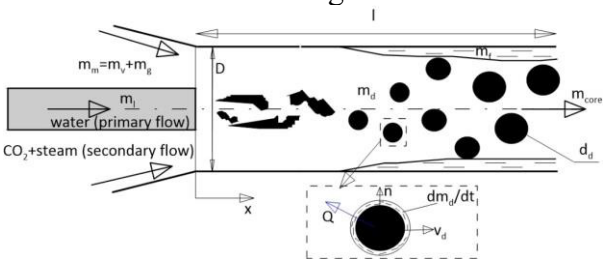


Fig. 1. Schematic of the nozzle

In order to maximize the device efficiency a proper ejector design and analysis is required. The ejector, being the crucial component of a considered thermodynamic cycle, which in our case is a negative $CO_2$ emission gas power plant, determines the overall performance and efficiency of the condensing steam from mixture of vapour-noncondensing gas system. Adiabatic irreversible flow model is used for the ejector analysis. For the ejector design, the study focuses on the ejector nozzle, pre-mixing chamber, mixing section and the diffuser. Flow properties and ejector geometry are considered

using the thermodynamic equations, conservation equations and other assumptions established based on literature.

## 3. Results

The experimental distributions of temperature along mixing length for different mass flow rate of steam (1.8, 3.6 and 5.4 g/s) when flow rate of $CO_2$ is 0, and 11.765 ($m^3$/h) at liquid jet flow rate = 20.1 (g/s) have been illustrated in Fig.2.

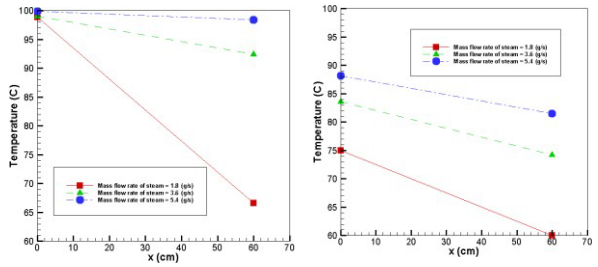


**Figure 2**. Distribution of temperature along mixing length for flow rate of $CO_2$ ($m^3$/h): a) 0, b) 11.765 ($m^3$/h) at liquid jet flow rate = 20.1 (g/s)

Temperature of droplet and mixture of steam resulting from analytical modelling are depicted in Figs. 3. It can be seen vividly that temperature of droplet along the length of throat is faced with a rising trend, whereas temperature of mixture of steam is experiencing a decreasing trend. In addition, having studied the data, it can be considered that temperature of droplet at the length of throat (x=0.2 m) for $u_{m0}$ = 0, 5, 15, 25, 35 and 45 (m/s) is 331.55, 332.08, 333.25, 334.66, 336.50 and 339.54 K, respectively, whilst temperature of mixture of steam for mentioned $u_{m0}$ is 339.31, 340.24, 342.40, 345.15, 348.99 and 356.21 K, respectively. So, increasing the value of $u_{m0}$ not only results in increasing the droplets temperature, but also leads to rise in temperature of mixture of steam at the length of throat. Moreover, the lowest value for temperature of droplet and mixture of steam is when the drop is moving in stagnant environment ($u_m(x) = 0$).

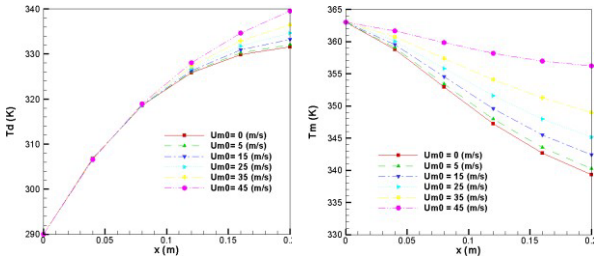


**Figure 3**. Distribution of temperature of droplet (left) and steam (right) for different initial velocity of mixture at $Ud_0$=50 m/s and diameter of droplet 1 mm

Through the thermal analysis, the following results were found in accordance to the following:

- Although the temperature of droplet along the length of throat is accosted a rising trend, the temperature of mixture of steam is confronted a decreasing trend.
- Increasing the value of $U_{m0}$ from 0 to 45 (m/s) results in increasing of 2.4% and 4.98% of the temperature of droplet and mixture of steam, respectively, at the end of the length of throat.
- Rising the value of initial velocity of droplet from 20 to 150 (m/s) causes decline of 3.3% and 5.2% of the temperature of droplet and mixture at the end of the length of throat.
- For 1 and 1.5 (mm) of diameter of droplet at $D_0$ = 9 (mm), maximum value of temperature of droplet takes place at 8 and 12 (cm) of length, respectively.
- Growth the diameter of droplet from 2 to 20 mm leads to decrease of 8.1% of the temperature of droplet and rise of 8.6% of the temperature of mixture of steam at x=0.2 (m).

## Acknowledgements

The research received funding from the Norway Grants 2014–2021 within the frame of project: “Negative CO2 emission gas power plant”—NOR/POLNORCCS/NEGATIVECO2-PP/0009/2019-00 under the Norwegian Financial Mechanisms 2014–2021 POLNOR CCS 2019—Development of CO2 capture solutions integrated in power and industry processes.

# Evaluation of the Use of Nanofluids in a Microchannel Based Cooler to be Integrated in a PV Panel

Pedro PONTES[1], Rodrigo SOLIPA[1], António MOREIRA[1], Ana MOITA[1,2,*]

1: IN+, Dep. of Mechanical Engineering, Instituto Superior Técnico, Universidade de Lisboa, Lisboa, PT
2: CINAMIL, Dep. of Exact Sciences and Engineering, Portuguese Military Academy, Lisboa, PT

* Corresponding author: Tel.: +351 938234268; Email: anamoita@tecnico.ulisboa.pt

**Abstract:** The use of solar energy has grown significantly, leading to an increasing need for higher solar cell efficiencies. One way to improve Photovoltaic (PV) cell efficiency is to introduce an active cooling system. Microchannel based coolers show significant potential to be used in commercial applications. Another possibility is the use of nanofluids as the cooling fluid. In this work, the cooling capabilities of different types of water based nanofluids (Au, Ag and $Al_2O_3$) were tested, for different nanoparticle weight concentrations (0.50, 0.75, 1.00 %wt), using a microchannel heat sink. An experimental analysis was performed, studying the microchannel geometry, nanofluid type and nanoparticle concentration, using five different flow rates (10, 15, 20, 30 and 40 ml/min). For the various geometries tested, the one with 0.50 mm of channel width presented the highest heat transfer coefficients, overall. When evaluating the effect of the type of nanoparticles, the nanofluid with gold (Au) nanoparticles showed better thermal behaviour, with heat transfer coefficients as high as 1895 W/($m^2$K) for a flow rate of 40 ml/min and depicted the least amount of sedimentation. Regarding the effect of nanoparticle concentration, the results indicated an increase in heat transfer coefficients with particle concentration, in agreement with the literature.

**Keywords:** Cooling, Heat sink, Microchannel, Nanofluid, PV cells.

## 1. Introduction

In general, the solar cell efficiency is strongly affected by temperature, so that cooling of the solar cells is an important request in solar panels, particularly when using concentrated systems. Several techniques can be used to maintain the photovoltaic (PV) cell temperature under its limit, being either active or passive cooling techniques. One common cooling technique is the use of microchannel heat sinks. Still, the major challenge in their production is the ability to downscale the experimental setup to this range, without undermining it.

Ali et al. [1] conducted both numerical and experimental work on the performance enhancement of PV cells, using microchannel heat sinks, to achieve maximum efficiency. The study was developed under high cell surface temperatures (up to 80ºC), using the climate of Taxila, in Pakistan, as a reference. The PV panel with a microchannel heat exchanger, with a cross section of 1mm by 1mm, showed an increase of 14 % in power output and 3% in efficiency, in comparison to a standard PV panel. An alternative cooling strategy is to engineer the working fluid. In this context, nanofluids provide interesting results, although they also show several obstacles to overcome. The use of nanofluids as a cooling fluid has gained increased attraction and it has started to be integrated in various studies, together with microchannel based coolers. For instance, Rajaee et al. [2] developed a numerical analysis on the performance enhancement of a concentrated Photovoltaic Thermal (PV/T) system. The model used a microchannel heat sink with two hybrid nanofluids as coolant, water-aluminum oxide-carbon nanotube (water-$Al_2O_3$-CNT) and water-silver-zinc oxide (water-Ag-ZnO). The analysis showed better cooling of the PV cell when using nanofluids, consequently resulting in higher exergy efficiency of the concentrated PV/T panel, showing good potential improvements. The research regarding the introduction of nanofluids in both microchannel heat

exchangers and PV solar cells, carried out throughout the years, presented encouraging results in terms of cooling performance. However, the use of nanofluids in heat transfer mechanisms, still needs to be extensively studied, to counteract some of their downsides, like sedimentation.

## 2. Sample Results and Conclusions

A two-step method was used to prepare different types of water based nanofluids, silver, gold and alumina (Ag, Au and $Al_2O_3$), for different nanoparticle weight concentrations (0.50, 0.75, 1.00 %wt). The fluids were tested in a PDMS (Polydimethylsiloxane) microchannels based heat sink. The heat sink was glued to a thin stainless-steel sheet (AISI340) 20µm thick, which was heated by Joule effect, using a 6274B DC power supply.

Figure 1 depicts the heat transfer coefficient, as a function of the Reynolds number, for water based nanofluids of silver, gold and alumina, for a fixed concentration of 1%wt. The nanoparticles concentration is quite low, so the changes in the thermophysical properties of the resulting nanofluids, when compared to the based fluid are not significant. Hence, as expected, the three nanofluids follow a similar thermal behaviour, being the heat transfer coefficient proportional to the increasing Reynolds number. According to Figure 1, the nanofluid that depicted the best heat transfer coefficient was, overall, the one composed of gold nanoparticles, having only the worst thermal behaviour for the lowest volumetric flow. So, some local improvement of the thermal conductivity of the fluid by the gold particles may explain these results. Sedimentation trend of these nanofluids was also investigated, by taking a photo to the stainless-steel sheet. The photos show sedimentation occurring with all nanofluids tested. However, sedimentation of gold (and silver) nanoparticles is residual when compared to that observed for alumina. Overall gold nanoparticles depicted the lowest sedimentation. Figure 2 shows the heat transfer coefficient, as a function of the Reynolds number, for three different concentrations of gold nanoparticles in the water based nanofluid. The heat transfer coefficient of the two smallest particle concentrations increases with similar slopes. However, for the highest particle concentration, the increase is far greater, with the heat transfer coefficient being over 50% higher for the fastest flow rate. The experimental data clearly shows that even for small concentrations, the effect of nanoparticles in the cooling performance, can be significant, depending on their nature.

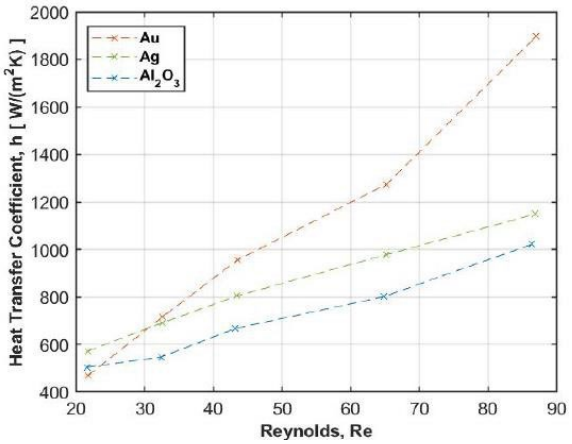


Figure 1: Heat Transfer Coefficient for water-Al2O3, water-Ag and water-Au nanofluids (1%wt), using a channel width of 0.75mm.

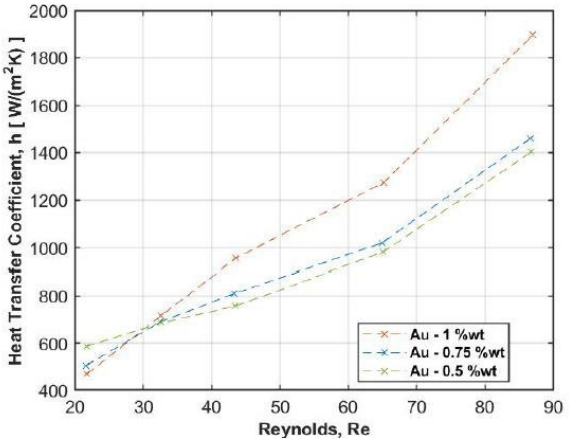


Figure 2: Heat Transfer Coefficient for water-Au nanofluid at different concentrations, using a channel width of 0.75mm.

## References

[1] Muzaffar Ali, Hafiz.M. Ali, Waqar Moazzam, and M. Babar Saeed. AIMS Energy, 3(4):699–710, November 2015.

[2] Fatemeh Rajaee, Alibakhsh Kasaeian, Mohammad Amin Vaziri Rad, and Kasra Aliyon. Solar Energy Advances, 1:100005, October 2021.

# Heat flux enhancement by copper micro sintered fiber attached to the heating surface

Edgar Santiago GALICIA[1,*], Akio MIYARA[1]

1: Department of Mechanical Engineering, Saga University, Japan

* Corresponding author: Tel.: +81 952-28-8479; Email: edgar@cc.saga-u.ac.jp

**Abstract:** Experimental research was performed to study the effects of the micro sintered fibers as a passive method to increase the heat flux using water as a working fluid in a horizontal rectangular 10mm channel. The increment of the heat transfer coefficient is almost neglected in the single-phase, nevertheless, in the two-phase regime an increment of around 2 times, also, a reduction of the wall superheat temperature was found. Bubble formation and flow pattern were also recorded and analyzed by using a high-speed camera in four different thicknesses of the porous layer at three different inlet water temperature ΔT sub 30, 50, and 70 K. The porous materials increased nucleation sites, heating area, and water supply capacity as a result the CHF was found at higher heat flux and lower wall superheat when the porous layer was attached to the surface. On the other hand, the vapor trapping capacity reduces the heat transfer coefficient on the high layer thickness, thus the best performance was found in the low thickness of the porous layer.

**Keywords:** Micro porous, CHF, Heat exchanger, Flow boiling, Bubble behavior

# Flow Boiling with HFE-7100 in a Single Rectangular Microchannel

Joseph J. WIDGINGTON[1,*], Atanas IVANOV[1], Tassos G. KARAYIANNIS[1]

1: Department of Mechanical and Aerospace Engineering, Brunel University London, UK

* Corresponding author: Tel.: +44 (0) 7905506202; Email: Joseph.Widgington@brunel.ac.uk

**Abstract:** Flow boiling of dielectric fluid HFE-7100 in a single 811 µm x 753 µm rectangular microchannel was investigated. Mass fluxes between 110- 400 kg/m$^2$s were studied with wall heat flux between 25- 141.5 kW/m$^2$ at an inlet subcooling of approximately 6 K. The resultant two-phase flow patterns of bubble, slug, churn and annular flows were observed for exit vapour qualities between 0 and 1. The heat transfer coefficient was found to be highly dependent on the applied wall heat flux with no clear mass flux effect.

**Keywords:** Micro Flow, Flow Boiling, Microchannel, Flow Pattern, Heat Transfer

## 1. Introduction

Flow boiling in microchannel heat sinks has potential cooling applications in the computer and IT industry, miniature refrigeration systems, insulated gate bipolar resistors and fuel cells (Karayiannis and Mahmoud, 2017 [1]). Despite their many potential applications, the scarcity of well-established heat transfer correlations is a present barrier to full adoption by industry. This is a consequence of a poor understanding of the two-phase microscale heat transfer mechanisms (Cheng and Xia, 2017 [2]), which depend on the prevailing flow regimes. Low global warming potential dielectric fluids are preferred to water in many of these applications due to cooling system design safety considerations (Lee et al., 2019 [3]). Therefore, there is a desire to understand the fundamental microscale flow boiling mechanisms of such fluids. This study investigated a two-phase pump loop using HFE-7100 in a single microchannel evaporator. Temperature, pressure and mass flow rate measurements were recorded to analyse the heat transfer and pressure drop across the channel. Flow visualisation was conducted to investigate the flow pattern development.

## 2. Experimental Facility

The experimental facility is displayed in Fig. 1 and consisted of a main flow and an auxiliary cooling loop. A single 811 µm x 753 µm cross section rectangular microchannel of length 75 mm was milled into a copper block with two 1 mm diameter circular plenums to form the test section. Flow visualisation was conducted using a clear polycarbonate cover plate and a Phantom MiroLab 110 high-speed, high resolution digital camera at 6000 fps with a resolution of 512 x 512 pixels.

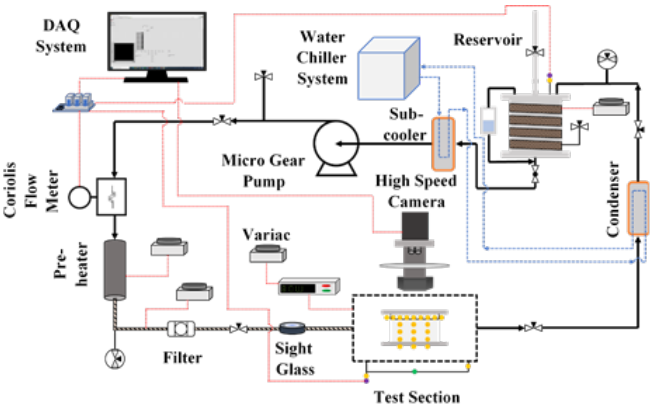


Fig. 1. Schematic diagram of experimental facility.

## 3. Results

The prevailing flow patterns are presented in Fig. 2 and consisted of bubble, slug, churn and annular flows. Nucleation was observed to start from the heated corners of the microchannel at the point of boiling incipience, both in the subcooled and saturated region. Flow reversal was present in the channel at certain mass fluxes due to the elongation of vapour slugs in both the upstream and downstream directions in the saturated region. This resulted in significant

differential and inlet pressure fluctuations as well as periodic flow patterns. For example, the rapid growth of vapour slugs resulted in intermittent collapsing of the slug and disturbance to downstream annular flow liquid films as the subsequent churn flow was forced downstream.

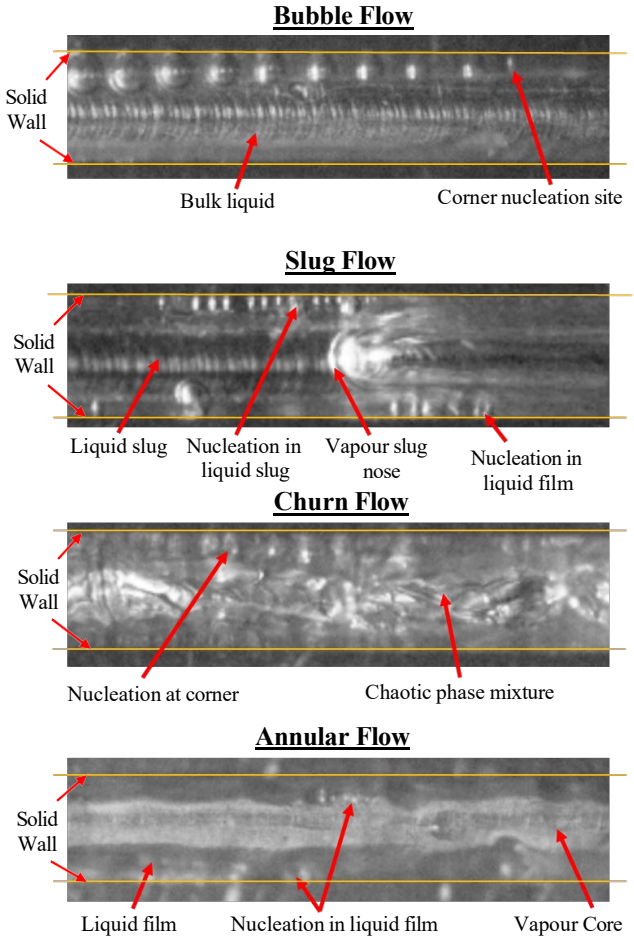


Fig. 2. Observed two-phase flow boiling flow patterns.

Disturbance to the annular flow liquid films resulted in the film being unable to thin, i.e. was thick enough for bubbles to be able to nucleate. This meant that bubble nucleation was not suppressed in any flow pattern regime, i.e. it was observed across all flow patterns. The flow pattern transition boundaries were compared with past reports and recent work with machine learning predictive tools.

Analysis of the local heat transfer coefficients are displayed in Fig. 3 and Fig. 4 which show the results for a constant mass flux of 400 kg/m$^2$s and constant heat flux of 55 kW/m$^2$, respectively. Fig. 3 shows that there was a clear increase in local heat transfer coefficients with increasing vapour quality. Fig. 4 shows no clear mass flux effect. This result was true for all studied mass fluxes. The fact that nucleation occurred in all flow patterns, may be a potential explanation for the increased heat flux effect. More nucleation sites became active as the heat flux was increased and a greater mixing of the bulk fluid/agitation of liquid films was achieved, with both effects increasing the heat transfer coefficient.

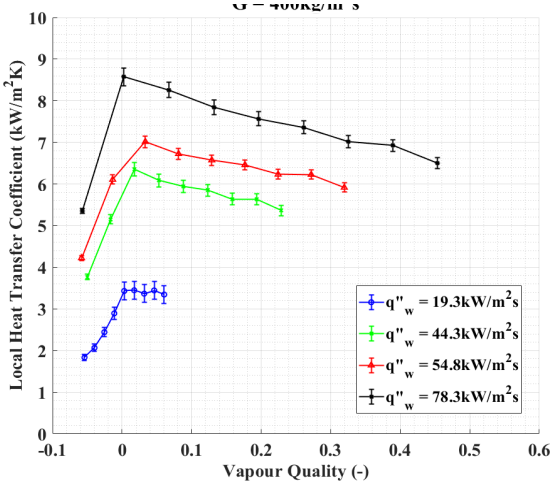


Fig. 3. Local heat transfer coefficients for a constant mass flux of 400 kg/m$^2$s.

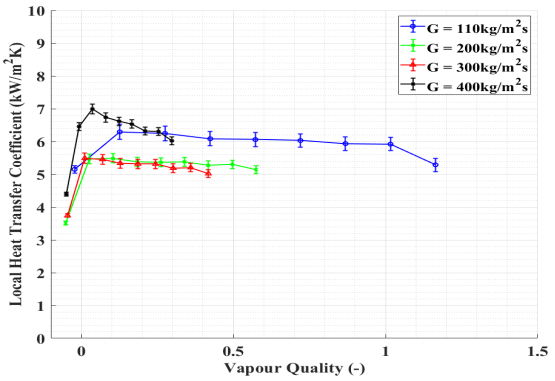


Fig. 4. Local heat transfer coefficients for a constant heat flux of 55 kW/m$^2$.

## References

[1] Cheng, L., Xia, G., 2017. Fundamental issues, mechanisms and models of flow boiling heat transfer in microscale channels. Int JHMT 108, 97– 127.

[2] Karayiannis, T.G., Mahmoud, M.M., 2017. Flow boiling in microchannels: Fundamentals and applications. Appl Therm Eng 115, 1372– 1397.

[3] Lee, V.Y.S., Al-Zaidi, A., Henderson, G., Karayiannis, T.G., 2019. Flow Boiling Results of HFE-7200 in a Multi-Microchannel Evaporator and Comparison with HFE-7100. Proceedings of the 4th World Congress on Momentum, Heat and Mass Transfer.

# Hydraulic and heat transfer performance of additively manufactured cooling channels

Giacomo FAVERO[1,2,*], Razvan DIMA[2], Adriano PEPATO[2], Filippo ZANINI[1], Simone CARMIGNATO[1], Simone MANCIN [1,2,3]

1: Department of Management and Engineering, University of Padova, Str.lla S. Nicola 3, 36100 Vicenza, IT
2: National Institute of Nuclear Physics, Padova Division, Via Marzolo 8, 35131 Padova, IT
3: Department of Chemical Engineering, Brunel University London, UK

* Corresponding author: email: giacomo.favero.1@phd.unipd.it

**Abstract**: In this work, the water pressure drops and cooling performance of three different straight channels, made via metal additive manufacturing, are investigated. The samples were made of AlSi10Mg alloy and built at different sloping angles with respect to the platform plane: 15°, 30°, and 45°. The size and surface topography of each channel were measured by X-ray computed tomography. The results showed that the internal roughness of the samples is not constant along the channel section, and it depends upon the building angle. The three samples were experimentally tested by varying the Reynolds number from 3000 to 55600 at different constant heat fluxes, in order to investigate the heat transfer and fluid flow performance. A total of eight T-type thermocouples were used to measure the channel wall temperature at different sections of each channel, while the water temperature difference between inlet and outlet was monitored using a T-type thermopile. The samples were compared with the most common models in literature to highlight their predicting capabilities.

**Keywords:** Surface texture, pressure drop, cooling channels, additive manufacturing, absolute roughness

## 1. Introduction

In the Additive Manufacturing (AM) field, Laser Powder Bed Fusion (LPBF) process has been proposed in recent years to improve the efficiency of compact heat exchangers and microchannels cooling applications. The possibility to design high-performing unconventional geometries opens novel frontiers in advanced cooling applications. One of the main limiting factors of AM is the complex surface texture with high roughness, which for some applications can become a critical issue in terms of cooling performance. As reported by Ventola et al. [1], the pressure drop can be difficult to predict due to the combined effects of surface texture and the cross sections' actual sizes of the channels. Both these factors strongly depend upon the channel orientation during the AM process, as demonstrated in previous works. For example, Klingaa et al. [2] studied the surface roughness and dross defects of channels manufactured via LPBF, varying the building direction. Favero et al. [3] studied the hydraulic performance of internally smoothed printed samples. They found that the friction factor of a straight channel follows the Blasius equation for smooth pipes and Computational Fluid Dynamics (CFD) tool is able to predict correctly the straight geometry and other ones if it is well calibrated. In this work, the roughness issue of AM cooling channels is presented and experimental results in thermal performance cooling channels are reported.

## 2. Samples construction

The aluminum alloy AlSi10Mg was chosen as material for the samples, because of its good printability and weldability, as well as low specific mass. The weldability helps for the LPBF process effectiveness, while the final low specific mass improves the quality of the X-ray

computed tomography scans, which were employed to non-destructively characterize the internal surface texture and size of the investigated channels. Although different metals are used with 3D printing to develop compact heat exchangers and components with internal cooling channels, the LPBF of aluminum is studied to develop compact heat exchangers fabrication, and to better evaluate the heat transfer enhancement [4]. The samples were manufactured using aluminum powder and process parameters that allowed to achieve an high relative density of the fabricated parts (99.89%). Due to the possibility of non-uniform thermal properties in the material, a couple of cylinder samples were manufactured in two different orientations (horizontal and vertical). Using the same material and process parameters, three straight channel samples were manufactured, at different building orientations: 15°, 30°, and 45°. The channel samples have the same geometry, which is a circular section of a 5 mm diameter and 180 mm total length. The channel samples are equipped with two pressure taps that were produced directly via AM process, while the heater is a Ni-Cr wire resistance, which was located in the spiral that can be seen in Figure 1 between the two pressure taps. Eight temperature holes were also manufactured along the channel at a distance of 33 mm between each other to host as many T-type thermocouples.

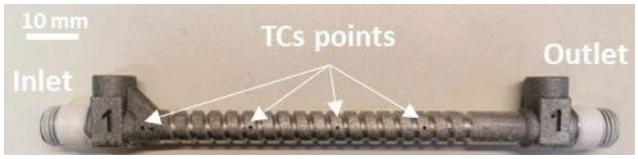


Fig. 1 Channel sample printed at 15° respect the horizontal plane of the printing process.

## 3. Experimental results

The tests of the samples were run in an experimental setup located at the Department of Management and Engineering of the University of Padua. The thermal conductivity of the printed aluminum was measured using an in-house thermal conductivity setup with an uncertainty of ±5%. The results showed that the thermal conductivity is equal to 113 W/m K for the cylinder sample printed in the horizontal direction and 105 W/m K for the vertical one. Concerning the hydraulic tests, the setup consists of a water loop in which the water flow rate and temperature can be independently controlled. The pressure drops were measured employing a differential pressure transducer with an uncertainty ($k = 2$) of ±0.065% on the full scale of 1 bar. The water temperature was monitored through T-type thermocouples calibrated with an uncertainty of ±0.05 K, at the inlet and outlet channel sample. The tests were run in a water flow range that varied from 0.7 to 12.6 l/min, and multiple curves were collected by increasing and decreasing the water flow rate to verify the repeatability of the results. The results for pressure drops are shown in Figure 2.

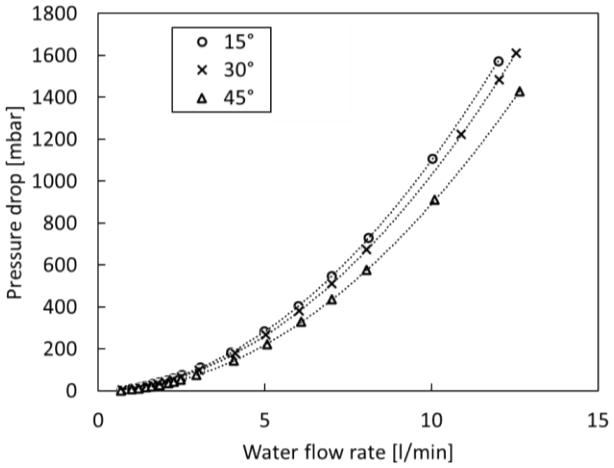


Fig. 2 Pressure drop results against water flow rate for different building orientations.

## 4. Conclusions

The results in terms of pressure drops and heat transfer performance were collected and demonstrate the great opportunities offered by the AM in thermal science.

## References

[1] L. Ventola, et al., Rough surfaces with enhanced heat transfer for electronics cooling by direct metal laser sintering, Int. J. Heat Mass Transf. 75 (2014) 58–74

[2] C.G. Klingaa, et al., X-ray CT and image analysis methodology for local roughness characterization in cooling channels
made by metal additive manufacturing, Addit. Manuf. 32 (2020) 101032

[3] G. Favero, et al., Experimental and numerical analyses of fluid flow inside additively manufactured and smoothed cooling channels, Int. Com. Heat and Mass Transfer 135 (2022) 106128

[4] S. Pracht, et al., Experimental and numerical study of a 3D-printed aluminium cryogenic heat exchanger for compact Brayton refrigerators, Cryogenics 123 (2022) 103418

## SESSION 4a
## Nanofluids and Applications
Chair: **O. Manca**



Soulayma GAL[1,2], David CABALEIRO[3], Walid HASSEN[2], Patrice ESTELLÉ[1]
1: LGCGM, Univ Rennes, Rennes, FR
2: LMES, Université de Monastir, Monastir, TU
3: CINBIO, Universidad de Vigo, Vigo, SP



Maria J. ABRANTES[1,2], Sofia B. ROCHA[1,2], Nelson MARTINS[1,2], Mónica S.A. OLIVEIRA[1,2]
1: Department of Mechanical Engineering, Centre for Mechanical Technology and Automation (TEMA), University of Aveiro, 3810-193 Aveiro, Portugal
2: Intelligent Systems Associate Laboratory (LASI), 4800-058 Guimarães, Portugal



Xueling ZHAO[1,2,3], Yufei FAN[1], Lifei CHEN[1,2,3]
1: College of Energy and Materials, Shanghai Polytechnic University, Shanghai, China
2: Shanghai Advanced Thermal Functional Materials Engineering Technology Research Center, Shanghai, China
3: Shanghai Hot Physical Property Big Data Professional Technical Service Platform, Shanghai, China



Iván CARRILLO-BERDUGO[1], Mario CAMACHO-CASTRO[1], Juan Jesús GALLARDO[1], Desireé M. DE LOS SANTOS[1], Javier NAVAS[1]
1: Departamento de Química Física, Facultad de Ciencias, Universidad de Cádiz, 11510 Puerto Real (Cádiz), Spain

# Thermal Conductivity of Industrial Graphene Water-Based Nanofluids

Soulayma GAL [1,2], David CABALEIRO [3], Walid HASSEN [2], Patrice ESTELLÉ [1,*]

1: LGCGM, Univ Rennes, Rennes, FR
2: LMES, Université de Monastir, Monastir, TU
3: CINBIO, Universidad de Vigo, Vigo, SP

* Corresponding author: Tel.: +33 0223234200; Email: patrice.estelle@univ-rennes1.fr

**Abstract:** Nanofluids consist of common heat transfer fluids containing nanoparticles with high intrinsic thermal properties. In this context, carbon nanostructures such as graphene are especially promising. Actually, next steps in nanofluid development are both their production and their usage at industrial scale and real energy systems. With that aim, we report the stability and thermal conductivity evaluation of few layer graphene (FLG) water-based nanofluids industrially prepared. FLG nanofluids were synthesized from ultrasonication-assisted mechanical exfoliation of graphite in water with a green solvent. Such a process allows the production of FLG with high structural quality and stable nanofluids as shown from both particle size analysis with time and zeta potential measurement. Their thermal conductivity is studied from the transient hot-wire method in the temperature interval 283.15–313.15 K and FLG concentration ranging from 0.005 to 0.2% in wt. The results evidence the thermal conductivity enhancement of nanofluids with FLG, up to 20%, and its dependence on temperature. Based on comparison with theoretical model, it is shown that the thermal conductivity improvement is mainly attributed to the thermal resistance at the FLG interface, the FLG nanosheet average dimensions, and their flatness ratio which evolves with the FLG content.

**Keywords:** Graphene nanofluids, Thermal conductivity, Stability, Modelisation

## 1. Introduction

The transition to a climate-neutral society is both an urgent challenge and an opportunity to build a better future for all. Thus, since 70% of energy is produced or used in the form of heat, the transition towards a sustainable economic development requires of smart strategies to efficiently transfer and store thermal energy. One of the most promising strategies is the improvement of the heat transfer processes that can be achieved by improving the properties of usual heat transfer fluids (HTFs). Recent progresses in nanotechnology have become an interesting research avenue to tailor the properties of HTFs. Thus, in the last years the suspension of solid particles with nanometer dimension(s), namely nanofluids, has proven a promising approach to enhance the thermal properties of conventional HTFs. In particular, carbon-based nanoparticles (e.g., carbon nanotubes, graphene nanoplatelets, etc.) have attracted attention because they exhibit much higher thermal conductivities than metal oxides and metal nanoparticles. In the current development of nanofluid technology, specific attention is focused on industrial production of stable nanofluids and their usage in real situation at large scale. As a contribution to this crucial step toward a wider usage of nanofluids, we report here the stability and thermal conductivity evaluation of graphene based nanofluids prepared in industrial context.

## 2. Materials and methods

The graphene based-nanofluids were industrially prepared in large quantities by mechanical exfoliation of graphite within water under ultrasonication and using a green solvent, with a procedure similar to the one described in [1]. Such a process allows the production of high quality few layer graphene nanoplatelets. The as prepared nanofluids were produced with different graphene content, varying from 0.2 to 0.005 wt.%. The stability of those nanofluids were evaluated from both zeta potential measurement (samples were diluted at 1:100)

and monitoring of particle size from Dynamic Light Scattering under static and shaken conditions [2]. These experiments were performed during 30 days. As a result, the zeta potential values for all samples are within -35 and -40 mV, while the particle size remains constant and centered around 800nm+/-50 regardless of the FLG content and conditions. This indicates a relevant stability for these nanofluids. Their thermal conductivity was measured in several replicates from the transient hot wire method according to the ASTM D7896 standard and using a THW-L2 device (Thermtest Inc., Richibucto Road, NB, Canada) in the temperature range 283.15 to 313.15 K. In this range, the uncertainty was evaluated to 1% from distilled water measurements and the experimental procedure initially used in [1] was followed.

## 3. Results and discussion

An enhancement of the thermal conductivity of graphene based nanofluids was observed with graphene content and temperature. A maximum enhancement of around 20% is obtained at 0.2% in wt. content of graphene. Interestingly, this enhancement reaches 10% for only 0.005 wt.% of graphene. This order of magnitude is similar when the graphene content is increased, as illustrated by the thermal conductivity ratio described in Figure 1. These experimental data were well compared to the Chu model [1,3] which includes average dimensions of the graphene nanosheet, thermal resistance at the graphene interface and the flatness ratio of the nanosheets.
Compared to ref. [1], it is shown here that the flatness ratio decreases with the FLG content. That means that higher is the number of nanosheets, more the nanosheets can be folded and wrinkled within the HTF. This differs from the case of FLG disperse in HTF from non-covalent functionalization where the flatness ratio remains constant due to the adsorption of surfactant molecules with a large content on the nanosheet surface [1].

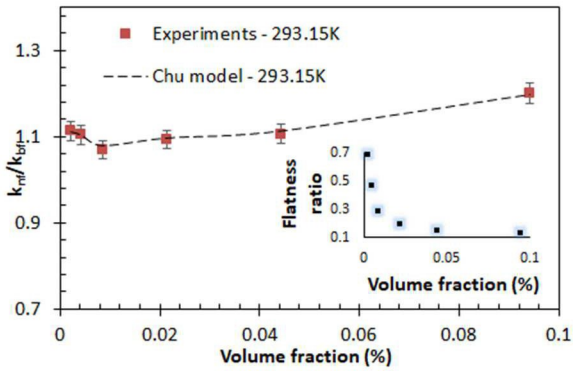


Fig.1 Thermal conductivity ratio of graphene- based nanofluids at 293.15K. Insert: graphene nanosheet flatness ratio evolution with graphene content.

## 4. Conclusion

We reported the thermal conductivity of stable industrially prepared few-layer graphene based nanofluids with different nanosheet contents. The thermal conductivity evolution was correlated to the average dimensions of FLG nanosheets, thermal resistance at their interface and flatness ratio that evolves with FLG content. Next steps will include: determining the full thermophysical profile and numerically simulate the heat transfer performance of these nanofluids. Some other base fluids and hybrid systems containing FLG could also be developed and tested in near future.

## Acknowledgements

The authors[1,2] gratefully acknowledge the financial support of CMCU through the grant n°23G1111 from the PHC Utique. SG also acknowledges Rennes Métropole for its financial support through the PhD student incoming mobility grant n°2022-987.

## References

[1] Hamze S; et al. Few-layer graphene-based nanofluids with enhanced thermal conductivity. Nanomaterials 2020, 10(7):1258.

[2] Vallejo JP; et al. Potential heat transfer enhancement of functionalized graphene nanoplatelet dispersions in a propylene glycol-water mixture. Thermophysical profile. The Journal of Chemical Thermodynamics 2018, 123:174-184.

[3] Chu, K.; Li, W.; Tang, F. Flatness-dependent thermal conductivity of graphene-based composites. PhysicsLetters A 2013, 377, 910–914.

# Tailoring nanofluids properties for transformers

Maria J. ABRANTES[1,2], Sofia B. ROCHA[1,2], Nelson MARTINS[1,2], Mónica S.A. OLIVEIRA[1,2,*]

1: Department of Mechanical Engineering, Centre for Mechanical Technology and Automation (TEMA), University of Aveiro, 3810-193 Aveiro, Portugal
2: Intelligent Systems Associate Laboratory (LASI), 4800-058 Guimarães, Portugal

* Corresponding author: Email: monica.oliveira@ua.pt

**Abstract:** New transformer oils have been envisaged and characterised. The developed nanofluids were accomplished by resorting to two different base fluids (i.e., mineral oil | Hyvolt I and vegetal oil | FR3) and three different nanoparticles (i.e., carbon nanotubes (CNT); carbon nanoplatelets (NPc) and $TiO_2$). All nanofluids were prepared using a two-step method, and particular attention was paid to the stability of the developed system. Moreover, surfactants (i.e., oleic acid) were used when applicable, and a thermal characterisation was carried out for each design. Concerning Hyvolt I/$TiO_2$, the results showed a slight improvement in thermal conductivity, a 3% increase for concentrations of 1%vol of $TiO_2$ concerning the base fluid at low temperatures, which was not expected, considering the values reported in the literature. Nevertheless, a wide variety of methods are documented and plenty of associated uncertainties, especially concerning sedimentation, which may justify the discrepancy. The best results were attained for the FR3/NPc nanofluids formulation, with nanoparticle concentrations of 0.1%vol, resulting in an increase of the thermal conductivity up to 9%.

**Keywords:** Dielectric Fluids, Nanofluids, Thermal Property Characterization, Thermal Conductivity

## 1. Introduction

The ideal transformer oil should have high thermal conductivity to dissipate heat, low viscosity to facilitate the continuous flow of oil and good electrical insulation characteristics [1]. To achieve this, nanofluids are being sought as a possible solution [1]–[3]. A nanofluid is a fluid containing nanoparticles (1 – 100 nm) that are homogeneously suspended in low volumetric percentages in a base fluid. Concerning this work involving high voltage and electrical insulating fluids, the term "nanofluid" corresponds to combining oil/nanoparticles in a transformer to properly insulate and cool down the electrical components [1]. Since conventional fluids have lower thermal conductivity than solid materials, different nanoparticles have been used to enhance the thermal dissipation of a base fluid [4]-[6]. The resulting suspensions are expected to improve the cooling properties without degrading their insulation capabilities, establishing a new class of dielectric fluids with better combined thermal and electrical properties. This work reports on the latest refrigeration fluids' development and characterisation.

## 2. Nanofluids Preparation and Characterization

This study involved the preparation of different nanofluids based on two base fluids: mineral oil and vegetable oil, and three nanoparticles (i.e., CNT, NPc and TiO2). The considered vol. concentration were 0.01, 0.05, 0.1, 0.5 and 1%. All nanofluids were prepared using a two-step method, and their stability was assessed via UV-Vis-NIR Spectrophotometry. Moreover, their thermal characterisation was conducted using a Hot Disk Thermal Constants Analyser, 2500 S. The method resorts to the Transient Plane Source (TPS) and complies with ISO 22007–2. The nanofluids' thermal conductivity was assessed at 20ºC, 40ºC, and 60ºC.

### 2.1 Nanofluids mineral oil | Hyvolt I based.

Hyvolt I/CNT best stability was observed for mixing amplitudes of 20% and lower nanoparticle concentrations (0.05 and 0.5%vol). The maximum stability period

observed was of seven days.

The thermal conductivity of these nanofluids increases with temperature and with the addition of nanoparticles. Moreover, from the results, increases of 2.5%, 2.6% and 2.9% were observed at 20°C, 40°C and 60°C, respectively, for a CNT concentration of 0.5%vol. However, it should be noted that at this concentration, the stability of the nanofluid tends to decrease.

Hyvolt I/ $TiO_2$ oleic acid was used as a surfactant, and FTIR was used to ascertain the desired covalent bonds. For these Hyvolt I /$TiO_2$ nanofluids, the best stability was attained for mixing amplitudes of 20% and lower nanoparticle concentrations (0.01 and 0.05%vol). Moreover, no periods of stability longer than seven days were observed.

Concerning the thermal conductivity of the fluids tested, with the increase in temperature, the thermal conductivity rises, as expected, for lower concentrations (0.01% and 0.05 %vol). Moreover, the thermal conductivity rise is consistent with the nanoparticle's concentration loading. Nevertheless, this behaviour was not observed for higher concentrations (0.1%, 0.5% and 1%vol). For the samples with lower concentrations (0.01% and 0.05%vol), there was an increase of about 2% for the different temperatures. In contrast, the remaining samples' thermal conductivity values were lower, consistent with the shorter periods of stability observed.

**2.2 Nanofluids vegetable oil | FR3 based.**

Nanofluids were produced using vegetable oil – FR3 as base fluid and $TiO_2$ with different concentrations (0.1%, 0.5%, 1%, 2%vol) and NPc functionalised with carboxylic groups. The new fluids were also characterised in terms of stability through the UV-Vis-NIR Spectrophotometry technique. Again, the period of stability did not exceed seven days.

Concerning these systems, it should be noted that only modest improvements (3%) in thermal conductivity were achieved with concentrations of 1% of $TiO_2$ about the base fluid and at low temperatures, which was not expected compared to the values reported in the literature. However, it should also be noted that a wide variety of measurement methods are reported and many associated uncertainties, especially concerning sedimentation. The best results were observed for the FR3/NPc nanofluids, where for concentrations of 0.1%vol, there were increases in thermal conductivity of up to 9% for all thermal levels analysed. It should be noted that such improvements were registered in the other thermal properties with relevance in the heat dissipation process.

## References

[1] M. Rafiq, Y. Lv, and C. Li, "A Review on Properties, Opportunities, and Challenges of Transformer Oil-Based Nanofluids," J. Nanomater., vol. 2016, 2016.

[2] S. U. S. Choi, "Enhancing thermal conductivity of fluids with nanoparticles," Am. Soc. Mech. Eng. Fluids Eng. Div. FED, vol. 231, no. January 1995, pp. 99–105, 1995.

[3] Charalampakos, Peppas, Pyrgioti, Bakandritsos, Polykrati, and Gonos, "Dielectric Insulation Characteristics of Natural Ester Fluid Modified by Colloidal Iron Oxide Ions and Silica Nanoparticles," Energies, vol. 12, no. 17, p. 3259, 2019.

[4] J. Taha-Tijerina et al., "Electrically insulating thermal nano-oils using 2D fillers," ACS Nano, vol. 6, no. 2, pp. 1214–1220, 2012.

[5] H. Jin, T. Andritsch, P. H. F. Morshuis, and J. J. Smit, "AC breakdown voltage and viscosity of mineral oil based SiO2 nanofluids," Annu. Rep. - Conf. Electr. Insul. Dielectr. Phenomena, CEIDP, pp. 902–905, 2012.

[6] M Oliveira, MA Fonseca, S Freitas, B Lamas, B Abreu, Hugo Calisto, N Martins, "Carbon Nanotubes in a Fluidic Medium: Critical Analysis," Intech, no. Intech, pp. 3–30, 2013.

## Acknowledgements

The authors acknowledge funding from projects: NEXTRA – Enabling the NEXT Generation of Smarter TRAnsformers" n.º 39906 and HORIZON-MSCA-2021-SE-01101082394 (Micro-FloTec).

# Preparation and Properties of MXene/Silicon Dioxide/Calcium Chloride Hexahydrate Composite Phase Change Heat Storage Materials

Xueling ZHAO[1,2,3*], Yufei FAN[1], Lifei CHEN[1,2,3]

1: College of Energy and Materials, Shanghai Polytechnic University, Shanghai, China
2: Shanghai Advanced Thermal Functional Materials Engineering Technology Research Center, Shanghai, China
3: Shanghai Hot Physical Property Big Data Professional Technical Service Platform, Shanghai, China

* Corresponding author: Email: xlzhao@sspu.edu.cn

**Abstract:** As a kind of low temperature bulk heat storage material, calcium chloride hexahydrate ($CaCl_2·6H_2O$) has a great application prospect in heat storage and energy saving. However, the single $CaCl_2·6H_2O$ phase change heat storage material has the disadvantages of low thermal conductivity and easy leakage when melting. Mesoporous silicon dioxide ($mSiO_2$) with large inner core and interpenetrating mesoporous channel structure can solve the above problems. $mSiO_2$ has the advantages of low density, low thermal expansion coefficient, low refractive index and large specific surface area. However, it has low thermal conductivity and needs to be combined with other materials with good thermal properties to enhance its thermal conductivity. In this paper, MXene was used as the thermal conductivity enhancement material, $mSiO_2$ was grown on its surface, and then the phase change material $CaCl_2·6H_2O$ was loaded into it. By means of TG, DSC and infrared thermal imager, it is proved that the heat storage performance, thermal stability and heat transfer rate of the composite phase change materials are significantly improved. The leakage of $CaCl_2·6H_2O$ in the oven was also obviously inhibited by the carrier material. A kind of composite phase change heat storage material with excellent thermal properties and stability was successfully prepared.

**Keywords:** Calcium Chloride Hexahydrate; Phase Change Heat Storage; Leakage; MXene; Silicon dioxide

# About the stability of graphene oxide/polydimethylsiloxane nanofluids under operation temperature in concentrating solar power plants

Iván CARRILLO-BERDUGO[1*], Mario CAMACHO-CASTRO[1], Juan Jesús GALLARDO[1],

Desireé M. DE LOS SANTOS[1], Javier NAVAS[1]

1: Departamento de Química Física, Facultad de Ciencias, Universidad de Cádiz, 11510 Puerto Real (Cádiz), Spain

[*] Corresponding author. Email: ivan.carrillo@uca.es

**Abstract:** Polydimethylsiloxane-based nanofluids are presented as heat transfer fluids for concentrating solar power plants with no hazard classifications. We are searching for a nanomaterial whose dispersion can satisfy a compromise between stability, efficiency, cost, and environment safety. Graphene oxide has been profusely proven in literature to meet the later three. Here we demonstrate via density functional theory simulations that that interactions at the graphene oxide/polydimethylsiloxane interface are sufficiently strong to guarantee colloidal stability at maximum operation temperature.

**Keywords:** concentrating solar power, nanofluids, graphene oxide, polydimethylsiloxane, computational chemistry.

## 1. Introduction

When combined with thermal energy storage, concentrating solar power (CSP) makes solar energy dispatchable and allows to align supply and demand, thus making more reliable energy conversion systems combined with other renewable technologies. The main limitation of CSP is the low achievable energy density under operation, due to the physical properties of the heat transfer fluid (HTF) that participates in solar-to-thermal energy conversion in parabolic-trough collectors. The currently used HTF is the eutectic and azeotropic mixture of diphenyl ether and biphenyl, commercially available as Dowtherm A for instance, which is suitable for liquid phase operation up to 673 K, with low vapour pressure and dynamic viscosity, and non-corrosive nature. Its specific heat (SH) and thermal conductivity (TC) are suboptimal. Besides, the manipulation of this mixture can cause skin, eye and respiratory irritation to human beings, and an accidental release to the environment can cause severe and long-lasting effects on aquatic life.

Polydimethylsiloxane (PDMS) has been recently introduced as an outstanding alternative HTF for CSP technology. This linear silicon-based fluid, commercially available as Helisol 5A for instance, has similar thermal and rheological properties compared to Dowtherm A, is thermally stable up to 698 K, and has no hazard classification. The later endorses PDMS as an alternative HTF to better comply with sustainability principles in this application. SH and TC of the new PDMS-based HTF can be improved by dispersing nanomaterials into it, generating a colloidal suspension that is typically named nanofluid. Nanofluids as HTF for CSP plants, using the Dowtherm A as base fluid, have been previously studied [1, 2]. The interest for a new HTF opens the search for a nanomaterial whose dispersion into the fluid can satisfy a compromise between stability, efficiency, cost, and environment safety. It is well reported throughout literature that suspensions with graphene oxide (GO) nanosheets can improve the thermal properties of the base fluid [1]. Its synthesis also complies with green chemistry principles while preserving a reduced cost. Therefore, GO nanosheets could be a good candidate for PDMS-based nanofluids, if we can confirm that interactions at the GO/PDMS interface are sufficiently strong to guarantee colloidal stability at maximum operation temperature. Such is the scope of this work.

## 2. Methods

We studied the interactions at the GO/PDMS interface via periodic density functional theory (DFT) simulations with VASP6 [3, 4]. Our models consist of a single graphene sheet that is either clean or functionalised with either a carboxyl, a hydroxyl, or an epoxide group. The monolayer is enclosed by a vacuum slab of 25 Å that allows to allocate a DMS

oligomer close to it and prevents unphysical interactions between periodic images along the direction normal to the graphene sheet. Different configurations for the siloxane and methyl groups of the DMS oligomer with respect to the graphene sheet and its functional groups were submitted for geometry optimisation. The GGA-PBE functional was used to solve Kohn-Sham equations. Grimme's dispersion corrections (D3) were included for an adequate description of van der Waals interactions. Valence wavefunctions were described by sets of planewaves with kinetic energies up to 520 eV. Interactions between valence electrons and ionic cores were described using PAW pseudopotentials. Brillouin-zone integrations were performed using a 3x3x1 k-point grid. Gaussian smearing with a smearing of 0.01 eV was used to describe orbital occupancies.

## 3. Results and discussion

The geometry and energy of the most stable interactions between functional groups at the GO/PDMS interface model are shown in **Figure 1**. The molecular architecture, the relative difference in electronegativity of the atoms that are part of it, and the magnitude of the interaction energy suggest all these are cases of H-bonding. Cases (a) and (b) are common examples of H-bonding, in which the H atom of carboxyl or hydroxyl group, bounded to a very electronegative O atom, acts as H-bond donor, and the O atom of siloxane groups of PDMS, with two lone pairs of electrons, acts as H-bond acceptor. Cases (c) and (d) are less trivial, but H-atoms in methyl groups of PDMS, due to the exceptional polarisation of Si–O bonds, can act as H-bond donors towards acceptors like lone pairs of O atoms in epoxide groups of GO or delocalised π-electrons in graphene.

Despite the depth details that characterise each case, the negative sign of the interaction energy indicates they are thermodynamically favoured, and the magnitude is indicative of good stability. Since the energetics of thermal effects are in the order of $k_B T$, which is 60 meV at 698 K, with interaction energies within 0.5-0.8 eV we can expect PDMS not to split off the GO nanosheet once physisorbed by H-bonding, even at the maximum operation temperature under which the nanofluid is expected to be used. Therefore, GO is proven a suitable nanomaterial for PDMS-based nanofluids.

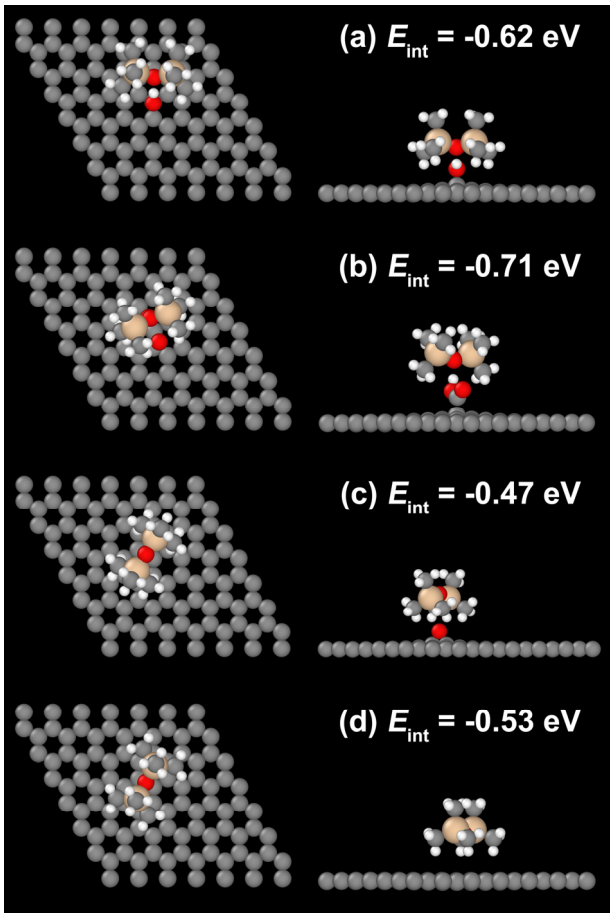


**Figure 1.** Geometry and energy of interactions between functional groups at the GO/PDMS interface. Visualisations made with OVITO [5].

## Acknowledgements

The authors acknowledge *Ministerio de Ciencia e Innovación del Gobierno de España* for funding under grant TED2021-132518B-I00. This work used computer resources of the *Red Española de Supercomputación*. The authors thankfully acknowledge the computer resources at *Altamira* and the technical support provided by UC (RES-QHS-2023-1-0002).

## References

[1] T. Aguilar et al. *J. Mol. Liq.* **306**, 112862 (2020).
[2] I. Carrillo-Berdugo et al. *Energy & Fuels* **36**, 8413-8421 (2022).
[3] G. Kresse, J. Furthmüller. *Phys. Rev. B* **54**, 11169-11186 (1996).
[4] G. Kresse, D. Joubert. *Phys. Rev. B* **59**, 1758-1775 (1999).
[5] A. Stukowski. *Modelling Simul. Mater. Sci. Eng.* **18**, 015012 (2009).

## SESSION 4b
## MINI SYMPOSIUM Part 2 of 2
## Near surface effects in two-phase flows
Chair: **M. Magnini**

# Pool boiling of Novec 649 on conditioned copper surfaces

Chiara FALSETTI[1,*], Edmond J. WALSH[2]

1: Propulsion and Power, Delft University of Technology, Delft, NL
2: Thermofluids Institute, Department of Engineering Science, University of Oxford, Oxford, UK

* Corresponding author: Tel.: +44 0745 990068; Email: cfalsetti@tudelft.nl

**Abstract:** The present study investigates pool boiling heat transfer of Novec 649, a relatively new fluid with similar thermophysical properties of FC-72 and low global warming potential (GWP). Its interaction with the surface and thermal characteristics requires further investigation to be used for cooling applications. Boiling is an effective way to remove high heat loads and its heat transfer efficacy can be optimized by altering the fluid-surface interaction. While it is desirable to operate in the upper region of the boiling curve, it is also dangerous as dry-out occurs, where vapor completely blankets the surface. This point is referred to critical heat flux (CHF) and it is arguably the most important design and safety parameter in boiling.
The effects of surface modifications on the boiling heat transfer performance and the CHF limit of Novec 649 have been assessed in this study. Samples with different surface roughness (Ra from 0.1 μm to 9 μm) and microstructures (in the range of 400-1200 μm) have been machined via sandblasting and electro-discharge machining (EDM).

**Keywords:** Micro Flow, Microcirculation, Boiling, Pumps

## 1. Introduction

Boiling heat transfer has been widely investigated and researched for cooling of high-power electronics, IT equipment, electric motors, and fuel cells to cite a few. In the past years, many research studies focused on increasing both the heat transfer coefficient (HTC) and critical heat flux limit (CHF) by surface modifications [1-3]. However, there is still a large discrepancy among studies on pool boiling heat transfer of enhanced surfaces, even for the same fluid and surface machining technique, as also concluded by the extensive review presented by Mahmoud and Karayiannis [4]. Additionally, most research studies carried out to date, used water as heat transfer fluid. So far, a very limited number of studies investigated pool boiling heat transfer of Novec 649 on engineered surfaces.
This study investigates the pool boiling heat transfer of Novec 649 with engineered copper surfaces. In particular, the effect of different surface modifications on boiling heat transfer and their potential positive impact on the CHF limit are assessed.

## 2. Experimental set-up

### 2.1 Pool boiling facility.

The facility consists of a polycarbonate cylinder of 150 mm inner diameter and 184 mm height, with a stainless steal base and an aluminum lid. A photograph and schematic of the pool boiling facility are shown in Figure 1. Two K-type thermocouples measure the liquid temperature inside the vessel and a pressure transducer on the top lid measure the vapor pressure. An auxiliary heater is used to degas the liquid to remove all the non-condensable gases and maintain the liquid at the desired

saturation conditions. The thermocouples and heater connection wires are going through the top lid and are sealed with epoxy glue.
To condense the vapor, a finned radiator is connected to a water loop controlled with a LAUDA thermostat. The temperature and pressure measurements were acquired via a LabVIEW system.

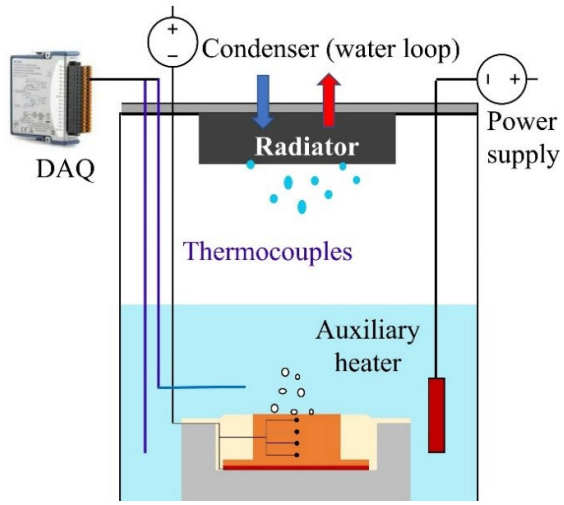


Figure 1 Pool boiling experimental facility.

### 2.2 Test sections

The test section consists of a T-shape copper block with a bottom plate of 51 mm x 51 mm and thickness of 5 mm, and the top (boiling) surface of 20 mm x 20 mm, see Figure 2. Four thermocouples 3mm apart measure the temperature and calculate the 1D heat flux in the copper test section. An OMEGA flexible heater is used to heats up the sample. The test section is housed in a PTFE support and insulated by epoxy glue, see Figure 2.

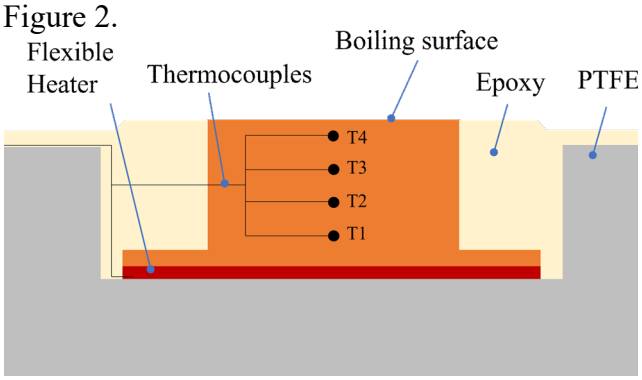


Figure 2 Schematic of the copper test section.

For the present study, the boiling surface has been modified by different machining and patterning techniques to investigate the heat transfer enhancements by surface modifications. Sandblasting was used to modify the surface roughness. Four different average roughness (Ra) of 0.1 µm, 2.5 µm, 6.1 µm and 9 µm have been obtained using different medium particle sizes.
Micro-structures have been machined via electro-discharge machining (EDM) on the boiling surface. The micro-structures have a squared section of 400 µm x 400 µm. The height of the microstructures ("H") and the spacing between two adjacent pins ("S"), have been varied in the range of 200 µm- 1200 µm. The effects of changing the height and spacing of the microstructures on the boiling heat transfer has been assessed in this study.

## References

[1] Z. Cao, Z. Wu and B. Sunden, "Pool Boiling of NOVEC-649
coated surfaces," Heat Transfer Engineering, vol. 42, p. 1732–1747, 2021.
[2] M. Može, V. Vajc, M. Zupancic and I. Golobic, "Hydrophilic and Hydrophobic Nanostructured Copper Surfaces for Efficient Pool Boiling Heat Transfer with Water, Water/Butanol Mixtures and Novec 649," Nanomaterials, vol. 11, no. 3216, 2021.
[3] Y. Song, C. Wang, D. Preston, G. Su, M. M. Rahman, H. Cha, Seong, B. Philips, J. Hiyun,
M. Bucci and E. Wang, "Enhancement of Boiling with Scalable Sandblasted Surfaces," *ACS Applied Materials & Interfaces,* vol. 14, p. 9788−9794, 2022.

[4] M. Mahmoud and T. Karayiannis, "Pool boiling review: Part II – Heat transfer enhancement," *Thermal Science and Engineering Progress,* vol. 25, 2021.

# POOL BOILING ON MICROSTRUCTURED SURFACES IN NORMAL AND REDUCED GRAVITY

Alekos I. GARIVALIS[1,*], Paolo DI MARCO[1]

1: DESTEC, University of Pisa, Vicenza, IT

* Corresponding author: Tel.: +39 050 2217116; Email: alekos.garivalis@ing.unipi.it

**Abstract:** In pool boiling, buoyancy force is one of the external actions that contribute most to the bubble detachment and vapor removal from the wall region. In microgravity conditions, the boiling process changes: primary mechanisms of boiling occur at the microscale level close to the heated surface and are weakly dependent on gravity, while secondary, far-heater, mechanisms include the bubble removal and are mainly driven by gravity. Recently, efforts were done with engineered surfaces, and the use of micropillars showed enhancement in Heat Transfer Coefficients and Critical Heat Flux. Even if the role of the engineered surfaces on the enhancement is still debated, it relies on capillary forces. One aim of this study is to verify the enhancement capabilities experimentally on different heater geometries; the second aim is to use an electric field to introduce an external action capable to remove vapor from the boiling region, on behalf of gravity force, thus combining active and passive enhancement techniques. The experiments conducted during parabolic flights clarified the role of the structures and electric field in boiling enhancement, with potential applications for space devices.

**Keywords:** Pool boiling, Microstructures, Electric field, Microgravity

## 1. Introduction

Buoyancy force, driven by gravity, is recognized as one of the external actions that contribute most to the bubble detachment and vapor removal from the wall region. Thus, in microgravity conditions, the boiling process changes. As described by Straub [1], primary mechanisms of boiling occur at the microscale level close to the heated surface and are weakly dependent on gravity, while secondary, far-heater, mechanisms include the bubble removal and are mainly driven by gravity. Recently, efforts were done with engineered surfaces, and the use of micropillars showed enhancement in heat transfer coefficients and Critical Heat Flux. Even if the role of the engineered surfaces on the enhancement is still debated, it is expected to be independent on gravity, as it relies on capillary forces [2]. One aim of this study is to verify this experimentally on different heater geometries; the second aim is to use an electric field to introduce an external action capable to remove vapor from the boiling region, on behalf of gravity force, thus combining active and passive enhancement techniques. The experiments conducted during parabolic flights (e.g., [3]) clarified the role of the structures and electric field in boiling enhancement, with potential applications for space devices.

The experimental apparatus consists of a test cell with a volume of 2.3 liters, filled with FC-72. The pressure and temperature of the liquid can be adjusted by means of dedicated subsystems. The boiling surface consists of 10 mm x 10 mm, electrically heated, silicon chips, where microstructures of different sizes are etched (see Fig. 1). To generate the electric field in the boiling region, a stainless-steel grid is placed at 6 mm above the surface. A DC voltage up to 15 kV was applied between the grid and the heated surface.

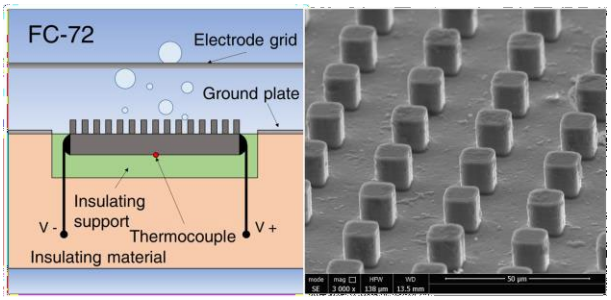


**Fig. 1.** Test section schematics and SEM image of the microstructured surfaces.

## 2. Results

Boiling patterns are different when buoyancy lacks. Fig. 2a shows the big primary bubble that remains above the boiling surface. However, when the electric field is present, the vapor is broken and pushed away, resulting in the pattern of figure 2b.

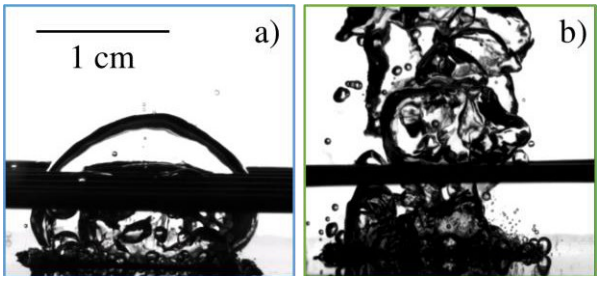


**Fig. 2.** Boiling pattern in microgravity without electric field (a) and with electric field (b).

This different vapor behavior results in an enhancement of Critical Heat Flux (whilt the Heat Transfer Coeffcient does not change much). An example is of some of the structures tested is reported in Fig. 3.

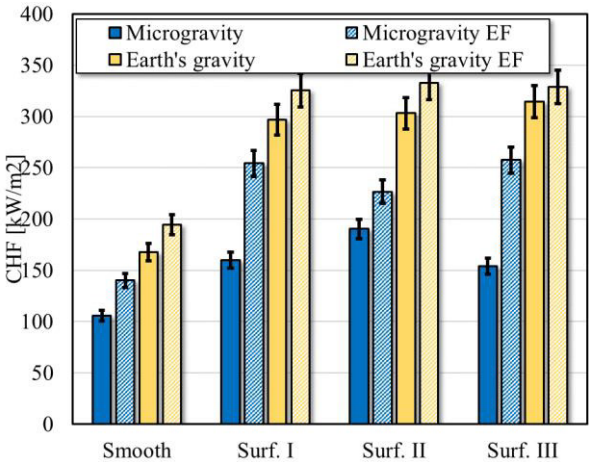


**Fig. 3.** Critical heat flux with different boiling surfaces, gravity, and electric field levels.

## 3. Conclusions

Results show that CHF enhancement always occurred in microgravity conditions, but the effect of microstructures alone is reduced in microgravity. In fact, by breaking the large bubble hovering over the heated surface, the electric field transforms the bubble dynamics, restoring the one observed on Earth. This allows the microstructures to work more efficiently, i.e., there is a synergistic effect. This is confirmed by visualizations of boiling patterns and suggests that substantial increase of boiling performance in microgravity conditions relies also on improvement of far-heater boiling patterns. It is worth noting that the enhancement encountered on some heaters is less than the surface increase due to the microstructures, while in others it was greater. This leaves room to optimization of the micropillar structure and size, to be performed in the future.

## References

[1] J. Straub, Boiling Heat Transfer and Bubble Dynamics in Microgravity, in: Adv. Heat Transf., 2001: pp. 57–172. https://doi.org/10.1016/S0065- 2717(01)80020-4.

[2] K.H. Chu, R. Enright, E.N. Wang, Structured surfaces for enhanced pool boiling heat transfer, Appl. Phys. Lett. 100 (2012). https://doi.org/10.1063/1.4724190.

[3] A.I. Garivalis, G. Manfredini, G. Saccone, P. Di Marco, A. Kossolapov, M. Bucci, Critical Heat Flux on Microstructured Surfaces in Microgravity and in the Presence of Electric Field: Preliminary Results of a Parabolic Flight Campaign, Proc. Therm. Fluids Eng. Summer Conf. 2021- May (2021) 1013–1016. https://doi.org/10.1615/TFEC2021.cnd. 32072.

# Importance of understanding near surface effects during bubble life cycle for enhanced nucleate boiling heat transfer

Matevž ZUPANČIČ[1,*], Mattia BUCCI[1], Iztok GOLOBIČ[1]

1: University of Ljubljana, Faculty of Mechanical Engineering, Ljubljana, SI

* Corresponding author: Tel.: +386 1 4771 309; Email: matevz.zupancic@fs.uni-lj.si

**Abstract:** Near surface effects in nucleate pool boiling can be considered on a scale of several micrometers (effects related to microlayer and contact line evaporation), tens of micrometers (i.e., the extent of the thermal boundary layer), of several hundreds of micrometers (micro convective flows due to bubble dynamics and coalescence events) being effective up to the phenomenological characteristic length (i.e., the bubble departure diameter). Interplay between different phenomena is still not fully understood, also because in-liquid transient temperature field around the growing/departing bubbles cannot be easily experimentally determined. This work will outline our current understanding about near surface effects related to enhanced nucleate boiling heat transfer, developed and emerging experimental techniques that would help in further studies, and new experimental results obtained on laser-textured surfaces through synchronized high-speed imaging, IR thermography and in-liquid temperature measurement through microthermocouple.

**Keywords:** Nucleate Boiling; Heat Transfer Enhancement; Bubble Dynamics; High Resolutioin Temperature Measurements; Mechanistic Modelling

## 1. Introduction

Nucleate pool boiling is an effective heat removal process that comprises (i) nucleation of bubbles and related heat removal due to liquid evaporation, (ii) bubble detachment associated with quenching of nucleation sites, and (iii) single-phase convective heat transfer in the intermediate region between active nucleation sites. Understanding the interplay between these contributions is fundamentally important in model development, but also to optimize the enhanced heat transfer surfaces.

In addition to geometrical bubble parameters and nucleation site distribution, the knowledge about transient temperature fields is fundamental for comprehensive studies. While the methods to measure the boiling surface temperature are relatively well advanced (e.g., IR thermography, temperature-sensitive paints, and fluorescence microscopy), the techniques that would allow high spatiotemporal temperature measurements of the fluid near the boiling surface are still underdeveloped.

## 2. State-of-the-art and open questions

Within the fundamental understanding of boiling and development of enhanced heat transfer surfaces, many studies highlight the importance of macroscale hydrodynamic effects (i.e., liquid-vapor pathways and related instabilities) that are taking place far from the boiling surface [1,2]. Historically the most relevant is of course the famous Zuber's correlation [3] for critical heat flux (CHF). Several studies, however, are postulating and proving that overall boiling heat transfer and CHF is instead much more related to the near-wall phenomenon [4,5]. To determine the length scale of these near-surface effects, one should consider several important aspects.

During the bubble growth, a significant part of the evaporation energy is coming from the superheated substrate, facilitated by microlayer and contact line evaporation. The significance of those contributions is mostly investigated through surface temperature measurements, as both phenomena are taking place extremely close to the boiling surface (i.e., up to 10 μm)

and are also dependent on surface morphology and wettability. Experimental techniques, capable of providing highly resolved temperature information at such small length scales within the liquid and so close to the boiling surface, still need to be (further) developed. Indirect observations through surface temperature measurements and numerical simulations (including molecular dynamics studies) are for now considered as the only solutions to study these effects.

For saturated or slightly subcooled boiling conditions, part of the bubble growth energy might also come from the thermal boundary layer that can reach several tens or even hundreds of micrometers above the boiling surface. At those distances, the effect of liquid perturbation due to bubble dynamics (including single bubble growth/detachment and horizontal bubble coalescence) that determines single-phase heat transfer by microconvection is also significant. Interestingly, the single-phase convection was found to be a dominant heat transfer mechanism in many boiling studies, even on enhanced heat transfer surfaces [6,7]. The missing part of the puzzle for comprehensive understanding of this convective effect is the temperature distribution within the liquid layer. By that we also consider the unknown temperature distribution around the growing bubble(s). Despite several different experimental attempts [8,9] for in-liquid temperature measurements, one of the most effective methods is still an old-fashioned microthermocouple. Despite being invasive and cannot provide spatial temperature distribution, it might reveal important and unknown effects when coupled with synchronous high-speed videography and IR thermography.

## 3. Conclusion

This work will present a short review of the latest achievements from different authors and our latest original experimental results in the field of understanding the near-surface effects in nucleate pool boiling phenomena. Special emphasis will be given on (i) the experimental techniques that can be used to obtain near-surface temperature data, (ii) utilization of obtained data in some existing models and (iii) the outlook of using new datasets for defining future surfaces for enhanced boiling heat transfer.

## Acknowledgements

The authors acknowledge the financial support from the Slovenian Research Agency: core funding No. P2-0223 and project No. J2-2486.

## References

[1] S. G. Kandlikar. Enhanced macro- convection mechanism with separate liquid–vapor pathways to improve pool boiling performance. *J. Heat Transfer* **139** (2017).

[2] M. M. Rahman *et al.* Increasing boiling heat transfer using low conductivity materials. *Scientific Reports* **5** (2015).

[3] N. Zuber. On the stability of boiling heat transfer. *Transactions of the American Society of Mechanical Engineers* **80** (1958).

[4] L. Zhang *et al.* Percolative Scale-Free Behavior in the Boiling Crisis. *Phys. Rev. Lett.* **122** (2019).

[5] K. Wang *et al.* Extended development of a bubble percolation method to predict boiling crisis of flow boiling. *Int J Heat Mass Transf* **165** (2021).

[6] M. Zupančič *et al.* The wall heat flux partitioning during the pool boiling of water on thin metallic foils. *Appl Therm Eng* **200** (2022).

[7] C. Wang *et al.* Decrypting the mechanisms of wicking and evaporation heat transfer on micro-pillars during the pool boiling of water using high-resolution infrared thermometry. **35** (2023).

[8] V. Voulgaropoulos *et al.* Simultaneous laser-induced fluorescence, particle image velocimetry and infrared thermography for the investigation of the flow and heat transfer characteristics of nucleating vapour bubbles. *Int J Heat Mass Transf* **187** (2022).

[9] V. Stoica *et al.* Phase shift interferometry for accurate temperature measurement around a vapor bubble. *Experimental Heat Transfer* **20** (2007).

# Numerical methods for drop interactions in viscous flow

Chiara SORGENTONE[1,*]

1: Department of Basic and Applied Sciences for Engineering, University of Rome "La Sapienza", IT

* Corresponding author: Tel.: +39 06 49766726; Email: chiara.sorgentone@uniroma1.it

**Abstract:** Microfluidics is an expanding research area, attracting special interest for droplet-based systems where, owing to the small scales, viscous forces dominate and inertial effects are often negligible. Due to the large surface to volume ratio, the importance of interface dynamics becomes pronounced and it is common to choose boundary integral methods for performing accurate numerical simulations.
The interaction of drops placed in external electric fields is at the heart of many practical application (separation and detection of particles, ink-jet printing, electrosprays etc). Nevertheless, modelling these microfluidic processes is a challenging task, especially in three dimensions, because of the complex multiscale physics involved. Fundamental computational challenges that are highly relevant also to other applications will be addressed: accurate quadrature methods for singular and nearly singular integrals, adaptive time-stepping and reparameterization techniques for deforming surfaces able to maintain a high quality representation of the domains throughout the simulations. Particular emphasis will be on quadrature methods applied to the evaluation of nearly singular layer potentials including error estimates.

**Keywords:** Boundary integral method, Drops, Close interactions, Error estimates

## 1. Introduction

The interaction of fluids and electric fields is at the heart of natural phenomena such as the disintegration of raindrops in thunderstorms and applications such as electrosprays, microfluidics, and crude oil demulsification. Many of these processes involve drops and there has been a long-standing interest in understanding drop dynamics in the presence of electric fields. However, fundamental knowledge of the demixing mechanisms by electric fields and also the influence of surfactants on drops, is limited. The surface active agents - surfactants
- are compounds that lower the surface tension, often used in pharmaceutical and engineering applications but also naturally present in heavy oils; consequently it is very important to develop an improved understanding of the complex physics involved.
Numerical methods can offer a powerful tool to closely study such physical systems. Novel numerical tools for accurate microfluidic simulations of 3D drops in Stokes flow will be presented; the numerical method is based on a boundary integral formulation, it considers drops interacting with other drops and includes the effects of insoluble surfactants [1] and external electric fields [2]. When dealing with boundary integral methods it is necessary to compute layer potentials on or close to the boundary where the underlying integral may be difficult to evaluate numerically and for which specialized quadrature techniques must be employed; being able to design such special techniques and make them adaptive represents an important step for the next generation of boundary integral methods.

## 2. Drop pair dynamics

In recent years, analytical, numerical and experimental studies, have approached the

problem of the droplet–droplet interactions in a leaky dielectric framework. By using new developed asymptotic theories and boundary integral simulations, investigations of the motility states of pairs of identical and dissimilar droplets at arbitrary orientation to the electric field will be discussed, showing a delicate balance between repulsion and contact [3,4,5]. The effect of insoluble surfactants on these dynamics will also be considered [6].

## 3. Close interactions

When two particles are getting closer, the integral defining such a layer potential has a rapidly varying integrand. A regular quadrature method will then yield large errors, and a specialized quadrature method must be used to maintain a good accuracy. In order to better understand these situations, error estimates for the quadrature method are needed. Numerical and analytical approaches to efficiently evaluate these estimates will be presented for quadrature methods based on the Gauss-Legendre and trapezoidal rules [7].

## References

[1] C. Sorgentone and A.-K. Tornberg. A highly accurate boundary integral equation method for surfactant-laden drops in 3D. Journal of Computational Physics, 360:167 191, 2018.

[2] C. Sorgentone, A.-K. Tornberg, P. M. Vlahovska. A 3D boundary integral method for the electrohydrodynamics of surfactant-covered drops. Journal of Computational Physics 389, 111 - 127, 2019.

[3] C. Sorgentone, J. I. Kach, A. S. Khair, L. M. Walker, and P. M. Vlahovska.. Numerical and asymptotic analysis of the three-dimensional electrohydrodynamic interactions of drop pairs. J Fluid Mech, vol. 914, A24, special JFM volume in celebration of the George K. Batchelor centenary, 2021.

[4] C. Sorgentone, P. Vlahovska. Tandem droplet locomotion in a uniform electric field. J Fluid Mech Rapids, 951 R2, 2022.

[5] C. Maass. An electrohydrodynamic dance of unequal partners. J Fluid Mech, 956, 2023.

[6] C. Sorgentone, P. Vlahovska. Pairwise interactions of surfactant-covered drops in a uniform electric field.
Phys Rev Fluids 6, 2021

[7] L. af Klinteberg, C. Sorgentone, A.-K. Tornberg, Quadrature error estimates for layer potentials evaluated near curved surfaces in three dimensions. Computers & Mathematics with Applications, Vol. 111, 2022

## SESSION 4c
## Micro Flow in Biomedical devices
Chair: **S. Mancin**



Fahrettin Gökhan ERGIN[1], Navish WADHWA[2]
1: Product Management Department, Dantec Dynamics, Skovlunde, DK
2: Department of Physics, Arizona State University, Tempe, AZ, USA



Dhiren MOHAPATRA[1,*], Rahul PURWAR[2], Amit AGRAWAL[1]
1: Department of Mechanical Engineering, IIT Bombay, Powai, Mumbai-400076, India
2: Department of Biosciences & Bioengineering, IIT Bombay, Powai, Mumbai-400076, India



Beyzanur ÖZOGUL[1], Rabia MERCIMEK[2], Morteza GHORBANI[3], Ali KOŞAR[4]
1: Department of Molecular Biology, Genetics and Bioengineering, Sabanci University, Istanbul, TR
2: Department of Material Science and Nanoengineering, Sabanci University, Istanbul, TR
3: Faculty of Engineering and Natural Sciences, Sabanci University, Istanbul, TR
4: Center of Excellence for Functional Surfaces and Interfaces, EFSUN, Sabanci University, Istanbul, TR



Panagiotis SKALTSOUNIS[1,2], George KOKKORIS[1,3] , Theodoros G PAPAIOANNOU[2], Angeliki TSEREPI[1]
1: Institute of Nanoscience and Nanotechnology, NCSR “Demokritos”, Patriarchou Gregoriou & 27 Neapoleos str., 153 41 Aghia Paraskevi, GR
2: School of Medicine, National and Kapodistrian University of Athens, 75 Mikras Asias str., 115 27 Athens, GR
3: School of Chemical Engineering, National Technical University of Athens, Zografou, 157 80 Athens, GR

# Estimation of Flow Disturbance Radius for Acartia Tonsa Naplius Using High Speed Micro Particle Image Velocimetry

Fahrettin Gökhan ERGIN[1,*], Navish WADHWA[2]

1: Product Management Department, Dantec Dynamics, Skovlunde, DK
2: Department of Physics, Arizona State University, Tempe, AZ, USA

* Corresponding author: Tel.: +45 4457 8000; Email: gokhan.ergin@dantecdynamics.com

**Abstract:** Marine organisms need to feed and avoid detection by predators at the same time. For this reason, they often perform quiet swimming in nature, where the flow disturbances are minimized during taxa. The spatial extent of flow disturbances can be measured by Particle Image Velocimetry (PIV), an optical technique that has minimal effect on the normal swimming behavior during experiments. The spatial extent of the flow disturbances generated by an Acartia Tonsa nauplius was measured using a high-speed PIV system. As the organism is in motion, a special dynamic masking technique is applied based on rigid object tracking. Time-resolved disturbance flow fields can reach up to 1.5 body lengths around the Acartia Tonsa, leaving even a longer wake behind of the organism.

**Keywords:** Quiet Swimming, Acartia Tonsa locomotion, Dynamic Masking, Particle Image Velocimetry

## 1. Introduction

*Acartia Tonsa* (*A. Tonsa*) nauplius (Figure 1) is sub-millimeter sized juvenile plankton species that thrives in most estuaries. From a locomotion point of view, it is a “puller” type swimmer that is known to perform breaststrokes. *A. Tonsa* nauplius locomotion technique is achieved using two pairs of appendages pulling two breaststrokes per cycle; first with the lateral pair, followed by the anterior pair. The shorter third pair in the posterior does not actively participate in propulsion, but mostly in steering. The two breaststrokes (i.e. the power strokes) are followed by a recovery stroke where both appendage pairs are pulled back in position to perform a new cycle [1]. There are certain advantages that come with breaststroke swimming, one of which is to achieve quiet swimming mode [2]. The flow disturbances produced by breaststroke like kinematics are shown to decay faster compared to dipole swimmers, i.e. with the inverse of distance cubed [2]. The result is a reduced detection possibility both by predators and by prey. For *A. Tonsa* nauplii, this means better feeding possibilities during initial stages of life without risking too much of becoming a meal for larger aquatic animals. This implies that a larger number of juveniles will reach the adult stages to reproduce. In short, the locomotion behavior adapted by the juveniles can define how that species will thrive in the aquatic environment.

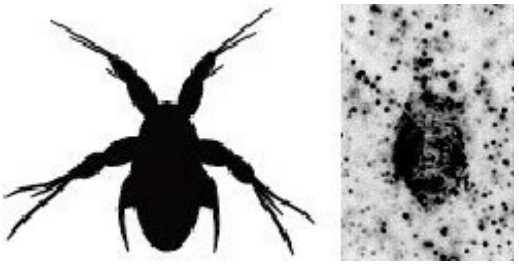

Figure 1: Schematic of A. Tonsa nauplius during a power stroke. From Ref. [1]

## 2. Experiments

Copepods Acartia Tonsa were cultured at 18°C and before experiments they were transferred to the test aquarium containing filtered seawater. Only a few individuals were transferred to avoid possible interactions between them. The test aquarium is a glass cuvette (10x10x40mm) placed on a horizontal stage and kept at room temperature, between 18°C and 20°C. The measurement setup is a long-distance Micro Particle Image Velocimetry (LDμPIV) system in which the light sheet propagation direction and the camera viewing direction are perpendicular to each other. In biological flows, high-power visible laser illumination is often not preferred as this can disable the organism, or it can affect the normal locomotion behavior of the organism. For these reasons, a low- power, continuous-wave infrared laser (Oxford Lasers Ltd, 808nm wavelength) was used for illumination. Sheet forming optics was assembled to produce a 150μm thick light sheet, defining the measurement depth of the experiments. TiO2 seeding particles smaller than 2μm were introduced in small quantities until a sufficient seeding density was achieved. The particle images were recorded on a high-speed CMOS detector (Phantom v210, Vision Research Inc.) at a frame rate of 2000 fps and at a resolution of 1280 × 800 pixels. The images were acquired with 11.65× magnification producing a 2.2 mm × 1.4mm field of view (FoV). Single frame image acquisition was performed with a constant time difference of 500μs between frames. Since the FoV was only approximately 3mm2, the images were stored in a ring buffer and a manual trigger stopped the acquisition after the organism had passed through the FoV.

Consecutive frames were analyzed for PIV processing - quite typical for time-resolved PIV measurements: 65 frames were analyzed to produce 64 flow field measurements, and 63 of these are used to perform phase locked averaging over 3 cycles. During the acquisition, a ~220μm-long A. Tonsa propels itself upwards through filtered seawater by pulling three breaststrokes, covering a vertical distance of 666μm (Average swim speed of 22 mm/s). It is observed that Acartia Tonsa moves in an almost-vertical straight line and its angular orientation does not change significantly. The image pre-processing, dynamic masking and PIV computations were performed using DynamicStudio software (Dantec Dynamics, Skovlunde, Denmark).

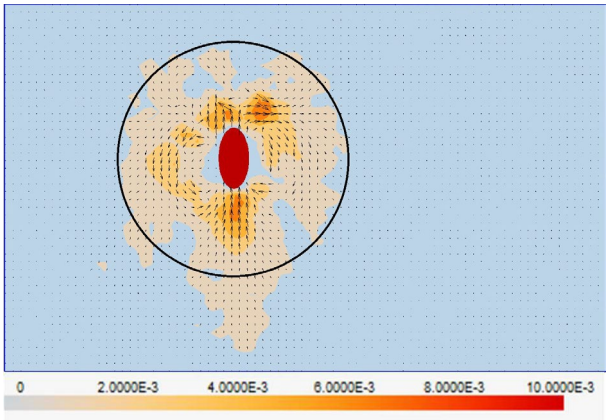


Figure 2: The time-resolved disturbance flow field around A. Tonsa nauplius. Black circle indicate the disturbance sphere during an upward power stroke. Colors indicate disturbance magnitude with values in m/s.

## 3. Results

The results indicate that the time-resolved disturbance flow fields can reach up to 1.5 body lengths around the Acartia Tonsa, leaving even a longer wake behind of the organism.

## References

[1] N. Wadhwa, A. Andersen, and T. Kiorboe, "Hydrodynamics and energetics of jumping copepod nauplii and copepodids," *J. Exp. Biol.*, vol. 217, no. 17, pp. 3085–3094, Sep. 2014, doi: 10.1242/jeb.105676.

[2] A. Andersen, N. Wadhwa, and T. Kiørboe, "Quiet swimming at low Reynolds number," *Phys. Rev. E*, vol. 91, no. 4, p. 042712, Apr. 2015, doi: 10.1103/PhysRevE.91.042712.

# Effect of Cell Concentration and Viscosity on the Margination of White Blood Cells (WBCs) in a Passive Microfluidic Device

Dhiren MOHAPATRA[1,*], Rahul PURWAR[2], Amit AGRAWAL[1]

1: Department of Mechanical Engineering, IIT Bombay, Powai, Mumbai-400076, India
2: Department of Biosciences & Bioengineering, IIT Bombay, Powai, Mumbai-400076, India

* Corresponding author: Tel.: +91 7735907012; Email: dhiren@iitb.ac.in

**Abstract:** WBCs are essential in resisting and removing infection-causing foreign factors such as viruses, bacteria, and fungi. These are indicators of various diseases, including inflammatory disorders, cancer, and allergies. In addition, applications like drug trials, viral load determination, and DNA sequencing need highly enriched WBCs for analysis. Passive microfluidic devices offer an edge in this field since they process samples accurately and quickly, which is essential for diagnosis. Compared to the existing ineffective conventional approaches, they are easy, affordable, and effective. So to get a pure, highly enriched sample, increased WBCs margination must be maintained in the channel's focusing plane. Out of several parameters on which the margination of WBCs depends, we've analyzed the effect of cell concentration and viscosity in a bifurcated rectangular channel inertial flow. We diluted the sample using PBS and viscoelastic fluid to vary the viscosity and cell concentration. WBC margination was analyzed in terms of enrichment to viscosities and dilution factors. It may be established that WBC margination is mostly determined by cell-cell interaction in the focusing zone. At low and high viscosity, the margination is hardly impacted. Regulating the blood sample's viscosity and fostering more cell-cell interaction in the focusing zone can maximize WBC margination.

**Keywords:** WBC, Margination, Enrichment, Viscosity, Viscoelastic, Microdevice, Passive, Hydrodynamic

# A Microfluidic Device based on Bubble Generation as an Organ-on-Chip Model

Beyzanur ÖZOGUL[1], Rabia MERCIMEK[2], Morteza GHORBANI[3,*], Ali KOŞAR[4,#]

1: Department of Molecular Biology, Genetics and Bioengineering, Sabanci University, Istanbul, TR
2: Department of Material Science and Nanoengineering, Sabanci University, Istanbul, TR
3: Faculty of Engineering and Natural Sciences, Sabanci University, Istanbul, TR
4: Center of Excellence for Functional Surfaces and Interfaces, EFSUN, Sabanci University, Istanbul, TR

* Corresponding author: Tel.: +905513998366; Email: morteza.ghorbani@sabanciuniv.edu
# Corresponding author: Tel.: +905325541543; Email: ali.kosar@sabanciuniv.edu

**Abstract:** Cavitation is a fast, energy-efficient, and emerging method for biomedical applications. With the developments in microfluidic technology, it has become easier to manipulate, visualize and analyze cavitation bubbles forming in functional microfluidic devices. In this sense, cavitation could be an alternative concept in the organ-on-chip studies. Clot or coagulation factors as the organ representative could cause dangerous and even fatal diseases in the presence of excess amount in the body. Although their treatment is usually accomplished with chemical drugs, there is a need for alternative treatment because of related side effects and inadequacies. In this study, a microfluidic system based on cavitation suitable for clot analysis is suggested to examine the clot characteristics. Our study is thus a pioneering study in the assessment of the effect of cavitation on clots.

**Keywords:** Cavitation, Microfluidics, Organ-on-a-Chip, Cavitation Assisted Catheter, Computational Fluid Dynamics (CFD)

## 1. Introduction

Pulmonary embolism (PE) and deep vein thrombosis (DVT) are two kinds of venous thromboembolism (VTE), which affect 1 to 2 in 1,000 individuals each year and is one of the major causes of vascular death after myocardial infarction and stroke [1]. DVT most commonly arises in the deep veins of the leg, groin, or arm in the peripheral circulation. When a blood clot travels through the circulation and becomes lodged in the pulmonary trunk, main pulmonary artery, or segmental or sub-segmental branches it might cause PE. Systemic thrombolysis using tissue-type plasminogen activator (t-PA) pharmacological dissolution, catheter-directed thrombolysis, or surgical removal could be used for high-risk PE patients [2]. Existing treatment approaches lead to disadvantages such as limited thrombolytic effectiveness, frequent bleeding problems, a high failure rate, vein injury-associated severe regional dysfunction, high recurrence rates, and the danger of distant embolism due to clot debris of an extremely large size [3]. To address the limitations of standard therapeutic approaches, ultrasound-aided thrombolysis is proposed as an alternate therapy modality [4]. During sonothrombolysis, cavitation was found to mechanically destroy the clot [5]. Among the ultrasound-assisted thrombolysis approaches, catheter-delivered transducer-tipped ultrasound has proven to be particularly beneficial [6]. Because low-power waves cannot disintegrate clots, this approach is used in conjunction with t-PA and/or microbubbles [7,8].

Cavitation is a physical phenomenon that happens when a liquid is pushed to flow at high speeds in a restricted channel or nozzle, where a sudden pressure reduction is triggered, thereby causing microscopic bubbles or cavities to develop and burst. The collapsing of bubbles

results in shock waves, microjets, shear forces, and pressure gradients in the microenvironment around the bubble [9]. Recent studies on biomedical applications of micro scale cavitation revealed the potential of cavitation to ablate ill tissue [10,11]. In this regard, it is believed that micro-scale cavitation could be a considerably more efficient approach in thrombolysis compared to acoustic cavitation (AC) due to its low energy consumption and efficiency. Due to promising results of cavitation in microfluidic devices related to biomedical applications and recent findings on the role of surface roughness in the generation of facile cavitating flows, the use of cavitation in organ-on-chip studies could pave the way for clot on a chip (COC) application.

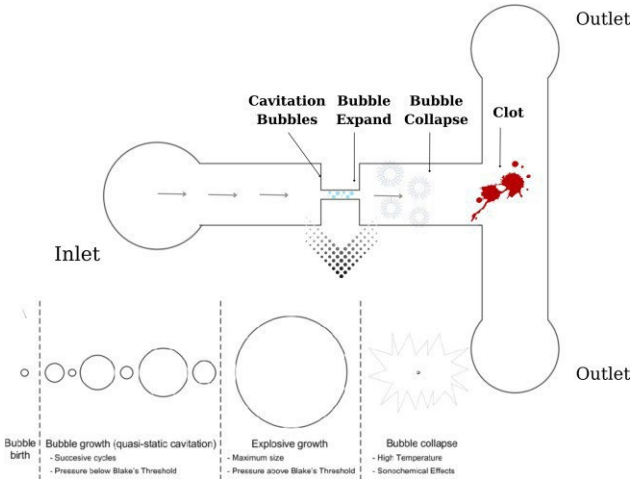


**Figure 1:** Single microchannel device configurations with an integrated COC platform

Microfluidic cavitation on a chip system was designed to study the mechanical properties of the clot and to analyze the effect of cavitation on the clot. This system mechanism is summarized in Fig. 1. The working fluid is supplied from the inlet at a constant inlet pressure. Cavitating flow forms in the microchannel and is targeted to the clot at the exit so that it destroys the clot. In Fig. 2, one of our previous studies, cavitating flow formed on the single channel microfluidic device is given.

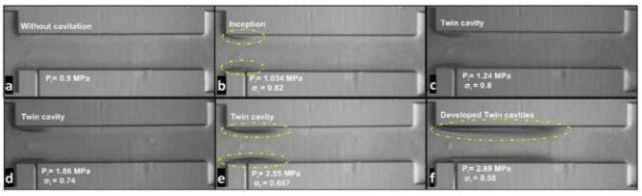


**Figure 2:** The cavitating flow regimes inside the microchannel [12]

In conclusion, the findings of this study will aid in the development of new technologies for drug-free catheter-directed thrombolysis prototypes and will increase the understanding of HC-induced thrombolysis in micro-scale.

## References

1) Fleck, D., Albadawi, H., Shamoun, F., Knuttinen, G., Naidu, S., & Oklu, R. (2017). *Catheter-directed thrombolysis of deep vein thrombosis: literature review and practice considerations.* Cardiovascular Diagnosis and Therapy, 7(S3), S228–S237. doi:10.21037/cdt.2017.09.15
2) Yamamoto, T. (2018). *Management of patients with high-risk pulmonary embolism: a narrative review. Journal of Intensive Care, 6(1).* doi:10.1186/s40560-018-0286-8
3) Wright, R. S., Reeder, G. S., Herzog, C. A., Albright, R. C., Williams, B. A., Dvorak, D. L., … Jaffe, A. S. (2002). *Acute Myocardial Infarction and Renal Dysfunction: A High-Risk Combination.* Annals of Internal Medicine, 137(7), 563. doi:10.7326/0003-4819-137-7-200210010-00007
4) Dixon, A. J., Rickel, J. M. R., Shin, B. D., Klibanov, A. L., & Hossack, J. A. (2017). *In Vitro Sonothrombolysis Enhancement by Transiently Stable Microbubbles Produced by a Flow-Focusing Microfluidic Device. Annals of Biomedical Engineering, 46(2), 222–232.* doi:10.1007/s10439-017-1965-7
5) Weiss, H. L., Selvaraj, P., Okita, K., Matsumoto, Y., Voie, A., Hoelscher, T., & Szeri, A. J. (2013). *Mechanical clot damage from cavitation during sonothrombolysis.* The Journal of the

Acoustical Society of America, 133(5), 3159–3175. doi:10.1121/1.4795774

6) Kim, J., Lindsey, B. D., Chang, W.-Y., Dai, X., Stavas, J. M., Dayton, P. A., & Jiang, X. (2017). *Intravascular forward-looking ultrasound transducers for microbubble-mediated sonothrombolysis. Scientific Reports, 7(1).* doi:10.1038/s41598-017-03492-4
7) Lee, H., Kim, H., Han, H., Lee, M., Lee, S., Yoo, H., … Kim, H. (2017*). Microbubbles used for contrast enhanced ultrasound and theragnosis: a review of principles to applications*. Biomedical Engineering Letters, 7(2), 59–69. doi:10.1007/s13534-017-0016-5
8) Dixon, A. J., Li, J., Rickel, J.-M. R., Klibanov, A. L., Zuo, Z., & Hossack, J. A. (2019). *Efficacy of Sonothrombolysis Using Microbubbles Produced by a Catheter-Based Microfluidic Device in a Rat Model of Ischemic Stroke.* Annals of Biomedical Engineering. doi:10.1007/s10439-019-02209-0
9) Filipić, A., Lukežič, T., Bačnik, K., Ravnikar, M., Ješelnik, M., Košir, T., Petkovšek, M., Zupanc, M., Dular, M., & Aguirre, I. G. (2022). *Hydrodynamic cavitation efficiently inactivates potato virus Y in water.* Ultrasonics Sonochemistry, *82*, 105898. https://doi.org/10.1016/j.ultsonch.2021.105898
10) Perk, O. Y., Sesen, M., Gozuacik, D., & Kosar, A. (2012). *Kidney Stone Erosion by Micro Scale Hydrodynamic Cavitation and Consequent Kidney Stone Treatment.* Annals of Biomedical Engineering, 40(9), 1895–1902. doi:10.1007/s10439-012-0559-7
11) Itah, Z., Oral, O., Perk, O. Y., Sesen, M., Demir, E., Erbil, S., … Gozuacik, D. (2013). *Hydrodynamic cavitation kills prostate cells and ablates benign prostatic hyperplasia tissue.* Experimental Biology and Medicine, 238(11), 1242–1250. doi:10.1177/1535370213503273
12) Rokhsar Talabazar, F. *et al.* (2022) "Chemical effects in 'hydrodynamic cavitation on a chip': The role of cavitating flow patterns," *Chemical Engineering Journal*, 445, p. 136734. Available at: https://doi.org/10.1016/j.cej.2022.136734.

# A closed-loop PCR-performing microdevice on PCB for ultra-fast DNA amplification

Panagiotis SKALTSOUNIS[1,2,*], George KOKKORIS[1,3] , Theodoros G PAPAIOANNOU[2], Angeliki TSEREPI[1]

1: Institute of Nanoscience and Nanotechnology, NCSR "Demokritos", Patriarchou Gregoriou & 27 Neapoleos str., 153 41 Aghia Paraskevi, GR
2: School of Medicine, National and Kapodistrian University of Athens, 75 Mikras Asias str., 115 27 Athens, GR
3: School of Chemical Engineering, National Technical University of Athens, Zografou, 157 80 Athens, GR

* Corresponding author: Tel.: +30 210 650 3237; Email: p.skaltsounis@inn.demokritos.gr

**Abstract:** The development of a closed-loop (CL) microdevice performing polymerase chain reaction (PCR) is reported herein. Compared to other types of continuous flow μPCR, the CL-μPCR uses a circular microchannel, allowing the DNA sample to pass consecutively through the different temperature zones, as many times as necessary for efficient DNA amplification. In this work, the performance of a CL-μPCR designed for fabrication on a printed circuit board (PCB) is evaluated by a computational study. PCB constitutes a great substrate as it allows for low-cost, reliable, reproducible, and mass-amenable chip fabrication incorporating microheaters. A 3D heat transfer model is used to calculate the temperature distribution in the chip, and the residence times in each thermal zone are extracted. The results of the computational study suggest a well-performing microreactor, in which a PCR of 30 cycles can be achieved in less than 3 min. The designed CL-μPCR is realized on PCB for the first time in the literature and is tested by measuring the temperatures on its surface with a thermal camera; The results are compared with those of the computational study. Finally, an on-chip peristaltic micropump is developed serving sample circulation in the microchannel, while DNA amplification is evaluated off-chip.

**Keywords:** MicroPCR, Closed-Loop, Printed Circuit Board, Computational Study, Point of Care systems

## 1. Introduction

Amplification of the genetic material (RNA, DNA) is a crucial step for sensitive and reliable pathogen identification, thus placing recently much emphasis on the development of diagnostic microdevices that accommodate amplification of the genetic material at the point of care [1]. Performance of PCR in microscale devices (μPCRs) promises potential advantages and new possibilities which include reagent and fabrication cost reduction, faster reaction times, portability, high automation, and integration.

Although continuous flow (CF) μPCRs exhibit great advantages (reduced thermal inertia and thus faster temperature changes, reduced reaction times and lower energy costs), some drawbacks have also emerged. Due to the long channel length, a large pressure difference is developed that requires very strong sealing of the microchannel to prevent leakage [2]. Further limitations include the fixed number of PCR cycles, dictated by the channel layout, as well as the relatively large reactor footprint. To overcome these drawbacks, an advantageous type of CF μPCR has been proposed, namely the closed-loop (CL) μPCR [3,4]. In this microdevice, the DNA sample flows through a circular microchannel passing consecutively through the temperature zones (Fig. 1) as many times as necessary in order to accomplish efficient DNA amplification. The aim of the current work is to upgrade CL-μPCRs through a) use of PCBs as substrate material, b) an improved design for very fast and efficient PCR, and c) development of an on-chip peristaltic pump for sample circulation.

## 2. Results and Discussion

### 2.1 Design and computational study

A well-performing CL-μPCR microdevice is sought through a computational study. Fig. 1 shows the design of the microdevice, comprising a circular microchannel on a PCB chip with integrated microheaters. The chip has a circular disk shape, with an external diameter of 40 mm and a 20 mm diameter hole in the

center. Three distinct temperature zones are shown, each zone corresponding to one of the three PCR steps. The circular microchannel is formed on the top of the PCB substrate and allows the sample to move through the different temperature zones. The microchannel is 100 μm deep, 1 mm wide, and 94.25 mm long. The chip is covered with a 50 μm-thick transparent layer of polyolefin, which will allow, in the future, for real-time optical monitoring of the amplification. The temperature zones are defined with copper microheaters, integrated into the PCB. The microheaters (25 μm-thick and 100 μm-wide) are used only for the denaturation and extension temperature zones (needing active heating), while the annealing zone is designed to let the sample cool naturally by releasing heat into the environment. On top of each temperature zone and exactly under the circular microchannel, a solid copper layer is used to improve the uniformity of the temperature zone. Through holes of elliptical shape are designed between the temperature zones, to ensure better thermal insulation and minimize thermal cross-talk.

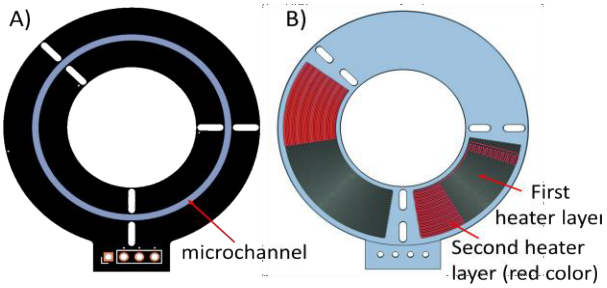


**Fig. 1.** A) Microdevice geometry. The circular microchannel is placed on top of the PCB chip. B) Interior of the chip. Two heater layers are formed.

The chip geometry (Fig. 1) is chosen appropriately for the device to perform 1:1:2 PCR protocols. In addition, at the beginning of each temperature zone, the microheaters are formed in two copper layers, so as to provide more heat to the specific areas, in order to achieve faster the desired sample temperature and reduce the transition time. This novel two-layer microheater design aims to optimize the PCR protocol by reducing the non-functional time in every cycle and is realized for the first time in a μPCR.

The temperature distribution and the residence times at each thermal zone are calculated by a 3D heat transfer model, and the effect of operating conditions on the speed of the PCR are investigated. Different cycle times (and thus volumetric flow rates) are examined; the aim is to seek the lowest time limits in which the microdevice can operate, providing an extension residence time (ERT) of at least 1.8 s, which is the minimum acceptable ERT in this study. The computations show that the microdevice can complete one PCR cycle in 5.7 s, which is equivalent to a total reaction time (30 cycles) of less than 3 min (171 s).

### 2.2 Chip fabrication and thermal evaluation

The designed microreactor is fabricated on a PCB substrate. The results obtained from the computational study are compared with the actual temperature distributions (Fig. 3) measured by means of a thermal camera, on the surface of the fabricated chip, verifying the accuracy of the developed model.

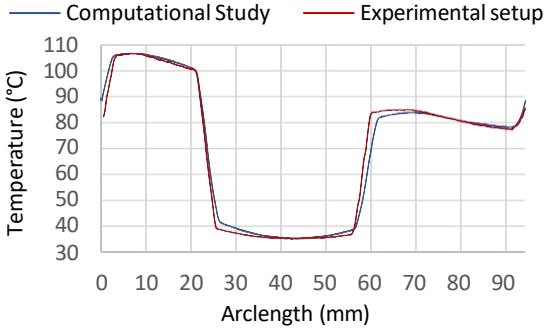


**Fig. 2.** Comparison of the temperature profiles calculated in the computational study and measured on the fabricated chip surface, along the microchannel periphery. No sample movement is considered in this case.

### 2.3 Sample circulation

Finally, an on-chip peristaltic micropump is developed serving sample circulation in the microchannel, while DNA amplification is evaluated off-chip.

[1] Mejía-Salazar, J.R. et *al.*, Microfluidic point-of-care devices: New trends and future prospects for ehealth diagnostics. *Sensors* **2020**, *20*, 1951.

[2] Kaprou, G.D. et *al.*, Ultrafast, low-power, PCB manufacturable, continuous-flow microdevice for DNA amplification. *Anal. Bioanal. Chem.* **2019**, *411*, 5297–5307.

[3] Sun, Y. et *al.*, A circular ferrofluid driven microchip for rapid polymerase chain reaction. *Lab Chip* **2007**, *7*, 1012–1017.

[4] Skaltsounis, P. et *al.*, Closed-Loop Microreactor on PCB for Ultra-Fast DNA Amplification: Design and Thermal Validation. *Micromachines* **2023**, 14, 172.

## SESSION 5a
## MINI SYMPOSIUM
## Phase field approaches to modeling multiphase micro-flows
Chair: **Prof. R. Mauri**

# Phase Separation of a Binary Mixture with an External Force Field

Roberto MAURI[1,*] and Antonio BERTEI[1]

1: Lab. of Multiphase Reactive Flow, DICI - University of Pisa, Italy

* Corresponding author: Email: roberto.mauri@unipi.it

**Abstract:** Here we simulate the phase separation of a regular binary mixture in the presence of an external force field. In general, when a partially miscible binary mixture is brought from the stable, single-phase region of its phase diagram to the unstable region, it separates into two coexisting phases, corresponding to a minimum of the free energy of the mixture. As the mass of each chemical species is conserved, phase transition consists of a reordering process, called spinodal decomposition.
Now, assume that an external force field is applied to the mixture, and that its effects on the species composing the mixture are different from each other. For example, the force field can be gravity or an electric field, applied to a mixture of fluids having different properties. In all these cases, the external force will enhance demixing: for example, gravity will tend to increase the concentration of the heavier species in the bottom of the container. Here we show that the non-homogeneity of the composition field induced by the external field may cause, locally, a phase transition even when, globally, the system is in a metastable, and even a stable, thermodynamic condition.

**Keywords:** Phase field approach, Phase transition, Microfluidics

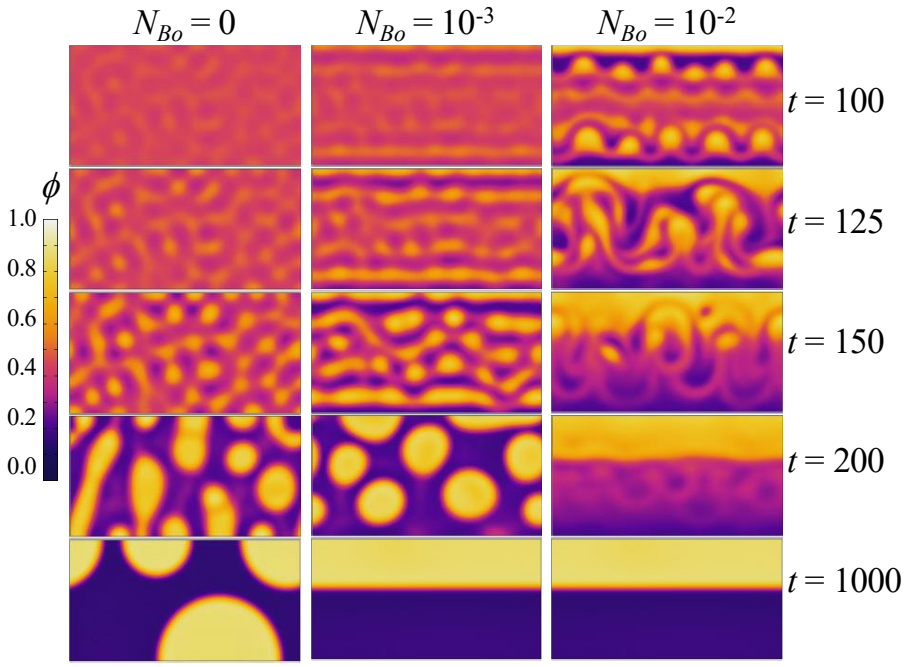


Phase separation in the presence of an external force for a mixture within the unstable region ($\phi_0 = 0.45$, $2/\Psi = 0.80$). Maps of the temporal evolution of mass fraction of species 1, $\phi$, which is preferentially pushed upward by the external force.

# Turbulence-controlled evolution of particle patterns on the interface of large deformable drops

Cristian MARCHIOLI[1,*], Arash HAJISHARIFI[1], Alfredo SOLDATI[2]

1: Dept. Engineering and Architecture, University of Udine, 33100 Udine, Italy
2: Institute of Fluid Mechanics and Heat Transfer, TU Wien, 1060 Wien, Austria

* Corresponding author: Tel.: +39 0432 558006; Email: marchioli@uniud.it

**Abstract:** We examine the interaction between a swarm of small (sub-Kolmogorov) inertial particles and large deformable droplets in turbulent channel flow. To simulate such solid-liquid-liquid flow, we exploit an Eulerian-Lagrangian methodology based on direct numerical simulation of turbulence, coupled with a Phase Field Model to capture the interface dynamics and Lagrangian tracking to compute particle trajectories. We quantify particle-interface interaction in a situation where the droplets have the same density and viscosity of the carrier liquid (mimicking a water-oil emulsion), and particles are one-way coupled with the carrier phase. Our results show that particles can get trapped at the interface and accumulate in the regions of highest positive curvature. Accumulation is modulated by particle inertia: low-inertia particles exhibit a stronger tendency to stay on the interface, whereas high-inertia particles can escape more easily and after shorter trapping.

**Keywords:** Turbulence, Surface Tension, Multiphase Flows

## 1. Introduction

A large variety of systems involves the adsorption of solid particles to the fluid interface between droplets/bubbles and a carrier liquid. Surface tension drives particle adhesion, thus forming a layer that may change the mechanical and mass transport properties of the interface. Important industrial applications where such phenomenon occurs include scrubbing processes, in which large liquid droplets are exploited to collect dust particles; froth flotation processes, in which particle adsorption to bubbles is essential for separating minerals from the slurry.Most of three-phase computational models available in the literature have been used to study the dynamics of a single particle trapped at a planar fluid interface, or the surface stress tensor modification for a pendant drop covered by a monolayer of particles in the low-Reynolds-number limit. Only recently, a multiscale DEM-VOF method was developed to reproduce droplet formation and interface perturbations from a single particle. In this paper, we perform a DNS (Direct Numerical Simulation)-based study of a three-phase turbulent flow in which a solid phase (particles) and a liquid phase (deformable droplets) are transported by a carrier phase (fluid). Specifically, we investigate the interaction between the particles and the droplets in a channel flow configuration. We consider particles with different size to investigate such interaction at varying particle inertia.

## 2. Methodology

The computational approach is based on DNS of the Continuity, Navier-Stokes and Cahn-Hilliard equations and on the solution of a Lagrangian equation of particle motion stemming from the balance of the forces acting on the particles (drag force and surface tension force, in the present study). The flow solver is based on a pseudo-spectral method that transforms the field variables into wave space to discretize the governing equations. In the homogeneous directions, all the quantities are expressed by Fourier expansions. In the wall-normal non-homogeneous direction, they are represented by Chebychev polynomials. The time integration algorithm follows an implicit/explicit scheme. All calculations

relative to Continuity, Navier-Stokes and Cahn-Hilliard equations are carried out in wave space except for the non-linear terms, which are computed in the physical space and then transformed back to wave space.
Particle tracking is performed in the physical space. The particle-interface interaction is modeled by considering a capillary force related to the liquid-liquid surface tension. This capillary force is exerted on the particles when they are close to the interface, and acts to push the particles towards the interface and capture them there. In other words, the force provides a potential well that drives particle accumulation at the interface, which acts as particle adsorber.

## 3 Results

In this paper we show results relative to friction Reynolds number $Re=150$ based on the channel half height $h$ (the channel dimensions being $4\pi h \times 2\pi h \times 2h$ in the streamwise, spanwise and wall-normal directions, respectively), Weber number $We=0.75$ (ratio between inertial forces and surface tension), Cahn number $Ch=0.02$ (dimensionless interface thickness), Péclet number $Pe=50$ (ratio between diffusive timescale and convective timescale) and particle friction Stokes numbers $St=0.1, 0.2, 0.4$ and $0.8$. For sake of brevity, we will show results for the $St=0.8$ particles only.
In our framework, particle accumulation is higher (resp. lower) for the lower-inertia (resp. higher-inertia) particles. The capillary force acting on the particles depends on the surface tension and on the local curvature of the droplet interface. The former changes with surface composition/temperature, remaining constant when these do not vary (as assumed in our simulations). Hence, the only parameter that can change the magnitude of the capillary force is the local curvature: The capillary force is stronger in regions with higher curvature.
While trapped within the interface, particles tend to move towards the regions of highest positive curvature. This sampling is observed for all particle sets, and appears modulated by particle inertia. Our results show that inertia provides particles with a way to escape from the interface and reduce the time window over which particles interact with the interface. Low-inertia particles are found to accumulate at higher rates and are able to stay longer in close proximity of the droplet interface.
Once trapped there, these particles exhibit the strongest tendency to collect in regions characterized by highly-positive values of the curvature, as shown qualitatively in Fig. 1. Indeed, the regions of long-term trapping and high particle concentration correlate well with portions of the interface characterized by higher-than-mean curvature. This finding is important since the presence of tiny particles at the interface is known to affect locally the surface tension, particularly in the presence of concentration gradients: present results suggest that particle-induced modifications of the surface tension should be stronger where the curvature of the interface is higher.

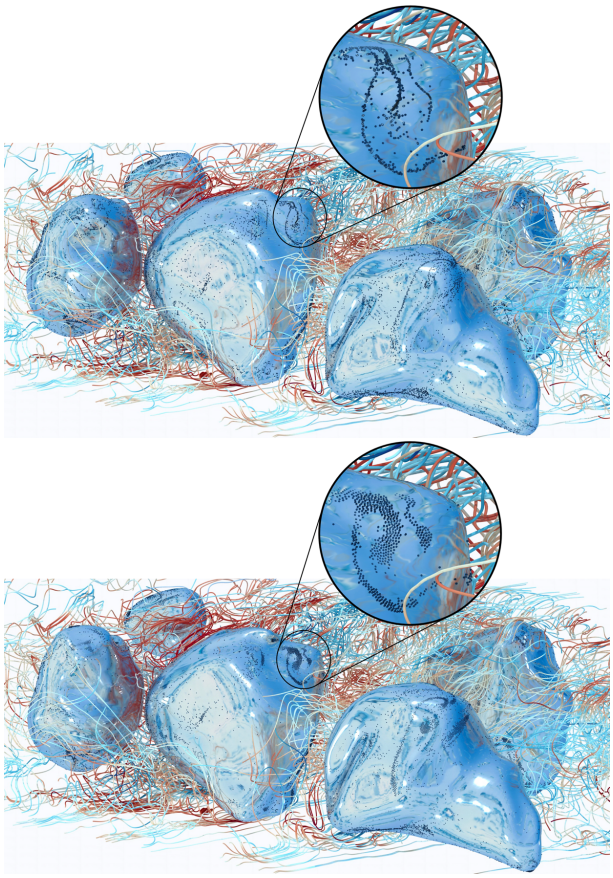

Figure 1: Snapshot of $St=0.1$ particle distribution on the drop surface. Non-interacting trapped particles form highly-concentrated filamentary clusters (top), but appear more evenly distributed when excluded-volume e ects are accounted for (bottom).

# The nucleation process and its coupling to the macroscale

Mirko GALLO[1], Francesco MAGALETTI[2], Carlo Massimo CASCIOLA[1,*]

1: Department of Mechanical and Aerospace Engineering, Sapienza University of Rome, IT
2: University of Brighton, UK

* Corresponding author: Tel.: +39 44585201; Email: Carlomassimo.casciola@uniroma1.it

**Abstract:** When the pressure falls below a critical level (cavitation) or the temperature raises above a threshold (boiling), the liquid-vapor transition takes place. Here we discuss a comprehensive model able to provide a unified description of the different phenomenologies described above. The model is based on the capillary Navier-Stokes equation where the liquid-vapor interface is treated by a diffuse interface model. In order to describe nucleation, a noise term is included (fluctuating hydrodynamics) leading to a system of stochastic partial differential equations able of describing the nucleation of vapor cavities from the liquid in the context of continuum mechanics.

**Keywords:** Bubble nucleation, Fluctuating Hydrodynamics, Phase Field Method.

## 1. Introduction

When the pressure falls below a critical level (cavitation) or the temperature raises above a threshold (boiling), the liquid-vapor transition takes place. The process starts with the nucleation phase, a rare event that is deeply rooted in the atomistic nature of the fluid. Successively, depending on the local thermodynamic conditions, the bubble may grow to the macroscopic size to couple with the inertial dynamics of the surrounding fluid.

In the classical approach, each phase is treated separately. Classical Nucleation Theory (CNT) deals with the nucleation rate (number of bubbles formed per unit of time and volume). Once the bubble is formed, the celebrated Rayleigh-Plesset equation, or extensions therein, is classically used to describe the bubble dynamics. After reviewing the state of the art in the field, the purpose of the talk is to discuss a comprehensive model able to provide a unified description of the different phenomenologies described above.

## 2. Nucleation Modelling

The model is based on the capillary Navier-Stokes equation where the liquid-vapor interface is treated by a diffuse interface model accounting for the relevant thermodynamic properties of the fluid (e.g., equation of state, phase change, and latent heat). In order to describe the nucleation phase, a noise term is included (fluctuating hydrodynamics) leading to a system of stochastic partial differential equations with the unique capability of describing the nucleation of vapor cavities from the liquid in the context of continuum mechanics. Several examples of numerical solutions will be illustrated, including bubble collapse in free space and near solid walls and their homogenous and heterogeneous nucleation in different geometries. New results concerning nucleation and bubble dynamics in a flowing liquid will also be presented to finally touch upon the rare event techniques aimed at accurately extracting the cavitation pressure for actual water in a wide range of temperatures.

# Bibliography

Magaletti, Gallo, CMC, Water Cavitation From Ambient to High Temperature, Scientific Reports 2021.
Gallo, Magaletti, CMC, Heterogeneous bubble nucleation dynamics", Journal of Fluid Mechanics 2021.
Gallo, Magaletti, Cocco, CMC, Nucleation and growth dynamics of vapor bubbles, Journal of Fluid Mechanics 2019.
Gallo, Magaletti, CMC, Thermally activated vapor bubble nucleation: the Landau-Lifshitz/Van der Waals approach", Phys. Rev. Fluids. 2018.

# Phase field simulations for solid-state dewetting with anisotropic surface energies

Harald GARCKE[1,*], Patrik KNOPF[1,*], Robert NÜRNBERG[2,*], Quan ZHAO[1,*]

1: Fakultat für Mathematik, Universitat Regensburg, 93053 Regensburg, Germany
2: Dipartimento di Mathematica, Università di Trento, 38123 Trento, Italy

* Corresponding author: Email: harald.garcke@ur.de; patrik.knopf@ur.de; robert.nurnberg@unitn.it; quan.zhao@ur.de)

**Abstract:** We present a diffuse-interface model for the solid-state dewetting problem with ani- sotropic surface energies. The introduced model consists of the anisotropic Cahn– Hilliard equation, with either a smooth or a double-obstacle potential, together with a degenerate mobility function and appropriate boundary conditions on the wall. Upon regularizing the introduced diffuse-interface model, and with the help of suitable asymptotic expansions, we recover as the sharp-interface limit the anisotropic sur- face diffusion flow for the interface together with an anisotropic Young's law and a zero-flux condition at the contact line of the interface with a fixed external boundary. Numerical results based on an appropriate finite element approximation are presented to demonstrate the excellent agreement between the proposed diffuse-interface model and its sharp-interface limit.

**Keywords:** Solid-state dewetting, phase field model, Cahn–Hilliard equation, anisotropy, finite element method.

## 1. Introduction

Deposited solid thin films are unstable and could dewet to form isolated islands on the substrate in order to minimize the total surface energy. This phenomenon is known as solid-state dewetting (SSD), since the thin films remain in a solid state during the process. SSD has attracted a lot of attention recently, and is emerging as a promising route to produce patterns of arrays of particles used in sensor technology, optical and magnetic devices, and catalyst formations.

The dominant mass transport mechanism in SSD is surface diffusion. For (isotropic) surface diffusion, the normal velocity of the interface is proportional to the surface Laplacian of the mean curvature. In the case of SSD the evolution of the interface that separates the thin film from the surrounding vapor also involves the motion of the contact line, i.e., the region where the film/vapor interface meets the substrate. The equilibrium contact angle is given by Young's law which prescribes a force balance along the substrate.

In this work, we aim to study the SSD problem with anisotropic surface energies in the diffuse-interface framework. In the isotropic case, diffuse-interface models are based on the Ginzburg–Landau energy

$$\mathcal{E}_{iso}(\varphi) = \int_\Omega \frac{\varepsilon}{2}|\nabla\varphi|^2 + \varepsilon^{-1}F(\varphi)\,\mathrm{d}x, \quad (1)$$

where $\Omega \subset \mathrm{R}^d$ is a given domain with $d \in \{2, 3\}$, $\varphi : \Omega \to \mathrm{R}$ is the order parameter, $\varepsilon > 0$ is a small parameter proportional to the thickness of the interfacial layer, and $F(\varphi)$ is the free energy density. A natural generalization of the free energy (1) to the case of anisotropic surface energies is given by

$$\begin{aligned}\mathcal{E}_\gamma(\varphi) &= \int_\Omega \frac{\varepsilon}{2}|\gamma(\nabla\varphi)|^2 + \varepsilon^{-1}F(\varphi)\,\mathrm{d}x \\ &= \int_\Omega \varepsilon A(\nabla\varphi) + \varepsilon^{-1}F(\varphi)\,\mathrm{d}x.\end{aligned} \quad (2)$$

Here, $\gamma : \mathrm{R}^d \to [0, \infty)$ is the anisotropic density function, which is positively homogeneous of degree one, and $A := \frac{1}{2}\gamma^2$. This then gives rise to the anisotropic Cahn–Hilliard equation

$$\begin{aligned} \partial_t \varphi &= \nabla \cdot (m(\varphi)\nabla\mu), \\ \mu &= -\varepsilon \nabla \cdot A'(\nabla\varphi) + \varepsilon^{-1} F'(\varphi), \end{aligned} \tag{3}$$

where $A'$ represents the gradient of the map $A : \mathrm{R}^d \to [0, \infty)$.

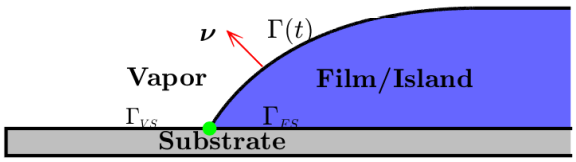


Figure 1: Sketch of the structure for SSD near the contact line (green point), where the vapor, film and substrate phases meet.

When it comes to SSD, as shown in Fig. 1, the total surface energy of the system consists of the film/vapor interface energy $\mathrm{E}_{inf}$ and the substrate energy $\mathrm{E}_{sub}$

$$\begin{aligned} \mathcal{E}_{inf} &= \int_{\Gamma(t)} \gamma(\boldsymbol{\nu}) \, \mathrm{d}S, \\ \mathcal{E}_{sub} &= \gamma_{FS} \int_{\Gamma_{FS}} \mathrm{d}S + \gamma_{VS} \int_{\Gamma_{VS}} \mathrm{d}S, \end{aligned} \tag{4}$$

where $\Gamma(t)$ is the dynamic film/vapor interface with $\boldsymbol{\nu}$ being the interface normal point- ing into the vapor phase, $\Gamma_{FS}$ and $\Gamma_{VS}$ are the interfaces between film/substrate and vapor/substrate, respectively, and $\gamma_{FS}$ and $\gamma_{VS}$ are the corresponding surface energy densities. In order to model SSD by the diffuse-interface approach, we associate the vapor phase with $\varphi \approx 1$ and the film phase with $\varphi \approx -1$. Then the Ginzburg–Landau type energy (2), up to a multiplicative constant, will approximate the sharp interface energy $\mathrm{E}_{inf}$. Moreover, the contribution to the wall energy $\mathrm{E}_{sub}$ can be approximated by

$$\begin{aligned} \mathcal{E}_w(\varphi) = &\int_{\Gamma_{FS} \cup \Gamma_{VS}} \frac{\gamma_{VS} + \gamma_{FS}}{2} \\ &+ (\gamma_{VS} - \gamma_{FS}) G(\varphi) \, \mathrm{d}S, \end{aligned} \tag{5}$$

where $G(\varphi)$ is a smooth function satisfying $G(\pm 1) = \pm 1/2$.

The main aim of this talk is to develop a diffuse-interface approach to SSD in the case

of anisotropic surface energies based on the energy contributions (2) and (5). The obtained diffuse-interface model consists of a degenerate anisotropic Cahn–Hilliard equation with appropriate boundary conditions. We study the sharp-interface limit and introduce a fully practical finite element approximation. The latter is exploited for several numerical tests, including a detailed comparison between sharp-interface approximations and diffuse-interface approximations

# Phase-Field models in Materials Science

Ingo STEINBACH[1,*]

1: Ruhr-University Bochum, Germany

* Corresponding author: Email: ingo.steinbach@rub.de

**Abstract:** "Phase Field" is a general concept of solving free boundary problems in applied science. It routs in hydrodynamic wave mechanics as well as in thermodynamics. The hydrodynamic rout bases on the Korteveg de-Fries equation for the description of shallow water waves, leading to a self-similar solution nowadays known as "solitonean wave". The thermodynamic route bases on Ginsburg- Landau description of phase transformation, where the "phase-field" is an order parameter in space and time.
The basic concepts and early numerical application have been worked out in the 1990th. Nowadays applications range from solidification over solid state transformation to materials degradation and fracture. Since the method mainly addresses microstructure evolution and phase transformations, fluid flow is not in its primary focus. There are, however, self-interacting mechanisms between fluid flow on the micro- and nano-scale and phase transformation, in particular solidification and melting: Solidification stops melt flow, melt flow may stop solidification. Ripening of solid particles is accelerated by melt flow which leads to a change of scaling in time. Hydrophilic or hydrophobic surfaces may cause or suppress micro-flows.
The talk will review shortly the historical background of "Phase Field" and demonstrate current applications in materials science with special focus to micro-flows.

**Keywords:** Phase Field, Solidification, Capillarity

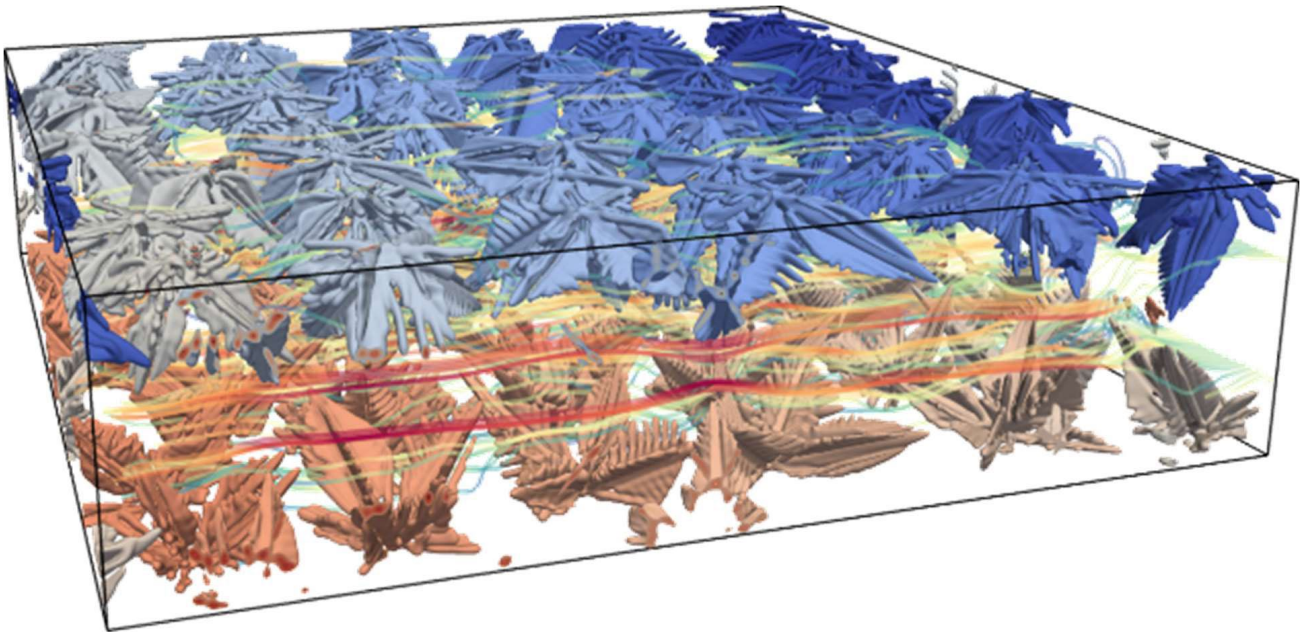

Figure: Dendritic solidification of MgAl with interdendritic melt flow

## SESSION 5b
## MINI SYMPOSIUM
## Contact line dynamics in heterogeneous environments
Chair: **N. Savva**



Nikos SAVVA[1]
1: Computation-based Science and Technology Research Center, The Cyprus Institute, Nicosia 2121, Cyprus



Ahlem MOKHTARI[1], Stefano LANDINI[1], Jack PANTER[1], Yogesh BHALERAO[1], Alexandros ASKOUNIS[1]
1: School of Engineering, University of East Anglia, UK



Marc PRADAS[1], Michael EWETOLA[1,2], Matthew HAYNES[1,3], and Rodrigo LEDESMA-AGUILAR[4]

1: School of Mathematics and Statistics, The Open University, Milton Keynes, UK
2: Department of Mathematics, University College London, London, UK 3: Bader College, Queen's University (Canada), Hailsham, UK
4: Institute for Multiscale Thermofluids, University of Edinburgh, Edinburgh, UK



Panayiotis-Yiannis VRIONIS[1], Nikos SAVVA[1]

1: Computation-based Science and Technology Research Center, The Cyprus Institute, Nicosia, 2121, Cyprus

# Asymptotic Methods for Reduced-order Modelling of Partially Wetting Droplets

Nikos SAVVA[1,*]

1: Computation-based Science and Technology Research Center, The Cyprus Institute, Nicosia 2121, Cyprus

* Corresponding author: Email: n.savva@cyi.ac.cy

**Abstract:** We consider the slow dynamics of an isolated thin droplet moving on heterogeneous surfaces, as described within the long-wave limit of the Stokes regime. Using matched asymptotics, we show that by considering regular perturbations from a nearly circular contact line and matching the flow in the vicinity of the drop with that of the bulk, it is possible to derive a simpler set of evolution equations for the Fourier coefficients of the contact line. Numerical experiments highlight the generally excellent agreement between the governing long-wave model and the derived equations. We also demonstrate that reduced-order model is also able to capture many of the salient features, which characterize the intricate interplay between substrate heterogeneities and the complexity in the environment, and how these impact the motion of the droplet.

**Keywords:** Wetting, Contact Lines, Droplets

## 1. Introduction

Long-wave modelling approaches for droplet dynamics, which are applicable for slow-moving droplets on hydrophilic surfaces, have been commonly employed to mitigate the computing costs associated with direct numerical simulations of the Navier Stokes equations. In this manner, the relevant parameter spaces can be more efficiently scanned for gaining physical insights, as well as for guiding experimental efforts.

However, simulating long-wave models, which typically consist of evolution equations for the droplet thickness and other pertinent fields, is also challenging due to numerical stiffness which is attributed to the presence of some microscopic scale that is introduced to alleviate the stress singularity in the vicinity of the contact line [1]. For example, models with a disjoining pressure depend on the precursor film thickness, just as the slip length appears in slip-based models. For this reason, numerical experiments are typically being carried out for unrealistically large values for this microscale.

Initial attempts to investigate the behavior of long-wave models began long before computer simulations were feasible through the pioneering works of Lacey [2] and Hocking [3], who utilized the method of matched asymptotic expansions to deduce simplified models for the evolution of the contact line. Since then, many authors provided extensions of these studies to account for different levels of complexity, but only recently non-circular contact line shapes were considered by Savva and co-workers, through an accurate and efficient methodology which is able to tackle the fully three-dimensional geometry [4,5].

## 2. Outline of analysis

In order to briefly highlight the key elements of the analysis, we focus on partially wetting droplets spreading on a heated, smooth, horizontal and chemically heterogeneous surface. The droplet consists of a one-component volatile liquid that evaporates into its own vapor, so that the problem reduces into a so-called one-sided model for the thickness of the droplet, $h$, as a function of position $\boldsymbol{x}$ and time $t$, which is cast in dimensionless form as

$$h_t + \boldsymbol{\nabla} \cdot [h(h^2 + \lambda^2)\boldsymbol{\nabla}\Delta h] = -\frac{E}{h + K},$$

where $\lambda$ is the slip length, $E$ is the evaporation number which is proportional to the difference of the substrate temperature from the saturation temperature, and $K$ is the kinetic resistance which compares the scale of kinetic effects to

some macroscopic scale; $\Delta$ and $\boldsymbol{\nabla}$ are the usual Laplace and gradient operators, respectively [6]. To close the system, extra conditions are imposed at the contact line, $\boldsymbol{x} = \boldsymbol{c}(t)$, namely

$$(\boldsymbol{c}_t - \lambda^2 \boldsymbol{\nabla}\Delta h) \cdot \boldsymbol{\nu} = -\frac{E}{\theta K},$$
$$h = 0, \qquad |\nabla h| = \theta,$$

where $\theta$ is the (locally) prescribed contact angle along the contact line, and $\boldsymbol{\nu}$ is the outward unit normal to the contact line.

There are four distinct regimes in the dynamics characterized in terms of the parameter $\varepsilon = 1/|\ln \lambda| \ll 1$ as $\lambda \to 0$: (i) the capillary action for $t = O(1)$, during which the droplet profile relaxes to a quasi-equilibrium shape, (ii) the spreading stage $t = O(1/\varepsilon)$, during which the droplet front moves without appreciable mass loss, (iii) the evaporation stage $t = O(\varepsilon/\lambda)$, during which the droplet loses $O(1)$ mass, and (iv) the extinction stage when $t \gg O(\varepsilon/\lambda)$, during which the droplet becomes so small that separation of scales is no longer possible. Stages (i) and (iv) are neglected due to their brief duration, deriving evolution equations for the contact line during stage (ii) and for the volume, $v(t)$, during stage (iii).

During stage (ii), the dynamics is assumed to be quasi-steady and the solution is treated differently away from the contact line (outer region) with that of its vicinity (inner region), where due to evaporation, the free surface bends to some evaporation-modified angle, $\vartheta_e$. Then, by matching these solutions within some overlap region, equations for the Fourier harmonics of $\boldsymbol{c}(t)$ are obtained. For the evolution of $v(t)$ during stage (iii), we assume that the apparent angle (from the outer region) tends to $\vartheta_e$ which allows us to obtain an integral expression for the rate of change of $v(t)$.

## 2. Results and discussion

Although the evolution equations for $\boldsymbol{c}(t)$ and $v(t)$ pertain to different stages of the dynamics, we have consistently found that combining them into a single model captures the dynamics well for all times. This is illustrated in Fig. 1, where we show a droplet evaporating on eggbox-like heterogeneous features. We see that the reduced-order model accurately captures the dynamics of the governing model, but requires a tiny fraction of the computational resources compared to the full model.

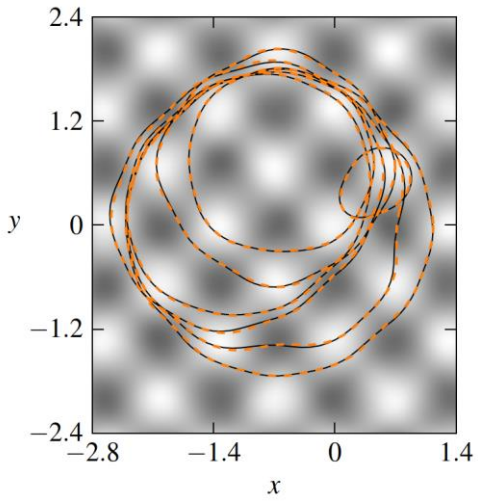


Fig 1: Evaporation of a droplet on an eggbox-like pattern with noise, comparing the solution to the long-wave model (solid) and its surrogate (dashed).

## Acknowledgements

The author acknowledges the support from the European Union's Horizon 2020 research and innovation programme under grant agreement No 810660 and from the Cyprus Research and Innovation Foundation under contract No. EXCELLENCE/0421/0504.

## References

[1] Bonn, D., Eggers, J., Indekeu, J., Meunier, J, Rolley, E., 2009. Wetting and spreading. *Rev. Mod. Phys.*, 81(2), 739-805.

[2] Lacey, A.A., 1982. The motion with slip of a thin viscous droplet over a solid surface. *Stud. Appl. Math.*, *67*(3), 217-230.

[3] Hocking, L. M. 1983 The spreading of a thin drop by gravity and capillarity. *Q. J. Mech. Appl. Maths* 36 (1), 55–69.

[4] Savva, N., Groves, D., Kalliadasis, S., 2019, Droplet dynamics on chemically heterogeneous substrates. *J. Fluid Mech.* 859, 321-361.

[5] Savva, N., Groves D. 2021, Droplet motion on chemically heterogeneous substrates with mass transfer. II. Three-dimensional dynamics. *Phys. Rev. Fluids*, 6, 123602.

[6] Savva, N., Rednikov, A., Colinet, P. 2017, Asymptotic analysis of the evaporation dynamics of partially wetting droplets. *J. Fluid Mech.* 824, 574–623.

# Inclination effect on the internal flows and evaporation kinetics of droplets

Ahlem MOKHTARI[1], Stefano LANDINI[1], Jack PANTER[1], Yogesh BHALERAO[1], Alexandros ASKOUNIS[1,*]
1: School of Engineering, University of East Anglia, UK
* Corresponding author: Tel.:01603592850; Email: a.askounis@uea.ac.uk

**Abstract**: Manipulating microfluidic flows inside evaporating sessile droplets deposited on horizontal substrates had been widely studied for more than twenty years. Briefly described here, the evaporative flux peaks at the pinned contact line and causes a strong mass loss due to evaporation, the mass loss is compensated by an outgoing radial flow directed from the apex to the pinned contact line. Despite the universality of drops deposited on tilted substrates the study of the evaporation kinetics and the resulting internal flows has not received much attention. Our numerical model studies the evaporation kinetics and internal flows of droplet at an incline. It was found that a small angle of inclination has a non-negligible effect on the evaporative flux. Although, the internal flow was totally distorted to compensate the asymmetrical evaporation.

**Keywords:** internal flow, droplets, evaporation, two phase flow, gravity.

## 1. Introduction

In many practical situations droplets dry on a slope, in solar panels, during spray coating, pectizing, printing and in crime scenes. Some researchers state that the deformed shape of the droplet under gravity effect has a negligible impact on the evaporation flux and evaporation kinetics [1], [2]. While others state that the distorted shape of the droplets affects the evaporation process [3], [4]. To our best knowledge there exist no numerical study that simulate internal flows inside inclined evaporating droplets. A COMSOL model is implemented to solve simultaneously the droplet deformation due to gravity and the phase change induced by evaporation. In this work an unsteady 2D numerical model for evaporating sessile droplet on an inclined substrate was simulated, while the interface location and the droplet deformation due to gravity was predicted at each time step.

## 2. Mathematical model

Equations for momentum, energy and vapor transport are solved in fluid and solid phases.

$$\frac{\partial U}{\partial t} + \vec{\nabla} \cdot \vec{U} = 0 \quad (1)$$

$$\frac{\partial U}{\partial t} + \rho(\mathrm{U}^{\rightarrow} \cdot \nabla^{\rightarrow})\vec{U} = -\vec{\nabla} P + \mu \Delta \vec{U} + \rho\, g \quad (2)$$

$$\frac{\partial T}{\partial t} + \gamma\, \vec{U} \cdot \vec{\nabla} T = \alpha_T \Delta \mathrm{T} \quad (3)$$

U and T are the velocity vector and temperature, respectively, $\gamma$ : is a coefficient equal to 0 in solid phase and 1 in fluid phases, g refers to gravity, $\mu^{\rightarrow}$is fluid viscosity, $\alpha_T$ is the

thermal diffusivity, and $\rho$ is phase density.
vapor transport equation is written as:

$$\frac{\partial C}{\partial t} + \vec{U} \cdot \vec{\nabla} C = D\, \Delta C \quad (4)$$

C is the vapor concentration; D is the diffusion coefficient of water vapor in ambient air (D = 25 $mm^2/s$).
At liquid-air interface

$$T_l = T_g \quad (5)$$

$$J\, h_{\mathrm{lg}} - q_l \cdot \mathrm{n} + q_g \cdot \mathrm{n} = 0 \quad (6)$$

$q = -k\nabla T$is the heat flux and $h_{lg}$ is the latent heat of evaporation.
Saturation concentration of vapor at the droplet interface is given by C(T)= $\sum_0^i a_i T^i$, The coefficients $a_i$are chosen to fit experimental data of Raznjevic [5]. Far from the droplet the vapor concentration is given by RH C(T), where RH is relative humidity.
mass continuity is given by:

$$\rho_l(U_l - U_I) \cdot n = \rho_g\left(U_g - U_I\right) \cdot n = J \cdot n \quad (7)$$

$\vec{\mathrm{n}}$is a normal unit vector, l an g denotes gas and liquid , $\vec{U}_I$ is the velocity of the moving interface, and J is the local evaporation flux evaluated by:

$$J = \vec{J} \cdot \vec{n} = -D\vec{\nabla} C \cdot \vec{n} \quad (8)$$

The stress at the liquid air interface must be balanced by:

$$\left[(n\bar{\bar{\tau}})_l - (n\bar{\bar{\tau}})_g\right] \cdot t = \nabla\sigma \cdot t \quad (9)$$

$$\left[(n\bar{\bar{\tau}})_l - (n\bar{\bar{\tau}})_g\right] \cdot n = -\nabla\sigma \cdot n \quad (10)$$

$\vec{t}$ and $\vec{n}$ are tangential and normal unit vector, $\sigma$: is the surface tension and $\tau = -PI + \mu[\nabla U + (\nabla U)^T]$ is the stress tensor. Velocity non-slip condition is applied between liquid and gas particles at the interface. The arbitrary Lagrangian–Eulerian (ALE) method is used to track the interface location at every time step, the numerical procedure is described in [6].

## 3. Model Validation

The model is validated against the numerical model of Mollaret and al [7] , and showed an excellent agreement between experimental and our numerical results.

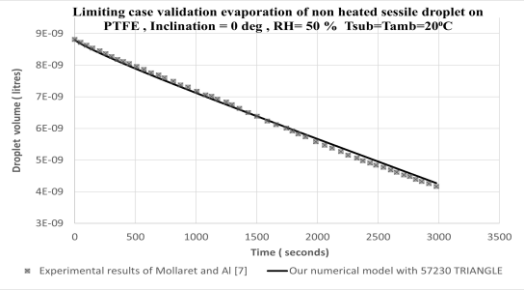


Fig 01a: experimental validation, droplet deposited on a horizontal substrate.


Fig 01b: ALE predicted (orange) and measured droplet profile, R=2.67 mm, contact angle: 20 deg, inclination: 40 deg, time = 1 s

## 4. Results

Results are for a water droplet with radius R=2.67 mm and initial contact angle 40 deg.

Figure 02 shows the evaporative flux of a sessile droplet on a horizontal substrate (the right side), and an inclined substrate with five-degree inclination (left side). The evaporative flux is more pronounced near the pinned contact line, since the droplet is thinner in this area. Moreover, the inclination affects the distribution of the evaporative flux at the rear contact angle and enhances the evaporative flux by 8%. The internal flow inside the horizontal is symmetrical and radial from the center of the droplet at the apex x= -2.67 mm to the contact line. But when at an incline, the flow is no longer symmetrical. This is explained by the fact that the evaporative flux is stronger at the rear contact angle. Thus, the liquid required to compensate the mass loss is unevenly distributed inside the droplet, which reflect the flow pattern.

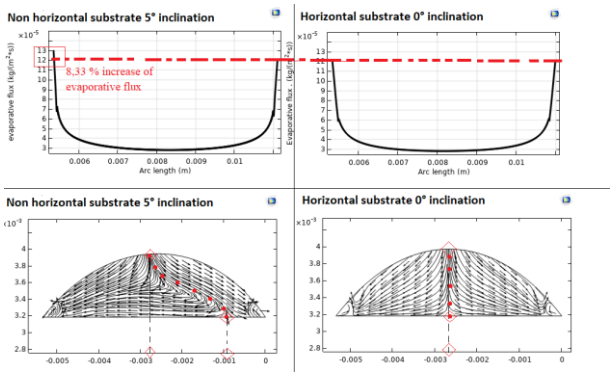


Figure 02: Top row: evaporative flux of a horizontal (right) and inclined (left) droplet. Bottom row: Internal flow field. Dashed line shows deflection due to symmetry (black) and inclination (red).

## 5. Conclusion

The evaporation phenomena and internal flow of pinned sessile droplet on inclined substrate was successfully simulated. The effect of inclination on the evaporative flux was pronounced at the rear contact angle. We showed that a small increase of the inclination only $5^o$ results in an asymmetrical evaporative flux at the two sides. These results clarify the controversial in the existing literature and confirm that the slope angle has a significant effect on the evaporation kinetics. Also, the internal flow reflects favorable convection toward the rear contact angle.

## References

**[1]** J. Y. Kim, I. G. Hwang, et Al,, 'Evaporation of inclined water droplets', Sci. Rep., vol. 7, no. 1, Art. no. 1, Feb. 2017.
**[2]** V. Charitatos, et Al ,'Droplet evaporation on inclined substrates', *Phys. Rev. Fluids*, vol. 6, no. 8, p. 084001, Aug. 2021
**[3]** P. Dhar, R et Al , 'Surface declination governed asymmetric sessile droplet evaporation', *Phys. Fluids*, vol. 32, no. 11, p. 112010, Nov. 2020
**[4]** X. Du and R. D. Deegan, 'Ring formation on an inclined surface', J. Fluid Mech., vol. 775, p. R3, Jul. 2015.
**[5]** K. Raznjevic 1995 Handbook of Thermodynamic Tables, Begell House, New York.
**[6]** Achim Bender, et Al, A fully coupled numerical model for deposit formation from evaporating urea-water drops, IJHMT,Volume 159, 2020.
**[7]** R. Mollaret, et Al, 'Experimental and Numerical Investigation of the Evaporation into Air of a Drop on a Heated Surface', Chem. Eng. Res. Des., vol. 82, no. 4, pp. 471–480, Apr. 2004.

# Dynamics of droplets evaporating on smooth patterns

Marc PRADAS[1,*], Michael EWETOLA[1,2], Matthew HAYNES[1,3], and Rodrigo LEDESMA-AGUILAR[4]

1: School of Mathematics and Statistics, The Open University, Milton Keynes, UK
2: Department of Mathematics, University College London, London, UK
3: Bader College, Queen's University (Canada), Hailsham, UK
4: Institute for Multiscale Thermofluids, University of Edinburgh, Edinburgh, UK

* Corresponding author: Email: marc.pradas@open.ac.uk

**Abstract**: We study the problem of droplet dynamics on patterned surfaces. We focus on droplets subjected to an external driving process that changes the droplet's volume, such as evaporation or microfluidic flow, and consider solid surfaces with smooth chemical variations. In our previous work, we reported the emergence of a hierarchy of bifurcation points arising when a droplet evaporates on smooth patterns. Building upon these results, here we use a combination of theory and simulations to study the dynamics of droplets through such bifurcation points, and how it depends on the physical properties of the system quantified in terms of the Ohnesorge and Bond numbers. Our results show that the interplay between a phase change and surface wettability can be exploited to control the motion of droplets on patterned solids.

**Keywords:** Droplet dynamics, smooth patterns, diffuse-interface modelling, bifurcation analysis

## 1. Introduction

Controlling droplet transport and localisation on structured solid surfaces is important for key technologies, such as liquid-repellent surfaces, microchemical reactors, and micro- and nano-fluidic systems. Consequently, considerable effort has been devoted to designing solid surfaces that enhance/inhibit wetting [1], control droplet's contact area [2], and direct droplet's motion [3,4].

Droplets that are subjected to external, time-dependent variations, such as evaporation and condensation, exhibit complex dynamics that strongly depends on the interaction with the solid surface [5]. Recently, we have shown that the shape and location of a droplet that is slowly evaporating on a smooth wettability pattern undergo changes due to surface instabilities. These arise from a hierarchy of bifurcations as the volume $V(t)$ of the droplet decreases [6,7]. At each bifurcation point, the stability changes so the droplet must change its shape and position $s(t)$ as dictated by the underlying solid pattern (Fig. 1a). The bifurcation diagram consists of connected branches that change stability at specific volumes (Fig. 1b), producing a rapid lateral shift (Fig. 1c).

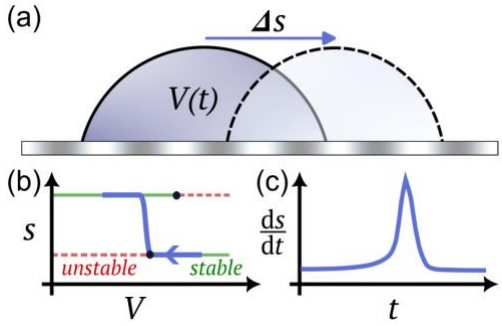


**Fig. 1.** (a) Droplet lateral displacement $\Delta s$ triggered by a bifurcation point as the volume $V$ decreases (b), leading to a sudden increase in droplet's speed (c).

Here, we study the dynamics of droplets undergoing bifurcation transitions and how it depends on the different physical mechanisms (capillarity, viscosity, inertia, and gravity). As a model system, we consider the problem of a 2D droplet slowly evaporating on an inclined plane with periodic wetting patterns (Fig. 2).

## 2. Mathematical modelling

For a given area $A$ the equilibrium state of the droplet is quantified by the total energy

$$E[h(x);A] = \int_a^b \left(\sqrt{1+h_x^2} - \cos\Theta\right) dx + Bo \int_a^b \left(xh\sin\alpha + \frac{h}{2}\cos\alpha\right) dx,$$

where $h(x)$ is the droplet's interface, $\Theta(x)$ is the wetting pattern, $Bo$ is the Bond number, and $\alpha$ is the inclination angle (see Fig. 2). By analysing the extrema of the energy for different droplet's areas, we construct the corresponding bifurcation diagram.

The dynamics of the droplet is studied by solving numerically the Cahn-Hilliard and Navier-Stokes system of equations:

$$\frac{D\boldsymbol{u}}{Dt} = -\boldsymbol{\nabla}\mathrm{p} + \frac{1}{Re}\nabla^2\boldsymbol{u} - \frac{1}{We}\,\phi\boldsymbol{\nabla}\eta + \frac{Bo}{We}\rho(\phi)\boldsymbol{g},$$

$$\frac{\partial\phi}{\partial t} + \boldsymbol{u}\cdot\boldsymbol{\nabla}\phi = \frac{1}{Pe}\nabla^2\eta,$$

where $\boldsymbol{u}(\boldsymbol{r},t)$ is the velocity field, $p(\boldsymbol{r},t)$ is the pressure, $\phi(\boldsymbol{r},t)$ is the phase field, $\rho(\phi)$ is the density of the two-phase system, and $\eta(\boldsymbol{r},t)$ is the chemical potential. $Re$, $We$, $Pe$, are the Reynolds, Weber, and Peclet numbers, respectively. We impose an open flux boundary that drives evaporation, and at the solid surface we impose a Neumann boundary condition for the phase field that models the wetting pattern [7].

## 3. Results

We first examine the limiting case of small Bond number and perform asymptotic analysis to obtain approximate solutions. For higher Bond numbers we derive exact solutions written in terms of elliptic integrals that can be solved numerically. We show in turn that gravity affects the topology of the bifurcation diagrams, reducing the stability regions of the phase space.

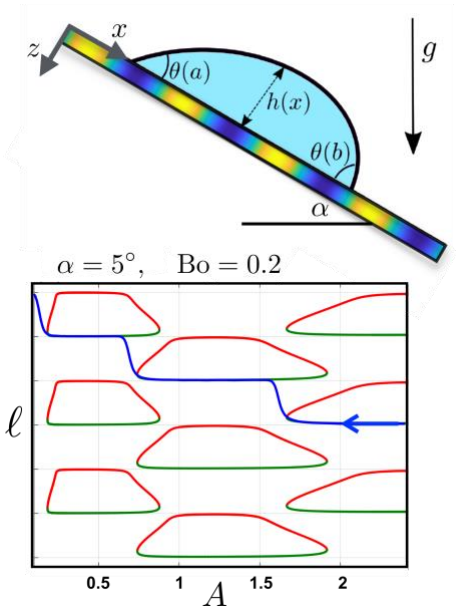


**Fig. 2.** 2D droplet resting on an inclined plane with a wetting pattern (top). Bottom panel shows the bifurcation diagram of droplet's displacement versus area compared to diffuse-interface simulations of a droplet evaporating (blue line).

The bottom panel of Fig. 2 shows an example of a bifurcation diagram for a symmetric wetting pattern, where red and green lines denote saddle nodes and stable points, respectively. The blue solid line shows the corresponding dynamic simulation of a droplet evaporating. We can see that the droplet position follows very closely the stable branches predicted by the bifurcation theory.

We also consider asymmetric patterns that naturally induce directed motion on the droplet, observing there is a competition between gravity and the wetting pattern in determining a droplet's direction of motion upon evaporation.

## References

[1] Quéré, *Annu. Rev. Mater. Res.* **38,** 2008.
[2] Raj *et al.*, *Nature Commun.* **5**, 2014.
[3] Savva *et al.*, *J. Fluid Mech.* **859,** 2019.
[4] Sadullah *et al.*, *Commun. Phys.* **3**, 2020.
[5] Zang *et al.*, *Phys. Rep.* **804**, 2019.
[6] Wells *et al.*, *Nature Commun.* **9**, 2018.
[7] Ewetola *et al.*, *Phys. Rev. Fluid.* **6**, 2021.

# Towards a flexible, highly-scalable, general-purpose thin film solver

Panayiotis-Yiannis VRIONIS[1,*], Nikos SAVVA[1]

1: Computation-based Science and Technology Research Center, The Cyprus Institute, Nicosia, 2121, Cyprus

* Corresponding author: Email: p.y.vrionis@cyi.ac.cy

**Abstract:** Simulation-driven studies of wetting and dewetting phenomena are commonly used to gain insight into their underlying mechanisms. We present a highly scalable, general-purpose thin fluid flow solver that can perform complex simulations of isolated or multiple droplets in the presence of complexity. The solver is based on the long-wave or lubrication approximation, and utilizes mesh adaptation techniques and a multigrid method to solve the governing fourth order non-linear partial differential equation that describes the thickness of the droplet. The solver's capabilities are demonstrated with representative cases, which include multiple droplet dynamics on heterogeneous surfaces and in the presence of thermal effects, body forces and electric fields.

**Keywords:** Contact lines, Thin film flows, Long-wave approximation

## 1. Introduction

Thin film flows commonly occur in everyday life, appearing in natural and engineered settings and thus, attracted significant interest and research efforts. invoked for the study of wetting hydrodynamics, particularly in the limit of small contact angles. However, these phenomena are complex and challenging to study due to their multi-scale and multi-physics nature, as the dynamics is influenced by multiple factors. These include, amongst others, substrate heterogeneities, thermal effects, body forces, the presence of electric fields, interactions with nearby droplets etc. Hence, the development of accurate and efficient numerical simulation tools can assist in understanding the underlying physics governing applications in which controllable droplet transport plays a key role.

In this work, we present a scalable, flexible, and general-purpose thin film solver that is valid in the limit of small contact angles. It can be extended to incorporate various effects and complexities, offering a compelling alternative to arguably more expensive direct numerical simulations. Our approach utilizes the Basilisk library [1], an open-source generic solver for partial differential equations (PDEs) based on multigrid methods. The library also allows for the use of mesh adaptation techniques, which is a desirable feature for accurately capturing the dynamics in the vicinity of the contact line.

## 2. Mathematical model

Herein, we consider thin droplets as they move over heterogeneous surfaces. In the limit of small slopes, strong surface tension effects, and negligible inertia, a PDE is derived Stokes equations using the long-wave approximation [2], which governs the evolution of the droplet profile $h$ at position $\vec{x}$ and time $t$, cast in dimensionless form as

$$\frac{\partial h}{\partial t} + \vec{\nabla} \cdot \{h^3 [\nabla (\Delta h - \Pi(\vec{x}, h)) - w_1(t)\vec{\nabla} h + w_2(t)\vec{e}_{x_1}]\} + \mathcal{J}(h) = 0, \quad (1)$$

with $\vec{e}_{x_1}$ being the unit vector projection of gravity onto the substrate and $\vec{\nabla}$, $\Delta = \vec{\nabla} \cdot \vec{\nabla}$ the gradient and Laplace operators, respectively.

The stress singularity at the moving contact line is relaxed by assuming that a precursor film covers the entire substrate through a spatially varying disjoining pressure term, $\Pi(\vec{x}, h)$,

which models substrate heterogeneities and molecular attractive and repulsive forces [2]. Body forces, which may be due to gravity or mechanical vibrations, introduce the additional terms $w_1(t)$ and $w_2(t)$ [3]. The last term, $\mathcal{J}(h)$, captures evaporation/condensation effects [4].

## 3. Illustrative examples

The developed framework enables the simulation of a broad range of thin fluid flows in different settings. These include droplets that interact both with the complexity in their environment and with each other, allowing us to efficiently study the underlying mechanisms. In the following, two simulations of multiple droplets are presented, influenced by different complexities. For simplicity, periodic boundary conditions are applied to both examples.

The first example presented also showcases the mesh adaptation capabilities of the solver, shown in Figure 1. The case is described by multiple droplets descending on an inclined surface with spatially varying contact angles. Here, interesting dynamics is observed, such as stick-slip and coalescence events, induced by the competition of heterogeneities slowing down the smaller droplets and gravity which makes larger droplets move faster.

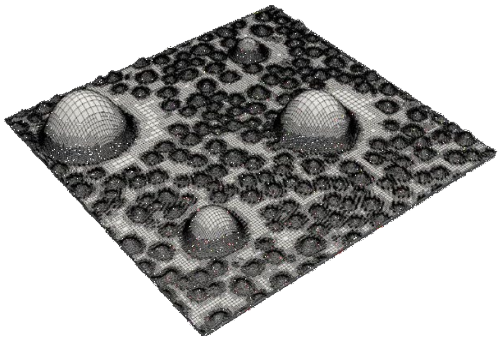

Figure 1. Adaptive mesh for droplets on an inclined surface, which is automatically coarsened away from

In the second example, we study the case of multiple droplets condensing on an inclined surface decorated with noisy striped features of alternating higher/lower wettability. The substrate is oriented at an angle to the downhill direction (Figure 2). In this example, droplets preferentially condense on the higher wettability regions, which then grow faster, coalesce with their neighbours and flow downhill due to gravity.

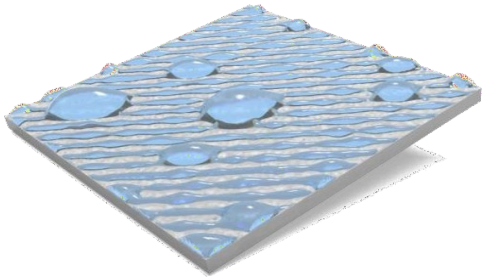

Figure 2. Simulation snapshot of condensing droplets on an inclined surface, which is decorated with stripes of alternating wettability. For clarity, the precursor film is not shown.

## Acknowledgements

The authors acknowledge the support from the European Union's Horizon 2020 research and innovation programme under grant agreement Innovation Foundation under contract No. EXCELLENCE/0421/0504.

## References

[1] S. Popinet, "An accurate adaptive solver for surface-tension-driven interfacial flows," Journal of Computational Physics, vol. 228, no. 16, pp. 5838-5866, 2009.
[2] D. Bonn, J. Eggers, J. Indekeu, J. Meunier and E. Rolley, "Wetting and spreading," Reviews of Modern Physics, vol. 81, no. 2, p. 739, 2009.
[3] U. Thiele, L. Brusch, M. Bestehorn and B. Markus, "Modelling thin-film dewetting on structured substrates and templates: Bifurcation analysis and numerical simulations," The European Physical Journal E, vol. 11, pp. 255-271, 2003.
[4] N. Savva and S. Kalliadasis, "Low-frequency vibrations of two-dimensional droplets on heterogeneous substrates," Journal of fluid mechanics, vol. 754, pp. 515-549, 2014.
[5] T. Pham and S. Kumar, "Drying of droplets of colloidal suspensions on rough substrates," Langmuir, vol. 33, no. 38, pp. 10061-10076, 2017.

## SESSION 5c
## Heat exchangers and reactors
Chair: **P. Di Marco**

# The Other Side of Micro – Rational Considerations for Implementation in Microscale Heat Transfer Devices

Matthew T. HUGHES[1], Girish KINI[2], Srinivas GARIMELLA[1,*]

1: Sustainable Thermal Systems Laboratory, GWW School of Mechanical Engineering, Georgia Institute of Technology, Atlanta, GA 30332
2: Advanced Micro Devices (AMD), 7171 Southwest Pkwy, Austin, TX 78735

* Corresponding author: Tel.: +1-404-894-7479; Email: sgarimella@gatech.edu;

**Abstract:** Microchannel heat exchangers offer significant advantages in terms of high heat transfer coefficients and surface area-to-volume ratios. However, when heat exchange is desired between fluids with disparate thermal capacities and properties, the dominant thermal resistance places upper bounds on the utility of microscale heat transfer. For example, decreasing the channel size to values below certain thresholds provides diminishing returns, and even worse, could significantly increase parasitic losses. Therefore, this study develops guidelines for the applicability and effectiveness of microscale geometries for a variety of applications for liquid-to- liquid, liquid-to-phase-change, liquid-to-air, phase-change-to-air, and other combinations. Microchannel diameters for representative examples of such transfer processes are analyzed and optimal ranges are recommended. This is achieved by calculating the single-phase and phase-change heat transfer coefficients for media with a range of transport properties and channel diameters. These microscale transfer resistances are then paired with the thermal resistances of different coupling fluids with representative surface area enhancements as needed to assess the effectiveness of microchannels for typical air-coupled and liquid- coupled heat exchangers. These results are then distilled into microchannel applicability maps based on the thermal resistance ratios, allowable pressure drop limits, fan/pumping power, and footprint to provide recommendations to guide designers of microchannel-based devices.

**Keywords:** Microchannels, Heat-exchangers, single-phase, two-phase

## 1. Introduction

Heat transfer and fluid flow in microchannels has been a large topic of interest the past few decades due to its large potential to miniaturize thermal systems and ability to reject heat at high fluxes [1]. However, these advantages may not be realized in practical heat exchangers because heat exchange is, by definition, between two fluids with each thermal resistance contributing to the determination of heat exchanger size. This is not the case in many previous microchannel heat sink optimization studies, where typically only one working fluid that is subject to a uniform heat flux [2-4] is considered. While this is a typical boundary condition in electronics cooling applications, the more generic case is heat transfer between two fluids, where there is neither a uniform heat flux nor wall temperature, additional thermal resistances, and diminishing driving temperature differences along the length of the heat exchanger, depending on the thermal capacity ratio of the two fluids. Therefore, in the more general case, when heat exchange is desired between fluids with disparate thermal capacities and thermophysical properties, the dominant thermal resistance and temperature pinching place upper bounds on the utility of microscale heat transfer. For example, an air-coupled microchannel heat exchanger is severely limited by the air-side heat transfer coefficient; therefore, any reductions in tube diameter will only primarily affect the heat transfer surface area. But simultaneously, the reduction in flow area will lead to rapidly rising

pressure drop, yielding an optimum channel diameter for a given pumping power, shown in Figure 1. This implies that decreasing the channel size to values below certain thresholds provides diminishing returns, and even worse, could significantly increase parasitic losses due to pressure drop. In a real device, the use of air-side fins helps balance the thermal resistances, and parallel flow in multiple microchannels mitigates pressure drop, but with increased maldistribution potential. Geometric optimizations have been performed for a few different configurations [5, 6], but few consider the coupling side, leading to recommendations about the benefits of microchannels of various diameters in isolation that would not apply for the more realistic overall thermal system.

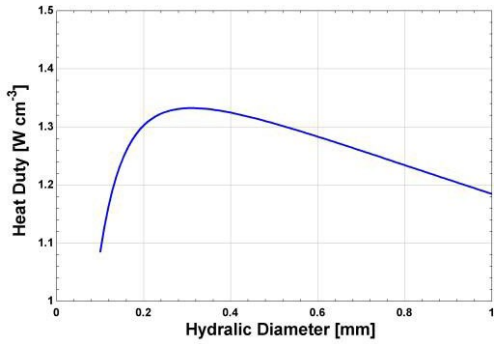


Fig. 1. Power density versus hydraulic diameter for an air coupled microchannel HX at a given pumping power.

The present study considers these different aspects and develops guidelines for the applicability and effectiveness of microscale geometries for a variety of liquid-to-liquid, liquid-to-phase-change, liquid-to-air, phase-change-to-air, and other common heat exchange applications. Microchannel diameters for representative examples of such transfer processes are analyzed and optimal ranges are recommended. This is achieved by calculating the single-phase and phase-change heat transfer coefficients for media with a range of transport properties (density, thermal conductivity, specific heat, viscosity, and latent heat of evaporation) across a range of channel diameters. These microscale transfer resistances are then paired with the thermal resistances of different coupling fluids with representative surface area enhancements through fins as needed to assess the effectiveness of microchannels for typical air-coupled and liquid-coupled heat exchangers. These results are then distilled into microchannel applicability maps based on the thermal resistance ratios, allowable pressure drop limits, fan/pumping power, and footprint to provide recommendations to guide designers of microchannel-based devices.

## References

[1] S.G. Kandlikar, S. Colin, Y. Peles, S. Garimella, R.F. Pease, J.J. Brandner, D.B. Tuckerman, Heat Transfer in Microchannels— 2012 Status and Research Needs, Journal of Heat Transfer, 135(9) (2013).

[2] S.J. Kim, Methods for Thermal Optimization of Microchannel Heat Sinks, Heat Transfer Engineering, 25(1) (2004) 37-49.

[3] M.B. Kleiner, S.A. Kuhn, K. Haberger, High performance forced air cooling scheme employing microchannel heat exchangers, IEEE Transactions on Components, Packaging, and Manufacturing Technology: Part A, 18(4) (1995) 795-804.

[4] A.M. Adham, N. Mohd-Ghazali, R. Ahmad, Optimization of an ammonia-cooled rectangular microchannel heat sink using multi- objective non-dominated sorting genetic algorithm (NSGA2), Heat and Mass Transfer, 48(10) (2012) 1723-1733.

[5] J.C.S. Garcia, H. Tanaka, N. Giannetti, Y. Sei, K. Saito, M. Houfuku, R. Takafuji, Multiobjective geometry optimization of microchannel heat exchanger using real-coded genetic algorithm, Applied Thermal Engineering, 202 (2022) 117821.

[6] B. Kwon, N.I. Maniscalco, A.M. Jacobi, W.P. King, High power density air-cooled microchannel heat exchanger, International Journal of Heat and Mass Transfer, 118 (2018) 1276-1283.

# Flow boiling of R32 and R410A inside brazed plate heat exchangers with different geometries

Giuseppe CENSI[1,*], Andrea PADOVAN[1]

1: Onda S.p.A., Lonigo, IT

* Corresponding author: Tel.: +39 0444 720721; Email: gcensi@onda-it.com

**Abstract:** A proposed midterm substitute of R410A, mixture with 1924 $GWP_{100}$ (Global Warming Potential over 100 years), is R32 ($GWP_{100}$ = 677), which, although mildly flammable, is pure, relatively cheap, already available on the market, with different suppliers due to the absence of patents. Increasingly stringent energy saving regulations are boosting the residential heat pump market, which typically requires reversible brazed plate heat exchangers to be used both as evaporators and condensers. This work reports an experimental analysis of the two refrigerants during evaporation in brazed plate heat exchangers, varying the channel volumes. It is shown that the differences in performance between the two fluids increase with the mass velocity, suggesting the influence of a convective component on the heat transfer coefficient. This is further confirmed by comparing the data with the results of two different models from literature.

**Keywords:** Heat pumps, brazed plate, R32, evaporators

## 1. Introduction

The behavior of R32 in vapor compression cycles is quite well known; Cavallini et al. [1] found that the direct use of R32 should permit the manufacture of a very efficient equipment with a limited impact in global warming, and its marginal flammability can be overcome by improving tightness and reducing refrigerant charge. Thus, intrinsic low-volume solutions are preferred, such as brazed plate heat exchangers. Numerical simulations show that R32 is a good alternative to R410A and essentially no change is required in the chiller design. As regard the heat transfer coefficient (HTC), different studies suggests that the performance of R32 is affected by both nucleate boiling and convective boiling mechanisms. The present paper reports experimental measurements of heat transfer coefficient during flow boiling in brazed plate heat exchangers, from practical industrial tests.

## 2. Experimental results

The experimental tests have been carried out at the laboratory of Onda S.p.A., with a facility consisting of a vapor compression system with a scroll compressor driven by an inverter, which allows to regulate the cooling capacity, using a 32 cSt viscosity (at 40 °C) lubrification oil.

Both tested evaporators are composed of 70 plates, 0.122 m wide and 0.530 m long, with a herringbone corrugation. The first model features refrigerant-side channels that have the same volume as the water-side channels (symmetrical), while the second model has refrigerant-side channels 24 % narrower (asymmetrical). From now on, the two configurations will be indicated as “standard channel” and “narrow channel” respectively.

The value of vapor quality at the evaporators inlet was kept at 0.2, while the value of superheating at 5.5 ±0.5 K. The performances were measured at different values of the heat flux, with saturation temperatures ranging from 3 to 5.5 °C.

From Fig. 1 we notice that the heat transfer coefficient obtained for the two fluids at the same heat flux is almost identical in the standard channels. With narrow channels the performance is improved for both fluids, but in

this configuration the fluid R410A overperforms R32.

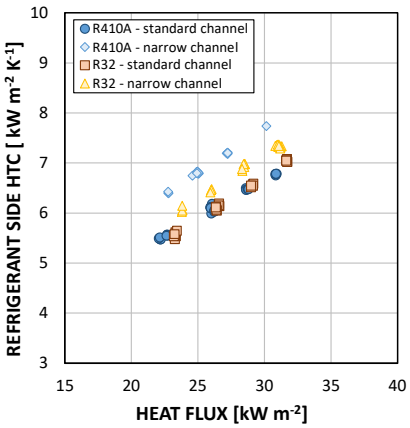


**Fig. 1** Experimental heat transfer coefficient as a function of the heat flux

On the contrary, if the same values of the heat transfer coefficients are plotted at the same mass velocity (Fig. 2), the comparison between the two fluids gives different results, suggesting that the performances of the fluid R32 are higher than those of R410A.

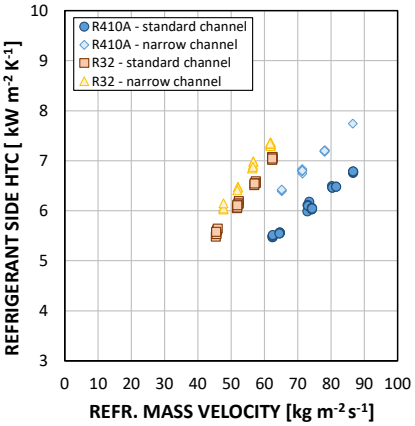


**Fig. 2** Experimental heat transfer coefficient as a function of the mass velocity

## 3. Comparison with literature

Fig. 3 shows that the Cooper [2] model, purely nucleate boiling based, tends to strongly underestimate the experimental data. On the contrary, the Longo et al. [3] model (Fig. 4), including both nucleate and convective boiling components, predicts the experimental results much better, even though the data for R410A in the narrow channel remain underestimated.

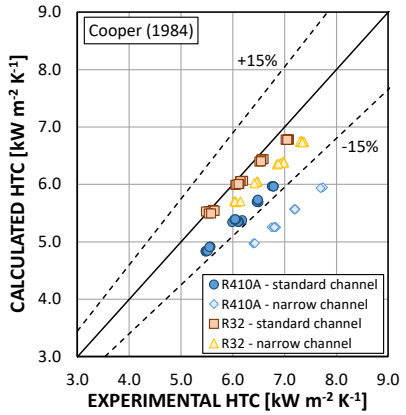


**Fig. 3** Comparison of the experimental data with the model by Cooper [2]

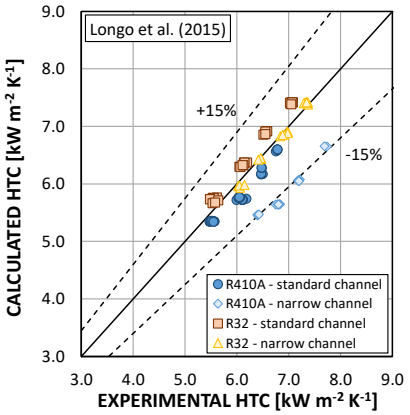


**Fig. 4** Comparison of the experimental data with the model by Longo et al. [3]

## 4. Conclusions

At the same heat flux, the boiling heat transfer performance of R32 and R410A are very similar each other. Both the experimental and calculated results suggest the presence (together with a nucleate boiling term) of a convective mechanism, which is more evident for narrow channels and for R410A where the mass velocity is higher.

## References

[1] Cavallini, A., Censi, G., Del Col, D., Doretti, L., Rossetto, L., Longo, G.A., 2001. Reduction of Global Warming Impact in the HP/AC Industry by Employing New HFC Refrigerants. CLIMA 2000. 7th REHVA World Congress. Napoli.

[2] Cooper, M.G., 1984. Saturation nucleate pool boiling - A simple correlation. First National Conference on Heat Transfer, The Institution of Chemical Engineers Symposium Series, 785-793.

[3] Longo, G.A., Mancin, S., Righetti, G., Zilio, C., 2015b. A new model for refrigerant boiling inside Brazed Plate Heat Exchanger (BPHEs). International Journal of Heat and Mass Transfer, 91, 144-149.

# Numerical simulation of the effect of micro tube-in-tube heat exchanger geometry on heat transfer performance

Mirjam ZNAIMER[1,*], Jan G. KORVINK[1], Jürgen BRANDNER[1]

1: Institute of Microstructure Technology (IMT), Karlsruhe Institute of Technology (KIT), Eggenstein-Leupoldshafen, GER

* Corresponding author: Tel.: +49 721 608-24430; Email: mirjam.znaimer@kit.edu

**Abstract:** In chemical reactions at high temperatures and pressures, especially with exothermic reactions, precise temperature control is essential to reduce the risk of thermal runaway. Conventional macro-scale reactors, provide only limited temperature control due to reduced heat dissipation [1]. In the contrary, micro reactors provide a high surface-to-volume ratio, and the associated increased heat dissipation supports the avoidance of local hot spots inside the reactor. A further advantage of micro process technology devices is the precise temperature control and equal temperature distribution. For NMR-based in-situ and operando monitoring of chemical reactions above 200 °C and 1 MPa, a micro reactor/heat exchanger has to be designed. To ensure that the micro reactor fits into a standard high-field NMR instrument, it has to be cylindrical with a maximum outer diameter of 10 mm. The number and geometry of the tubes as well as the L/D ratio of the implemented micro heat exchanger are to be determined. For the comparison of the heat transfer performance, the thermal efficiency, overall heat transfer coefficient and pressure loss of the micro heat exchanger at different mass flow rates will be modelled using the finite element method (FEM). In addition, the heat flux as well as the flow profile over the entire length of the micro heat exchanger will be simulated. The next step will then be to verify the results of the numerical simulation by experiments.

**Keywords:** Heat transfer performance, Micro-Heat Exchanger, FEM simulation, reaction monitoring at high temperature/pressure

[1] Ulrich Hauptmanns, *Process and Plant Safety*, Springer-Verlag Berlin Heidelberg **2015**, DOI 10.1007/978-3-642-40954-7

# On the Coupling between Heat and Momentum Transfer in a micro U bend

Jais MOHAMED[1], Giorgio MOSCATO[1], Giovanni P. ROMANO[1,*]

1: Department of Mechanical and Aerospace Engineering, University La Sapienza, Roma, IT

* Corresponding author: Tel.: +39 0644585217; Email: giampaolo.romano@uniroma1.it

**Abstract:** Heat transfer in a microfluidic cell with a U-bend shape is investigated experimentally by non-intrusive measurement methods. The objective of this study is to detail relations between heat and momentum transfer, both in straight channel sections and especially in recirculating regions as those developing at the corners of the tested U-bend. To this end, thermal and velocity fields are acquired and processed using high-resolution infrared and optical video cameras at different flow rates and Reynolds numbers, ranging from laminar to almost turbulent conditions. Algorithms and procedures usual in Thermal Infrared Imaging (TII) and Particle Image Velocimetry (PIV) are used. The acquired images are coupled with local measurement devices for temperature and flow rate, in order to get well-calibrated values. Instantaneous fields are obtained from both side and top views of the microchannel U-bend and analyzed in space and time. The main result is that correlations among temperature and velocity fields are obtained when fluctuating variables are considered, as for example thermal transient rate and velocity fluctuations. Indeed, especially in near turbulent conditions, velocity fluctuations developing at U-bend corners show good matching with thermal transient rates in the same regions.

**Keywords:** Microfluidic cell, Heat transfer, Thermal Imaging, PIV, Thermal transients

## 1. Introduction & Motivations

Microfluidic devices gained a significant amount of interest in recent years, in particular through specific studies on phenomenology and applications regarding heat transfer. Even if some results have been obtained regarding global efficiency of specific devices, the detailed investigation and understanding of local thermo-fluidic interactions is still an open field. This would allow deriving and testing general assumptions to be applied in modelling and design of new concept devices. The former argument is here considered for defining heat transfer performances as related to the local fluid flow conditions, laminar or turbulent, and to the specific device geometry. So far, a specific micro-cell and set-up are designed in order to allow measurements of local behaviors of velocity and temperature flow fields in presence of heating. The objective of the present work is to relate local thermal efficiency and cooling performances to local fluid mechanics phenomena.

## 2. Experimental Set-up

The used micro-channel is shown in Figure 1, consisting of a U-bend configuration heated from below. Measurements are performed in the whole channel, but here the attention is focused on inversion region, as detailed in Figure 1. Thermal measurements are obtained by thermocouples and Thermal Infrared Imaging (TII), whereas velocimetry images by means of Particle Image Velocimetry (PIV), using high resolution cameras.

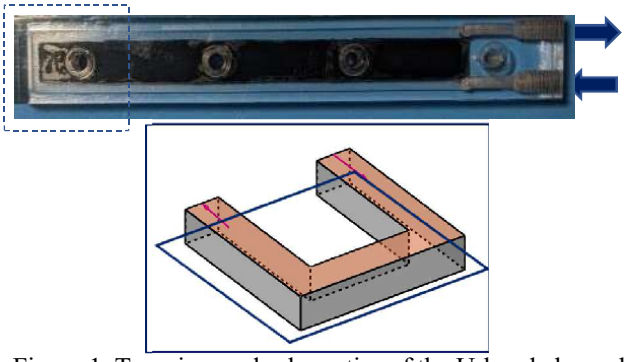

Figure 1. Top view and schematics of the U-bend channel used in present work.

## 3. Results

An example of obtained results is given in Figure 2, with thermal transients recorded by infrared camera, positioned at the top. At U-bend, temperature decreases from about 50°C (the hot plate temperature, in red) to around 25°C (the inlet water temperature, in blue).

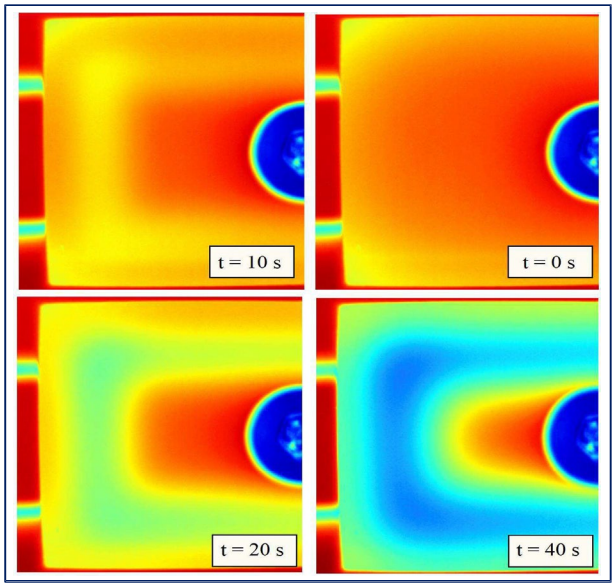


Figure 2. Thermal fields as recorded by infrared camera during cooling process.

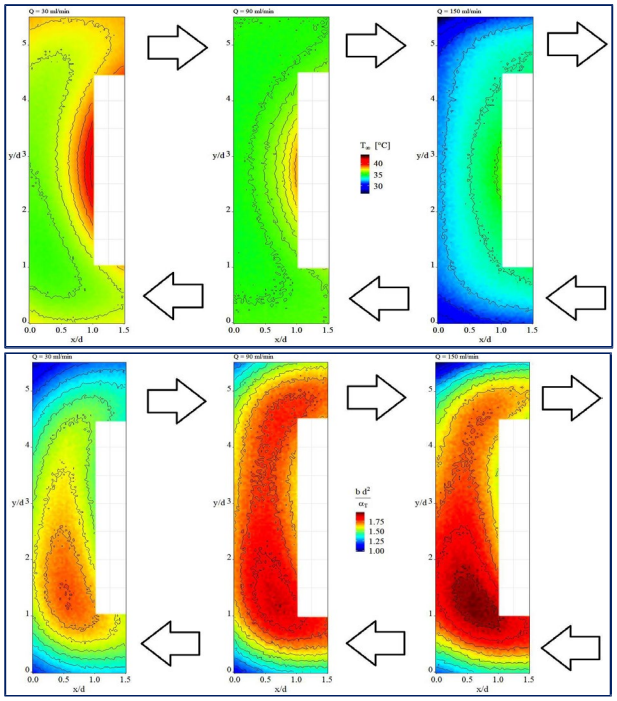

Figure 3. Equilibrium temperature (top) and thermal transient rate (bottom) for three cooling fluid flow rates (increasing from left to right).

From these fields, initial and final temperatures, cooling magnitude and thermal transient rate are derived at each point. In Figure 3, the final temperature and the normalized thermal transient rate are presented for three different cooling fluid flow rates, roughly corresponding to Reynolds numbers ranging from 300 to 1500. It is important to highlight that both fields are dependent on the fluid condition, *i.e.* on Reynolds number.

These fields are compared to those derived from velocimetry measurements, as those plotted in Figure 4. Recirculation regions at bend corners develop high values of velocity magnitude, vorticity and fluctuations, spatially well related to thermal transient rates of Figure 3, especially at high Reynolds numbers, thus indicating strict coupling between the two.

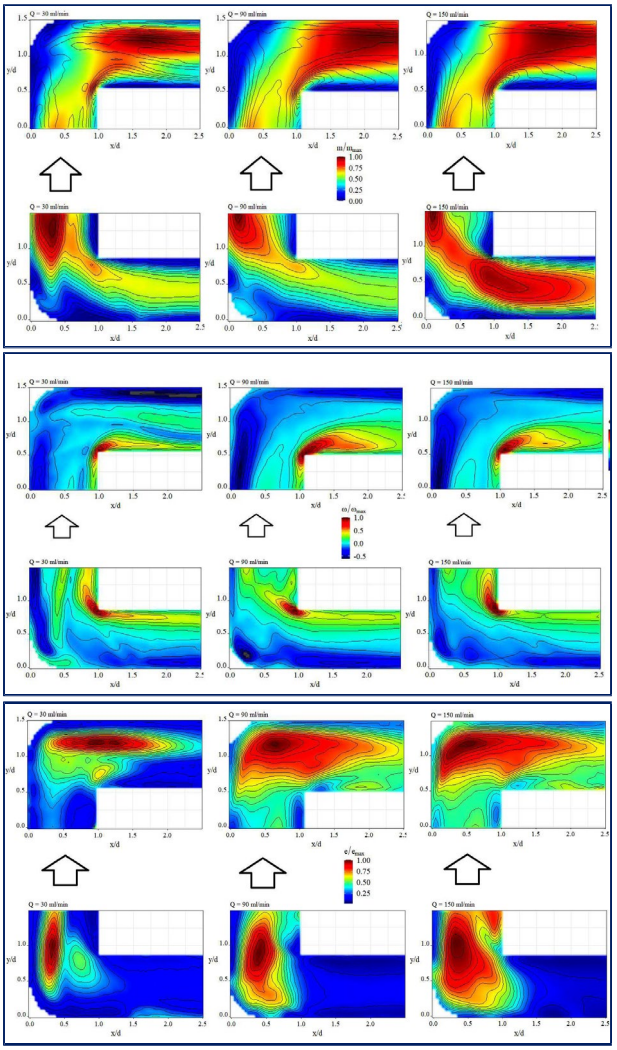

Figure 4. Velocity magnitude, vorticity and velocity fluctuations (top, middle and bottom) for three cooling fluid flow rates (from left to right).

# From Coffee Rings to Uniform Deposits: Insights from 1D Modelling.

Nathan COOMBS[1,*], Mykyta CHUNBYNSKY[1], James SPRITTLES[1]

1: Mathematics Institute, University of Warwick, Coventry, UK.

* Corresponding author: Email: Nathan.Coombs@warwick.ac.uk

**Abstract:** Coffee ring formation, a well-known phenomenon observed in drying sessile droplets, has been understood theoretically in the past with aid of 1D modelling. These models typically assume infinitely fast vertical diffusion of the solute, and so are formulated in terms of depth averaged quantities. The coffee ring can then be understood as a is a shock front, beyond which solute particles are immobile, that propagates into the droplet interior. In a study by Li et al. it was found that the ring can be attenuated simply by increasing the ambient temperature. This has the effect of increasing the evaporation rate and hence the free surface recession speed, meaning more particles in the droplet bulk will adhere to the surface (rather than being transported towards the contact line). Here, we make the first steps towards a 1D model that incorporates this behavior. Building on models in existing coffee ring literature, we have lifted the assumption of fast vertical diffusion. Using some preliminary results in diffusive boundary layer theory, we present a model that is capable of reproducing both coffee ring and surface capture phenomena in their respective asymptotic limits.

**Keywords:** Coffee ring effect, Surface capture, Free surface flows, Evaporation-induced flows

## 1. Introduction

Evaporation-induced particle transport in sessile droplets has been the focus of many experimental and theoretical studies due to its industrial relevance (in inkjet printing for example). The *coffee ring effect* (CRE), referring to the accumulation of solute particles near the contact line of the drop leading to enhanced deposition there, is a ubiquitous phenomenon occurring in particle suspensions across a range of length scales. In the simplest sense, coffee rings are the result of evaporation-induced capillary flow which carries solute particles towards the droplet contact line. On arrival, these particles are observed to pack into a semi crystalline array, as shown in Fig. 1. We refer to this behavior as "jamming". The inclusion of jamming into a CRE model is crucial to yield coffee rings with finite thickness by the time all the solvent has evaporated.

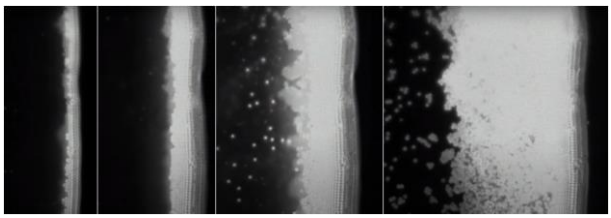

**Fig. 1.** Solute particles arriving at the contact line and "jamming" into a semi-crystalline array. Adapted from reference [1].

Particle jamming has successfully been incorporated into a model by Popov [2], in which the jammed particle deposit enforces droplet pinning. Popov's model assumes full vertical homogeneity, allowing a formulation in terms of depth-averaged quantities that reduces the framework from 2D to 1D. Since radial diffusion is also neglected in this model, finding the progression of the jammed particle front is an application of weak shock theory [2-3].

Another phenomenon observed by Li et al. [4] in experiments with droplets at high evaporation rates, $J_{evap}$, is that particles in the droplet bulk tend to aggregate at the air-liquid interface. Jamming which occurs at the

interface prevents particles from reaching the contact line, meaning they do not contribute to the coffee ring. We refer to this effect as *surface capture*. Mathematical models of surface capture have been attempted in references [5-6]. However, to the authors knowledge no 1D approach complimentary to the CRE models currently exists. Such a model would be advantageous as breaking the assumption of axisymmetry (for inkjet-printed lines for example) would then only require a generalization from 1D to 2D.

## 2. Modelling approach

Motivated by the success of 1D models in reproducing coffee rings, we have developed an interpolative model which captures both coffee ring and surface capture phenomena. To do this, we have extended Popov's modelling approach by lifting the assumption of vertical homogeneity. To keep our model one dimensional, the $z$-dependence of the concentration profile is specified *a priori* with aid of diffusive boundary layer theory:

$$c(r,z,t) = 1 + (C-1)\exp\left[\frac{J_{evap}}{\rho D}(h-z)\right],$$

where $\rho$ is the fluid density, $h(r,t)$ is the free surface height and $C(r,t)$ is an unknown pre-factor used to satisfy mass conservation. Depending on evaporation strength and initial solute dilution, our interpolative model is capable of qualitatively reproducing both CRE and surface capture phenomena, with a variety of intermediate behaviors.

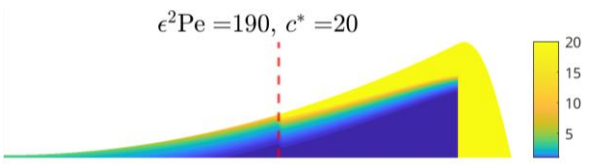


**Fig. 2.** 2D concentration distribution in a drop just before touchdown of the free surface. The yellow regions indicate where the solute has jammed ($c = c^*$). For this set of parameters, both a coffee ring and surface layer are visible.

Since most available experimental data shows the deposit morphology after drying rather than any transient behavior, our model must be extended until all solute has evaporated. Fig. 2 shows the concentration distribution at the final timestep in our simulation: just before the free surface meets the substrate (touchdown). Beyond this stage, numerous complications arise with film de-wetting and changes to the evaporation profile. Different scenarios are also expect depending on whether the free surface or jammed particle layer meets the substrate first. Some progress has already been made in modelling post-touchdown dynamics.

## References

[1] Marín, Á.G., Gelderblom, H., Lohse, D., Snoeijer, J.H., 2011. Rush-hour in evaporating coffee drops. Physics of Fluids 23, 091111. https://doi.org/10.1063/1.3640018

[2] Popov, Y.O., 2005. Evaporative deposition patterns: Spatial dimensions of the deposit. Phys Rev E 71, 36313. https://doi.org/10.1103/PhysRevE.71.036313

[3] Zheng, R., 2009. A study of the evaporative deposition process: Pipes and truncated transport dynamics. The European Physical Journal E 29, 205–218. https://doi.org/10.1140/epje/i2009-10469-7

[4] Li, Y., Yang, Q., Li, M., Song, Y., 2016. Rate-dependent interface capture beyond the coffee-ring effect. Sci Rep 6, 24628. https://doi.org/10.1038/srep24628

[5] Jafari Kang, S., Vandadi, V., Felske, J.D., Masoud, H., 2016. Alternative mechanism for coffee-ring deposition based on active role of free surface. Phys Rev E 94, 63104. https://doi.org/10.1103/PhysRevE.94.063104

[6] Nguyen, T.A.H., Biggs, S.R., Nguyen, A. v, 2017. Manipulating colloidal residue deposit from drying droplets: Air/liquid interface capture competes with coffee-ring effect. Chem Eng Sci 167, 78–87. https://doi.org/https://doi.org/10.1016/j.ces.2017.04.001

# Effect of Presence of Inlet Restriction on Fluid Flow and Boiling Inside the Microchannel: A Numerical Study

Darshan M. BASAVARAJA[1], Mirco MAGNINI[2,*], Omar MATAR[1]

1: Department of Chemical Engineering, Imperial College London, UK
2: Department of Mechanical, Materials and Manufacturing Engineering, University of Nottingham,UK

* Corresponding author: Tel.: 0115 7487427 ; Email: mirco.magnini@nottingham.ac.uk

**Abstract:** This article presents a numerical study to understand the effect of presence of inlet restriction in a microchannel. A single microchannel with fluidic channel surrounded by heated walls on its three sides is simulated and the conjugate heat transfer problem is solved. The simulations have been performed using VOF method in OpenFOAM v2106. The effect of introducing inlet restriction inside a microchannel on pressure drop and its further effect on saturation temperature of the fluid have been discussed. Simulations will also be performed to study the flow boiling inside the microchannel with inlet restriction.

**Keywords:** Microchannel, Flow Boiling, Inlet Restriction

## 1. Introduction

The advancements in micro-electronic chips, micro-electro-mechanical systems (MEMS), fuel cells etc., has led to the need for compact microchannel heat sinks/exchangers which can remove the high heat generated in them and enable efficient working of such devices. Especially, the flow boiling inside a microchannel has been recognized as one of the efficient ways of cooling such devices. But the sudden expansion of vapour bubbles formed in the channel leading to flow reversal and unstable boiling has been recognized as one of major problems with microchannel flow boiling [1]. Mukherjee and Kandlikar [2] have reported that this can be mitigated either by having a diverging channel geometry or a restriction at the inlet. But the effect of pressure drop on the fluid flow inside a microchannel with inlet restriction has never been discussed. In the present work, an attempt has been made to understand the effect of pressure reduction due to the presence of inlet restriction in a microchannel.

## 2. Simulation setup

The simulations have been performed using OpenFOAM version 2106 and built in VOF solver with the addition of models to handle liquid-vapour phase change. The detailed description of the phase change model and the solver can be found in Municchi et al. [3]. The domain considered for the simulation has

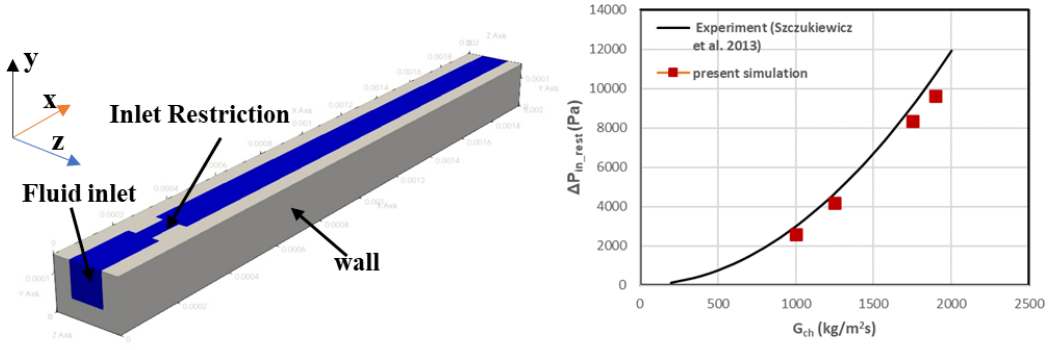


(a) (b)

Figure 1: (a) Simulation domain (b) Variation in pressure drop at the inlet restriction with mass flux

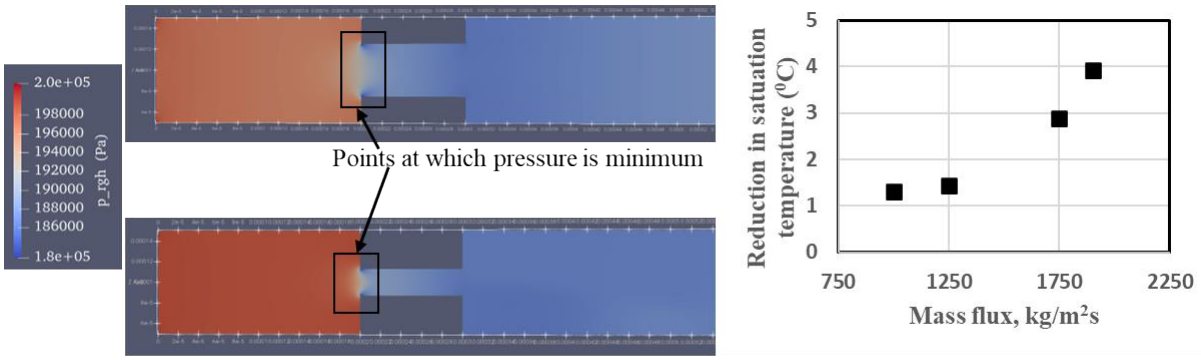


(a) (b)

Figure 2: (a) Pressure contour for microchannel with inlet restriction taken on a plane which is at the center of y-axis. (b) Variation in reduction in saturation temperature with mass flux.

been shown in Fig 1(a). A square microchannel of cross section $100 \times 100$ μm² having a length of 2 mm with inlet restriction of length 100 μm has been considered in the present simulations. The heating configuration corresponds to a three-side heated channel as heat is transferred to the microchannel through the bottom wall and the two vertical walls. The thickness of bottom and the vertical wall is taken as 50 μm. Refrigerant R245a has been considered in the study with thermofluidic properties taken at saturation temperature of 31.5 °C from REFPROP. At the fluid inlet, a liquid with velocity $U_l$ (corresponding to mass flux range of 1000-1900 kg/m$^2$s) and saturation temperature has been considered. At the outlet zero-gradient condition is set for velocity and temperature with uniform pressure. A constant heat flux boundary condition is applied at the base of the microchannel. At the top, adiabatic condition is considered for both fluid and solid regions.

## 3. Results and Discussion

The presence of restriction at the inlet of a microchannel results in significant drop in pressure. Figure 1(b) shows the variation in pressure drop at the inlet restriction with mass flux. A comparison with the experimental results from Szczukiewicz et al. [4] has also been shown in the figure. Pressure contours are shown in Fig. 2(a) for microchannel with inlet restriction ratio 0.5 and 0.25 in which one can observe the regions where the pressure is minimum. Interestingly, for both the microchannels, the pressure is found to be minimum at the central plane of the microchannel near the inlet corners of the restriction. Such reduction in pressure leads to reduction in saturation temperature of the fluid which in turn might significantly influence flow boiling behavior inside the microchannel. An assessment of reduction in saturation temperature calculated based on the difference between inlet pressure and the minimum pressure observed in the domain is shown in Fig. 2(b). It can be observed that a reduction in saturation temperature up to 4 °C is possible at higher mass flux. Such reduction in saturation temperature might trigger flashing phenomenon which in turn can cause significant changes in flow boiling behavior inside the microchannel. Further, the single bubble dynamics during flow boiling inside a microchannel with inlet restriction will be studied.

## Acknowledgements

The authors wish to acknowledge the financial support provided by EPSRC via BOiliNg flows in SmAll and mIcrochannels **(BONSAI)** project (grant: EP/T03338X/1).

## References

[1] S.G. Kandlikar, M.E. Steinke, S. Tian, L.A. Campbell, High speed photographic observation of flow boiling of water in parallel minichannels, ASME National Heat Transfer Conference, Los Angeles, CA, June 10–12, 2001.

[2] A. Mukherjee, S.G. Kandlikar, The effect of inlet constriction on bubble growth during flow boiling in microchannels, International Journal of Heat and Mass Transfer, vol. 52, 2009.

[3] F. Municchi, I. El Mellas, O.K. Matar, M. Magnini,

Conjugate heat transfer effects on flow boiling in microchannels, International Journal of Heat and Mass Transfer, vol. 195, 2022.
[4] S. Szczukiewicz, N. Borhani, J.R. Thome, Two-phase heat transfer and high-speed visualization of refrigerant flows in 100X100 $\mu m^2$ silicon multi-microchannels, International Journal of Refrigeration, vol. 36, 2013.

## SESSION 6a
## Nanofluids and Applications
Chair: **A. Moita**



Roger RIEHL[1], Matthias H. BUSCHMANN[2]
1: GamaTech Thermal Solutions Ltda, São José dos Campos, SP Brazil
2: Institut für Luft- und Kältetechnik gGmbH Dresden, 01309 Dresden, Germany



Khalad A ALMUHAYSH[1, 2], Antonis SERGIS[1], Yannis HARDALUPAS[1]
1: Department of Mechanical Engineering, Imperial College London, UK
2: Department of Mechanical Engineering, King Faisal University, Saudi Arabia



Firat SEZGIN[1], Nur COBANOGLU[2], Nejc VOVK[3], Elif Begum ELCIOGLU[1], Ziya Haktan KARADENIZ[4], Lovro BOBOVNIK[3], Erdem OZYURT[1], Andrej SPILER[3], Blaz KAMENIK[3], Timi GOMBOC[3], Alpaslan TURGUT[5], Jure RAVNICK[3]
1: Department of Mechanical Engineering, Eskişehir Technical University, Eskisehir, Turkey
2: Graduate School of Natural and Applied Sciences, Izmir Katip Celebi University, Izmir, Turkey
3: Faculty of Mechanical Engineering, University of Maribor, Maribor, Slovenia, SI
4: Department of Energy Systems Engineering, Izmir Institute of Technology, Izmir, Turkey
5: Department of Mechanical Engineering, Dokuz Eylul University, Izmir, Turkey



Agathe BJELLAND ERIKSEN[1], Pawel KOSINSKI[1], Boris V. BALAKIN[2], Anna KOSINSKA[2]
1: Department of Physics and Technology, University of Bergen, Bergen, Norway
2: Department of Mechanical and Marine Engineering, Western Norway University of Applied Sciences, Bergen, Norway

# Galinstan-Water Suspension as Working Fluid for Oscillating Heat Pipes

Roger RIEHL[1], Matthias H. BUSCHMANN[2,*]

1: GamaTech Thermal Solutions Ltda, São José dos Campos, SP Brazil
2: Institut für Luft- und Kältetechnik gGmbH Dresden, 01309 Dresden, Germany

* Corresponding author: Tel.: +4935140815311; Email: Matthias.Buschmann@ilkdresden.de

**Abstract:** The study presents experimental investigations on a glass oscillating heat pipe. Subsidising the reference fluid deionised water by a mixture of deionised water and particles shows an increase of the thermal performance between 5 and 12 % depending on the heat supplied at the evaporator and on the condenser cooling volume flux. However, this effect quickly disappears due to the chemical reactions taking place during operation.

**Keywords:** Oscillating heat pipe, Hybrid working fluid, Experiment, Statistical analysis

## 1. Introduction

Differently than heat pipes, the inner surfaces of oscillating heat pipes (OHP) and thermosyphons (TS) are not structured. Evaporation and condensation takes place on manufacturing rough surfaces. To enhance the phase change heat transfer – especially the evaporation – changing these surfaces seems to be an option. Several techniques are currently investigated among them micromachining, laser ablation or simple sand blasting. None of these technologies is suitable for narrow channels or pipes as found in OHP's and TS's. Furthermore, most of these technological approaches are expensive.

Here we follow another approach. It is a long standing idea to add particles to the working fluid of phase change probes [1, 2]. The size of such particles may reach from nanometers to some millimeters. Depending on their size the particles act differently. Large particles millimeter size) might become boiling chips and very small once (nanometer size) may adhere to the wall and increase the number of nucleation sites. Our research question is what happens if the usually solid particles are subsidized by a liquid metal or alloy?

To answer this question galinstan – the eutectic gallium / indium / tin alloy liquid at room temperature – is added to the basefluid water. Experiments are carried out with deionised water (reference fluid) and the emulsion mentioned above employing a glass OHP.

## 2. Test rig and experimental procedure

The test rig consists of a glass body with eight connected capillaries. The lower part of the glass body (evaporator) is heated with an electrical wire. The upper part (condenser) is cooled by a water stream with constant inlet temperature of 10 °C. The whole system is insulated with 20 mm Armaflex mattes. Experiments are carried out at three different cooling volume fluxes (6, 20 and 40 l/h). Heat input at evaporator is varied from 10 to 60 W in steps of 5 W. By measuring the condenser outlet temperature the efficiency of the OHP is calculated. Statistical analyses are employed to reveal the heat transfer characteristics.

## 3. Experimental results

Figure 1 shows the efficiency $\eta$ (ratio of heat retrieved at the condenser and electrical power supplied at evaporator). The upper plot of Fig. 1 indicates a clear enhancement of 10 % compared to the reference fluid water.

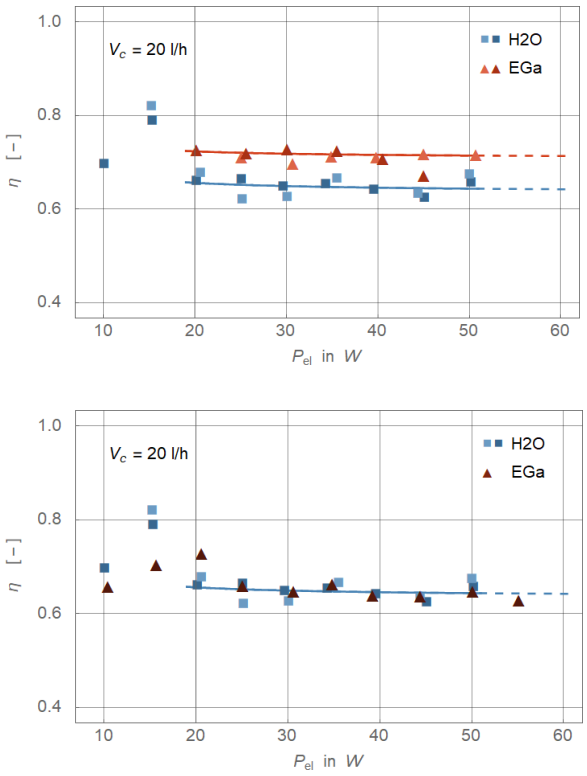


Fig. 1: Efficiency of oscillating heat pipe operated with 20 l/h cooling volume flow at condenser. Upper plot results after 24 h and lower plot after 48 h.

These results are obtained about 24 hours after the preparation of the galinstan/water working fluid. Repeated measurements about 48 hours after preparation show the deterioration of these improvements (lower plot of Fig. 1).

Scanning electron microscopy and energy dispersive X-ray spectroscopy show that both the evaporator (Fig. 2) and the condenser surfaces are coated with the alloying partners Ga, In and Sn of Galinstan. The coating is very thin and does not appear to form a wick-like structure. However, the roughness of the evaporator in particular is increased. Thus, the number of nucleation sites is much higher than on a pure glass surface and the boiling heat transfer at the evaporator is enhanced.

Unfortunately, the advantages caused by the coating are compensated by the development of non-condensable gases (NCG) like oxygen and hydrogen. NCG gather at the upper end of the OHP the condenser where they suppress the

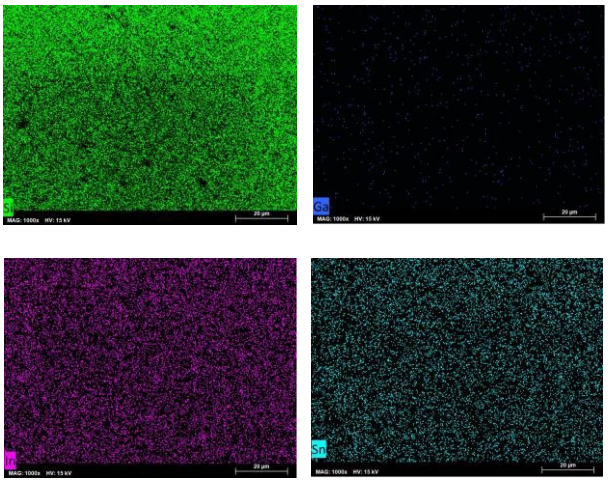

Fig. 2: EDX-image of evaporator surface after operation. Upper line silicon from glass body and gallium, lower line indium and tin.

condensation of the basefluid vapour fraction. That of course increases the thermal resistance of the oscillating heat pipe.

## 4. Conclusion

Adding particles to the working fluid of OHP's is one way to improve the thermal performance of such devices. However, it strongly depends on the chemical reactivity of the particulate material whether these positive effects last in the long term.

In summary, the addition of particles ranging in size from nanometers to micrometers can improve the heat transfer of phase change probes. Further and detailed research is needed to obtain these beneficial effects in the long-term operation of oscillating heat pipes.

## References

[1] R.R. Riehl, N. dos Santos, Water-copper nanofluid application in an open loop pulsating heat pipe, App. Thermal Engineering 42 (2012) 6-10.
[2] A. Kujawska, B. Zajaczkowski, L.M. Wilde, M.H. Buschmann, Geyser boiling in a thermosyphon with nanofluids and surfactant solution, Int. J. Thermal Sci. 139 (2019) 195-216.

# Effects of pH Level and Volume Concentration on $Al_2O_3$ - $H_2O$ Nanofluid Stability

Khalad A ALMUHAYSH[1, 2, *], Antonis SERGIS[1], Yannis HARDALUPAS[1]

1: Department of Mechanical Engineering, Imperial College London, UK

2: Department of Mechanical Engineering, King Faisal University, Saudi Arabia

* Corresponding author: Email: k.almuhaysh21@imperial.ac.uk

**Abstract** Nanofluid thermal performance is affected by the dispersion quality of nanoparticles in the carrier fluid. So far, research into the standardisation of nanofluid preparation process in the field has been lacking. This has historically led to large discrepancies between the findings of research groups performing experiments under similar boundary conditions. Nanofluid stability is influenced by several variables including pH and volumetric nanoparticle concentration. The aim of the current study is to investigate parametrically the influence of pH and nanoparticle volumetric concentrations on $Al_2O_3$ - $H_2O$ nanofluid stability. Alumina nanoparticles were prepared using a two-step method, and characterized by electron microscopy, zeta potential, dynamic light scattering and sedimentation test methods. The results showed that an optimum pH value exists that creates the most stable $Al_2O_3$-$H_2O$ nanofluid for the specific type of particles used. Nanoparticle loading effects have also been investigated and quantified. The findings were explained by morphological and electrostatic stabilization quantification methods to understand and provide an optimum and prescriptive method of preparation for the specific type of nanofluids created. This is expected to facilitate the nanofluid preparation standardisation process, which is urgently needed.

**Keywords:** Nanofluid, $Al_2O_3$ Nanoparticle, Stability, Adjusted pH, Volume nanoparticle Concentrations

## 1. Introduction

In 1995, Choi discovered that utilizing nanoparticles led to an increase in the thermal conductivity of ordinary fluids [1]. Subsequently, numerous studies demonstrated that nanoparticles can significantly improve heat transfer characteristics when mixed with a conventional fluid, e.g., water, oil, refrigerant, alcohol, etc. [2], [3]. The effectiveness of nanofluids (NF) and its dependence on the stability of nanoparticle suspensions in heat transfer applications is important [4]. There exists a fundamental difficulty in ensuring the optimum dispersal of nanoparticles in base fluids as in many cases, the nanoparticles have larger densities than those of the carrier liquids. A need to prevent the irreversible formation of sedimentation and potentially agglomeration that might accentuate the former hence exists. As such, the combination of Electrostatic attractive forces (i.e., Van der Waal) and gravitational forces can cause nanoparticle suspension destabilisation.

NF stability is found to depend on several factors affected by their preparation method, base fluid and nanoparticle type, mixture pH and the use of surfactants. For example, Sharma *et al.* [5] reported that the pH value of NF can indicate the degree of NF stability when it is away from the isoelectric point (IEP). This indicates that the particles' surface charge, which is referred to as the zeta potential value, is zero. Although few studies have presented the effect of using volumetric concentrations on $Al_2O_3$-$H_2O$ stability, they did not consider the consequence of pH and did not explain the reasons leading to the existence of optimum stabilisation parameters [6]. Therefore, the current study attempts to explain the link between nanoparticle loading and pH regulation on the stability of $Al_2O_3$-$H_2O$ mixtures.

## 2. Experimental Methods

The focus of the experiments is to understand the NF stability mechanism in a stationary sample (i.e., without a flow). The pH level of prepared $Al_2O_3$-$H_2O$ NF was varied from a value of 2 to 12 and, whilst the nanoparticle volumetric loading was varied from 1.5% to 0.0001%, pH values were measured using a pH meter (Hanna Instruments Ltd, HI-98129). HCl and NaOH (VWR, 20252.335 and 28226.327) were added to adjust the pH level of the NF. Eq. (1) was used to calculate the volumetric concentrations of the NF.

$$\phi = \left[ \frac{\frac{m_{np}}{\rho_{np}}}{\frac{m_{np}}{\rho_{np}} + \frac{m_{bf}}{\rho_{bf}}} \right] \times 100 \qquad (1)$$

where ϕ is the volumetric concentration, $m_{np}$ is the mass of nanoparticles, $\rho_{np}$ is the density of nanoparticles, $m_{bf}$ is the mass of base fluid, and $\rho_{bf}$ is the density of base fluid.

Alumina dry nanopowder with an average particle size of 40 - 50 nm (Alfa Aesar, 44931) was suspended in deionised water with the use of an ultrasonic bath (more information can be found in Kouloulias *et al.* [5]). The stability was evaluated and characterised through Scanning and Transmission Electron microscopy (SEM - TESCAN MIRA, TEM - T12 Spirit, ThermoFischer) to quantify the true nanoparticle size, shape, and morphology. 24 hours after NF preparation, TEM was used to detect changes in particle/agglomerate morphology of the prepared NF. NF stability was additionally evaluated using zeta potential values, and Dynamic Light Scattering (DLS, Zetasizer Pro Red Label, Malvern Panalytical Ltd.) measurements. A desired zeta potential lying outside the range of ±30mV was used to optimise stability, Vandsburger [6].

## 3. Results and Discussion

SEM imaging of the alumina nanoparticles, before the suspension in the liquid took place, indicated that the primary $Al_2O_3$ nanoparticles are roughly spherical (40-50 nm).

Fig. 1 shows the IEP of one of the NF samples tested for pH values of 6 and 8 and for φ of 0.005%. It illustrates that the NF has high stability for the pH range from 2 to 6. Fig. 1 demonstrates the pH level effect on NF stability by controlling agglomeration size.

The TEM measurements indicated the presence of large agglomerates in the suspension. Precipitation of the mixture with

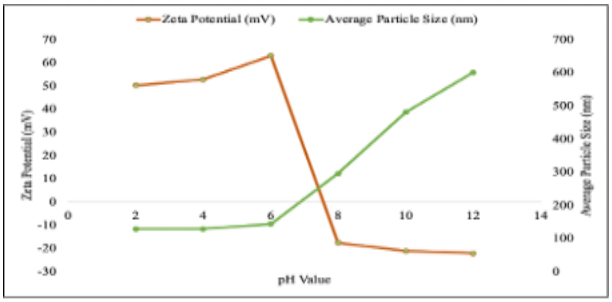


**Fig. 1.** Zeta potential values and DLS measurements of $Al_2O_3$ NF with pH 4 and ϕ = 0.005%.

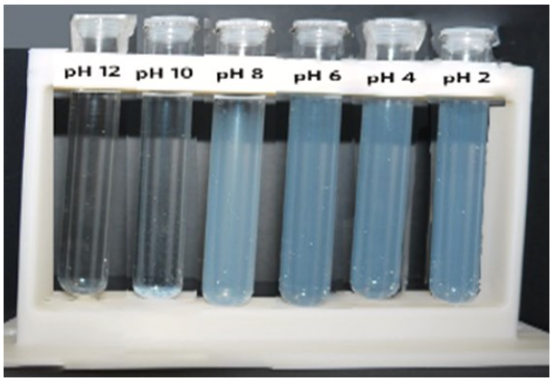


**Fig. 2.** Sedimentation rates image of $Al_2O_3$ NF with adjusting pH level and ϕ = 0.005%.

pH 8, 10 and 12 was visually observed 24 hours after mixing (See Fig. 2).

A parametric study of φ and pH revealed that an optimum pH of 4 exists for the range of φ investigated. Fig. 3. demonstrates that volume concentrations influence NF stability. It is shown that low nanoparticle concentration may reduce pH level effects.

Moreover, Fig. 3 suggests that lower

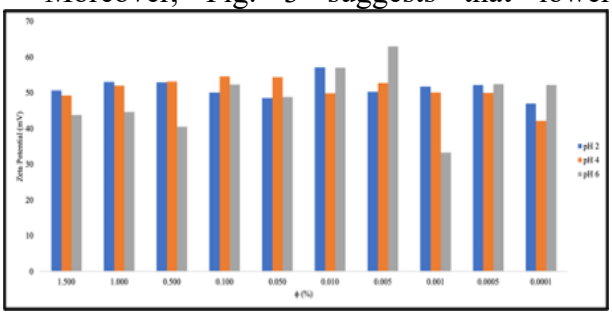

**Fig. 3.** Zeta potential values of $Al_2O_3$ NF with adjusting pH level and volume concentration.

nanoparticle concentration enhances NF stability due to the fewer number of nanoparticles present in the solution and the strong repulsive forces, which reduce the probability of particle collision/agglomeration. The findings demonstrate the effects of both pH level and volume concentration on NF stability. The final presentation will include results for after 35 days of mixing.

## References

[1] S.U.S. Choi and J.A. Eastman, "Enhancing Thermal Conductivity of Fluids with Nanoparticles," in *1995 International Mechanical Engineering Congress and Exhibition*, 1995. [2] V. Etminan-Farooji, E. Ebrahimnia-Bajestan, H. Niazmand, and S. Wongwises, "Unconfined laminar nanofluid flow and heat transfer around a square cylinder," *Int. J. Heat Mass Transf.*, vol. 55, no. 5–6, pp. 1475–1485, Feb. 2012. [3] E. Ebrahimnia-Bajestan, H. Niazmand, W. Duangthongsuk, and S. Wongwises, "Numerical investigation of effective parameters in convective heat transfer of nanofluids flowing under a laminar flow regime," *Int. J. Heat Mass Transf.*, vol. 54, no. 19–20, pp. 4376–4388, Sep. 2011. [4] K. Kouloulias, A. Sergis, and Y. Hardalupas, "Sedimentation in nanofluids during a natural convection experiment," *Int. J. Heat Mass Transf.*, vol. 101, pp. 1193–1203, Oct. 2016. [5] Babita, S. K. Sharma, and S. M. Gupta, "Preparation and evaluation of stable nanofluids for heat transfer application: A review," *Exp. Therm. Fluid Sci.*, vol. 79, pp. 202–212, Dec. 2016. [6] T. Zhang, Q. Zou, Z. Cheng, Z. Chen, Y. Liu, and Z. Jiang, "Effect of particle concentration on the stability of water-based SiO2 nanofluid," *Powder Technol.*, vol. 379, pp. 457–465, Feb. 2021. [7] L. Vandsburger, "Synthesis and covalent surface modification of carbon nanotubes for preparation of stabilized nanofluid suspensions," 2009.

# Comparative Simulations on Nanofluids: A Case Study Based on Natural Circulation Mini-Loops

Firat SEZGIN[1], Nur COBANOGLU[2], Nejc VOVK[3], Elif Begum ELCIOGLU[1,*], Ziya Haktan KARADENIZ[4], Lovro BOBOVNIK[3], Erdem OZYURT[1], Andrej SPILER[3], Blaz KAMENIK[3], Timi GOMBOC[3], Alpaslan TURGUT[5], Jure RAVNICK[3]

1: Department of Mechanical Engineering, Eskişehir Technical University, Eskisehir, Turkey
2: Graduate School of Natural and Applied Sciences, Izmir Katip Celebi University, Izmir, Turkey
3: Faculty of Mechanical Engineering, University of Maribor, Maribor, Slovenia, SI
4: Department of Energy Systems Engineering, Izmir Institute of Technology, Izmir, Turkey
5: Department of Mechanical Engineering, Dokuz Eylul University, Izmir, Turkey

* Corresponding author: Tel.: +90 535 635 9446; Email: ebelcioglu@eskisehir.edu.tr

**Abstract:** Research on nanofluid heat transfer has been performed either via experimental settings developed to stand as the lab-scale twin of the real system, or numerical analysis accompanied by application-specific simulations with carefully selected boundary and initial conditions, algorithms, and convergence criteria. For some time, nanofluids heat transfer has been simulated by means of one-phase or two-phase methods, and when possible, the results from these two approaches have been compared to each other/a benchmark case (experiment results) based on convergence, error margins, representability, and comprehensiveness. This work, as the first report of our ongoing long-term research, aims to present a systematic comparison between the one-phase and two-phase simulation results, in comparison to the experimental demonstration of the system of choice. $Al_2O_3$-water nanofluids are considered to be employed in a single-phase natural circulation mini-loop (SPNCmL). Two independent one-phase simulations (via ANSYS CFX and ANSYS FLUENT), while we also report on ongoing efforts in developing two-phase simulation strategy in OpenFoam. The results of this work are expected to shed a light on the long-waited problem to be answered: "Onephase vs. two-phase nanofluid modeling: which to choose?".

**Keywords:** Nanofluids, Modeling, Natural Circulation, Mini-Loop.

## 1. Introduction

The current state of the nanofluids literature reveals that nanofluids are considered either as one- or two-phase substances. In numerical models, researchers prefer one-phase over two-phase approach since the former mostly yields results with appreciable errors and is less computationally expensive. Two-phase simulation strategies are more complicated but expected to yield higher accuracy. Here, we aim to differentiate one- and two-phase approach accuracies with systematic comparison of numerical predictions with experimental data from the literature. The Single-Phase Natural Circulation mini Loop (SPNCmL) is selected as the system of the study due to its passive nature as well as its simplicity, easy control, safety, and reliability. The accuracy of the numerical approaches is evaluated by SPNCmL's effectiveness with $Al_2O_3$-$H_2O$ nanofluid as the working fluid.

## 2. Material and Methodology

In this work, we analyze SPNCL's effectiveness via comprehensive one-phase and two-phase simulations. The geometry of the SPNCmL is obtained from experimental study (Doganay and Turgut, 2015). Çobanoğlu and Karadeniz (2021) developed a numerical model by using ANSYS CFX and validated by solving the heat transfer problem for fluid flow and conjugate heat transfer including the pipe and insulation. Further information on the numerical model is given in (Çobanoğlu and Karadeniz, 2021) where thermophysical properties were temperature dependent.

The effectiveness factor is introduced to define

the performance of SPNCmLs, as in Eq. 1.

$$\varepsilon = \frac{T_{L,5} - T_{L,2}}{T_{L,5} - T_C} \quad (1)$$

The one-phase simulations performed on ANSYS CFX are compared against the ones obtained via ANSYS FLUENT. The latter is performed using pressure-based solver and the SIMPLEC algorithm. The second-order upwind solution scheme is used for the discretization of momentum and energy. In order to capture gravitational effects, PRESTO! scheme is used for pressure discretization, and the average temperatures at thermocouples location are monitored. The solution is assumed to be converged if the average temperature change is $<10^{-3}$ and residual values reach $10^{-10}$ for energy and $10^{-6}$ for others. In order to see the effect of Boussinesq approximation, density is defined both according to Boussinesq approximation and as a function of temperature.

An updated version of OpenFoam is being developed to support two phase simulations of nanofluid flow and heat transfer. It operates by employing the Euler-Lagrange strategy. Particles are tracked in the flow field via one-way coupled Lagrange simulation by numerically integrating the Maxey-Riley equation and adding two effects: thermophoresis and Brownian motion. After a fluid simulation time step, particle tracking is performed, the resulting distribution of particles analyzed and redistributed to the Eularian mesh as a concentration field. This concentration field is then used to evaluate thermophysical properties of the nanofluid and used in the Eulerian part of the simulation.

## 3. Results and Discussions

One-phase simulation results show that the numerical model developed by ANSYS FLUENT predicts the effectiveness values for all cases up to 14.81% (for water) variation. However, the error margin of the numerical model developed by ANSYS CFX ranges from -8% to +3%. As nanofluid concentration increases, the predicted values converge to the experimental data, and the best convergence is observed for 1 vol.% at 10 W of heater power with -8.73% error for ANSYS FLUENT and +1.33% for ANSYS CFX. Higher heater powers result in underprediction of the effectiveness values for one-phase numerical models developed on both platforms. When conjugate heat transfer is considered with the addition of Cu pipe and insulation material, both ANSYS FLUENT and ANSYS CFX results differ up to -8.41% and -8.56% from the experimental results for the one-phase approach, respectively. The effectiveness values are very similar for these solvers. A linear variation of the effectiveness with the heater power and nanofluid concentration was not observed according to the results obtained in both platforms. However, approach of conjugate heat transfer problem improves the accuracy of the numerical simulations.

## 4. Conclusions

We have shown that single phase simulations of nanofluid flow and heat transfer are able to accurately predict the transport phenomena in natural circulation mini-loop. We hope that ongoing work on two-phase simulations will further improve the accuracy of numerical predictions.

## Acknowledgments

This work is supported by TUBITAK-ARRS Bilateral Collaboration program under grants 122N346 (TUBITAK) and BI-TR/22-24-05 (ARRS).

## References

Çobanoğlu, N., Karadeniz, Z.H., 2021. Stability And Flow Propagation In Single Phase Natural Circulation mini Loops During The Developing Flow Phase. Presented at the 23rd Congress on Thermal Science and Technology with International Participation, Gaziantep, Turkey, pp. 1777–1785.

Doganay, S., Turgut, A., 2015. Enhanced effectiveness of nanofluid based natural circulation mini loop. Appl. Therm. Eng. 75, 669–676.

# Exploring the Use of Stationary Nanofluids in a Direct Absorption Solar Collector System

Agathe BJELLAND ERIKSEN[1], Pawel KOSINSKI[1,*], Boris V. BALAKIN[2], Anna KOSINSKA[2]

1: Department of Physics and Technology, University of Bergen, Bergen, Norway
2: Department of Mechanical and Marine Engineering, Western Norway University of Applied Sciences, Bergen, Norway

* Corresponding author: Tel.: +47 55582817; Email: pawel.kosinski@uib.no

**Abstract**: The Direct Absorption Tube Solar Collector (DASC) is a commonly used device for harnessing solar radiation, which absorbs incident radiation using a heat transfer fluid containing particles. To address some of the challenges associated with pumping nanofluids, a novel system involving a stationary nanofluid located in an irradiated transparent tube was studied. Six different concentrations of carbon black were investigated, with the highest performance observed for a nanofluid concentration above 0.0015%.

**Keywords:** nanofluid, direct absorption solar collectors, solar energy

## 1. Introduction

Nanofluids (fluids containing materials of nano-sized solid particles) are used to improve the performance of solar collectors because of their favorable absorption properties. With the goal of boosting the efficiency of solar energy harvesting devices, research into the use of nanofluids is a crucial area of study [1].

The Direct Absorption Tube Solar Collector (DASC) is an effective way to harness solar radiation using a transport medium. Unlike conventional solar collectors, DASC absorbs the incident radiation directly by a heat transfer fluid containing particles [2].

The most common design involves irradiation of nanofluid as it flows. The heated nanofluid is later transferred to a heat exchanger where it releases heat to water. Nevertheless, this strategy requires pumping of nanofluids that may influence the lifetime of pumps, erosion of the piping etc. Therefore, in the present research, we studied a stationary nanofluid located in an irradiated transparent tube. The heated water passed through the nanofluid. Thus, this novel system is essentially less complex than the existing DASCs.

## 2. Experimental set-up

In our experiments, a two-step process for preparing nanofluids was employed. All the experiments used ENSACO 350G carbon black with an equal amount of sodium dodecyl sulfate (SDS) for stabilizing the obtained nanofluids. Both carbon black and CB were dispersed in distilled water. The mixture was stirred for 20 minutes using a magnetic stirrer, and then sonicated for 60 minutes in a Branson 3510 ultrasonic bath with the frequency of 50-60 kHz.

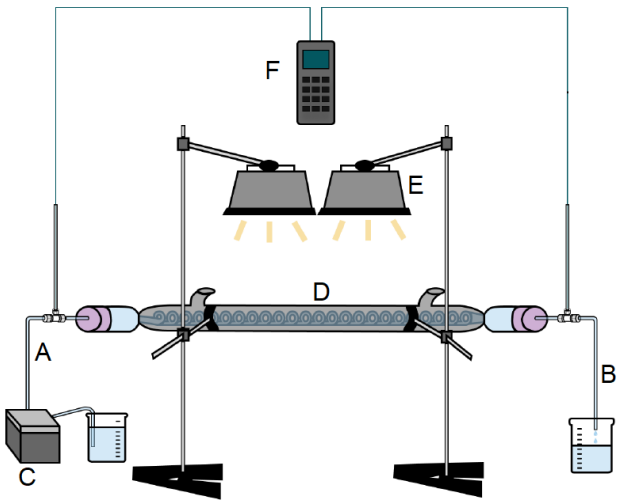


**Fig. 1** Schematic of the experimental set-up

In this research, six different concentrations of carbon black were manufactured: 0.0015 wt.%, 0.005 wt.%, 0.01 wt.%, 0.015 wt.%, 0.02 wt.%, and 0.05 wt.%.
The experimental set-up is depicted in Fig. 1. The working fluid (water) was pumped through the system from point A to B using a Preciflow LAMBDA peristaltic pump (denoted as C). The flow rate was 360 ml/h.
The working fluid entered a system (denoted by D) consisting of an outer glass tube (outer diameter 38 mm, length 50 cm) filled with nanofluid, irradiated by two 400W halogen lamps (denoted by E). The distance between the glass tube and lamps was 8 or 12 cm.
This fluid was transported in an internal pipe (inner diameter 5 mm) spiraling inside the shell with a pitch of 10 mm. The coil had an external diameter of 30 mm. The absorbed heat resulted in a temperature increase of the nanofluid, which heated the working fluid. The glass shell was equipped with two openings extended by short rubber pipes for filling the system with nanofluid. This also allowed the nanofluid to freely expand due to the temperature rise. In addition, the pipes at the inlet and outlet contained T-junctions for measuring the temperatures using K-type thermocouples. For temperature logging, the Multilogger Thermometer from Omega Engineering was used (denoted as F in the figure). During the experiments, the temperatures at the inlet and outlet were recorded every 2 seconds. The experiments lasted for 60 minutes. The average room temperature was 22ºC at the experiment start.

## 3. Results and conclusions

At first, for illustration Figure 2 depicts the history of temperature difference between the outlet and inlet for the case where the carbon black concentration was 0.0015%. The figure presents results for five experiments.
Furthermore, Figure 3 collects all studied results and shows the final temperature difference (after 60 min, as indicated above). The figure compares the nanofluid concentration, as well as the distance between the lamps and irradiated set-up.
The first conclusion is that all the investigated nanofluids outperformed water, and the maximum performance was observed for nanofluid concentration above 0.0015%. It is interesting to note that previous findings (e.g. [3]) reported an increase in heat transfer performance for nanoparticles at an optimal concentration of 0.005%, although they focused on a different geometry with a flowing nanofluid. Therefore, their results are consistent with ours.

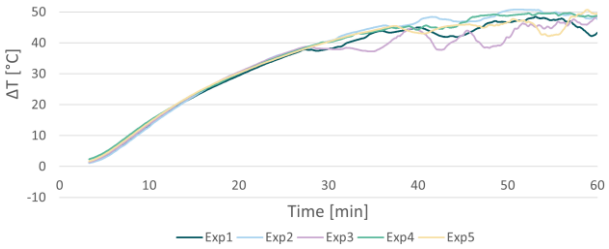


**Fig. 2** History of temperature increase for carbon black concentration 0.0015% for five different experiments.

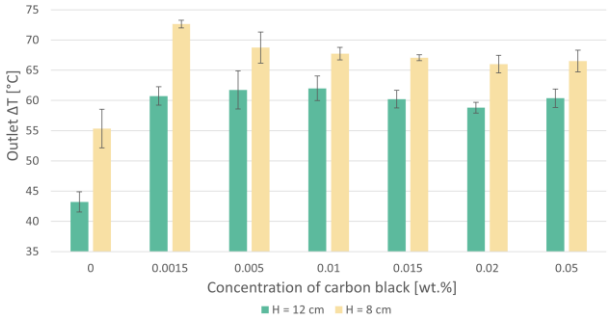


**Fig. 3** The obtained temperature difference for various nanofluid concentrations and distances of the set-up from the irradiating lamps.

## References

[1] A.K. Hamzat, M.I. Omisanya, A.Z. Sahin, O.R. Oyetunji, N.A. Olaitan: Energy Conversion and Management 266 (2022) 115790
[2] J.E. Minardi, H.N. Chuang: Solar Energy 17 (1975) 179–83
[3] P. G. Struchalin, V. S. Yunin, K. V. Kutsenko, O. V. Nikolaev, A. A. Vologzhannikova, M. P. Shevelyova, O. S. Gorbacheva, B. V. Balakin: International Journal of Heat and Mass Transfer 179 (2021) 12171

## SESSION 6b
## Boiling and condensation in micro systems
Chair: **S. Bortolin**



Giovanni Antonio LONGO[1], Simone MANCIN[1], Giulia RIGHETTI[1], Claudio ZILIO[1]
1: Department of Management and Engineering, University of Padova, Vicenza, IT



Michał PYSZ[1] , Dariusz MIKIELEWICZ[1]
1: Institute of Energy, Gdańsk University of Technology, Gdańsk, PL



Yutaku KITA[1, 2], Masamichi KOHNO[2, 3], Yasuyuki TAKATA[2]
1: Department of Engineering, King’s College London, UK
2: International Institute for Carbon-Neutral Energy Research (WPI-I[2]CNER), Kyushu University, Japan
3: Department of Mechanical Engineering, Kyushu University, Japan



Jungtaek KIM[1], Yeonsu JUNG[2], Ho-Young KIM[1]
1: Department of Mechanical Engineering, Seoul National University, Seoul, Republic of Korea
2: School of Engineering and Applied Sciences, Harvard University, Cambridge, MA, USA



Lin GUO[1] , Cong WANG[1] , Huiling LIU[1] , Zhigang LIU[1]
1: Energy Research Institute, Qilu University of Technology, Jinan, 250014, China

# Condensation Heat Transfer of Propylene Inside a Compact Horizontal Microfin Tube

Giovanni Antonio LONGO[1] , Simone MANCIN[1], Giulia RIGHETTI[1,*], Claudio ZILIO[1]

1: Department of Management and Engineering, University of Padova, Vicenza, IT

* Corresponding author: Tel.: +39 0444 998746; Email: giulia.righetti@unipd.it

**Abstract:** In the last decades, HC refrigerants attracted a new interest, first as substitutes for CFC and HCFC refrigerants subjected to phase-out for their large Ozone Depleting Potential (ODP) and, more recently, as alternatives for HFC refrigerants with large Global Warming Potential (GWP). Nevertheless, the open literature collects just a few experimental data on HCs two-phase heat transfer and pressure drop inside small diameter tubes (ID<6 mm), most of them are quite recent. This paper presents some new experimental data collected during propane condensation inside a 4.2 mm ID horizontal copper microfin tube. Tests were carried out at 30 °C of saturation temperature, and refrigerant mass flux in the range 75–400 kg m $^{-2}$ s $^{-1}$ at increasing vapor quality. The effect refrigerant mass velocity and mean vapor quality are evaluated separately. Finally, the experimental data were then used to assess some classical literature correlations.

**Keywords:** Microfin, Condensation, Heat transfer coefficient, Pressure drop

## 1. Introduction

Hydrocarbons found large utilisation in refrigeration since the beginning for the good thermodynamic and thermophysical properties, the high compatibility with construction materials and lubricants that promoted the use in vapour compression systems. The high flammability is the major handicap for the extensive application of hydrocarbon refrigerants, actions to reduce the risk of hydrocarbon refrigerants include:
- reduction of the refrigerant charge in refrigerating machines;
- application of refrigerating units with secondary fluids.

The use of microfin tubes is particularly effective in both cases.
In the open literature, there are only scarce experimental data points concerning hydrocarbons boiling and condensation inside microfin tubes [1-2]
This paper presents some new experimental tests carried out at 40 °C of saturation temperature, with refrigerant mass flux in the range 75–400 kg m $^{-2}$ s $^{-1}$ at decreasing vapor quality during propylene condensation inside a 4.2 mm ID microfin tube. Average heat transfer coefficients and frictional pressure drop are analysed and compared against some classical literature correlations.

## 2. Set up and data reduction

The experimental facility consists of a pumped refrigerant loop. The liquid refrigerant is partially evaporated to achieve the set quality at the inlet of the microfin test section, then it partially condenses into the test section and finally it is completely condensed inside a brazed plate condenser. The test-section is a 1300 mm tube-in-tube microfin tube in which the condensing refrigerant flows in the inner tube, while water flows counter-current in the annulus. It is instrumented with four copper-constantan thermocouples embedded in the tube wall for the direct measurement of the surface temperature.
The experimental results are reported in terms of condensation average heat transfer coefficient (HTC):

$$HTC = Q / (A \, \Delta T) \quad (1)$$

Where:

$$A = \pi \, D_{fintip} \, L \quad (2)$$

and frictional pressure drop $\Delta p_f$, computed by subtracting the inlet / outlet local pressure drop $\Delta p_c$, and adding the momentum pressure recovery $\Delta p_a$ from the total pressure drop measured $\Delta p_t$:

$$\Delta p_f = \Delta p_t - \Delta p_c + \Delta p_a \quad (3)$$

For a more detailed data reduction and set up description, please refer to [3].

## 3. Experimental results

Figure 1 presents the average HTC ad a function of the vapor quality at different mass velocity (from 75 to 400 kg $m^{-2}$ $s^{-1}$). It shows a great sensitivity to vapour quality and a nonmonotonic trend versus mass velocity. In fact, the slope becomes higher at higher refrigerant mass fluxes, indicating a dominant effect of the forced convection condensation mechanism. It can be explained considering the effects of the surface tension in the condensate drainage in a micro-finned surface and of the turbulence induced by the helical micro-fins.

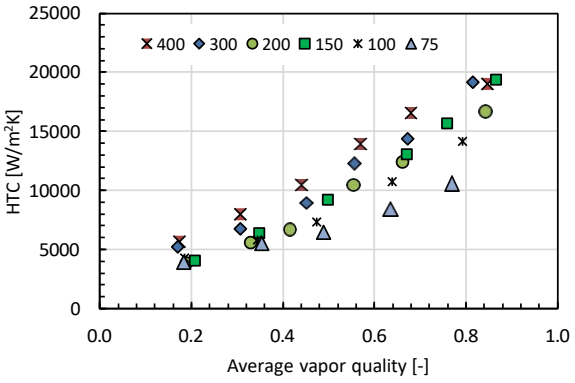


Figure 1. HTC vs average vapor quality at several mass flow rates

Figure 2 presents the condensation frictional pressure drop at 40°C of saturation temperature and different refrigerant mass fluxes, ranging from 75 to 400 kg $m^{-2}$ $s^{-1}$. It exhibits a great sensitivity to mass velocity and vapour quality, as expected.

The present experimental data were compared against some well-established heat transfer correlations for condensation inside microfin tubes. The Hirose et al. [4] model satisfactorily predicted the HTC data (mean relative error = -1.9 %, mean absolute error= 23.9 %), while the Diani et al. [5] model well predicted the frictional pressure drop data (mean relative error= -1.2 %, mean absolute error= 14.3 %).

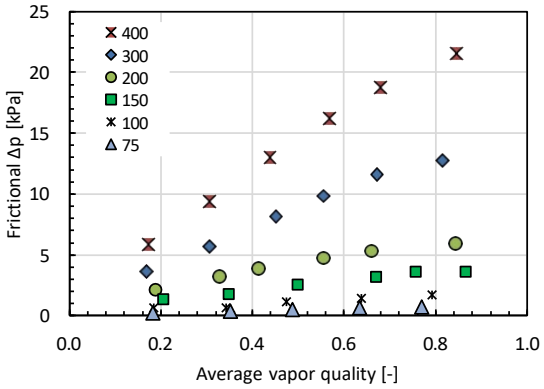


Figure 2. Frictional pressure drops vs average vapor quality at several mass flow rates

The microfin tube HTC were compared against experimental data collected with propylene on an equivalent smooth tube [6]. HTC exhibits a maximum heat transfer enhancement with respect to the smooth tube above 5 times at a mass velocity of 100 kg $m^{-2}$ $s^{-1}$ and a vapour quality higher than 0.6. At the highest tested mass velocity, 400 kg $m^{-2}$ $s^{-1}$, the enhancement is just above 1.6 which is the surface area increase over the smooth tube.

## References

[1] J. Wu et al. 2021. Exp Heat Transf doi.org/10.1080/08916152.2020.1713255
[2] E. Allymehr et al. 2021. Energies doi.org/10.3390/en14092647
[3] G. A. Longo, et al. 2022. Int J Heat Mass Transf. doi.org/10.1016/j.ijrefrig.2022.10.001
[4] M. Hirose, et al. 2018.Int. J. Refrigeration doi.org/10.1016/j.ijrefrig.2018.04.014
[5] A. Diani, et al. 2018. Int. J. Heat Mass Transf. doi.org/10.1016/j.ijheatmasstransfer.2018.06.0 47
[6] G. A. Longo et al. 2017. Int J Heat Mass Transf. doi.org/10.1016/j.ijheatmasstransfer.2016.12.0 87

# Pressure drop and heat transfer of R1233zd(E) at moderate and high reduced pressures in vertical tubes

Michał PYSZ[1] , Dariusz MIKIELEWICZ[1, *]

1: Institute of Energy, Gdańsk University of Technology, Gdańsk, PL

* Corresponding author: Tel.: +48 347 2254; Email: dariusz.mikielewicz@pg.edu.pl

**Abstract:** The study presents an extensive database concerning flow boiling of R1233zd(E) in vertical stainless steel tubes with 2 and 3 mm inner diameters. The heat transfer coefficient and both adiabatic and non-adiabatic pressure drops were measured for reduced pressures ranging from 0.4 to 0.7. Effects of heat flux, saturation temperature, vapor quality, mass flux, and flow regime were analyzed. Three different heat fluxes were considered: 20, 30, and 45 kW/m$^2$. Mass velocities ranged from 200 to 1000 kg/m$^2$s. The general conclusion is that the higher the saturation temperature the bigger the influence of nucleate boiling phenomena. The latter can be observed not only in thermal properties but in flow patterns as well. The higher the value of reduced pressure the harder it is to determine the boundary between intermittent flow and annular flow.

**Keywords:** High reduced pressures, Flow boiling, Heat transfer coefficient, Pressure drop; Minichannels

## 1. Introduction

Fluid behavior in the vicinity of the thermodynamic critical point is not still well understood. Additionally, there is a gap of knowledge in such area in the case of low boiling point of perspective refrigerants. The increased interest in Organic Rankine Cycle systems as well as high-temperature heat pumps requires a detailed information about the thermal performance of such working fluids. Currently most of the literature concerning high values of reduced pressure refers to carbon dioxide and water. Accomplishing detailed experimental data at high reduced pressures is challenging due to observed difficulties in obtaining steady state parameters. In that light even for carbon dioxide data there can be seen significant discrepancies. Data obtained for the same experimental conditions on different experimental facilities can differ by a factor of 2 [1]. In the paper new experimental evidence together with data from [2], [3] have been considered in order to evaluate the effect of reduced pressure on both heat transfer and pressure drop at moderate and high reduced pressure to enhance an in-house model [4].

## 2. Experimental facility

The study has been performed in a dedicated experimental facility. The laboratory facility is able to maintain pressures up to 50 bar and temperatures up to 250 ˚C. The flow of liquid refrigerant is realized by means of the gear pump and the pressure is built in the system with the use of a bladder hydro-accumulator located on the liquid side of the loop. The test section consists of the preheater, heat transfer section, and visualization test section. Both the preheater and test section are heated by the Joule effect with the use of two separate DC power suppliers. There are nine temperature measurement locations with eighteen K-type thermocouples which are soldered to the outer wall of the test tube. Mass flow rate is measured by means of the Coriolis mass flow meter. Flow structure analysis is possible thanks to the borosilicate glass tube placed right after the heat transfer test section. A fast camera is used to collect visualisations. Vapor quality is calculated based on the enthalpy-based energy balance of the preheater and test section.

## 3. Results

Figure 1 presents the sample of the results of heat transfer coefficient obtained for reduced pressure equal to 0.6. Letters A to D correspond the different flow structures which are in detail presented in Figure 2.

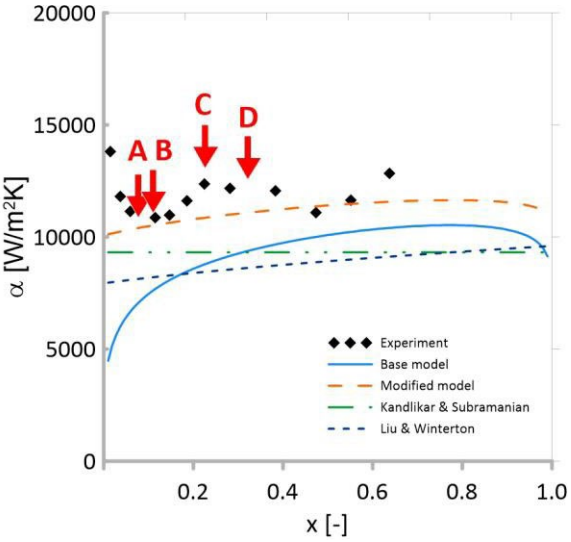


Figure 1. Comparison between experimental heat transfer coefficient presented in the function of vapor quality and the theoretical heat transfer coefficient calculated for several heat transfer models (reduced pressure 0.6, G=800 kg/m$^2$s, and q=20 kW/m$^2$)

The experimental results were compared with several heat transfer models [5], [6] including the enhanced version of the in-house model.

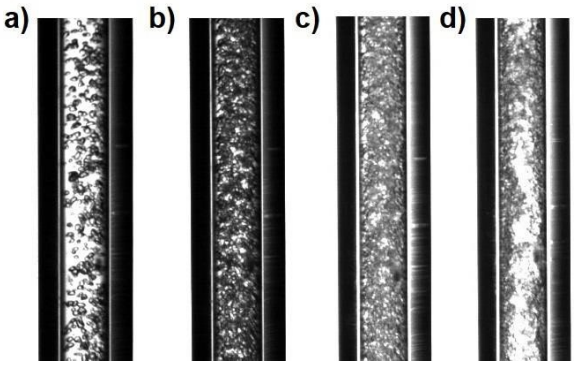


Figure 2. Flow structures for reduced pressure $p_r$=0.6, q=20 kW/m$^2$ and G=800 kg/m$^2$s: a) vapor quality x=0.077; b) x=0.111; c) x=0.226; d) x=0.321

The results show that nucleate boiling can be seen for vapor qualities as high as x=0.226 which is significantly different from a similar case at small reduced pressures. Additionally, the transition from intermittent flow to annular flow starts around x=0.321. The full annular flow was not observed until x=0.5. The obtained trends and flow structures confirm the dominance of nucleate boiling. The enhanced version of the model approximates the experimental data with high accuracy (mean absolute percentage error MAPE, for the whole database was equal to 23.17%).
On the basis of collected observations relevant modifications to the in-house model have been introduced which significantly improve its performance.

## Acknowledgements

Work was funded from the research project 2017/25/B/ST8/00755 by National Science Centre, Poland.

## References

[1] D. B. Marchetto, D. C. Moreira, R. Revellin, and G. Ribatski, “A state-of-the-art review on flow boiling at high reduced pressures,” *Int J Heat Mass Transf*, vol. 193, p. 122951, Sep. 2022, doi: 10.1016/j.ijheatmasstransfer.2022.122951.

[2] M. Pysz, S. Głuch, and D. Mikielewicz, “Experimental study of flow boiling pressure drop and heat transfer of R1233zd(E) at moderate and high saturation temperatures,” *Int J Heat Mass Transf*, vol. 204, p. 123855, May 2023, doi: 10.1016/j.ijheatmasstransfer.2023.123855.

[3] M. Pysz, S. Głuch, and D. Mikielewicz, “Study of R-1233zd(E) convective boiling heat transfer at moderate reduced temperature,” in *17th UK Heat Transfer Conference*, 2022.

[4] D. Mikielewicz, J. Mikielewicz, and J. Tesmar, “Improved semi-empirical method for determination of heat transfer coefficient in flow boiling in conventional and small diameter tubes,” *Int J Heat Mass Transf*, vol. 50, no. 19–20, pp. 3949–3956, Sep. 2007, doi: 10.1016/j.ijheatmasstransfer.2007.01.024.

[5] S. G. Kandlikar and P. Balasubramanian, “An Extension of the Flow Boiling Correlation to Transition, Laminar, and Deep Laminar Flows in Minichannels and Microchannels,” *Heat Transfer Engineering*, vol. 25, no. 3, pp. 86–93, Apr. 2004, doi: 10.1080/01457630490280425.

[6] Z. Liu and R. H. S. Winterton, “A general correlation for saturated and subcooled flow boiling in tubes and annuli, based on a nucleate pool boiling equation,” *Int J Heat Mass Transf*, vol. 34, no. 11, pp. 2759–2766, Nov. 1991, doi: 10.1016/0017-9310(91)90234-6.

# Prediction of Quench: Applicability of Droplet Model to Spray Cooling

Yutaku KITA[1, 2,*], Masamichi KOHNO[2, 3], Yasuyuki TAKATA[2]

1: Department of Engineering, King's College London, UK
2: International Institute for Carbon-Neutral Energy Research (WPI-I$^2$CNER), Kyushu University, Japan
3: Department of Mechanical Engineering, Kyushu University, Japan

* Corresponding author: Email: yutaku.kita@kcl.ac.uk

**Abstract:** We performed spray cooling tests at various ambient pressures to determine the mechanism that triggers quench (transition from film boiling to nucleate boiling). The experiments were carried out in a pressure vessel filled with argon gas to minimize the effect of surface oxidization. Among several existing theories, we found a mechanistic model to predict our quench temperatures reasonably well over the ambient pressures tested. Moreover, we developed a model to predict the cooling rate during the film boiling regime considering heat transfer by a single droplet. The applicability of the model to spray cooling was discussed.

**Keywords:** Spray cooling, Quench, Boiling, Droplets

## 1. Introduction

In spray cooling for steelmaking, the transition from the film boiling regime to the nucleate boiling regime is termed "quench" and is paramount to predict as it remarks the thermal history of the product. Despite several analytical and empirical models being proposed to predict quench temperature, deviation from reported experimental values remains enormous. This could be attributed to the lack of systematicity of the experiments which potentially has led to some influential factors unaccounted for e.g. surface oxidization [1]. In the present contribution, we performed spray cooling tests in a controlled environment to minimize the effect of oxidation. Cooling curves were obtained for the ambient pressures ranging 0.1 MPa –0.5 MPa. Several existing models for the onset of quench were compared with our experimental results. Furthermore, we attempted to predict the cooling curve in the film boiling regime until the quench point using single droplet impingement models [2].

## 2. Experimental Procedures

Our spray cooling test rig is assembled in a pressure vessel. First, the vessel was evacuated to ~$10^{-3}$ Pa. An iron disk (mirror-polished, 50 mm in diameter and 10 mm in thickness) was heated up to 730 °C with a halogen lamp heater. Then, we introduced argon gas until the system pressure reached target values i.e. 0.1, 0.2, 0.3, 0.4 and 0.5 MPa. Once the steady state was confirmed, degassed DI water at 24 °C was sprayed on to the sample. We used a nozzle with a conical spray angle of 70°, which was located 60 mm above the sample surface. Two volumetric fluxes were tested i.e. 54 and 79 L/($m^2$·min), resulting in the mean droplet diameter and velocity of 121 μm and 6.23 m/s, and 128 μm and 10.48 m/s, respectively. The sample temperature was monitored every 0.1 sec using a thin thermocouple embedded 1 mm below the top surface.

## 3. Results and Discussion

Quench temperatures were determined by the cooling curves obtained in our test. In Fig. 1, quench temperatures are plotted as a function of ambient pressure. Quench occurred at higher temperatures at higher ambient pressure and at higher volumetric flux. We calculated the quench temperatures using several models i.e. the thermodynamic limit of superheat [3], the hydrodynamic approach [4] and the mech-

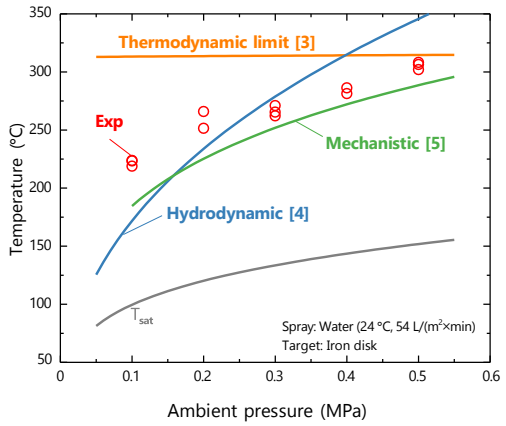


Fig. 1 Quench temperatures as a function of ambient pressure.

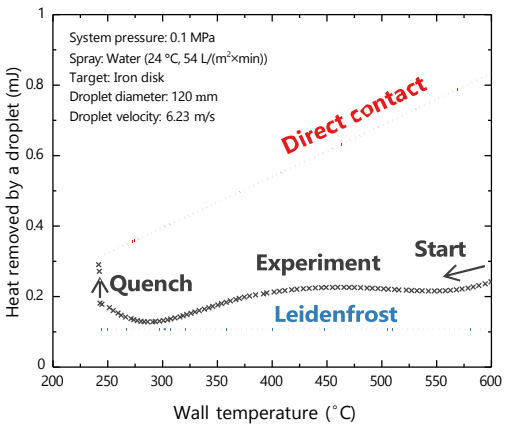


Fig. 2 Heat removed by each droplet.

anistic model [5]. As compared in Fig. 1, we found the mechanistic model to predict our quench temperatures reasonably well.

Next, we attempt to predict the cooling rate during the film boiling regime. We evaluated two extreme cases of droplet impingement i.e. the Leidenfrost scenario and direct liquid-solid contact. The former is modelled following Castanet et al. [6] while the latter is appr-oximated as the contact of semi-infinite bodies. These models provide the amount of heat removed by a single droplet. Experimental values of this quantity were calculated by dividing the heat transfer rate, which can be obtained from our cooling curve, by the number of droplets impacting the surface per unit time, which can be estimated based on the spray condition. Fig. 2 presents the heat removed by a droplet, both experimental and theoretical, as a function of the surface temperature. We found the experimental values between the two extreme models, which seems reasonable as it is possible that some fraction of droplets was in contact with the surface even in the film boiling regime. As the surface temperature decreased, the experimental value approached the direct contact model until quench was induced.

## 4. Conclusions

We demonstrated the applicability of some predictive models for quench temperature and for cooling rates in the film boiling regime. These models agreed reasonably well with our controlled experiments. Our results also sugge-sted some contributions to the cooling rate by direct heat conduction due to local liquid-solid contact during the film boiling regime, which could be worth further investigation.

## References

[1] Tsukamoto, K., Kita, Y., Inoue, S., Hamanosono, T., Hidaka, S., Ueoka, S., Fukuda, H., Kohno, M., Takata, Y., 2020. On the onset of quench during spray cooling: The significance of oxide layers. Appl. Therm. Eng. 179, 115682.

[2] Kita, Y., Nakamatsu, M., Hidaka, S., Kohno, M., Takata, Y., 2022. Quenching mechanism of spray cooling and the effect of system pressure. Int. J. Heat Mass Transf. 190, 122795.

[3] Lienhard, J.H., 1976. Correlation for the limiting liquid superheat. Chem. Eng. Sci. 31, 847–849.

[4] Berenson, P.J., 1961. Film-boiling heat transfer from a horizontal surface, J. Heat Transf. 83, 351–356.

[5] Cai, C., Mudawar, I., Liu, H., 2020. Mechanistic method to predicting minimum heat flux point wall temperature in saturated pool boiling. Int. J. Heat Mass Transf. 156, 119854.

[6] Castanet, C., Chaze W., Caballina, O., Collignon, R., Lemoine, F., 2018. Transient evolution of the heat transfer and the vapor film thickness at the drop impact in the regime of film boiling. Phys. Fluids 30, 122109.

# Capillary Rise in Open Microchannels with Evaporation

Jungtaek KIM[1], Yeonsu JUNG[2], Ho-Young KIM[1,*]

1: Department of Mechanical Engineering, Seoul National University, Seoul, Republic of Korea
2: School of Engineering and Applied Sciences, Harvard University, Cambridge, MA, USA

* Corresponding author: Tel.: +82 2 880 9286, Email: hyk@snu.ac.kr

**Abstract:** We study the capillary rise dynamics of evaporative liquid in vertical open channels, where the evaporative loss of the liquid severely limits the rise height. We first quantify the evaporation enhancement near the solid-liquid-gas contact line, which is responsible for the so-called coffee ring stains. Then we construct a differential equation that describes the rise height of the liquid with time by considering mass conservation of evaporating viscous liquid drawn against gravity via capillarity. We find an optimal channel width that maximizes the equilibrium rise height under a given channel depth, unlike nonevaporative rise whose equilibrium height monotonically increases with the reduction of channel width.

**Keywords:** Capillary rise, Evaporation, Open Channel, Optimal Channel Width

## 1. Introduction

Capillary rise in a vertical hydrophilic tube is a classical example of surface-tension-driven flows, whose study dates back to the 18th century. Here we extend this problem to a case where the liquid rises in a vertical open channel, where the rising liquid evaporates leading to the mass loss in the course of capillary rise, as shown in Fig. 1. To predict the temporal rise height evolution, we first need to evaluate the evaporation rate from the liquid contained in a submillimetric channel, which is deeply affected by the presence of the three phase (solid-liquid-gas) contact line at the channel corners. Then we set up a differential equation for the rise height considering the effects of surface tension, gravity, viscosity and evaporation. Our results of theory and experiment allow us to find the optimal channel width that maximizes the evaporative capillary rise height [1].

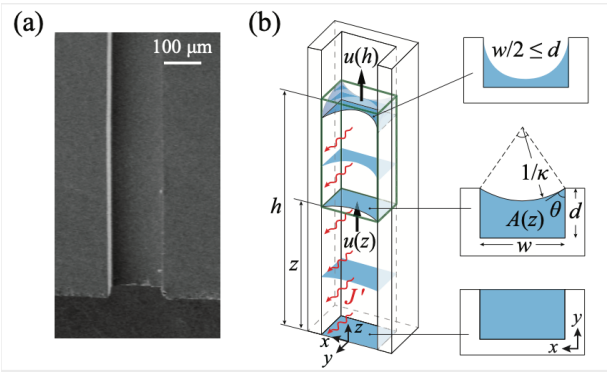


Fig. 1. (a) A vertical open channel on a Si wafer, 0.44 mm wide and 0.094 mm deep. (b) The cross-sections of a liquid column.

## 2. Results

### 2.1 Evaporation rate at open microchannel

Our experimental measurement results indicate that the evaporation rate of ethanol per unit length, $J'$, is given by $J'=J_0 w^{(1-n)}$, where $n$=0.62 and $J_0$=4.1X10-8 $m^{1+n}s^{-1}$, as shown in Fig. 2.

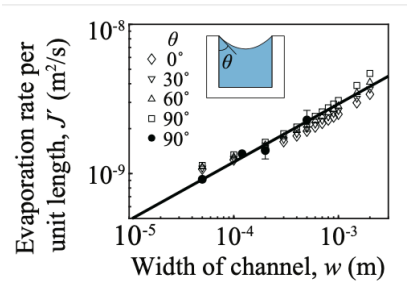


Fig. 2. Evaporation rate as a function of channel width.

### 2.2 Capillary rise height

For a control volume containing the advancing liquid interface, a green cuboid in Fig. 1, the mass conservation is written as

$$A(z)u(z)\text{-}(h\text{-}z)J'=A(h)\mathrm{d}h/\mathrm{d}t, \quad (1)$$

where $A(z)$ and $u(\mathbf{z})$ are respectively the cross-sectional area of the liquid column and the average velocity at the elevation $z$ from the reservoir, and $h$ is the rise height. We relate the pressure gradient and the flow velocity via Darcy's law, which is combined with Eq. (1) to give the temporal evolution of the rise height.

Fig. 3 shows the experimental and theoretical results of the rise height of ethanol versus time, clearly revealing the critical effects of evaporation in the rise dynamics. The equilibrium rise height with evaporation is severely limited to a lower value than without evaporation, and the rise within narrower channels is more affected by evaporation than within wider ones by showing slower speed and lower equilibrium height.

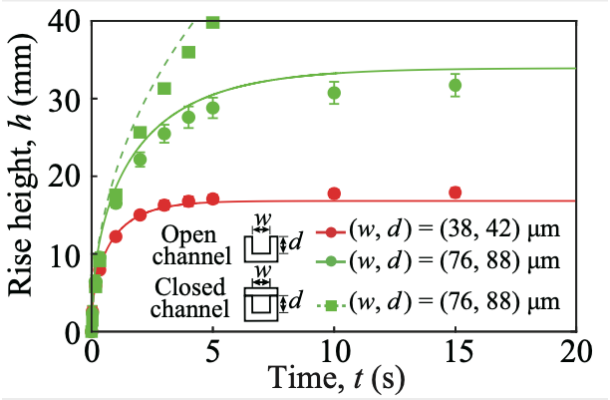


Fig. 3. The rise height versus time. Circles and squares are experimental results and the lines are theoretical predictions.

### 2.2 Optimal channel dimension

Fig. 4 shows that an optimal channel width exists that maximizes the equilibrium rise height at a given channel depth. When the width is smaller than the optimal width, the height increases with the width because the ratio of the evaporative flux to the liquid volume is higher for a narrower channel. When the width is greater than the optimal width, the rise height decreases with the width due to combined effects of the excessive evaporative loss and the decreased capillary effects.

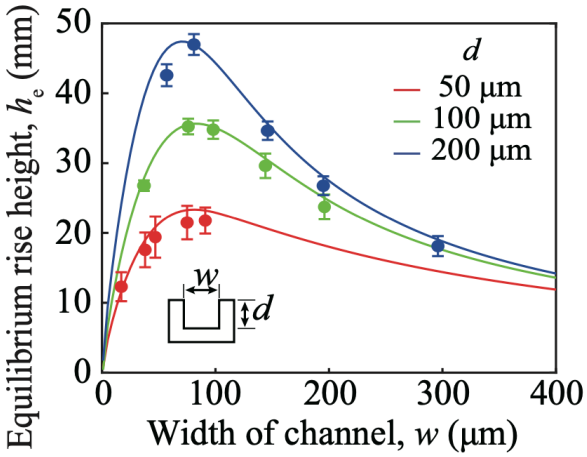


Fig. 4. Equilibrium rise height versus channel width for different channel depths.

## 3 Conclusion

We have investigated the capillary rise dynamics of an evaporative liquid in a vertical open microchannel using a combination of experiment and theory. Unlike the capillary rise within closed channels involving no evaporation, there exists an optimal channel width that maximizes the height of evaporative capillary rise once the channel depth is given. This work can help us to design optimal fluid networks relying on both evaporation and capillarity, such as animal wrinkles and air-conditioning equipment.

### Reference

[1] J. Kim, Y. Jung, H.-Y. Kim, Evaporative capillary rise. Phys. Rev. Fluids **7**, L032001 (2022).

# The Effect of Surface Roughness upon Nucleate Boiling with Different Surface Wettabilities: Insights from Molecular Dynamics

Lin GUO[1] , Cong WANG[1] , Huiling LIU[1] , Zhigang LIU[1,]*

1: Energy Research Institute, Qilu University of Technology, Jinan, 250014, China

* Corresponding author: Email: linguo@sderi.cn

**Abstract:** Despite the fact that engineered surface enabling remarkable phase change heat transfer have elicited increasing attention due to their ubiquitous applications in thermal management, the underlying mechanisms of intrinsic rough structures as well as the surface wettability on bubble dynamics remain to be explored. Therefore, a modified molecular dynamics simulation of nanoscale boiling was conducted in the present work to investigate bubble nucleation on rough nanostructured substrates with different liquid–solid interactions. Specifically, the initial stage of nucleate boiling was mainly investigated and the bubble dynamic behaviors were quantitively studied under different energy coefficients. Results shows that as the contact angle decreases, the nucleation rate increases, because liquid obtains more thermal energy there compared with that on less wetting surfaces. The rough profiles of the substrate can provide nanogrooves, which can enhance initial nucleate embryos, thereby improving thermal energy transfer efficiency. Moreover, atomic energies are calculated and adopted to explain how bubble nuclei are formed on various wetting substrates. The simulation results are expected to provide guidance towards surface design in state–of–the art thermal management systems, such as the surface wettability and the nanoscale surface patterns.

**Keywords:** Engineered Surface, Nucleate Boiling, Molecular Dynamics Simulation

## 1. Introduction

Pool boiling, as a complex, non-equilibrium process with spatial inhomogeneity, depends on the nature of solid−liquid interactions which are not explainable using existing meso- and macro-scale approaches [1]. Nucleate boiling, as an efficient and controllable boiling stage, has found wide application in industry [2]. Nanostructures can increase the area over which heat transfer occurs, which enables acquisition of more energy by liquid from solid surfaces and faster growth of bubble nuclei. Variation of wettability has been proven to be conflictive with improvement of the onset of nucleate boiling (ONB) and CHF at the same time, making it necessary to clarify the working mechanism underlying liquid–solid interactions on rough structure surfaces during nucleate boiling [3]. A nucleate boiling model of liquids on a rough structural surface is constructed in the present work.The mechanism of the liquid–solid interactions on the heat transfer is explained from the microscopic perspective.

## 2. Simulation Method

Simulated system consists of the following three parts: argon liquid, argon vapor, and a nanostructured copper surface. The initial simulation box measures 300 Å (x) × 50 Å (y) × 432 Å (z). Solid surfaces are set at the top and bottom of the simulation box. The bottom wall is set as the heat source during the boiling process. Rough structures are generated on the solid surface. The upper wall is set to control the system pressure. Argon atoms are placed above the rough substrate. The periodic boundary conditions are applied to x- and y-directions, while the fixed boundary condition is applied to the z-direction. The atomic interactions in the present study are characterized by the pairwise LJ potential.

## 3. Results and Discussion

### 3.1 Preliminary Visualization of Bubble Dynamics

Representative snapshots of nucleate boiling of liquid argon on nanostructured surfaces with different solid-liquid interactions are shown in Figure 1. The simulation is conducted in two stages. First, balance the

system. After the system reaches equilibrium, the bottom wall is heated, and the phase-change process starts. Different phenomena are found under variation of the surface wettability. The growth process of a bubble can be portioned into two stages: slow void growth and coalescence, and rapid growth of the bubble.

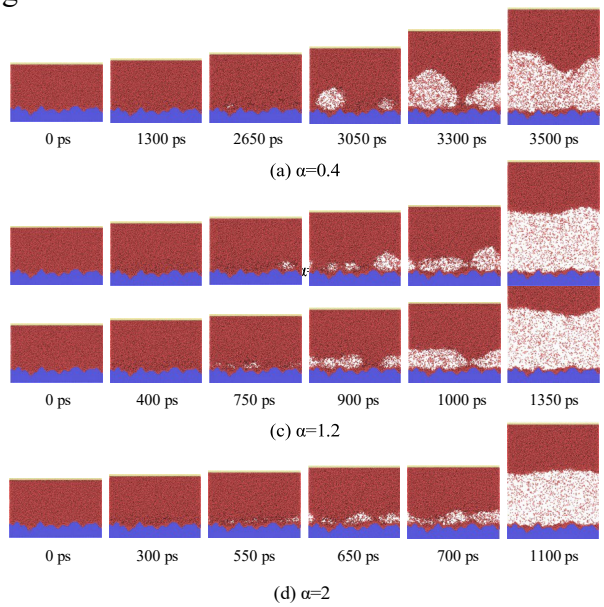


Figure 1.Snapshots of nucleate boiling of liquid argon on nanostructured surfaces with different solid-liquid interactions.(a) a = 0.4; (b) a = 0.8;
(c) a = 1.2; (d) a = 2

### 3.2 Quantitative Research into the Effect of Solid–Liquid Interactions

Figure 2 shows the temporal evolution of the bubble volume. It can be obtained that the entire boiling processes is classified into two stages based on the volume change trend: a slow nucleation stage and a rapid growth stage to form stable bubbles. Figure 2 indicates that the time taken by voids to grow to the size of critical nuclei shortens as the surface wettability increases in the formation process of critical nuclei.

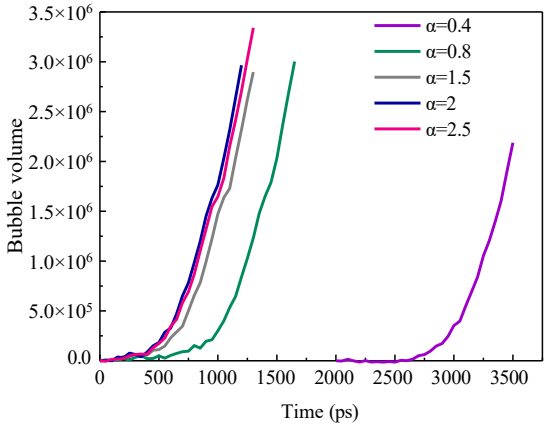


Figure 2. The time evolution of the bubble growth curve of the boiling process with different solid-liquid interactions

## 4. Conclusions

The bubble dynamics of nucleate boiling on the rough nanostructured surface with different wettability was analyzed by conducting a modified molecular dynamics method. The following key findings are drawn from the simulated results. Bubbles can be observed if the energy coefficient α between surfaces and fluid atoms is in a reasonable range ($0.4 \leq \alpha \leq 2.5$). Explosive boiling would be formed if the surface were superwetting. Void generation and bubble growth rate were increased by increased liquid–solid interactions. The rough structured surfaces were reported to generate new contact lines on structures, which included more microlayers and the heat transfer was enhanced as a result. The simulation results are expected to reveal boiling phenomena in nanoscale and provide guidance towards surface design in state-of-the-art thermal management systems.

## References

[1] Liang, G.T.; Mudawar, I. Review of pool boiling enhancement by surface modification. Int. J. Heat Mass Transf. 2019, 128, 892–933.
[2] Chen, Z.H.; Haginiwa, A.; Utaka, Y. Detailed structure of microlayer in nucleate pool boiling for water measured by laser interferometric method. Int. J. Heat Mass Transf. 2017, 108, 1285–1291.
[3] Bai, P.; Zhou, L.P.; Huang, X.N.; Du, X.Z.
How wettability affects boiling heat transfer: A three–dimensional analysis with surface potential energy. Int. J. Heat Mass Transf. 2021, 175, 121391.

## SESSION 6c
## Measuring, sensing and control
Chair: **C. Mira-Hernández**

# Electrical impedance solid fraction sensor for a panel filled with nanocomposite phase change material

Carolina MIRA-HERNÁNDEZ[1,*], Simone MANCIN[1]

1: Department of Management and Engineering, University of Padova, Vicenza, IT

* Corresponding author: Tel.: +39 0444 998746; Email: carolina.mirahernandez@unipd.it

**Abstract:** Monitoring the solid fraction in a latent thermal energy storage system can enable the implementation of smart control strategies for improved performance. However, measuring the solid fraction in a non-invasive, easy-to-implement and accurate manner is challenging. The present study analyzes a parallel plate impedance sensor to measure the solid fraction in a panel filled with phase change material (PCM). The use of nano-additives is proposed to increase the contrast in electrical properties between the solid and liquid phases, which increases the sensor sensitivity. An equivalent electrical circuit model is used to estimate the sensor impedance. The sensor sensitivity is assessed for a nanocomposite PCM (NPCM) of hexadecane with functionalized carbon nanotubes. The electrical properties of the solid and liquid NPCM are drastically different at low frequencies, but the impedance for the melted PCM can be unpractically large. As the frequency increases, the impedance and sensor sensitivity decrease simultaneously. Hence, proper sensor design requires a balance between sensor size and excitation frequency.

**Keywords:** Phase Change Material, Nano Additives, Electrical Impedance, Solid Fraction.

## 1. Introduction

Low-cost latent heat thermal energy storage (LTES) can be hugely advantageous for renewable energy. Smart control systems can improve the efficiency of LTES but require accurate monitoring of the solid fraction of the phase change material (PCM), because the solid fraction represents the total stored energy.

Methods to determine solid fraction during melting/freezing of PCMs take advantage of differences in the properties between the phases. Temperature measurements are a common approach, but they are invasive, and have low accuracy for the phase fraction. Optical imaging is usually used in academic research [1], but it is impractical for real-world applications. An energy balance for the heat transfer fluid that charges and discharges the LTES [2] is also commonly used to assess the overall performance. However, the phase fraction cannot be determined precisely. An electrical impedance sensor could be a non-intrusive and accurate alternative to determine the phase fraction but requires a sufficient contrast in electrical properties between the liquid and solid phases.

The present study proposes a parallel plate impedance sensor to determine the solid fraction inside a thin panel filled with PCM. Nano-additives are considered to enhance the contrast in electrical properties between the liquid and solid PCM [3].

## 2. Materials and Methods

The schematic illustration of the proposed parallel plate impedance sensor is presented in **Fig. 1a**. A circular electrode is placed at the center of each side of a PCM panel. The impedance across the electrodes is measured to determine the solid fraction. The phase change process is assumed to have a one-dimensional behavior as illustrated in **Fig. 1b**, and the space between the parallel electrodes is filled by two adjacent slabs of liquid and solid PCM. An equivalent circuit model (**Fig. 1c**) is used to estimate the impedance between the sensing electrodes. The impedances of the solid and liquid regions are connected in series and the total impedance is expressed by **Eq.1**.

$$Z = -j\frac{L}{A}\left(\frac{\varphi_s}{\omega\varepsilon_s^*} + \frac{1-\varphi_s}{\varepsilon_l^*}\right) \quad (1)$$

Where, $L$ is the electrode spacing, $A$ is the electrode area, $\varphi_s$ is the solid fraction, $\omega$ is the excitation angular frequency, and $\varepsilon_l^*$ and $\varepsilon_s^*$ are the values of complex permittivity for the liquid and solid, respectively. The complex permittivity of a substance is defined as $\varepsilon^* = \varepsilon - j\,k/\omega$, where $\varepsilon$ is the permittivity and $k$ the conductivity.

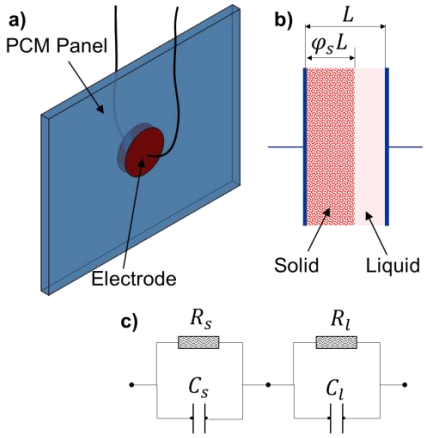


**Fig. 1**. (a) Schematic illustration, (b) geometrical parameters and (c) equivalent circuit representation of the sensing system.

In general, the solid and liquid phases of PCMs have similar electrical properties, which severely limits the sensitivity of an impedance sensor. However, nano-additives could be used to increase the contrast in electrical properties. To evaluate the feasibility of the proposed impedance sensor, the electrical properties of a nanocomposite PCM (NPCM) are considered. The NPCM is hexadecane with 2.0% volume fraction of octadecylamine-grafted multiwalled carbon nanotubes [3]. The NPCM has a significantly enhanced permittivity in the solid phase.

## 3. Results and Discussion

**Fig. 2** shows the behavior with frequency of the equivalent sensor resistivity when the PCM is fully meted and fully frozen. Due to the high contrast in complex permittivity, the impedance difference between the melted and frozen states, i.e., sensor sensitivity, is very large at low frequencies. As the excitation frequency increases, the sensitivity decreases until reaching zero. It is important to consider that a very large impedance in the melted state could prevent proper measurement. To reduce the impedance, a larger sensor area could be used but the sensor size could be constrained depending on the application. Alternatively, the excitation frequency can be increased at the expense of reduced sensitivity.

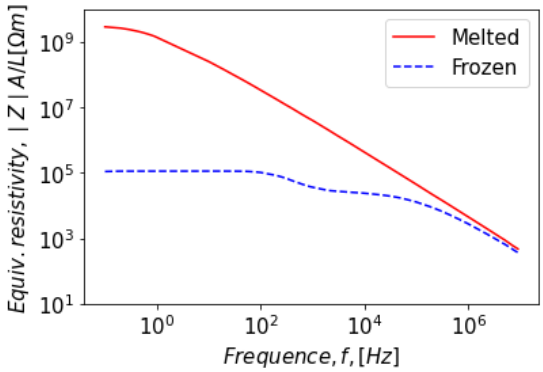


**Fig. 2**. Equivalent sensor resistivity for fully frozen and melted conditions as a function of frequency.

## Conclusion

The study demonstrates the feasibility of a parallel plate impedance sensor to non-intrusively determine the solid fraction during phase change processes in a flat panel. To guarantee adequate sensor sensitivity it is necessary to use a NPCM with sufficient contrast in electrical properties between the liquid and the solid phases. The sensor design requires a balance between size and excitation frequency.

## Acknowledgement

Authors acknowledge financial support from the European Union through the call HORIZON-MSCA-2021-PF-01 for the project ET4PCM (No. 101065152).

## References

[1] S. F. Hosseinizadeh, A. A. Rabienataj Darzi, F. L. Tan, and J. M. Khodadadi, 'Unconstrained melting inside a sphere', Int. J. Therm. Sci. (2013).
[2] G. Zsembinszki, C. Orozco, J. Gasia, T. Barz, J. Emhofer, and L. F. Cabeza, 'Evaluation of the State of Charge of a Solid/Liquid Storage Tank', Energies (2020).
[3] Y. Wu, P. Meng, Q. Zhang, Z. Tan, G. Cheng, and X. Wu, 'Room-Temperature Switching Behavior in CNT/Hexadecane Composites', MRS Adv. (2018).

# An Influence of Sinusoidal Pulsations of the Dispersed Phase Flow Rate on the Liquid-Liquid Flows in a Microchannel with T-junction

Alexander KOVALEV[1,2], Anna YAGODNITSYNA[1,2], Artur BILSKY[1]

1: Kutateladze Insitute of Thermophysics SB RAS, Novosibirsk, RU
2: Novosibirsk State University, Novosibirsk, RU

* Corresponding author: Tel.: +7 983 3170394; Email: therfmig@gmail.com

**Abstract:** The influence of sinusoidal pulsations of the dispersed phase flow rate on the characteristics of the flow of immiscible liquids in a T-shaped microchannel is studied. The flow regimes are visualized in both the undisturbed flow and flow with the imposition of external disturbances of various frequencies and amplitudes. It is found that the pressure and flow rate in the dispersed phase are linearly related, and the transition from the plug regime to the parallel one does not affect this dependence in the case of an undisturbed flow. A dimensionless complex is proposed that describes the transition from the parallel flow pattern to the plug flow regime due to external pulsations for a fixed capillarity number of the continuous phase. For the case of perturbations applied to the plug flow, a decrease in the standard deviation of plug length is observed when perturbation frequency is equal to the basic frequency of undisturbed plug formation. The data obtained on the stability of the parallel flow pattern provide insights on the active control methods application to expand the region of existence of the plug flow.

**Keywords:** Liquid-liquid Flow, Flow Patterns, Flow Rate Pulsations, Plug Flow

## 1. Introduction

Flows of immiscible fluids inside microchannels or microcapillaries are extensively studied in the last decades. Microfluidic devices incorporating liquid-liquid and gas-liquid flows are put into practice in analytic biology [1], catalysis [2], and many other areas. Specific flow patterns such as a plug or droplet flow and high surface-to-volume ratio provide enhanced heat and mass transfer coefficients. To control flow patterns and form plugs or droplets two ways are typically used, namely active and passive techniques [3]. Passive methods are more convenient, however, a number of drawbacks limit their applications. For instance, a formation of plugs and droplets occurs in an extremely narrow velocity range in the case of highly viscous liquids [4]. Therefore, various active methods are applied to expand the limits of plug or droplet formation and to define its properties with higher precision.

We proposed a pulsatile flow rate of the dispersed phase to control liquid-liquid flow patterns in the T-junction microchannel. The influence of frequency and amplitude of sine flow rate signal on different liquid-liquid systems was experimentally studied. Parallel flow segmentation was observed and described for certain liquid properties and pulse parameters. The influence of pulse parameters on the resulting plug or droplet sizes was characterized.

## 2. Experimental setup

The experiments were carried out in T-junction microchannels made of polymethylmethacrylate by micromilling. The outlet channel width was 425 μm, the inlet channel width was 223 μm, and the channel height was 212 μm with outlet hydraulic diameter $D_h$ = 283 μm. Silicone oil with dynamic viscosity 200 cSt and water glycerol solutions of volumetric glycerol concentrations 50%, 70%, 85% and 95% were used as working fluids. The silicone oil was continuous phase, and its flow rate was set by a KDS Gemini 88 syringe pump maintaining a constant volumetric flow rate (relative flow rate setting accuracy of 0.35%). To set the flow of the

dispersed phase and control pulse parameters, the pressure controller Elveflow OB-1 with Bronkhorst BFS Cori-flow flowmeter were used. The liquid-liquid flow was visualized using pco.1200 hs high-speed camera, connected to a Zeiss Axio Observer.Z1 inverted microscope with 5x and 10x lenses.

## 3. Results and discussion

Flow visualization was performed in a wide range of fluid velocities. Flow pattern maps were plotted in the case of constant flow rates of continuous $Q_c$ and dispersed $Q_d$ phase as well as for pulsatile dispersed phase flow rate. Segmentation of parallel flow was observed for certain parameters of the pulse. It was found that an increase in the period or amplitude of the pulse, with other constant parameters, leads to the segmentation of the parallel flow. At the same time, when amplitude and period are fixed instability is caused by a decrease in the velocity of the dispersed phase $U_d$. Based on these observations, the influence of pulsations on the stability of the parallel flow is presented in the form of a regime map plotted in terms of dimensionless parameters that consider all the abovementioned factors (Fig. 1). The X-axis shows the capillarity number for the carrier phase $Ca_c = \mu_c U_c/\sigma$, here $\mu_c$ - carrier phase viscosity and $\sigma$ – interfacial tension. The Y-axis represents the parameter $10^{-6}(A/Ca_d)(T/t_{vc})$, where A and T are the dimensionless amplitude and the period of sine flow rate, correspondingly, $Ca_d$ is dispersed phase capillary number, $t_{vc} = \mu_d D_h/\sigma$ is visco-capillary time, and the free factor $10^{-6}$ is chosen for convenience. This parameter takes into account the trends found for the amplitude, period, and flow velocity, and additionally supposes interfacial tension as a destabilizing factor.

In the case of imposition of flow rate pulsations on the plug flow, a decrease in plug length deviation was found, when the pulse period is equal to the plug formation period in undisturbed flow. The data obtained can be used to control flow patterns in the T-junction microchannel by means of dynamic dispersed phase flow rate.

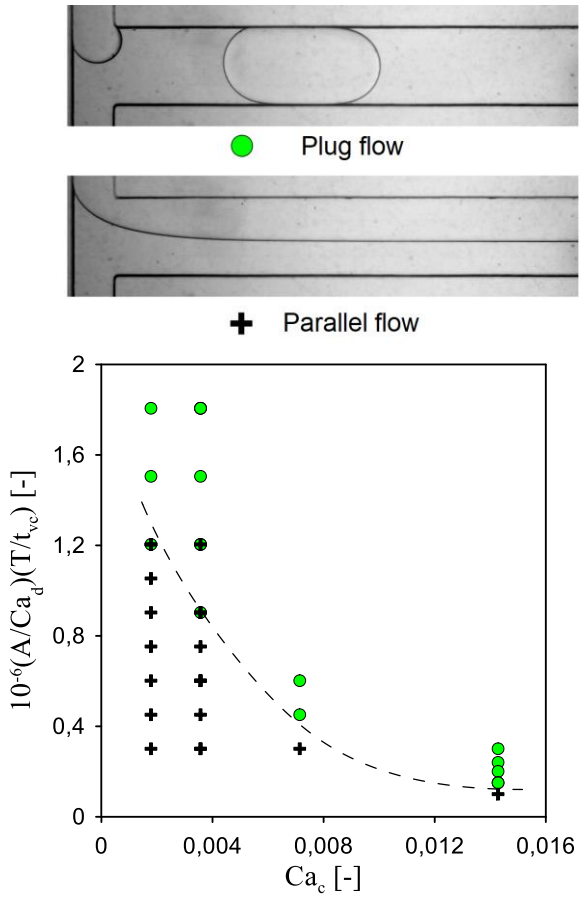


Fig. 1. Examples of flow pattern images and flow pattern map in the case of sine flow rate of dispersed phase for silicone oil and 85% water glycerol solution.

## Acknowledgments

This research was funded by the Russian Science Foundation (Grant No. 21-79-10307).

## References

[1] O. Scheler, W. Postek, P. Garstecki, Recent developments of microfluidics as a tool for biotechnology and microbiology, Curr Opin Biotechnol. 55 (2019) 60–67.

[2] A. Tanimu, S. Jaenicke, K. Alhooshani, Heterogeneous catalysis in continuous flow microreactors: A review of methods and applications, Chemical Engineering Journal. 327 (2017) 792–821.

[3] P. Zhu, L. Wang, Passive and active droplet generation with microfluidics: a review, Lab Chip. 17 (2017) 34–75.

[4] A. V. Kovalev, A.A. Yagodnitsyna, A. V. Bilsky, Viscosity Ratio Influence on Liquid-Liquid Flow in a T-shaped Microchannel, Chem Eng Technol. 44 (2021) 365–370.

# Measuring Multiphase Flow In Miniature Devices Using PEPT

Yu-Fen CHANG[1,2,*], Boris V. BALAKIN[1], Alex C. HOFFMANN[3]

1: Department of Mechanical and Marine Engineering Management and Engineering, Western Norway University of Applied Sciences, Bergen, Norway
2: Department of Clinical Medicine, UiT The Arctic University of Norway, Tromsø, Norway
3: Department of Physics and Technology, University of Bergen, Bergen, Norway

* Corresponding author: Email: yu-fen.chang@hvl.no; Email: yu-fen.chang@uit.no

**Abstract:** This paper reports the development of a multiphase flow visualisation technique for measuring high- speed flows within miniature devices. A mini-hydrocyclone with an internal flow field that is highly complex is used to demonstrate the developed flow visualisation technique. Scrutinizing flow phenomena and related physical quantities, which could not be revealed as clearly using conventional experimental methods, is made possible.

**Keywords:** Micro Flow Visualisation, Miniature multiphase devices, Positron emission particle tracking

## 1. Introduction

Mini-devices, such as microfluidic systems and lab-on-a-chip, are undergoing intensive development for extensive applications in sophisticated fields, including DNA detection and cell selection. In-depth investigations on the flow field are necessary to ensure effectiveness and safety.

Hydrocyclones have been used to replace barrier-based separators in bioreactors to maintain clogging-free, high-density perfusion. To obtain the required intensity of centrifugal field for continuous perfusion, hydrocyclones with diameters smaller than 10 mm are recommended [1]. Miniature cyclones can be manufactured by micro-fabrication or 3D printing for direct integration into lab-on-a-chip systems [2]. Although computational fluid dynamic (CFD) simulations can be carried out to evaluate and verify the cyclone design, it is difficult to measure the flow pattern experimentally using conventional methods in such a small geometry, which hinders optimisation of the design and operating conditions. A breakthrough in measuring techniques is needed to stimulate advances in understanding, performance optimisation, theoretical models and computational simulation. In this study, we aim to further develop "positron emission particle tracking" (PEPT) to capture 3D particle trajectories with millisecond temporal resolution and high spatial resolution for detailed investigation and further analysis of the flow field.

## 2. Materials and Methods

Positron emission particle tracking (PEPT) makes use of positive beta decay. Following its release from the nucleus, the positron collides with an electron and the collision leads to annihilation, producing two photons emitted at an angle of approximately 180°. The radionuclide is therefore close to the line, aka "line of response" (LOR), connecting the detection sites of the two photons if they are detected within a short time window. In this study, an algorithm based on processing the cross points of every LOR pair in each 2D plane is employed. The algorithm is refined in combination with an analytical expression for the point minimizing the sum of the squared distances from the LORs in 3D. Meanwhile, a filter is developed and applied to account for the continuity of the tracer location. In this way, the small tracer particle can be tracked over time

and space. Here, the strong base, anionic, macroreticular, macroporous polymeric resin beads, Amberlyst A26 hydroxide form (Sigma-Aldrich), are used as tracers and labelled with positron-emitting isotopes $^{18}F$ through ion exchange.

The positron emission tomography (PET) scanner "LabPET 8" (Triumph) is used as the gamma sensor array. The scanner consists of 3072 phoswich detectors surrounding a cylindrical space with a radius of 80.762 mm and an axial length of 75 mm [3].

## 3. Results

The 3D coordinates of the tracer particle were obtained by using PEPT and then post-processed using the Savitzky–Golay filter with a polynomial order of 2 and a window of 9 points to increase the precision and mitigate the scatter in the millisecond positions due to the scatter inherent to the PEPT method [4]. The data between timestamps, which are inserted by the scanner into the data stream, can be split to achieve high temporal resolution.

The radial, tangential and axial velocities in the rotational motion of the particle provide details of the separation process in the cyclone. The tangential velocity is related to the centrifugal force acting on the particle and thus to the separation performance. Therefore, the tangential velocity is a key parameter in cyclone models [5].

Figure 1 shows an example of a particle trajectory with temporal resolution of 2.62 ms colour-coded by the magnitude of the tangential velocity. Within this 655 millisecond passage, the particle seemed to experience a few "wandering" periods where it swirled around the same axial section at a smaller radius for a few turns before proceeding towards the outlet. Comparing the velocity components in cylindrical coordinates between the "wandering" and other sections enables scrutinization and root cause analysis of the anomalous phenomenon.

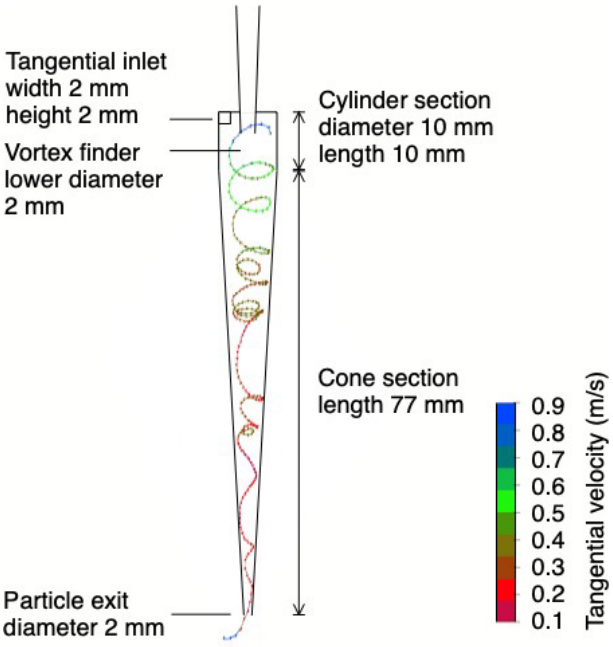


Figure 1. Trajectory colour-coded by tangential velocity.

## 4. Conclusion

In this work, refined PEPT for visualising and investigating multiphase flow in miniature flow devices was developed and successfully demonstrated using a mini-hydrocyclone with a diameter less than or equal to 10 mm. The particle was found to deviate from its original swirling motion, which led to long residence time and can have adverse effects on the separation efficiency. The refined PEPT rendered possible scrutinizing this phenomenon which could not have been revealed as clearly using conventional experimental methods based on determining only local velocities.

## References

[1] Bettinardi I, Castan A, Medronho R A and Castilho L R 2020 Biotechnology and Bioengineering 117 1915– 1928
[2] Syed M S, Rafeie M, Henderson R, Vandamme D, Asadnia M and Ebrahimi Warkiani M 2017 Lab on a Chip 17 2459–2469
[3] Rechka S, Fontaine R, Rafecas M and Lecomte R 2009 IEEE Transactions on Nuclear Science 56 3672–3679
[4] Chang Y F, Ilea C G, Aasen Ø L and Hoffmann A C 2011 Chemical Engineering Science 66 4203–4211
[5] Hoffmann A C and Stein L E 2007 Gas Cyclones and Swirl Tubes, Principles, Design and Operation

# Microfluidic flow sensor based on chronoamperometric measurements in a microchannel

Harsh DESWAL[1], Shiv Govind SINGH[2], Amit AGRAWAL[3,*]

1: Department of Mechanical Engineering, IIT Bombay, Mumbai, India
2: Department of Electrical Engineering, IIT Hyderabad, Hyderabad, India
3: Department of Mechanical Engineering, IIT Bombay, Mumbai, India

* Corresponding author: Tel.: (+91) 22 - 2576 7505; Email: amit.agrawal@iitb.ac.in

**Abstract:** Microfluidics is an emerging field with various applications, including biosensing, drug delivery, and microreactors. Flow sensors are an essential component of microfluidic systems that enable accurate control of fluid flow. In this study, we present a chronoamperometry-based flow sensor for microfluidics applications. The sensor is based on the measurement of current transients produced by redox reactions at the electrode surface, which are modulated by the flow rate of the solution. With increase in the flow rate of an electrolyte (0.1M NaCl), the charge transfer at the electrodes is observed to increase, leading to an increase in the percentage deviation from no flow case. The sensor was fabricated on a Si wafer using the standard photolithography, soft lithography and vapor deposition techniques. It consists of Si wafer substrate, Ti/Pt interdigitated electrodes and a PDMS microchannel. The sensor demonstrated high sensitivity and linearity over 5 µl/min to 200 µl/min range of flow rates, making it suitable for various microfluidics applications. The 3σ resolution of the sensor is 9.3 µl/min. The sensor exhibited good stability (> 100 operating hours) and repeatability (RSD < 7%), indicating its potential for long-term monitoring of fluid flow in microfluidic systems.

**Keywords:** Chronoamperometry, flow sensor, microfluidics, microchannel

## 1. Introduction

Flow rate detection is a critical parameter in many fields and has important implications for health, safety, and environmental sustainability. Accurate and precise flow rate detection can help improve the performance and efficiency of systems, reduce costs, and enhance the quality of products and services. In biomedical applications, flow rate detection is critical for monitoring the flow of blood, cerebrospinal fluid, urine, and other bodily fluids. Flow rate detection is also important in drug delivery systems, where the flow rate must be controlled to ensure the proper dosage of the medication. State of the art on-chip flow rate sensors suffer from several deficiencies such as high overheat temperature, complex integration among others. Chronoamperometry based flow sensing is easy to integrate on a microchip and also the nature of process does not cause a significant rise in the fluid temperature.

Fig. 1 Electrochemical station used for sensor characterization

Chronoamperometry is an electrochemical technique that measures the current generated by an electrochemical reaction over time, while a constant potential is applied to an electrode. In chronoamperometry-based flow rate detection, a solution containing an electroactive species is flowed through a cell containing two

or more electrodes. By applying a constant potential to one electrode, the electroactive species is oxidized or reduced, and the resulting current is measured over time. The flow rate of the solution can then be calculated from the change in current over time.

## 2. Experiment, Results and Conclusions

### 2.1 Experiment

CH instruments electrochemical workstation was used to perform sensor characterization experiments. Electrolyte (0.1 M aqueous NaCl) was pumped through a 100 µm PDMS microchannel using a cole-palmer syringe pump. Fig. 2 shows a schematic of the sensing device used. Interdigitated electrodes (Ti/Pt) were subject to three different constant voltage settings (1V, 2V, and 3V).

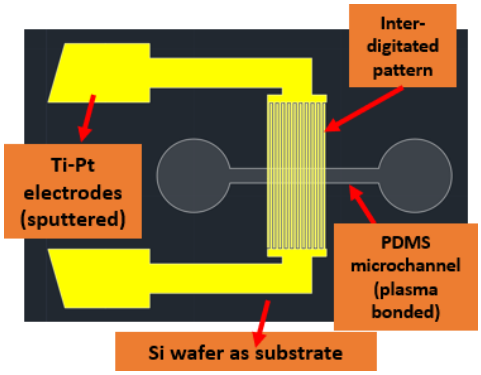


Fig. 2 Schematic of the flow sensor

### 2.2 Results

Theoretically, there are two methods for calculating the flow rate from chronoamperometry data: the Levich equation [1] and the Randles-Sevcik equation [2]. In the present work, a different approach based on integral of current vs time graph is used to detect flow rate. The percentage change in charge transfer over a period of 120 sec is plotted against flow rate. The total charge transfer is observed to increases with the flow rate as depicted in Fig. 3. This is due to increase in the number of charge carriers interacting with the electrode surface due to increased flow rate. The change in real-time current is observed to be too small to detect, hence, the area of current-time curve i.e., the charge transfer is used as a correlation parameter.

For aqueous NaCl, the electrolysis voltage was found to be ≥ 3V, leading to gas bubble formation. As a result, the percent change in case of 3V is less than at 2V (due to gas bubbles hindering the electrode surface and charge carrier interaction). 2V is used as a reference for sensor calibration as the graph is linear for the entire concerned flow rate range.

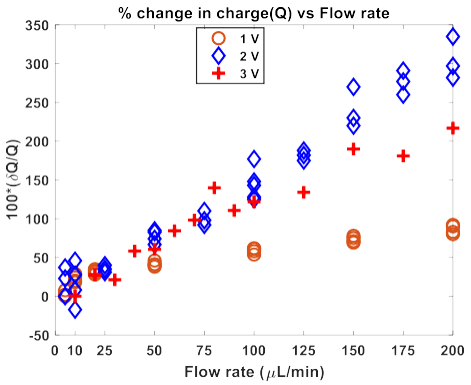


Fig. 3 Calibration curve for flow rate sensor at three different voltage settings

### 2.3 Conclusions

The sensor demonstrated high sensitivity and linearity over 5 µl/min to 200 µl/min range of flow rates, making it suitable for various microfluidics applications (overheat < 1 °C). The 3σ resolution of the sensor is 9.3 µl/min. Furthermore, the sensor exhibited good stability and repeatability (RSD < 7%), indicating its potential for long-term monitoring of fluid flow in microfluidic systems.

## References

[1] Bard, A. J., Faulkner, L. R., & White, H. S. (2022). Electrochemical methods: fundamentals and applications. John Wiley & Sons.
[2] Zanello, P., Nervi, C., & De Biani, F. F. (2019). Inorganic electrochemistry: theory, practice and application. Royal Society of Chemistry.

# Development of AFM Measurement Method for Slip Length Considering the Effect of Electric Double Layer Force

Haruya ISHIDA[1] , Hideaki TESHIMA[1,2*], Koji TAKAHASHI[1,2]

1: Department of Aeronautics and Astronautics, Kyushu University, Fukuoka, JP
2: International Institute for Carbon-Neutral Energy Research (WPI-I2CNER), Kyushu University, Fukuoka, JP

* Corresponding author: Tel.: +81 92 802 3016; Email: hteshima05@aero.kyushu-u.ac.jp

**Abstract:** Micro and nano fluid systems have numerous applications in the fields of chemical, engineering and biomedical sciences. To reduce fluid resistance in such systems, characterization and utilization of slip phenomena are highly desired. However, current method for measuring slip length using an atomic force microscope is limited to use in electrolyte solutions due to inevitable effect of the electric double layer (EDL) force. To achieve the slip length measurements in pure water, we propose a theoretical formula that takes into account the effect of EDL force and measure the slip length of silica surfaces both with and without considering it. The results indicate that our new method provides a plausible value, whereas neglecting the EDL force leads to an underestimation of slip length. These findings will help improve the accuracy of slip length measurements in low ion concentration fluids such as pure water.

**Keywords:** Boundary slip, Electric double layer, Atomic force microscopy

## 1. Introduction

Micro and nano fluidic systems have various applications in the fields of biology, chemistry, and medicine, and reducing fluid resistance is important when the specific surface area is large. Fluid slippage on solid surfaces is known to reduce fluid resistance, and the slip length is defined by Equation 1

$$v_s = b\frac{\partial v}{\partial z} \tag{1}$$

where $b$ is the slip length, $v$ is the flow velocity in the direction parallel to the solid surface, and $v_s$ is flow velocity at the solid-liquid interface. The slip length can be measured by fitting the force curve obtained using an atomic force microscope (AFM) with a theoretical equation developed based on fluid dynamics equations and has been reported to range from several nanometers to several hundred nanometers(Vinogradova., 1995). However, when measuring the force curve, electric double-layer (EDL) force appears as a result of the interaction between the substrate and the AFM probe, which is not taken into account in the conventional theory. Therefore, previous studies were forced to use electrolyte solutions to eliminate the effect of the EDL force, and the development of a new method is highly desired. In this study, we propose a theoretical equation and method that enables accurate measurement of slip length in pure water.

## 2. Theory

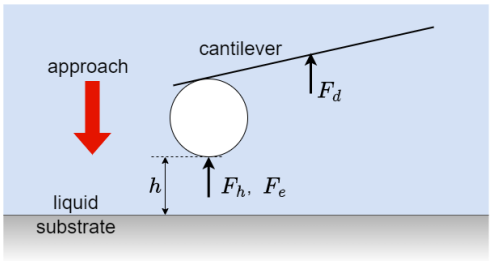


**Fig. 1** Schematic illustration of the experimental system.

There are three types of forces acting on the cantilever as shown in Fig. 1: $F_h$ is the viscous force acting on the probe sphere, $F_d$ is the viscous force acting on the cantilever body, and $F_e$ is the EDL force acting on the probe. When the slip length of the sphere and the underlying substrate are equal, the viscous force acting on the probe can be expressed as Equation (2).

$$F_h = -\frac{6\pi\eta R^2}{h}\frac{dh}{dt}f^* \qquad (2)$$
$$f^* = \frac{h}{3b}\left[\left(1+\frac{h}{6b}\right)\ln\left(1+\frac{6b}{h}\right)-1\right]$$

In this study, we calculated numerical solutions taking into account the electrostatic force by using experimentally measured EDL force in the force calculations. The balance of forces acting on the cantilever yielded the following equation, where $F_e$ represents the experimental data.

$$\dot{x}_{n+1} = \frac{-k\left(x_n+\frac{1}{2}\Delta t x_n\right)-\frac{6\pi\eta R^2 \dot{z}_{n+1}}{h_{n+1}}f^* - 6\pi\eta L_e \dot{z}_{n+1} + F_e(h_{n+1})}{\frac{1}{2}k\Delta t + \frac{6\pi\eta R^2}{h_{n+1}}f^*} \qquad (3)$$

## 3. Experiments

A colloidal probe was prepared by attaching a silica sphere to the tip of a tipless cantilever using adhesive. A measurement substrate was prepared by bonding a thermally oxidized Si substrate to the bottom of a liquid cell. Force curve measurements were performed at two different speeds, 80 and 0.2 µm/s. The sum of the viscous and electrical double layer forces is measured at the faster scanning speed. At the slower scanning speed, because the viscous force is sufficiently small, only the electrical double layer force is measured.

## 4. Results and Discussion

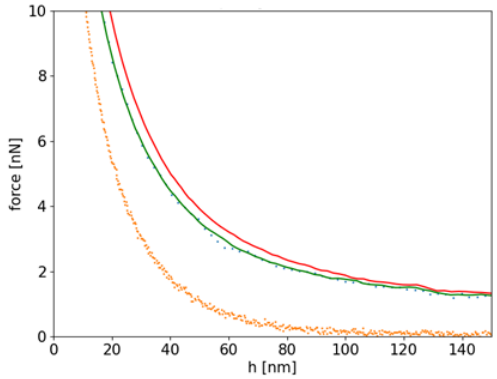


Fig. 2 Force curves measured at 0.2 m/s (yellow dots) and at 80 m/s (blue dots). Solid lines are theoretical curves. The theoretical force estimated by eq. (3) with slip boundary condition and no-slip boundary condition are represented by the green and red lines, respectively.

Fig 2 shows an example of a measured force curve and fitting result. It was found that the EDL force begins to act when the probe and substrate approach about 100 nm. Without considering the EDL force, the estimated slip length on the silica surface is an unrealistic negative value of -3.2 nm. However, considering the EDL force for the fitting gives a slip length on the silica surface of 5.6 nm, which is close to the values measured in previous studies(Bonaccurso et al., 2002.). At distances less than 100 nm, both the EDL force and viscous force are of similar magnitude, indicating that the EDL force cannot be ignored. It was also found that neglecting the EDL force leads to an underestimation of the slide length.

## 5. Conclusions

In this study, we proposed a new theoretical formula considering the effect of EDL force for measuring slip length using AFM. The slip length was calculated by measuring the force curve. As a result, the slip length of 5.6 nm was obtained on the silica surface. The proposed method enables a more accurate measurement of slip length in fluids with low ion concentrations, such as pure water.

## References

Vinogradova, O.I., 1995. Drainage of a Thin Liquid Film Confined between Hydrophobic Surfaces. Langmuir 11, 2213–2220.

Bonaccurso, E., Kappl, M., Butt, H.-J., 2002. Hydrodynamic force measurements: boundary slip of water on hydrophilic surfaces and electrokinetic effects. Phys. Rev. Lett. 88, 076103.

## SESSION 7a
## MINI-SYMPOSIUM
## Biological flows at the microscale: physics and application

Chairs: **S. Balabani, C. Koenig and E. Kaliviotis**



Dimitris PASIAS[1], Andreas PASSOS[1] Loucas KOUTSOKERAS[1], Georgios COSTANTINIDES[1], Stavroula BALABANI[2] and Efstathios KALIVIOTIS[1]
1: Dept. of Mechanical Engineering and Material Science and Engineering, Cyprus University of Technology, Limassol, Cyprus
2: Dept. of Mechanical Engineering, University College London, London, United Kingdom



Antonios STATHOULOPOULOS[1], Efstathios KALIVIOTIS[2], Stavroula BALABANI[3]
1: FluME, Department of Mechanical Engineering, University College London (UCL), London, UK
2: Department of Mechanical Engineering and Material Science and Engineering, Cyprus University of Technology, Limassol, CY
3: Wellcome/EPSRC Centre for Interventional and Surgical Sciences, University College London (UCL), London, UK



Carola KOENIG[1] , Stavroula BALANBANI[2], Antonios STATHOULOPOULOS[2], Sudarshan RAMACHANDRAN[1,3,4,5]
1: Department of Mechanical and Aerospace Engineering, Brunel University London, Uxbridge, UK
2: Department of Mechanical Engineering, University College London, London, UK
3: Department of Clinical Biochemistry, University Hospitals Birmingham NHS Foundation Trust, Birmingham, UK
4: Department of Clinical Biochemistry, University Hospitals of North Midlands, Staffordshire, UK
5: Institute for Science and Technology in Medicine, Keele University / Faculty of Health Sciences, Staffordshire University, Staffordshire, UK



Stephanie HALLAM[1], Pranav VASANTHI BATHRINARAYANAN[1], Zoe SCHOFIELD[1], Nina KOVALCHUK[1], Mark SIMMONS[1]
1: School of Chemical Engineering, University of Birmingham, Birmingham, UK

# Blood flows on passive microfluidics – Role of blood physiology and biomechanical properties

Dimitris PASIAS[1], Andreas PASSOS[1] Loucas KOUTSOKERAS[1], Georgios COSTANTINIDES[1], Stavroula BALABANI[2] and Efstathios KALIVIOTIS[1,*]

1: Dept. of Mechanical Engineering and Material Science and Engineering, Cyprus University of Technology, Limassol, Cyprus
2: Dept. of Mechanical Engineering, University College London, London, United Kingdom

* Corresponding author: Tel.: +357 25002289; Email: e.kaliviotis@cut.ac.cy

**Abstract:** The study of blood flow and rheology is essential for understanding fundamental flow physics and blood behaviour in physiological/pathological conditions. Passive microfluidic flow has emerged as a promising platform for developing blood diagnostic tools for assisting in health monitoring. This work describes recent work on passive blood flows in microfluidic devices, where the influence of blood physiology and blood biomechanical properties was studied. Hemorheological factors of human blood and erythrocyte suspensions where quantified, and the flow of samples in hydrophilic/superhydrophilic rectangular microchannels was characterised using micro-Particle Image Velocimetry and Particle-Tracking techniques. The effects of altered physiological factors, such as erythrocyte concentration (haematocrit), deformability and aggregation were investigated, and meniscus velocities, velocity profiles, local and bulk shear rates were derived and correlated. The findings suggested that viscosity and erythrocyte deformability and concentration negatively affect the velocity of blood in the channel. Interestingly, increased erythrocyte aggregation was observed to have a non-monotonic effect on the velocity of the fluids tested, favouring samples of normal deformability and reduced haematocrit. The relatively high shearing rates observed near the entrance of the channels seem to substantially minimise erythrocyte aggregation, therefore supressing the non-Newtonian nature of the samples for a substantial part of the channel length.

**Keywords:** Blood flow, Passive microfluidics, Blood Biomechanics, Blood rheology

## 1. Introduction

Microscale blood flow and rheological characteristics are fundamentally important, as they affect the efficiency of microfluidic devices. The area of microfluidics has been widely developed and received a considerable interest over the last decades [1]. Microfluidic devices are appropriate for small sample manipulation and are suitable for miniaturizing laboratory techniques. Passive flow devices have many benefits and are popular in blood diagnostics and medical applications: they are cost effective and simple in manufacturing, and can be designed as disposable. Furthermore, they have good potential to enhance improvements in areas such as blood characterization, drug discovery, biosensing and chemical synthesis, where handling small volumes is critical [2]. In this work, results on passive blood flows in microfluidic channels are presented, where the influence of blood physiology and blood biomechanical properties was studied.

## 2. Methods

Blood samples were acquired according to the guidelines, and with the approval of the Cyprus Bioethics Committee (ref: ΕΕΒΚ/ΕΠ/2016/18). Hemorheological and physiological factors considered included erythrocyte concentration (haematocrit), aggregation and deformability, and sample viscosity. Haematocrits were fixed to 40% and 45%, except of those of whole blood, native samples. Erythrocyte deformability was decreased by heat treatment (measured by a Rheoscan D300 instrument), and erythrocyte aggregation was adjusted by the use of Dextran solutions, and measured by a Rheoscan A200 instrument. Velocity in the rectangular microchannels was characterised using micro-Particle Image Velocimetry, and Particle-Tracking techniques and tools (JPIV and Matlab-PIV) [3,4]. Fluid viscosity, was

examined using a Brookfield DV2T viscometer. Microchannels (see Figure 1) were produced by xurography techniques using microsope slides and double sided tape (Tessa, 100μm thickness). Channel surfaces were coated with $TiO^2$ for enhancing hydrophilicity (contact angles ~5°).

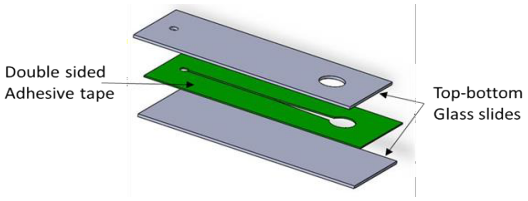


Fig. 1. Exploded schematic of the microchannel. The large hole is the filling well with an entrance width of ~5 mm leading to a ~1 mm exit, after 20 mm, with a convergence angle of ~3°.

## 3. Results and Discussion

Mean velocity curves as a function of channel distance are shown in Figure 2, illustrating high magnitudes at the initial stages of the flow.

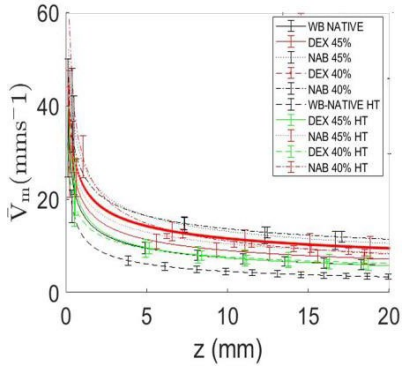


Fig. 2. Meniscus velocity in the channel for native whole blood (WB), Dextran suspensions (DEX), and for non-aggregative blood samples (NAB). The heat-treated counterparts of the samples, for reduced deformability, are noted with "HT", and the haematocrits are noted as 40% and 45%.

The resulted shear-rates from the meniscus velocity behaviour are presented in Figure 3, showing intense shearing near the entrance of the channel. The relatively high shearing rates observed near the entrance of the channels seem to substantially minimise erythrocyte aggregation, therefore supressing the non-Newtonian nature of the samples for a substantial part of the channel length. The 5% increase in haematocrit found to negatively affect the viscosity of the fluid, and also decrease the meniscus velocity in all cases. The increase of erythrocyte aggregation was observed to have a non-monotonic effect on the velocity of the fluids, favouring samples of normal deformability and decreased haematocrit.

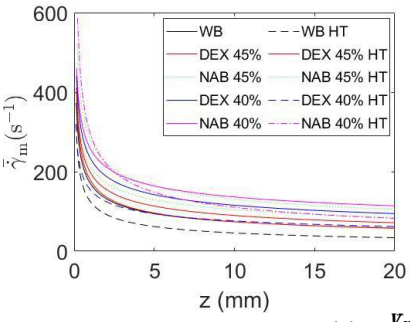


Fig. 3. Shear rates calculated as $\bar{\dot{\gamma}}_m(z) = \frac{V_m(z)}{h}$ with h the channel gap at 100μm.

Figure 4 shows the combined effect of erythrocyte aggregation and viscosity on the meniscus velocity ($AI^*_{visc} = \bar{A}^* \times \bar{\bar{\mu}}^*$, with $\bar{A}^*$ and $\bar{\bar{\mu}}^*$ non-dimensional indices of aggregation and viscosity respectively).

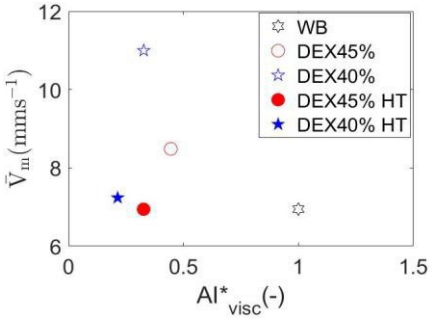


Fig. 4. The effect of aggregation and viscosity on the meniscus velocity.

## 4. Concluding remarks

The results of the present study illustrated the need for considering the biomechanical and physiological properties of blood in the design of relevant devices and processes.

## References

[1] Sackmann E.K, etal. (2014). The present and future role of microfluidics in biomedical research. Nature. 507(7491):181–9. 10.1038/nature13118.

[2] Kim, H., etal. (2023). Microfluidic systems for blood and blood cell characterization. Biosensors, 13(1) doi:10.3390/bios13010013

[3] Pasias D., etal. (2020). Surface tension driven flow of blood in a rectangular microfluidic channel: effect of erythrocyte aggregation. Physics of Fluids, 32, 071903 (2020); https://doi.org/10.1063/5.0008939.

[4] Pasias D., etal. (2022). Effects of biomechanical properties of blood on surface tension driven flows in superhydrophilic channels. Physics of Fluids, 34, 051907; https://doi.org/10.1063/5.0088643.

# Partitioning of dense RBC suspensions in microfluidic bifurcations

Antonios STATHOULOPOULOS[1], Efstathios KALIVIOTIS[2], Stavroula BALABANI[3,*]

1: FluME, Department of Mechanical Engineering, University College London (UCL), London, UK
2: Department of Mechanical Engineering and Material Science and Engineering, Cyprus University of Technology, Limassol, CY
3: Wellcome/EPSRC Centre for Interventional and Surgical Sciences, University College London (UCL), London, UK

* Corresponding author: Email: s.balabani@ucl.ac.uk

**Abstract:** Red blood cells (RBCs) are a key determinant of blood rheology and human physiology. Their transport through the complex geometries of microvascular networks is heterogeneous and depends on their mechanical properties. A number of studies have focused on examining RBC motion and partitioning of dilute suspensions, neglecting the importance of cell-cell interactions in confined spaces. In the present study, the effect of deformability on the spatial distributions of dense RBC suspensions in a microfluidic Y-shaped bifurcation is examined experimentally. Human RBC suspensions (healthy and artificially hardened) at 20% haematocrit and physiological flow rates were perfused through the channels and local hematocrit and velocity distributions were measured. Hardened RBCs exhibited more uniform haematocrit distributions downstream of the bifurcation in comparison with the healthy ones, which tend to accumulate along the apex of the bifurcated geometry. A comparison with distributions measured in T-junction microchannels revealed that healthy RBCs are more sensitive to changes in bifurcation angle compared to hardened cells. The study highlights the heterogeneous nature of RBC flows in microvascular networks and the impact of impaired RBC deformability on microhaemodynamics.

**Keywords:** Red blood cells, Blood microscale flows, RBC deformability, haematocrit distribution

## 1. Introduction

RBCs are the most abundant cells in blood; their deformability and their propensity to aggregate are key determinants of blood rheology affecting local haemodynamics. RBC deformability is impaired in many diseases like diabetes, sepsis and sickle cell disease leading to microvascular implications. Microfluidics can provide insight into the role of RBC properties in microvascular flows. The majority of published works have been conducted with dilute RBC suspensions neglecting cell-cell interactions [1, 2]. It is evident that the impact of impaired RBC deformability on microhaemodynamics of dense RBC suspensions is scarcely explored. In the present study, we elucidate the role of RBC deformability on the transport of dense suspensions of RBCs on a Y-shaped bifurcated geometry using microfluidics, aiming to establish a link between RBC biomechanical properties and haemodynamics in physiological and pathological conditions.

## 2. Methods

Human blood samples were obtained from healthy donors according to an approved protocol (South East London NHS Research Ethics Committee 10/H0804/21)**.** Red blood cells were separated and their deformability was artificially varied by means of glutaraldehyde; a 40% reduction of RBC deformability was measured for hardened cells using RheoScan (Rheoscan-D300, Sewon Meditech, Inc., Seoul, Korea). A Y-shaped bifurcated geometry featuring a 50x50 $\mu m^2$ square cross-sectional area and a 60-degree angle between the outlet branches was

employed. Healthy and artificially hardened RBC suspensions at 20% haematocrit were perfused through the channels at physiological flowrates (0.5-1 μL/min) and their flows were imaged using a micro Particle Image Velocimetry (microPIV) setup comprising an inverted microscope and LED illumination. The velocities were determined by PIV algorithms, using RBCs as tracers, and the normalised haematocrit distributions ($H^*$) were inferred from image intensity as in our previous works [3, 4].

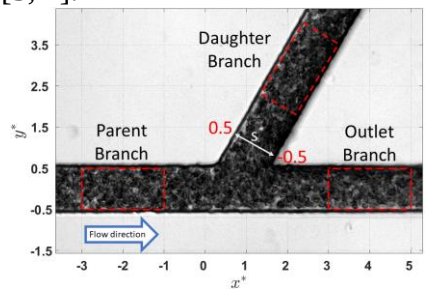


Figure 1. Sample instantaneous image of healthy RBCs flowing in the Y-shaped bifurcated geometry. Red rectangles indicate the ROIs where haematocrit profiles were extracted.

## 3. Results

The haematocrit profiles downstream of the Y-bifurcation revealed differences between the transport of healthy and hardened RBCs. The latter produce more uniform cell distributions in comparison with healthy RBCs which feature steep hematocrit gradients near the walls. Healthy RBCs tend to accumulate around the inner channel walls of the geometry close to the apex of the bifurcation; further analysis was conducted around this region to examine the velocity distributions of both suspensions based on the PIV measurements. The results of the Y-shaped bifurcating channels were compared against those obtained with a T-junction and same cross-sectional area [5]; the Y-junction produces more skewed cell distributions compared to the T-junction for healthy RBCs. On the other hand, similarly skewed haematocrit distributions were observed for hardened RBCs in both bifurcations.

## 4. Conclusions

The study shows that impaired RBC deformability leads to distinct differences in the spatial RBC organisation in bifurcating geometries with healthy RBCs found to be more sensitive to changes in the bifurcation angle. The present study complements experimental efforts towards understanding cell transport in microvascular networks, providing biophysical insight into the organisation of RBCs in pathologies. It can also aid the development of numerical models, taking into account local hemodynamic and hemorheological effects of impaired RBC deformability therein.

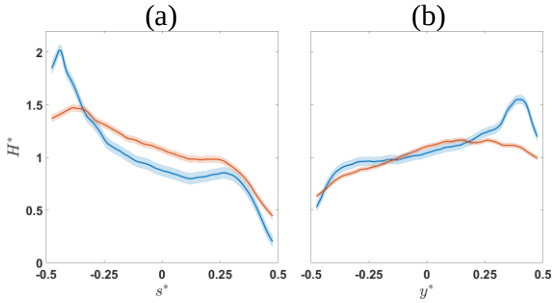


Figure 2. Indicative $H^*$ profiles between healthy (blue) and hardened (orange) RBC suspensions in the (a) daughter and (b) the outlet branches for a flow ratio of $Q^*$=0.2 of the outlet branch. Shaded regions show one standard deviation.

The support from the EPSRC DTP programme (EP/R513143/1) is gratefully acknowledged.

## References

1. Pskowski A, Bagchi P, Zahn JD, (2021) Investigation of red blood cell partitioning in an in vitro microvascular bifurcation. Artif Organs 45: 1083–1096
2. Merlo A, Berg M, Duru P, Risso F, Davit Y, Lorthois S, (2022) A few upstream bifurcations drive the spatial distribution of red blood cells in model microfluidic networks. Soft Matter 18: 1463–1478
3. Sherwood JM, Holmes D, Kaliviotis E, Balabani S, (2014) Spatial Distributions of Red Blood Cells Significantly Alter Local Haemodynamics. PLoS One 9: e100473
4. Passos A, Sherwood JM, Kaliviotis E, Agrawal R, Pavesio C, Balabani S, (2019) The effect of deformability on the microscale flow behavior of red blood cell suspensions. Phys Fluids 31: 91903
5. Passos A, (2020) The effect of red blood cell deformability on microscale blood flows. Ph.D. Thesis UCL

# Microhemodynamic impact of Testosterone Therapy in Late-Onset Hypogonadism; hypothesis testing using microfluidics

Carola KOENIG[1,*], Stavroula BALANBANI[2], Antonios STATHOULOPOULOS [2], Sudarshan RAMACHANDRAN[1,3,4,5]

1: Department of Mechanical and Aerospace Engineering, Brunel University London, Uxbridge, UK
2: Department of Mechanical Engineering, University College London, London, UK
3: Department of Clinical Biochemistry, University Hospitals Birmingham NHS Foundation Trust, Birmingham, UK
4: Department of Clinical Biochemistry, University Hospitals of North Midlands, Staffordshire, UK
5: Institute for Science and Technology in Medicine, Keele University / Faculty of Health Sciences, Staffordshire University, Staffordshire, UK

* Corresponding author: Tel.: +44 1895 259502; Email: carola.koenig@brunel.ac.uk

**Keywords:** Testosterone, Red Blood Cells, Microflow, Cell Membrane Stiffness

## 1. Introduction

Late-onset hypogonadism (LOH) in males, defined by low serum testosterone levels and associated clinical symptoms has a prevalence of 0.6–12%, though this figure is much higher (up to 40%) in men with Type 2 Diabetes Mellitus (T2DM) [1,2]. LOH has been associated with low testosterone concentrations and related phenotypes (e.g., sexual dys-function, cognitive dysfunction, fatigue, sleep disturbance, depression, hot flushes/sweats, osteoporosis, hypertension, anaemia etc.) and has been associated with increased all-cause mortality [3]. Restoring serum testosterone levels using testosterone therapy (TTh) may improve sexual dysfunction, bone mineral density, physical activity, mood, depression, anaemia, regression of T2DM, and, in men with T2DM, reduce mortality [4,5].

TTh is known to increase hematocrit (HCT) levels which in turn lead to an increase in blood viscosity, a known adverse effect [6]. HCT levels have been associated with changes in morbidity and mortality, although findings vary. Whilst the association between cardio-vascular disease (CVD), all-cause mortality and HCT levels is not fully clear, statistical evaluation hints towards a favourable relationship when low testosterone levels are adjusted.

## 2. Hypothesis

This reduced morbidity and mortality may partly be due to improved oxygenation of tissues due to increased haemoglobin (Hb). However, many clinical observations suggest that in the case of ageing the fluidity of blood is impaired; a rise in blood and plasma viscosity, impaired erythrocyte deformability and enhanced aggregation have been reported [7]. Human ageing, erythrocyte ageing, smoking, and pathologies, such as diabetes, may induce changes to the inter-dependent mechanical properties of erythrocytes such as lifespan, morphology, deformability and aggregation etc. Such changes could have a profound impact on blood rheology, haemodynamics, and tissue perfusion leading to severe vascular complications. It is suggested that increased erythrocyte lifespan, in addition to possible increased erythropoietin levels, though there is conflicting evidence [8,9], may be a possible mechanism for the TTh associated elevated HCT. Therefore, the interplay between erythrocyte lifespan, deformability and elevated haematocrit is to be investigated via microfluidics. Increased RBC elasticity may result in reduced filtering by the spleen and

therefore aid increasing HCT.

## 3. Methodology

Preliminary tests with animal blood were pursued to test the hypothesis of the potential link of enhanced erythrocyte deformability. A microfluidic channel comprising an array of pillars mimicking a porous medium was fabricated via soft lithography. The pillars were 20 μm in diameter (D), arranged in a staggered configuration of 16 rows with a pitch ratio of 2D and 1.5D in the lateral and transverse directions, respectively. Fresh pig blood was mixed with K2EDTA anticoagulant. RBCs were separated via centrifugation and suspended in PBS at a concentration of 5%. One sample was used as control and the second one was treated with statins to increase the deformability using the protocol described in [10]. The dynamic viscosity of whole blood and the suspensions were measured using an ARES rheometer. The deformability of RBCs was also measured using a microfluidic-based ektacytometer (Rheoscan-D300, Sewon Meditech, Inc., Seoul, Korea). RBC suspensions (both control and statin-treated) were perfused through the microfluidic device by means of a syringe pump (Nemesys S, Cetoni, Germany) and imaged using an inverted microscope (Nikon Diaphot 200, Japan) equipped with a high-speed camera (NanoSense MkIII, IDT, USA) and a 20x objective (NA=0.4). The microchannel flow was illuminated using a 100W halogen lamp and 1000 images were acquired for 20s. The flow rate in the parent branch was kept constant at 0.5 μL/min, which is physiologically relevant for microvascular flows [11].

## 4. Results

Preliminary results showed that statin-treated RBCs feature higher mean values of the maximum elongation index (0.4652±0.007) compared to the control sample (0.4350±0.005), meaning that statins increase cell deformability. Particle Tracking Velocimetry (PTV) revealed that statin-treated cells flow through the pillar array with more ease compared to the healthy RBCs, featuring more uniform distributions in the whole domain (Fig 1).

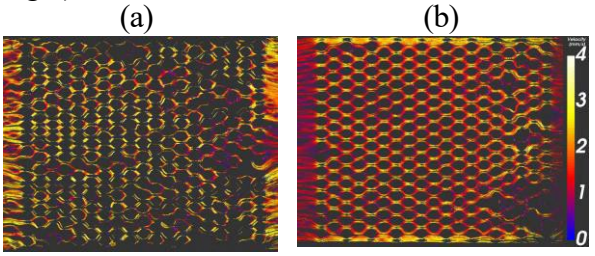


Figure 1. Time-resolved Particle Tracking Velocimetry (PTV) RBC trajectories of the (a) control and the (b) stain-treated sample.

## 5. Conclusions

This preliminary study shows that statins can alter the biomechanical properties of RBCs, making RBCs more deformable, and can be used as a proxy for an initial hypothesis testing on the effects of testosterone treatment. Softening of RBCs has a direct implication in perfusion in complex domains whereby statin-treated RBCs can pass through easier compared to healthy RBCs. Also, the use of statins affects spatial organization of RBCs, with statin-treated cells featuring more uniform cell distributions in the pillar array geometry. Work is under way to explore density-based differentiation of RBC populations using density gradients media like Percoll and Optiprep to explore the effects of RBC age.

## References

[1] Dudek P, Kozakowski J, Zgliczyński W., Prz Menopauzalny. 2017 Jun; 16(2): 66–69.
[2] Cheung K K T, Luk A O Y, So W Y, *et al*. J Diabetes Investig. 2015 Mar; 6(2): 112–123.
[3] Pye S R, Huhtaniemi I T, Finn J D, *et al*., J Clin Endocrinol Metab, 2014 Apr;99(4):1357-66.
[4] Shores M M, Smith N L, Forsberg C W, *et al*., J Clin Endocrinol Metab, 2012 Jun;97(6):2050-8.
[5] Muraleedharan V, Marsh H, Kapoor D, *et al*., Eur J Endocrinol, 2013 Oct 21;169(6):725-33.
[6] König C S, Balabani S, Hackett G I, *et al.*, Sex Med Rev, 2019 Oct;7(4):650-660.
[7] Simmonds M J, Meiselman H J, Baskurt OK., J Geriatr Cardiol, 2013 Sep;10(3):291-301.
[8] Coviello A D, Kaplan B, Lakshman K M, *et al*., J Clin Endocrinol Metab. 2008 Mar; 93(3): 914–919.
[9] Bachman E, Travison T G, Basaria S, *et al*., J Gerontol A Biol Sci Med Sci. 2014 Jun; 69(6): 725–735.
[10] Sheikh-Hasani V, Babaei M, Azadbakht A *et al.*, Biomedical Optics Express, 2018, 9(3): 1256-1261
[11] Chaigneau E, Roche M, Charpak S, Front. Neurosci., 2019, 13:644.

# A microfluidic in vitro model of microvascular collapse

Stephanie HALLAM[1,*], Pranav VASANTHI BATHRINARAYANAN[1], Zoe SCHOFIELD[1], Nina KOVALCHUK[1], Mark SIMMONS[1]

1:School of Chemical Engineering, University of Birmingham, Birmingham, UK

* Corresponding author: Tel.: +44 7544154703; Email: SMH604@student.bham.ac.uk

**Abstract:** A microfluidic model of a blood vessel network was created to investigate the effect of microvascular collapse on wall shear stress and flow distribution. Trauma conditions, such as Acute Compartment Syndrome (ACS), result in microvascular collapse and thus increase resistance in the microvascular network, decreasing the flow rate in the vessel and thus decreasing the shear stress profile. The wall shear stress in the blood vessel network will influence behavior in endothelial cells lining the blood vessel walls. These phenomena have been modelled using a microfluidic device representative of the microvasculature. The Young's modulus of the blood vessel wall was mimicked in the device design to maintain physiological relevance. Ghost particle velocimetry (GPV) was used to assess the flow distribution, velocity profile and shear stress profile when increasing resistance in the microfluidic model. As the resistance in the system increases, at constant pressure, the flowrate decreases; however, at the localized area of collapse there will be an increased shear stress on the channel walls due to the increased velocity. The position of the increased resistance within the network will determine the direction of flow between branched channels which may further influence the localised shear stress in vessels of different diameter.

**Keywords:** Blood vessel, Micro Flow, Ghost Particle Velocimetry, Acute Compartment Syndrome

## 1. Introduction

Acute compartment syndrome, ACS, is an emergency trauma condition that affects the microvasculature and requires a fast diagnosis to prevent harm to the patient. During ACS the pressure in the muscular compartment surrounding the microvascular network rises to a point where the blood flow is restricted. If resistance to blood flow is not removed, cell necrosis occurs due to a lack of blood supply, leading to limb loss or in some cases death [1]. A microfluidic model of a microvascular network was created to investigate physiological processes accompanying development of ACS.

When flow pressure is maintained, increased resistance in the microvasculature reduces the flowrate in the system and leads to a change in wall shear stress, affecting endothelial cell behavior. The resistance depends on the degree at which the blood vessel is collapsed/stenosed. Resistance may occur in different places in the network resulting in a change in flow distribution. Diversion of flows due to increased resistance in arteries and the effect of branching has been investigated in the literature [2]; however, the situation differs for veins and the related capillary network due to their smaller diameter, Young's moduli and different physiological behavior. The aim of this study is to investigate processes in microvascular systems upon deformation (stenosis) of an adjacent vein or large capillary using a microfluidic model.

## 2. Experimental Set Up

Branched and stenosed microfluidic devices were created using a standard soft lithography process from Polydimethylsiloxane (PDMS SYLGARD™184, DOW), a commonly used polymer for microfluidic device fabrication. This is advantageous for the investigation of ACS due to its flexibility and ability to vary the Young's modulus.

The Young's Modulus of PDMS was varied using 10:1, 15:1, 20:1 and 25:1 base to curing agent ratios and tested on the Zwick Roell Z030 Universal Tester (ZwickRoell, Germany). The

samples were secured into 10 kN grips and pulled from 0 force at 10 mm/min until failure and the elongation and stress recorded.

The flow distribution was measured using Ghost Particle Velocimetry [3] in which a dispersion of nano-particles is passed through the microfluidic device under brightfield illumination creating a speckle pattern from scattered light. Polystyrene nanoparticles with average size of 200 nm 10% solids (Merck, UK) were used in concentration of 0.2% v/v. The liquid was supplied to the microfluidic device using a Elveflow OB1 pressure controller at varied pressures. The flow was recorded using a high-speed camera (Photron Nova s15) at 1000-10000 fps and exposure of 0.08-0.2 ms depending on the flowrate. The camera was connected to an inverted microscope (Nikon TI Eclipse) with a 20x lens (Nikon, CFI Plan Fluor DLL) providing a 1 µm/pixel spatial resolution. 400 frames were recorded and processed using ImageJ software and analysed using MATLAB PIVLab [4].

## 3. Results

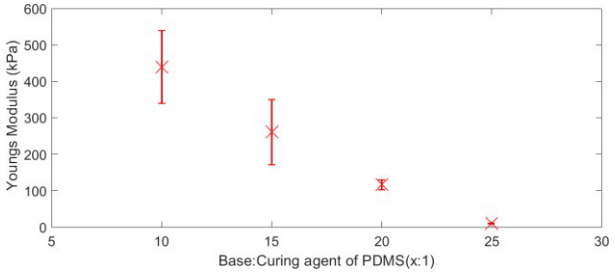


Figure 1: Effect of the ratio of PDMS base to curing agent on Youngs modulus

Figure 1 shows that as the ratio of base to curing agent increases, the Young's modulus decreases, therefore, to match the modulus of a capillary, 10 kPa, the 25:1 ratio of PDMS was chosen at 7 kPa.

The microfluidic channel was also collapsed dynamically using micropumps to control the level of resistance. Figure 2 shows the velocity profile from GPV in a 300 µm channel that is deformed dynamically supplying external pressure to the channel walls, increasing the resistance and velocity in the centre.

We can also see the downstream effect of increased resistance when there is branching in the blood vessel network.

The degree of stenosis increases the resistance and thus decreases flowrate when at a constant pressure. The shear stress in the localised area of the stenosis will be increased with increasing resistance. The effect of increasing resistance in the channel will divert the flow to the path of least resistance in branched channels depending on the location of stenosis in the microfluidic network.

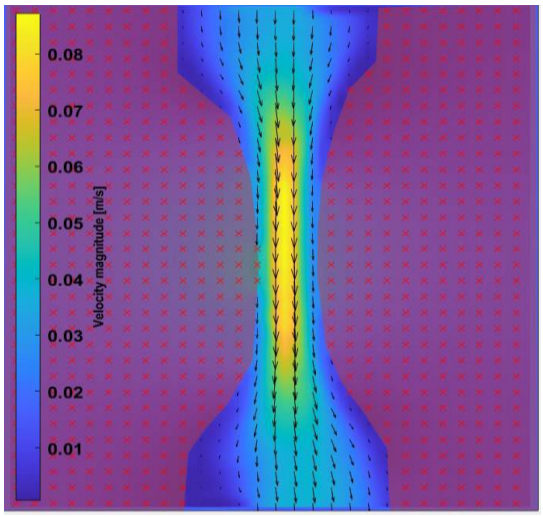


Figure 2: GPV analysis of a dynamically collapsed 300 µm channel showing the resultant velocity distribution

## Acknowledgements

This research was funded by EPSRC, UK, through the PREMIERE Programme Grant EP/T000414/1.

## References

[1] Von Keudell AG, Weaver MJ, Appelton PT Bae DS, Dyer GSM, Heng M, 2015, Diagnosis and Treatment of Acute Compartment Syndrome The Lancet Vol. 386
[2] Chiu J, Chien S, 2011, Effects of Disturbed Flow on Vascular Endothelium: Pathophysiological Basis and Clinical Perspectives Physiol Rev. 91(1)
[3] Riccomi M, Alberini F, Brunazzi E, Vigolo D, 2018, Ghost Particle Velocimetry as an alternative to µPIV for micro/milli-fluidic devices, Chemical Engineering Research and Design 133(95)
[4] Thielicke, W.; Stamhuis, E.J. PIVlab— Towards User-friendly, Affordable and Accurate Digital Particle Image Velocimetry in MATLAB. J. Open. Res. Softw. 2014, 2, e30.

## SESSION 7b
## Mathematical and computational approaches
Chair: **M. Magnini**

# Predicting rare rupture of nanoscale thin films

Jingbang LIU[1,*], Tobias GRAFKE[1], Duncan A. LOCKERBY[2], and James E. SPRITTLES[1]

1: Mathematics Institute, University of Warwick, Coventry, UK
2: School of Engineering, University of Warwick, Coventry, UK

* Corresponding author: Email: jingbang.liu@warwick.ac.uk

**Abstract:** The spontaneous rupture of nanoscale thin films plays an important role in many industrial applications. Past theoretical work based on a long wave approximation has successfully identified a critical film height, below which the free surface nanowaves become linearly unstable, leading to spontaneous rupture in the so-called 'spinodal regime'. However, for much thicker films which are considered linearly stable, rupture is also observed in a different manner and the accountable theory is missing. In this work, we propose a theoretical framework based on fluctuating hydrodynamics and rare event theory to explain the spontaneous rupture in the 'thermal regime'. Molecular dynamics simulations are performed, and the results agree with numerical simulations for 2D films. To overcome the computational barrier for 3D films, adaptive multilevel splitting method is to be used to speed up the sampling process.

**Keywords:** Instability, nanofluidics, free surface flows, rare events

## 1. Introduction

The spontaneous rupture of nanoscale thin films has attracted increasing attention due to its importance in various applications such as thin-film solar cell manufacturing [1], producing nanoparticles [2] and patterning biological molecules [3]. At such a small scale, two physical effects that would normally be neglected come into play: nanoscale surface waves induced by thermal fluctuations (Brownian motion of liquid particles) [4] and inter-molecular forces that create a disjoining pressure [5]. Over the past few decades, theoretical work based on a long wave approximation has successfully identified a critical film height, below which the nanowaves become linearly unstable, which lead to spontaneous rupture [6]. This dewetting in the so-called 'spinodal regime' has been confirmed repeatedly in experiments with polymer [6-7] and atomic films [8]. However, it is also observed that much thicker films, which are considered linearly stable, rupture as well [6]. It is believed that thermal fluctuations are the cause of dewetting in this "thermal regime", but a theory predicting the rupture is missing.

In this work, we propose a theoretical framework to account for the rupture of linearly stable films in two and three dimensions as follows.

## 2. Theory and preliminary results

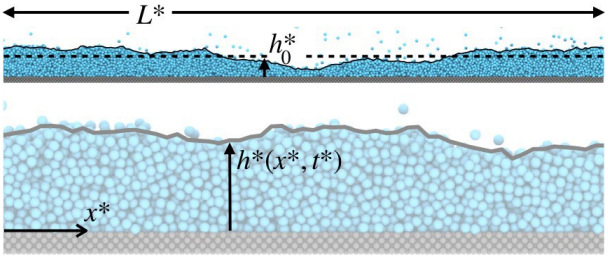


Fig. 1. Schematic of the 2D setup, showing the free surface extracted from MD simulations.

The governing equation comes from fluctuating hydrodynamics. By applying the long wave approximation to the Landau-Lifshitz Navier-Stokes equations one arrives at the stochastic thin film equation (STF) [9], which can then be solved numerically using a pseudo-spectral method in the Fourier space. The setup for 2D films is shown in Fig. 1., in which $L^*$ is the length of film and $h_0^*$ is the initial film height. A linear stability analysis gives the critical film height $H^*$ above which

the film is linearly stable. Molecular dynamics (MD) simulations with the Lennard-Jones potential are also performed for validation.

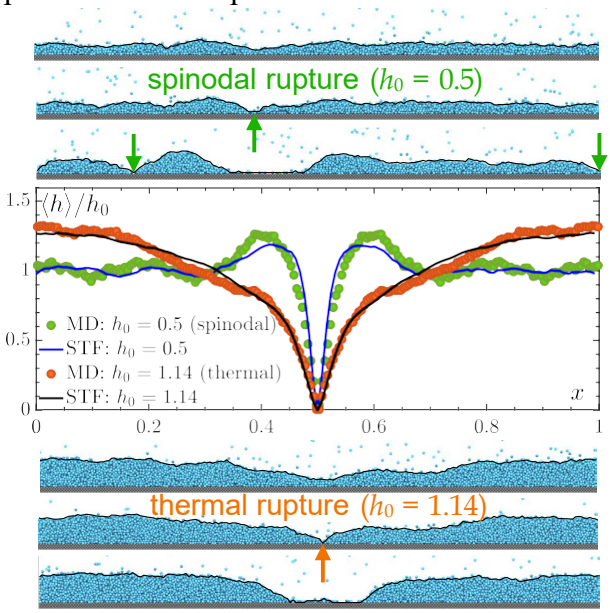


Fig. 2. Snapshots of MD as films approach rupture and average rupture shape compared between MD and STF. $h_! = h_!^*/H^*$ is the normalised initial film height.

Fig. 2. shows that the average rupture shape obtained from MD agrees well with STF, with the two regimes clearly identified: films in the spinodal regime rupture locally at multiple points whereas rupture in thermal regime is more global.

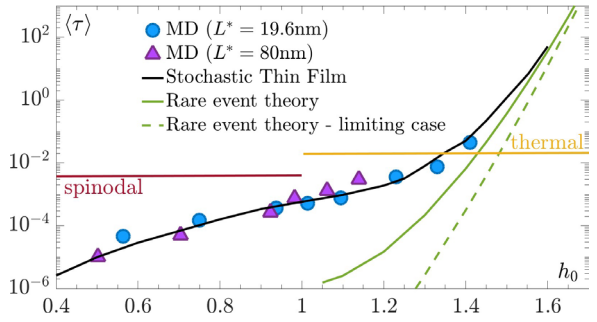


Fig. 3. Average rupture time for 2D films obtained from MD, STF and rare event theory.

To further simplify the analysis, we rewrite the STF in a gradient flow form. This then allows us to use the Kramer's Law from the rare event theory to estimate the mean rupture time ⟨τ⟩. Fig. 3. shows that for 2D film rupture time the MD, STF agrees nicely, and as the film gets thicker the rare event theory takes effect.

For even thicker and 3D films the computational cost increase as the rupture time increases exponentially. To overcome this barrier, we plan to use the adaptive multilevel splitting method [10] to speed up the sampling process.

## References

[1] Makarov, S.V., Milichko, V.A., Mukhin, I.S., Shishkin, I.I., Zuev, D.A., Mozharov, A.M., Kras- nok, A.E., Belov, P.A., 2016. Controllable femto- second laser-induced dewetting for plasmonic ap- plications. Laser & Photonics Reviews 10, 91–99.

[2] Stannard, A., 2011. Dewetting-mediated pat- tern formation in nanoparticle assemblies. Journal of Physics: Condensed Matter 23, 083001.

[3] Gentili, D., Foschi, G., Valle, F., Cavallini, M., Biscarini, F., 2012. Applications of dewetting in micro and nanotechnology. Chem. Soc. Rev. 41, 4430.

[4] Zhang, Z., Wang, Y., Amarouchene, Y., Bois- gard, R., Kellay, H., Würger, A., Maali, A., 2021. Near-Field Probe of Thermal Fluctuations of a Hemispherical Bubble Surface. Phys. Rev. Lett. 126, 174503.

[5] Kavokine, N., Netz, R.R., Bocquet, L., 2021. Fluids at the Nanoscale: From Continuum to Sub-continuum Transport. Annu. Rev. Fluid Mech. 53, 377–410.

[6] Seemann, R., Herminghaus, S., Jacobs, K., 2001. Dewetting Patterns and Molecular Forces: A Reconciliation. Phys. Rev. Lett. 86, 5534–5537.

[7] Xie, R., Karim, A., Douglas, J.F., Han, C.C., Weiss, R.A., 1998. Spinodal Dewetting of Thin Polymer Films. Phys. Rev. Lett. 81, 1251–1254.

[8] Bischof, J., Scherer, D., Herminghaus, S., Lei- derer, P., 1996. Dewetting Modes of Thin Metallic Films: Nucleation of Holes and Spinodal Dewetting. Phys. Rev. Lett. 77, 1536–1539.

[9] Grün, G., Mecke, K., Rauscher, M., 2006. Thin-Film Flow Influenced by Thermal Noise. J Stat Phys 122, 1261–1291.

[10] Cérou, F., Guyader, A., Lelièvre, T., Pom- mier, D., 2011. A multiple replica approach to sim- ulate reactive trajectories. The Journal of Chemical Physics 134, 054108.

# Study of the vapor-liquid interface during annular flow in a minichannel: OpenFOAM numerical simulations vs optical measurements

Emanuele ZANETTI[1], Arianna BERTO[1], Stefano BORTOLIN[1,*], Mirco MAGNINI[2], Davide DEL COL[1]

1: Department of Industrial Engineering, University of Padova, Padova, IT
2: Department of Mechanical, Materials and Manufacturing Engineering, The University of Nottingham Nottingham, UK

* Corresponding author: Tel.: +39 049 8276729; Email: stefano.bortolin@unipd.it

**Abstract:** Annular flow is one of the most frequently encountered two-phase flow regimes during condensation inside small diameter channels. Since the main heat transfer resistance is associated to the liquid annulus, the knowledge of the vapour-liquid interface evolution in time and space is fundamental for the study of in-tube condensation. In this work, a new approach for the simulation of vapour-liquid annular flow is proposed. The Volume of Fluid (VoF) method is employed to compute the vapour-liquid interface and OpenFOAM open-source code is used to perform transient numerical simulations with refrigerant R245fa flowing inside a 3.4 mm circular channel at 40 °C saturation temperature, mass velocity $G$ = 100 kg m$^{-2}$ s$^{-1}$ and different values of vapour quality. The numerical setup consists of 2D axisymmetric domain, downflow configuration, turbulence modelling in both phases and adaptive mesh refinement performed in correspondence of the liquid/vapour interface. Simulations are used to predict the instantaneous and averaged values of the liquid film thickness. Numerical results are compared against optical measurements performed during in-tube condensation inside a vertical test section equipped with a glass window.

**Keywords:** CFD, Liquid film thickness, Volume of Fluid, Annular flow

## 1. Numerical setup

CFD numerical simulations of R245fa annular flow inside a vertical channel have been performed with the open-source code OpenFOAM. A novel transient solver has been developed starting from a Volume of Fluid (VoF)-based adiabatic solver already available ad called *interIsoFoam*. With the VoF method, in addition to the standard set of equations (continuity and momentum), a transport equation related to the advection of the so-called "volume fraction" scalar field ($\alpha$=1 for the liquid, $\alpha$=0 for the vapour) has to be solved. In the absence of phase-change, Eq. 1 must be solved

$$\frac{\partial \alpha}{\partial t} + \nabla \cdot (\alpha \boldsymbol{u}) = 0 \qquad (1)$$

where $t$ is time and $\boldsymbol{u}$ is the velocity vector. The computational domain considered in the present work consists of a 2D axisymmetric channel, as depicted in Figure 1. Simulations have been run considering a channel radius $R$ equal to 1.7 mm (to match the experimental test conditions reported in [1]) and a total length of the channel equal to 40$R$. The $k$-$\omega$ SST model is used for turbulence modelling in both the liquid and vapor phases and the correction proposed by [2] is applied to the $\omega$ equation to damp the turbulence at the vapor-liquid interface. The damping parameter proposed in [2] and named $B$ has been varied between 0 and 1 depending on the considered inlet conditions.

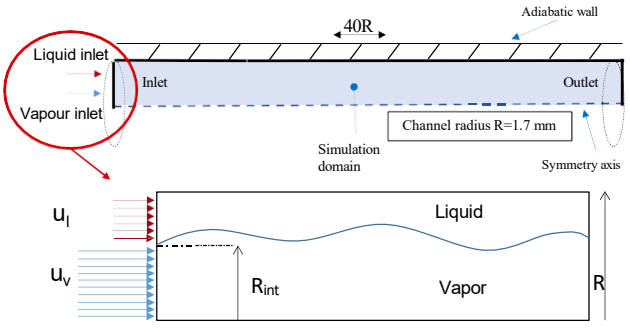


Figure 1. Setup used for the numerical simulations of annular flow.

Since, for a given condition of mass velocity $G = \dot{m}/A$ and vapor quality $x$, the radius of the vapor core ($R_{int}$) and the inlet velocity are not fixed, the following procedure has been used to set inlet boundary conditions. A guess value for the interface position is assumed with a void fraction correlation (Eq.2, [3]) and the inlet velocities of the vapor phase $u_v$ and liquid phase $u_l$ are calculated (Eqs. 3-4)

$$A_v = \varepsilon A \quad (2)$$

$$u_v = \frac{\dot{m} x}{\rho_v A_v} \quad (3)$$

$$u_l = \frac{\dot{m}\,(1-x)}{\rho_l\,(A-A_v)} \quad (4)$$

where $A$ is the channel cross section area, $A_v = \pi \cdot R_{int}^2$, and $\varepsilon$ is the void fraction. Numerical simulations showed that, after a certain axial position, the liquid film thickness LFT ($R$-$R_{int}$) reaches a stable value (time average) independently from the inlet value used for $R_{int}$.

## 2. Adaptive mesh refinement

An adaptive mesh refinement (AMR) model has been implemented. When AMR is activated, a rectangular cell is divided into four cells. A generic cell is refined if $\alpha \in [0.1,0.9]$. In addition, the near-wall region is also refined. Therefore, three mesh zones can be identified: a) refined cells at the wall; b) refined cells near the interface; c) unrefined cells in the vapor bulk and in the liquid film (far from the wall). After a mesh-independence study, a mesh with unrefined cell size equal to $R/64$ and 3 refinement levels both at the wall and at the interface has been chosen. Figure 2 shows the computed mesh during the passage of a liquid wave. The liquid wave is depicted in red ($\alpha$=1), the vapor bulk in blue ($\alpha$=0).

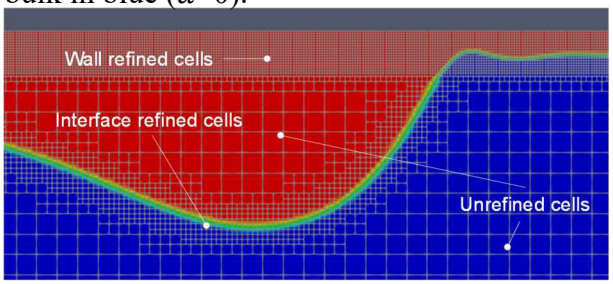


Figure 2. Mesh structure during the passage of a liquid wave in annular flow.

## 3. Numerical results compared against experimental data

Figure 3 displays a comparison between the experimental and numerical data of liquid film thickness. The results refer to annular flow of refrigerant R245fa at 40 °C saturation temperature and mass flux equal to 100 kg m$^{-2}$ s$^{-1}$. Three different values of vapour qualities have been considered: 0.39, 0.58 and 0.77. The coefficient $B$ for turbulence damping in the $k$-$\omega$ SST model has been set equal to 0.1, 0.25 and 1 respectively for the three different vapor qualities (0.39, 0.58, 0.77) here considered (thus assuming that the turbulence damping is reduced at high liquid Reynolds numbers). The time average LFT has been evaluated in correspondence to a fixed axial position, close to the channel outlet (28$R$). As reported in Fig. 3, the numerical results show a good agreement with experimental data measured by coupling shadowgraph technique with measurements performed by a chromatic confocal sensor.

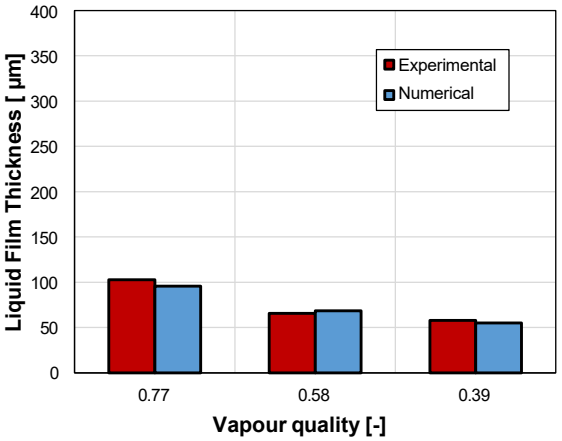


Figure 3. Comparison between calculated and measured values of the mean liquid film thickness.

## References

[1] A. Berto, P. Lavieille, M. Azzolin, S. Bortolin, M. Miscevic, D. Del Col, Liquid film thickness and heat transfer measurements during downflow condensation inside a small diameter tube, Int. J. Multiph. Flow. (2021). https://doi.org/10.1016/j.ijmultiphaseflow.2021.103649.

[2] W. Fan, H. Anglart, Progress in phenomenological modeling of turbulence damping around a two-phase interface, Fluids. (2019). https://doi.org/10.3390/fluids4030136.

[3] S.Z. Rouhani, E. Axelsson, Calculation of void volume fraction in the subcooled and quality boiling regions, Int. J. Heat Mass Transf. 13 (1970) 383–393. https://doi.org/10.1016/0017-9310(70)90114-6.

# AI for capillary-driven droplet dynamics

Andreas DEMOU[1,*], Nikos SAVVA[1]

1: Computation-based Science and Technology Research Center, The Cyprus Institute, Nicosia 2121, Cyprus

* Corresponding author: Email: a.demou@cyi.ac.cy

**Abstract:** This study presents the application of surrogate modelling approaches for wetting hydrodynamics, leveraging data-driven multi-fidelity modelling to enable an accurate inference of wetting dynamics. More specifically, datasets are derived from droplet trajectories moving on chemically heterogeneous surfaces, as obtained by the evolution of their contact lines. These datasets are then used to train and evaluate data-driven models based on the Fourier neural operator, in predicting the motion of droplets on different surfaces. The findings of this study can pave the way towards efficient surface design in applications.

**Keywords:** Contact lines, machine learning, wetting, capillary phenomena

## 1. Introduction

The study of the motion of droplets on heterogeneous surfaces is a topic of active interest due to the wide applicability of contact line phenomena in a broad spectrum of areas, including microfabrication, biomedicine, smart materials, pharmaceutics, printing, as well as energy conversion and water harvesting in environmental applications, to name a few [1]. Nevertheless, resolving the dynamics via direct numerical simulation (DNS) remains a challenge due to the presence of interfaces. The advent of data-driven methodologies and their application in the solution of partial differential equations emerges as a promising alternative to mitigate the computing costs required for DNS. The Fourier neural operator (FNO) was recently proposed for accurately and efficiently learning resolution-invariant solution operators for families of partial differential equations [2]. In this study, we utilize FNO-based models to capture contact line dynamics and predict droplet trajectories on chemically heterogeneous surfaces. Ground-truth data for training and validation are generated using both low and high-fidelity data. Our assessment of the FNO architecture is based on two distinct approaches, one of which deploys the FNO as an iterative architecture as originally proposed in Ref. [2] (iterative approach), whereas the other augments a low-order approximation to the contact line velocity [3,4] with a data-driven counterpart for the higher-order corrections, which is then evolved in time by standard discretization techniques (blended approach).

## 2. AI model training and testing

Firstly, a proof-of-concept is established via cheaply generated datasets from long-wave equations [1]. This best performing candidate is then applied to datasets obtained from direct numerical simulations with the Basilisk open-source software [5].

### 2.1 Low fidelity data

Asymptotic models that are applicable in the long-wave limit (low capillary number, Stokes limit and small contact angles) were used to generate a dataset of droplets traveling on chemically heterogeneous surfaces. The dataset was then used to train the FNO-based model following both the iterative and the blended approach, both of which were able to reach testing errors in the region of 1%. Fig. 1 shows a visual comparison between the predicted contact line and the reference results for the two approaches,

for an out-of-distribution sample. As evidenced in Fig. 1, the blended approach outperforms the iterative approach, yielding an AI model that generalizes well to unseen heterogeneity profiles.

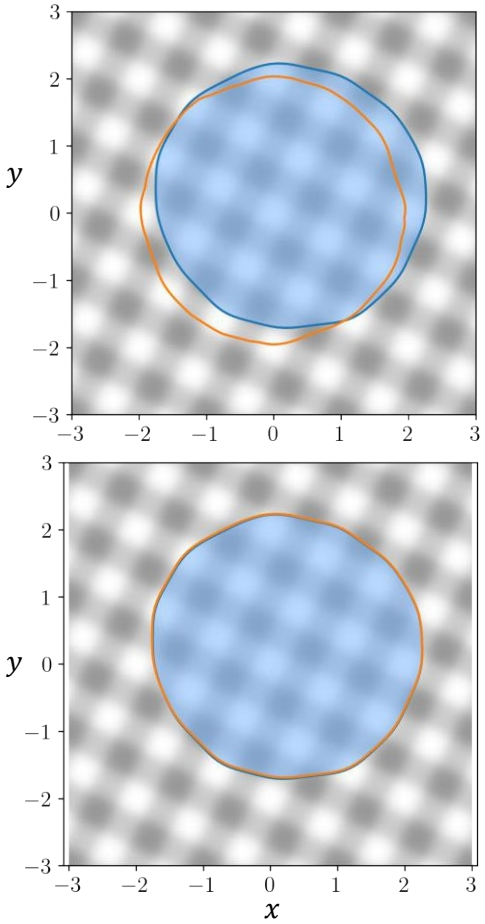


Fig. 1. Comparison between the AI-predicted contact lines (orange curves) and reference droplet position (blue region), using low fidelity data. (top) Iterative approach, and (bottom) blended approach. Darker shaded regions in background correspond to more hydrophobic regions on the surface.

### 2.2 High fidelity data

The blended approach is then followed to train FNO-based models using DNS simulations (a sample is shown in Fig. 2), to allow the modelling of more realistic scenarios with larger contact angles. After overcoming a set of new challenges, in terms of the appropriate base analytical approximation and contact angle calculation, an accurate AI model is trained that can successfully capture the contact line position, achieving a speedup of three orders of magnitude compared to carrying out a DNS.

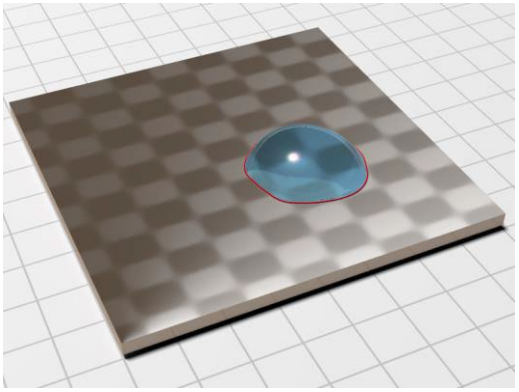

Fig. 2. DNS sample of a droplet traveling on a heterogeneous surface. The contact line is shown in red colour. Darker shaded regions in background correspond to more hydrophobic regions on the surface.

## Acknowledgements

The authors acknowledge the support from the European Union's Horizon 2020 research and innovation program under grant agreements No 951733 and No 810660, and from the Cyprus Research and Innovation Foundation under contract No. EXCELLENCE/0421/0504.

## References

[1] Bonn, D., Eggers, J., Indekeu, J., Meunier, J. and Rolley, E., 2009. Wetting and spreading. *Rev. Mod. Phys.*, 81(2), p.739.

[2] Li, Z., Kovachki, N., Azizzadenesheli, K., Liu, B., Bhattacharya, K., Stuart, A. and Anandkumar, A., 2020. Fourier neural operator for parametric partial differential equations. *arXiv preprint arXiv:2010.08895*.

[3] Lacey, A.A., 1982. The motion with slip of a thin viscous droplet over a solid surface. *Stud. Appl. Math.*, *67*(3), p.217.

[4] Cox, R. G. (1986). The dynamics of the spreading of liquids on a solid surface. Part 1. Viscous flow. *J. Fluid Mech*, 168, p.169.

[5] Popinet, S. (2015). A quadtree-adaptive multigrid solver for the Serre–Green–Naghdi equations. *J. Comp. Phys.*, 302, p.336.

# Towards a Multi-Scale Modelling Approach for Boiling Heat Transfer: Exploring the Applicability of an Enhanced Volume of Fluid Method in Sub-micron Scales

Bhaskar CHAKRABORTY[1,*], George LAWRENCE[1], Mirko GALLO[1, 2], Marco MARENGO[1,3], Anastasios GEORGOULAS[1]

1: School of Architecture, Technology and Engineering, Advanced Engineering Centre, University of Brighton, Brighton, UK

2: Department of Mechanical and Aerospace Engineering, La Sapienza University of Rome, Rome, IT
3: Department of Civil Engineering and Architecture, University of Pavia, Pavia, IT

* Corresponding author: Tel.: +44 (0)1273 642443; Email: B.Chakraborty@brighton.ac.uk

**Abstract**: Developments in modern applications are encountered with escalation in heat dissipation. These developments have triggered an interest in replacing single-phase cooling systems with phase-change technologies. There are various computational methods to model single-phase systems. However, their effectiveness with phase-change systems is limited to simple configurations. Due to the complexity of phase-change applications, there is an urgent need to enhance the capability of computational tools to tackle such scenarios. To study boiling heat-transfer, models like the Volume of Fluid (VOF) and the Diffuse Interface (DI) are adopted. The VOF methodology is prevalent for macro-scale while the DI is more suited for mesoscale simulations. To develop a multi-scale modelling approach for the future, there is scope to test the applicability of both methodologies exploring their spatial scale limits. Here, using an enhanced VOF-based method within the OpenFOAM CFD framework, cases of single bubble growth and detachment from a superheated plate in saturated pool boiling conditions as well as analytical benchmark cases of a vapour bubble growing within a superheated liquid domain are simulated using progressively lower sub-micron scales. The results conclude that the proposed VOF method is indeed applicable for sub-micron scales, paving the way for its integration with mesoscale approaches.

**Keywords:** VOF, Boiling, Multi-Scale Modelling

# Measurement of Solid-Liquid Friction Coefficient by Using Molecular Dynamics: Role of Timescale

Haruki OGA[1,*], Takeshi OMORI[2], Laurent JOLY[3], Yasutaka YAMAGUCHI[1, 4]

1: Department of Mechanical Engineering, Suita, Osaka University, Osaka, JP
2: Department of Mechanical Engineering, Osaka Metropolitan University, Sumiyoshi, Osaka, JP
3: Univ Lyon, Univ Claude Bernard Lyon 1, CNRS Institut Lumière Matière, VILLEURBANNE, FR

* Corresponding author: Email: haruki@nnfm.mech.eng.osaka-u.ac.jp

**Abstract:** Solid-liquid friction plays a key role in nanofluidic systems. Following the pioneering work of Bocquet and Barrat, who proposed to extract the friction coefficient (FC) from the plateau of the Green–Kubo (GK) integral of the solid–liquid shear force autocorrelation, the so-called plateau problem has been identified when applying the method to finite-sized molecular dynamics simulations. A variety of approaches have been developed to overcome this problem. Here, we propose another method that is easy to implement, makes no assumptions about the time dependence of the friction kernel, does not require the hydrodynamic system width as an input, and is applicable to a wide range of interfaces. In this method, the FC is evaluated by fitting the GK integral for the timescale range where it slowly decays with time. The fitting function was derived based on an analytical solution of the hydrodynamics equations [Oga et al., Phys. Rev. Res. 3, L032019 (2021)]. By comparing the results with those of other GK-based methods and non-equilibrium molecular dynamics, we show that the FC is extracted with excellent accuracy by the present method, even in wettability regimes where other GK-based methods suffer from the plateau problem.

**Keywords:** solid-liquid, slip, friction Green-Kubo, molecular dynamics

## 1. Introduction

Solid-liquid (S-L) slip particularly affects the fluid transport, and the Navier boundary condition (BC) was proposed as the slip model:[1]

$$\tau_{\mathrm{w}} = \lambda_0 u_{\mathrm{slip}}, \qquad (1)$$

where $\tau_{\mathrm{w}}$ is the S-L friction force per area, $\lambda_0$ is the S-L friction coefficient (FC) and $u_{\mathrm{slip}}$ is the slip velocity. The FC can be directly calculated by using non-equilibrium molecular dynamics (NEMD) simulations of Poiseuille or Couette flow; however, this requires a high shear rate, typically above $10^9\ \mathrm{s}^{-1}$, to reduce the statistical error due to thermal fluctuation. On the other hand, several methods for calculating the FC from equilibrium molecular dynamics (EMD) with zero shear rate have been proposed. In their pioneering work, Bocquet and Barrat (BB)[2] introduced a Green-Kubo (GK) integral defined by

$$\Lambda(t) \equiv \frac{1}{Sk_{\mathrm{B}}T}\int_0^t \langle F_{\mathrm{w}}(t)F_{\mathrm{w}}(0)\rangle \mathrm{d}t\,, \qquad (2)$$

where $S, k_{\mathrm{B}}, T$ and $\langle F_{\mathrm{w}}(t)F_{\mathrm{w}}(0)\rangle$ denote the surface area, Boltzmann constant, absolute temperature and equilibrium autocorrelation function of instantaneous shear force $F_{\mathrm{w}}$ on the solid as function of time $t$, respectively, for the calculation of FC. However, unlike the bulk GK, the GK given by Eq. (2) does not converge to the transport coefficient $\lambda_0$. In this study[4], we propose a new measurement method of the FC based on time separation in the GK integral $\Lambda(t)$, and we show the advantages of this method by comparing its results with NEMD results as well as existing EMD-based results.

## 2. Measurement Method

Let us consider a system where a liquid is confined between two fixed planar solid walls like Fig. 1. The author derived a theoretical expression[3] of the GK integral for that system by coupling the Stokes equation for the liquid

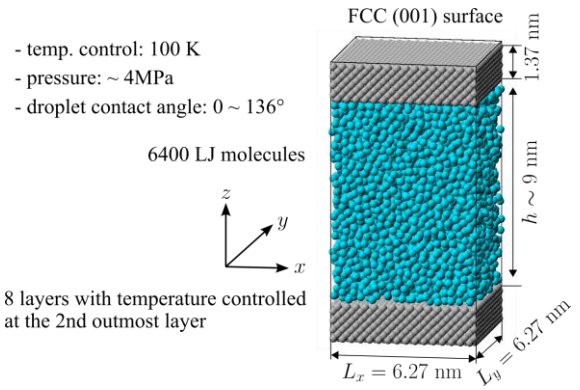


**Fig. 1.** MD simulation system of LJ liquid between flat fcc walls.

motion and a Langevin equation for the motion of one of the walls in direction parallel to the interface. We simplified the theoretical expression of GK integral:

$$\Lambda_{\mathrm{mid}}(t) = \lambda_0 \exp\left(\frac{t}{t_{\mathrm{slip}}}\right) \mathrm{erfc}\left(\sqrt{t/t_{\mathrm{slip}}}\right) \quad (3)$$

with $t_{\mathrm{slip}} = \rho\eta/\lambda_0^2$ by introducing two limits $t_{\mathrm{fk}} \to +0$ and $t_{\mathrm{sys}} \to \infty$, where $t_{\mathrm{fk}}$ is decay time constant of friction kernel and $t_{\mathrm{sys}} \equiv \rho h^2/\eta$ is time constant related to the system size.

We compared four measurement methods of FC $\lambda_0$ by using EMD and NEMD: $\lambda_{\mathrm{mid}}$ denote the FC obtained by our new method of fitting the GK integral with Eq. (3) from EMD, $\lambda_{\mathrm{max}}$ denote maximum value of $\Lambda(t)$ from EMD, $\lambda_\infty$ denote the FC obtained from $\Lambda(\infty)$ from EMD and $\lambda_{\mathrm{NEMD}}$ denote the FC obtained from NEMD directly.

## 3. Results and Discussion

Figure 2 shows GK integral from EMD and illustrates the three EMD calculation methods of the FC from the GK integrals. We fitted the GK integral with Eq. (3) in the red region of the Fig. 2 and obtained $\lambda_{\mathrm{mid}}$ as one of the fitting parameters. Figure 3 shows the FCs obtained for various wettabilities –controlled through solid-liquid interaction. Regarding the comparison with the reference NEMD value $\lambda_{\mathrm{NEMD}}$, $\lambda_{\mathrm{mid}}$ –proposed in this study– reproduced $\lambda_{\mathrm{NEMD}}$ the best in comparison with $\lambda_{\mathrm{max}}$ and $\lambda_\infty$. We also performed a similar analysis on non-flat solid surfaces and showed that present method extracts the FC with excellent accuracy for various system.

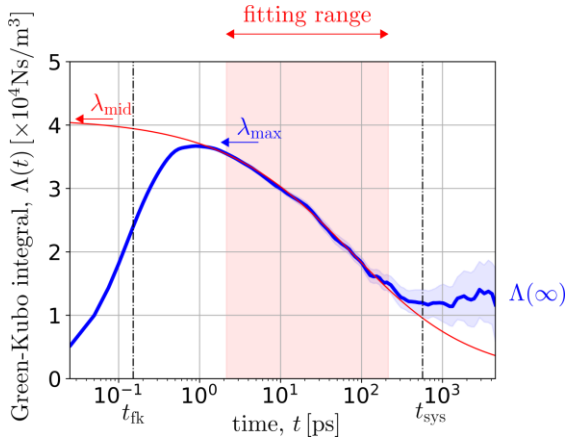


**Fig. 2.** (Blue) GK integral $\Lambda(t)$, and fitting curves for (red) MD simulation system of LJ liquid between flat fcc walls.

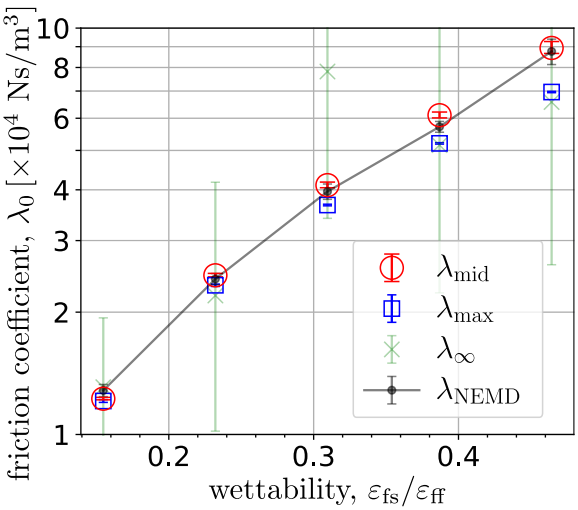


**Fig. 2.** FC for various wettability. the calculation methods are explained at the end of Section 2.

## References

[1] C. Navier, Mémoires, 1823, Mémoire sur les lois du Mouvement des Fluides, de I'Académie Royale des Sciences de I'Institut de France 6 389

[2] L. Bocquet and J. L. Barrat, 1994, Hydrodynamics boundary conditions, correlation functions, and Kubo relations for confined fluids, Phys. Rev. E 49 3079

[3] H. Oga, T. Omori, C. Herrero, S. Merabia, L. Joly, and Y. Yamaguchi, 2021 Theoretical framework for the atomistic modeling of frequency-dependent liquid-solid friction, Phys. Rev. Res. 3 L032019

[4] H. Oga, T. Omori, L. Joly and Y. Yamaguchi (in press), 2023 Equilibrium molecular dynamics evaluation of the solid-liquid friction coefficient: role of timescales, J. Chem. Phys.

## SESSION 7c
## Mathematical and computational approaches
Chair: **C. Markides**

# Ghost Particle Velocimetry – an easy and robust technique for flow visualization in microfluidics

Nina M. KOVALCHUK[1,*], Alex GERROW[1], Bettina WOLF[1], Mark J.H. SIMMONS[1]

1: School of Chemical Engineering, University of Birmingham, Birmingham, UK

* Corresponding author: Tel.: +44 7762 864263; Email: n.kovalchuk@bham.ac.uk

**Abstract:** Flow visualization is crucial for understanding of microfluidic processes. Here, Ghost Particle Velocimetry (GPV), a novel technique which enables quantification of flow fields not just in the middle plane, but in different cross-sections of microfluidic devices is discussed with emphasis on application in drop microfluidics. The main advantages of GPV in comparison to μ-PIV are usage of common optical microscopy (no need for a laser and synchronization with a camera) and possibility to follow processes in the real time. Examples of flow fields during drop formation, movement within a microfluidic channel and drop coalescence are provided. Questions of image preprocessing (ImageJ), analysis using free software PIVlab for Matlab as well as possible problems during the measurements and analysis and their mitigation are addressed. A new type of seeding particles allowing simultaneous flow visualization in both oil and aqueous phase is presented.

**Keywords:** Microfluidics, Multiphase flow visualization, Optical microscopy, Seeding particles

## 1. Introduction

Visualization of flow fields is crucial for better understanding of microfluidic processes. For example, flow fields determine mixing within microfluidic reactors and therefore reactor performance, completion time and yield. In microfluidic synthesis of nano-particles mixing is detrimental for particle size and size distribution.

Microscale Particle Image Velocimetry, μ-PIV, is the most used technique for quantification of microflows. It requires sophisticated and expensive equipment and cannot follow events in real time. The latter is especially important for drop microfluidics, where flow evolution during drop formation or coalescence is of interest, in particular for process optimization.

Ghost Particle Velocimetry [1], GPV, is a novel technique which uses a white light from a standard bright-field microscope and high-speed camera to record the movement of speckle patterns of light scattered by particles whose size is smaller than the diffraction limit. The light coherence is tuned by changing the numerical aperture of the microscope condenser. The recorded videos can be preprocessed with ImageJ [2] to reduce noise and then analyzed with PIVlab for Matlab [3]. GPV is proven to be an easy and reliable tool for analysis of continuous flows [4], but its application to segmented flows or drop microfluidic is not so straightforward.

Here a general GPV approach and its application to drop microfluidics is discussed.

## 2. Materials and methods

Experiments were performed in various microfluidic devices made of PDMS (SYLGARD 184, Dow Corning) using standard soft lithography.

Both oil-in-water and water-in-oil emulsions were considered. A series of silicone oils of varying viscosity, sunflower oil, water and water/glycerol mixtures were used as working liquids.

200 nm polystyrene particles (dispersion of 10% solid, Sigma Aldrich, diluted 1:50 (v:v)) were used for GPV in aqueous phase. Newly developed lignin nano-particles, also 200 nm in diameter, were used for flow visualization in both aqueous and oil phase.

Flow was recorded by a high-speed video

camera (Photron SA-5) connected to an inverted microscope (Nikon Eclipse Ti2-U) at 2-10 kfps depending on flow velocity. Exposure time was set at 0.05 ms. Spatial resolution was in the range 0.5 – 2 µm/pixel.

## 3. Results and discussion

While using GPV for visualization of stationary continuous flow, the noise inevitable in each processed pair of images, hereafter called frame, can be easily eliminated by averaging the flow field over a number of frames. This procedure provides a smooth and consistent flow field such as shown in Fig. 1.

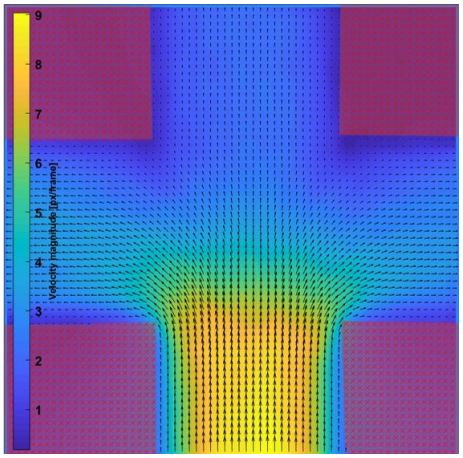


Figure 1. Stationary flow field in a branched channel.

Such approach is not possible for drop microfluidics where drops are growing, moving, or coalesce and therefore all frames are different and averaging is impossible. Three different approaches are possible in this case. First, one can attempt to remove maximum noise for each individual frame. If good quality flow fields are obtained, comparison of the results for several different drops or the same drop in different positions enables calculation of the average flow characteristics and standard deviations.

In the case when the results for single frames are too noisy, results for several drops at the same stage of the process can be averaged in the case of drop formation or coalescence, whereas frames can be shifted to the same position and then averaged for the drop moving in the channel. The averaged flow field for a drop moving in a channel, resolved in both water (dispersed) and oil (continuous) phase, while using lignin particles for creating speckle patterns is shown in Fig. 2

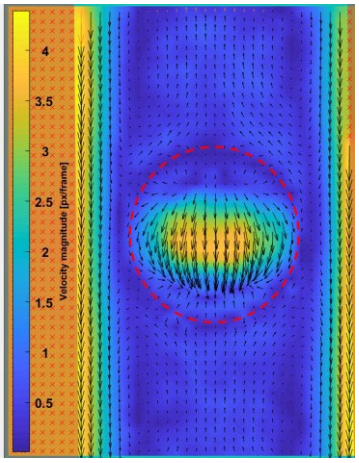


Figure 2. Flow field for a drop of water moving in continuous phase of sunflower oil. Co- ordinate system is moving with the drop.

## 4. Conclusion

GPV can be successfully used in drop microfluidics. Suitable choice of tracers enables simultaneous flow visualization in both oil and aqueous phase.

## Acknowledgement

This work was funded by the Engineering and Physical Sciences Research Council, UK, through the PREMIERE Programme Grant EP/ T000414/1.

## References

[1] Buzzaccaro S., Secchi E., Piazza R. Ghost Particle Velocimetry: Accurate 3D Flow Visualization Using Standard Lab Equipment. Phys. Rev. Lett. 2013, 111, 048101.

[2] Schneider C.A.; Rasband W.S.; Eliceiri K.W. NIH Image to ImageJ: 25 years of image analysis. Nat. Methods 2012, 9, 671.

[3] Thielicke, W.; Stamhuis, E.J. PIVlab— Towards User-friendly, Affordable and Accurate Digital Particle Image Velocimetry in MATLAB. J. Open. Res. Softw. 2014, 2, e30.

[4] Riccomi, M.; Alberini, F.; Brunazzi, E.; Vigolo, D. Ghost Particle Velocimetry as an alternative to µPIV for micro/milli-fluidic.

# Effect of Self-Propelled Microparticles on Heat Transfer in Liquids

Jacob VELAZQUEZ[1], Amit K. SINGH[1], Sajad KARGAR[1], Jeffrey L. MORAN[1,2,*]

1: Department of Mechanical Engineering, George Mason University, Manassas, VA, USA
2: Department of Bioengineering, George Mason University, Manassas, VA, USA

* Corresponding author: Tel.: +1 (703) 993-5636; Email: jmoran23@gmu.edu

**Abstract:** Self-propelled microparticles have been widely studied for their ability to propel themselves in liquids, often without moving parts. We explore the effects of self-propelled particle shape, size, material, and volume fraction on heat transfer in liquids, as quantified by convective heat transfer coefficient or the altered temperature distribution in the liquid. Preliminary results show that significant enhancements may be possible, especially when the self-propelled particles are concentrated in (and therefore disrupt) thermal boundary layers. This work lays the foundation for a new class of high-performance coolants, which we term "active heat transfer fluids" (AHTF), and which have potential applications including particle-based solar collectors, heat exchangers, and more.

**Keywords:** Mixing, Self-propelled particles, Heat transfer enhancement, Active matter

## 1. Introduction

Liquid coolants containing nanoparticles (nanofluids) have been widely studied since the 1990s [1] for various applications, including electronics cooling, desalination, and others. Although nanoparticles lead to an overall increase in the suspension's thermal conductivity, this increase is known to be limited [2] and entails additional complications such as increased viscosity. One limitation of conventional nanofluids is that the nanoparticles cannot move on their own and undergo only Brownian motion, and the fluid "stirring" resulting solely from Brownian motion exerts a negligible effect on heat transfer [3].

In the last two decades, a new field of research has emerged focusing on *self-propelled particles* (SPPs). SPPs typically range from 0.1 to 10 micrometers (μm) in size and move autonomously through liquids, usually without moving parts. SPPs use a variety of energy sources, including chemical fuels (e.g., hydrogen peroxide), magnetic or electric fields, or light. As they move, SPPs agitate the fluid around them, inducing mixing of mass, momentum, and energy. In dense suspensions, SPPs can exhibit "active turbulence," in which hydrodynamic interactions among SPPs induce chaotic flows and efficient mixing at the macroscale [4], [5]. Similar phenomena have been observed in nature: bacteria in a Swiss lake can induce mixing of salt and thermal energy on length scales four orders of magnitude larger than an individual organism [6] by virtue of their continuous upward and downward motions.

In this study, we aim to quantify the extent to which artificial SPPs induce thermal mixing as a function of their size, speed, material, and volume fraction. These insights can inform our understanding of the transport of thermal energy in oceans, rivers, and lakes induced by small animals and could be exploited for next-generation coolants in a variety of applications.

## 2. Methods

The experimental setup consists of a thermoelectric heater positioned vertically in a Petri dish containing a thin film (~4 mm deep) of deionized water. The temperature distribution in the water is approximately two-dimensional and natural convection is negligible. A constant voltage (2.4 V) and current (0.5 A) are supplied to the heater,

resulting in a constant heating power in all experiments.

Two SPP designs are investigated. In the preliminary experiments, the SPPs are camphor particles (~1 mm in size) sprinkled onto the free surface. Camphor dissolves in water and lowers its surface tension in the process; therefore, an asymmetric camphor particle can self-propel by dissolving unevenly around its edges, producing a surface tension gradient that propels the particle towards increasing surface tension. We also employ magnesium (Mg) microparticles (~10-50 μm) partially coated in gold that self-propel in water via asymmetric growth and ejection of hydrogen bubbles on the exposed Mg surface due to a chemical reaction.

## 3. Results and Discussion

Figure 1 shows two infrared snapshots of the temperature distribution in water in the absence and presence of SPPs. In water without SPPs (left), heat transfer occurs almost entirely by conduction. When SPPs are present (right), they induce convective mixing in the fluid, visibly altering the temperature distribution compared to the control case.

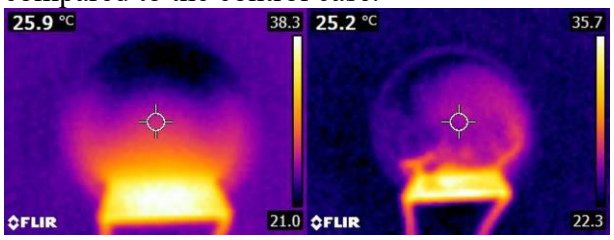


***Figure 1: Preliminary results.*** *Infrared images of temperature distribution in pure water (left) and water containing self-propelled camphor particles (right). Both images were captured 4 minutes after power was first supplied to the heater (bottom of both images). The heater power and water film depth are the same in both cases. The temperature in the center of the dish (shown at upper left) fluctuates in time in the SPP case due to convective mixing.*

Figure 1 shows that the maximum heater temperature is almost 3°C lower in the presence of SPPs (35.7°C) than in the control case (38.3°C). Since the heater power (and therefore the steady-state heat transfer rate to the fluid) is the same in both cases, these results suggest that the presence of SPPs nontrivially reduces the temperature gradient in the fluid and thus increases the heat transfer coefficient.

These results lay the foundation for characterizing the effect of SPP properties on thermal transport in liquids. Future work will exploit SPPs' unique capabilities, e.g., externally guided motion, to produce desired results (e.g., enhancing/suppressing natural convection), and will investigate the effects of SPPs on the suspension viscosity. Because of their desirable thermal properties, these "active heat transfer fluids" (AHTF) could have many applications in particle-based solar collectors, heat exchangers, desalination, and more.

## References

[1] S. U. S. Choi and J. A. Eastman, "Enhancing thermal conductivity of fluids with nanoparticles," Argonne National Lab., IL (United States), ANL/MSD/CP- 84938; CONF-951135-29, Oct. 1995. Accessed: 13 Apr 2023. [Online]. Available: https://www.osti.gov/biblio/196525-enhancing-thermal-conductivity-fluids-nanoparticles

[2] J. Buongiorno *et al.*, "A benchmark study on the thermal conductivity of nanofluids," *J. Appl. Phys.*, vol. 106, no. 9, p. 094312, Nov. 2009, doi: 10.1063/1.3245330.

[3] H. Babaei, P. Keblinski, and J. M. Khodadadi, "A proof for insignificant effect of Brownian motion-induced micro- convection on thermal conductivity of nanofluids by utilizing molecular dynamics simulations," *J. Appl. Phys.*, vol. 113, no. 8, p. 084302, Feb. 2013, doi: 10.1063/1.4791705.

[4] J. Dunkel, S. Heidenreich, K. Drescher, H. H. Wensink, M. Bär, and R. E. Goldstein, "Fluid Dynamics of Bacterial Turbulence," *Phys. Rev. Lett.*, vol. 110, no. 22, p. 228102, May 2013, doi: 10.1103/PhysRevLett.110.228102.

[5] D. Nishiguchi and M. Sano, "Mesoscopic turbulence and local order in Janus particles self-propelling under an ac electric field," *Phys. Rev. E*, vol. 92, no. 5, p. 052309, Nov. 2015, doi: 10.1103/PhysRevE.92.052309.

[6] T. Sommer *et al.*, "Bacteria-induced mixing in natural waters," *Geophys. Res. Lett.*, vol. 44, no. 18, pp. 9424–9432, 2017, doi: 10.1002/2017GL074868.

# Thermally Induced Nucleation, Growth, and Dissolution of Surface Nanobubbles

Hideaki TESHIMA[1,*], Qin-Yi LI[2], Koji TAKAHASHI[3]

1: Department of Aeronautics and Astronautics, Kyushu University, Fukuoka, JP
2: International Institute for Carbon-Neutral Energy Research (WPI-I2CNER), Kyushu University, Fukuoka, JP

* Corresponding author: Tel.: +81 92 802 3016; Email: hteshima05@aero.kyushu-u.ac.jp

**Abstract:** Nanobubbles at solid-liquid interfaces have been studied for more than two decades but still remain unclear, especially about the response to temperature changes. In this study, we conducted *in-situ* three- dimensional measurements of nanobubbles attached to a graphite surface before and after heating using an amplitude-modulation atomic force microscope. It was found that the nanobubbles do not sit on the bare graphite surface but always on micropancakes, which is a gas phase with a thickness of a few nanometer and a horizontal spread of several hundred nanometers. Upon heating, nucleation, growth and dissolution of the nanobubbles were observed simultaneously on the same graphite surface. This behavior was explained by taking into consideration the underlying micropancakes. Specifically, the nucleation site of nanobubbles was depending on the positions of the micropancakes. Their growth and dissolution were determined by the relative size of the underlying micropancakes. Our findings extend fundamental knowledge of gas molecular dynamics at solid-liquid interfaces.

**Keywords:** Nanobubble, Micropancake, Heating, Graphite, Atomic force microscopy

## 1. Introduction

Nanoscale gas bubbles existing at solid-liquid interfaces are called surface nanobubbles and have attracted increasing attention because of their unique properties, such as extremely high contact angles, a long-lifetime that cannot be explained by the Epstein-Plesset model, co-existence with micropancakes that spreads laterally for hundreds nanometer with several nanometer thicknesses, and superstability against disturbances(Lohse and Zhang, 2015). Especially, the responses of the nanobubbles to temperature changes are still under debate. For example, one reports that nanobubbles spontaneously form during heating and do not disappear(Shangjiong et al., 2007), but other reports that some nanobubbles grew as the temperature dropped while others shrank(Berkelaar et al., 2012). Furthermore, though a study indicates that surface nanobubbles can be the nuclei of the onset of nucleate boiling(Nam and Ju, 2008), one proposes that they do not grow into large bubbles even when the water reaches temperatures close to the boiling point(Zhang et al., 2014). To resolve these discrepancies, we conducted simultaneous measurements of surface nanobubbles and underlying micropancakes before and after heating using atomic force microscopy (AFM).

## 2. Experiments

A highly ordered pyrolytic graphite (SPI-1 grade, Alliance Biosystems, Japan) was used as a substrate. The amplitude modulation mode of AFM (SPM-8100FM, Shimadzu Corp., Japan) was used for the measurements. The interfacial gas layers were first generated through the protocol of the solvent exchange method, which has been widely used for the nucleation of the nanobubbles(Kimura et al., 2021). After the solvent exchange method, the pure water/graphite interface was measured at room temperature. Then, the interface was heated up

to 45°C and 60°C using a ceramic heating unit. After stabilizing at the high temperatures, the heater was turned off and thus returned to room temperature. We note that all AFM measurements were performed at room temperature.

## 3. Results and Discussion

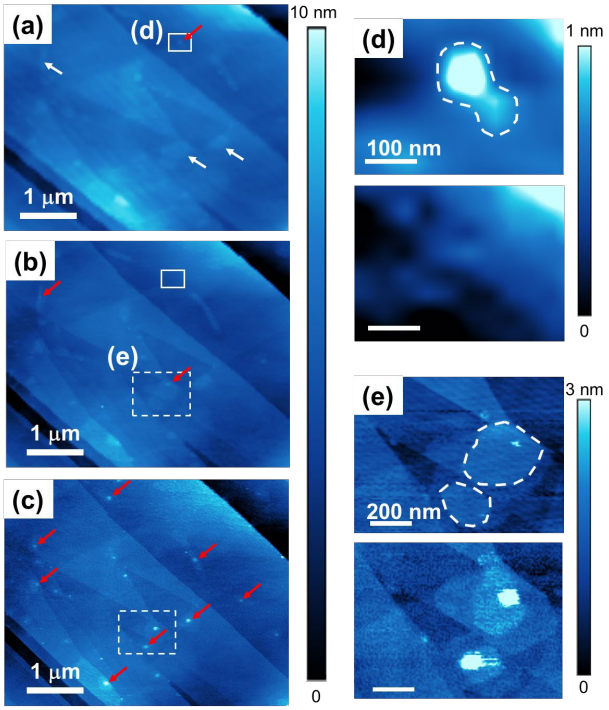


**Fig. 1.** AFM images of a water/HOPG interface measured (a) before heating and after heating to (b) 45°C and (c) 60°C. White and red arrows indicate the micropancakes and nanobubbles, respectively.
(d) disappeared and (e) generated nanobubbles upon heating, which correspond to the area indicated by the white solid and dashed frames, respectively.

Fig. 1(a) shows a few nanobubbles and micropancakes formed by the solvent exchange method. As indicated by the red arrows in Fig. 1(b) and (c), many nanobubbles were newly nucleated after heating. It was found that their nucleation sites are always on the pre-existed micropancakes. Moreover, new micropancakes and nanobubbles did not appear on the bare HOPG surface. This may be because it is thermodynamically preferable for dissolved gas molecules to gather on the pre-existing gas phases rather than for nucleation on the bare surface.

Fig. 1(d) and (e) show the enlarged images of the disappeared and nucleated nanobubbles on the micropancakes, respectively. In the cases of nucleation, the initial ratio of the nanobubbles divided by the area of micropancakes was 1.7 % and 2.2 % but increased to 11 % and 28 % after heating. On the other hand, in the case of the disappearance, the initial ratio was already high (43 %). From these, we suppose that the relative size of the underlying micropancakes to the nanobubble determines their response to heating(Kimura et al., 2021).

## 4. Conclusions

We observed the responses of the nanobubbles and micropancakes to heating. It was found that the micropancake is a key to determining the nanobubble nucleation, growth and dissolution. Our findings expand knowledge of the behavior of gas molecules at solid-liquid interfaces and contributes to resolving the discrepancies previously reported.

## References

Berkelaar, R.P., Seddon, J.R.T., Zandvliet, H.J.W., Lohse, D., 2012. Temperature dependence of surface nanobubbles. ChemPhysChem 13, 2213–2217. https://doi.org/10.1002/cphc.201100808

Kimura, R., Teshima, H., Li, Q.Y., Takahashi, K., 2021. Thermally induced mass transfer between nanobubbles and micropancakes. Int. J. Heat Mass Transf. 181, 122001. https://doi.org/10.1016/j.ijheatmasstransfer.2021.12 2001

Lohse, D., Zhang, X., 2015. Surface nanobubbles and nanodroplets. Rev. Mod. Phys. 87, 981–1035. https://doi.org/10.1103/RevModPhys.87.981

Nam, Y., Ju, Y.S., 2008. Bubble nucleation on hydrophobic islands provides evidence to anomalously high contact angles of nanobubbles. Appl. Phys. Lett. 93, 103115. https://doi.org/10.1063/1.2981572

Shangjiong, Y., Dammer, S.M., Bremond, N., Zandvliet, H.J.W., Kooij, E.S., Lohse, D., 2007. Characterization of nanobubbles on hydrophobic surfaces in water. Langmuir 23, 7072–7077. https://doi.org/10.1021/la070004i

Zhang, X., Lhuissier, H., Sun, C., Lohse, D., 2014. Surface nanobubbles nucleate microdroplets. Phys. Rev. Lett. 112, 1–5. https://doi.org/10.1103/PhysRevLett.112.144503

# Unravelling the regimes of interfacial conductance at a solid/liquid interface

Abdullah EL-RIFAI[1], Sreehari PERUMANATH[2], Matthew K. BORG[1], and Rohit PILLAI[1,*]

1: Institute for Multiscale Thermofluids, University of Edinburgh, Edinburgh EH9 3FD, UK
2: Mathematics Institute, University of Warwick, Coventry CV4 7AL, UK

* Corresponding author: Email: R.Pillai@ed.ac.uk

**Abstract:** It has been long argued that the interfacial thermal conductance at a solid/liquid interface exhibits two distinct regimes: exponential dependence on wettability for weakly-bonded, or nonwetting liquids, and linear dependence for strongly-bonded, or wetting liquids. The transition between these regimes has been attributed to the relative importance of interfacial interactions, i.e., the switch occurs once the magnitude of solid/liquid interactions exceeds liquid/liquid interactions. In this work, we show that this explanation is contingent on the system pressure. We use non-equilibrium molecular dynamics simulations to apply a temperature gradient at a Lennard-Jones solid/liquid interface and use this setup to determine the interfacial conductance for a wide range of surface wettabilities. By spectrally decomposing the heat flux within both the interfacial solid and liquid, we instead show for the first time that the regime transition occurs due to changes in the structural and thermal properties of the interfacial layers. These results have application to design of systems where manipulating interfacial conductance is important, such as liquid-based cooling solutions for electronic devices.

**Keywords:** Interfacial Thermal Conductance, Molecular Dynamics, Spectral Heat Flux Decomposition

## 1. Introduction

Increasing transistor densities and on-chip clock speeds have resulted in higher thermal loads on modern integrated circuits (ICs), leading to a severe degradation in their performance. These higher thermal loads have spurred interest in two-phase cooling devices, which exploit the latent heat of vaporization of the working fluid. Compared to conventional single-phase cooling systems, these devices can extract a significantly greater amount of heat from ICs[1]. The performance of such devices is dictated by how efficiently heat can be transported across the solid/liquid interface[2]. The interfacial thermal conductance ($G$) determines how much heat is transferred at such interfaces and is therefore the key to optimising the performance of these devices. It is well established that the solid/liquid interaction strength (quantified by surface wettability $\varepsilon_{SL}$) directly correlates to $G$. Xue et al[3] were the first to characterise this and to observe that a single functional form did not fit all the wettabilities. However, dividing the data into two regimes based on relative values of $\varepsilon_{SL}$ and liquid/liquid interaction parameter $\varepsilon_{LL}$ (i.e., wetting if $\varepsilon_{SL} > \varepsilon_{LL}$ and non-wetting if $\varepsilon_{SL} < \varepsilon_{LL}$, respectively) allowed for excellent functional fits. They found that for wetting cases, a linear fit ($G \propto \varepsilon_{SL}$) holds, while for non-wetting cases an exponential fit ($G \propto e^{1.9\varepsilon_{SL}}$) is more appropriate. This regime transition has since been reproduced in other works[4,5]. However, as we show here, this explanation is at best contingent on the choice of system parameters, and at worst, simplistic.

## 2. Methodology

As shown in Fig. 1(a), we study a Lennard-Jones (LJ) fluid positioned between two LJ face-center cubic (FCC) solids with the [100] crystallographic plane oriented along the $x$-axis. The domain boundaries are periodic except in the $x$ direction, and the solid layers at either end of the domain are rigid. The domain is equilibrated at 100 K and 50 MPa in the NVE ensemble for 2.5 ns. The pressure is controlled by iteratively adjusting the number of liquid atoms such that the bulk density of the liquid is equal for all values of $\varepsilon_{SL}$. Following this, heat $Q$ is continuously injected and extracted at a fixed rate of 80 meV/ps for 10 ns from portions of the left and right walls respectively.

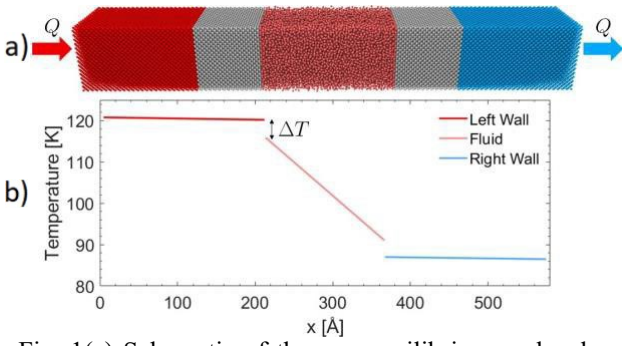


Fig. 1(a) Schematic of the non-equilibrium molecular dynamics (NEMD) system. (b) Temperature distribution yielded by steady-state NEMD simulation showing the temperature jumps (ΔT) at both liquid/solid interfaces.

Once a steady-state is achieved, the temperature distribution of the system is determined (see Fig. 1(b)). From this, the interfacial temperature discontinuity (or 'jump') $\Delta T$ can be obtained and used to compute $G$ using $G=Q/(A\Delta T)$, where $A$ is the cross-sectional area.

## 3. Results

In Figure 2, we plot the variation of $G$ with wettability for a broader range of values than previously studied. We observe an exponential regime within $0 < \varepsilon_{SL} < 40$ meV and a linear regime afterwards. However, crucially, our observed crossover point $\varepsilon_{SL}$= 40 meV is well beyond the previously reported crossover point ($\varepsilon_{SL} \sim \varepsilon_{LL}$ at 10 meV) studied under identical conditions, except for the system pressure, which is kept at 50 MPa here compared to 0 MPa in the literature[3-5]. This indicates that the previously reported regime transition is not independent of system pressure. Existing literature attributes $G$ to the mismatch in the vibrational spectra of the materials forming the interface, quantified by the overlap of the vibrational density of states (VDOS) of the interfacial solid and liquid layers. To verify whether this correlates to the observed regime transition, we compute the VDOS of the interfacial solid and liquid layers and show that the VDOS overlap does not show any regime transition. Instead, we find that the spectral decomposition of the heat flux in the interfacial layers is necessary to understand their contribution to $G$, evaluate the role of wettability on the heat transport, and understand the transition between the two regimes of $G$ vs $\varepsilon_{SL}$. We also present new spectral overlap measurements that better predict this regime transition.

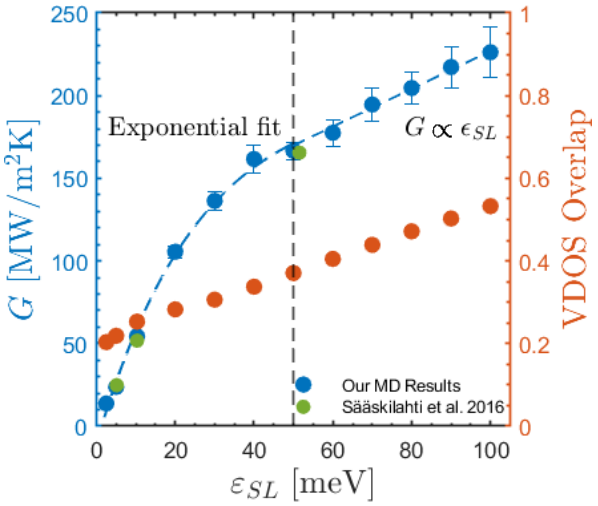


Fig. 2: Interfacial thermal conductance (G) and interfacial vibrational density of states (VDOS) overlap, plotted against the solid-liquid interaction strength ($\varepsilon_{SL}$ ). MD results generated by this study are validated against results by Sääskilahti et al[6]. The dashed line indicates the transition in G vs $\varepsilon_{SL}$ from regime 1 to regime 2. No transition is seen in VDOS overlap vs $\varepsilon_{SL}$.

## References

[1] J. D. Sircar, D. F. Hanks, Z. Lu, T. Salamon, K. R. Bagnall, S. Narayanan, D. Antao, B. Barabadi, and E. N. Wang, "High heat flux evaporation from nanoporous silicon membranes," Proceedings of the 16th Conference on Thermal and Thermomechanical Phenomena in Electronic Systems, ITherm 2017, 505–513 (2017).

[2] D. F. Hanks, Z. Lu, J. Sircar, T. R. Salamon, D. S. Antao, K. R. Bagnall, B. Barabadi, and E. N. Wang, "Nanoporous membrane device for ultrahigh heat flux thermal management," Microsystems and Nano-engineering 4, 1–10 (2018)

[3] L. Xue, P. Keblinski, S. R. Phillpot, S. U. Choi, and J. A. Eastman, "Two regimes of thermal resistance at a liquid-solid interface," Journal of Chemical Physics 118, 337–339 (2003).

[4] A. Giri and P. E. Hopkins, "Spectral analysis of thermal boundary conductance across solid/classical liquid interfaces: A molecular dynamics study," Applied Physics Letters 105 (2014).

[5] A. Giri, J. L. Braun, and P. E. Hopkins, "Implications of interfacial bond strength on the spectral contributions to thermal boundary conductance across solid, liquid, and gas interfaces: A molecular dynamics study," Journal of Physical Chemistry C 120, 24847–24856 (2016).

[6] Sääskilahti, J. Oksanen, J. Tulkki, and S. Volz, "Spectral mapping of heat transfer mechanisms at liquid-solid interfaces," Physical Review E 93, 1–8 (2016).

# A One-Step Approach to Generate Triple-layered Droplet

Sihang LIU[1], Shuai YIN[2], Ran GAO[1], Yi HUANG[1,*], Teck Neng WONG[2]

1: Research Institute of Aero-Engine, Beihang University, Beijing, CHN
2: School of Mechanical and Aerospace Engineering, Nanyang Technological University, Singapore, SG

* Corresponding author: Tel.: +86 188 1103 5560; Email: huangyi_buaa@buaa.edu.cn

**Abstract:** Multilayer droplet, due to each layer with different functions, is widely used in biomedicine, energy and other fields. Other than microchip based methods which requires complicated fabrication process and expensive facilities, we propose a one-step approach of generating multilayer droplet via impingement of a core droplet drops through a deep pool with multi-layer liquids. By adjusting the diameter of core droplet, falling height, the surface tension of each layer and the thickness of liquid films, we systematically investigated the role of viscous force, inertial force and interfacial tension in the formation process. By coordinating the action of three forces, we successfully generate different sizes of stable triple-layered droplet. With our method, triple-layered droplet can be generated readily and cheaply. And by adding different substances into different layers, triple-layered droplet can be programmed into different functions to meet different needs.

**Keywords:** Triple-layered droplet, Droplet impact, Interfacial action

## 1. Introduction

Figure 1 shows the dynamic process of triple-layered droplet formation by using a high-speed camera. The core droplet is made by 70wt% glycerol and 30wt% DI water, and the multilayer liquid in the pool from top to bottom is silicon oil, 1, 6-hexanediol Diacrylate and ethylene glycol. According to the characteristics of core droplet deformation, the process can be divided into three stages. In the first stage, from 0 to 9.3ms, the core droplet with initial velocity slows down because of surface tension and viscous force. At the same time, the core droplet changes from a ball to a pancake, transforming kinetic energy into surface energy. In the second stage, from 9.3ms to 18.2ms, the core droplet recovers from a pancake into a droplet, releasing the accumulated surface energy. In the third stage from 18.2ms to 78ms, with the interaction of viscous force and interfacial tension, the neck of core droplet shrinks, which drives two layers of liquid film to separate from the original system and generates a triple-layered droplet finally.

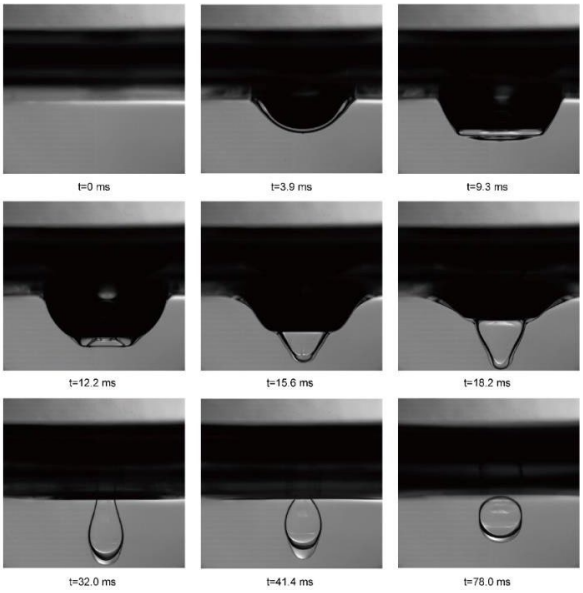


Figure. 1. triple-layered droplet dynamic formation process.

## SESSION 8a
## Multi-scale phase change processes
Chair: **M. Bucci**

# Numerical simulation of flow boiling in a micro-pin fin evaporator

Ismail EL MELLAS[1, *], Mirco MAGNINI[1]

1: Department of Mechanical, Materials and Manufacturing Engineering, University of Nottingham, Nottingham NG7 2RD, United Kingdom

* Corresponding author: Email: ismail.elmellas1@nottingham.ac.uk

**Abstract:** We present the results of a numerical study of flow boiling in a micro-pin evaporator. The evaporator has a heated area of 1 $cm^2$ and contains 66 rows of cylindrical micro-pin fins with an in-line configuration and diameter, height and pitch of respectively 50 μm, 100 μm and 91.7 μm. The fluid tested is refrigerant R236fa, with operating pressure leading to saturation temperatures of about 30 °C. Inlet restrictions consisting of an extra line of pin fins of larger diameter of 100 μm are considered. The evaporator is heated from below, with heat fluxes on the order of 10 $W/cm^2$. Mass fluxes in the range 500-2500 $kg/m^2s$ are considered. The numerical setup is first validated in terms of single-phase friction factor and Nusselt number versus literature data, with excellent agreement. The two-phase simulations are started by seeding a small vapour bubble at the contact point between pin fin and base wall. As time elapses, the bubbles grow channeled by the pin fins and elongate in the flow direction. As the contact line sweeps the heated walls, the temperature locally reduced as expected due to the latent heat dissipated by the evaporation process.

**Keywords:** Boiling, Simulation, Micro-evaporators.

## 1. Introduction

Micro-pin fin evaporators are a viable alternative to multi-microchannel heat sinks for the thermal management of power electronics. The presence of the pin fins enhances mixing and potentially improves flow stability [1]. While the literature for flow boiling in microchannels is rather vast, pin fin heat exchangers have received far less attention. A few studies have investigated the influence of the pin shape, varying from circular to triangular, square and diamond [1, 2, 3]. Other studies [4] performed parametric analyses on the effect of different geometrical dimensions including diameter, spacing and height of the fins. Falsetti et al. [5] characterised the heat transfer performance of a micro-evaporator for different refrigerant fluids. Vapour bubbles were observed to nucleate over the surface of the pin fins and grow along the gaps in between the pin fins arrays. All the aforementioned works were focused on the heat transfer performance, and no detailed studies of the liquid film evolution or bubble dynamics around the obstacle walls were performed. The objective of this work is to investigate the fundamental aspects of bubble dynamics, liquid film formation, and their impact on pressure drop and heat transfer by employing numerical simulations. We emulate the evaporator geometry and experimental setup of Falsetti et al. [5].

## 2. Methods

We employ a numerical solver for two-phase boiling flows that we have developed in OpenFOAM v2106 [6]. The solver uses a Volume-Of-Fluid method to track the two phases and calculates the phase change rate based on the model of Schrage [7]. The details of the solver were published by Municchi et al. [6] and for the sake of brevity are not repeated here. The simulation domain is depicted in Fig.1 and consists of the portion of a micro-evaporator that incorporates two arrays of cylindrical pin fins, each of diameter of $D_{fin}$=50 μm, height H=100 μm, cross-stream pitch $d_y$=150 μm and streamwise pitch of $d_x$=91.7 μm. The geometry and simulation setup emulates the experiments of Falsetti et al. [5].

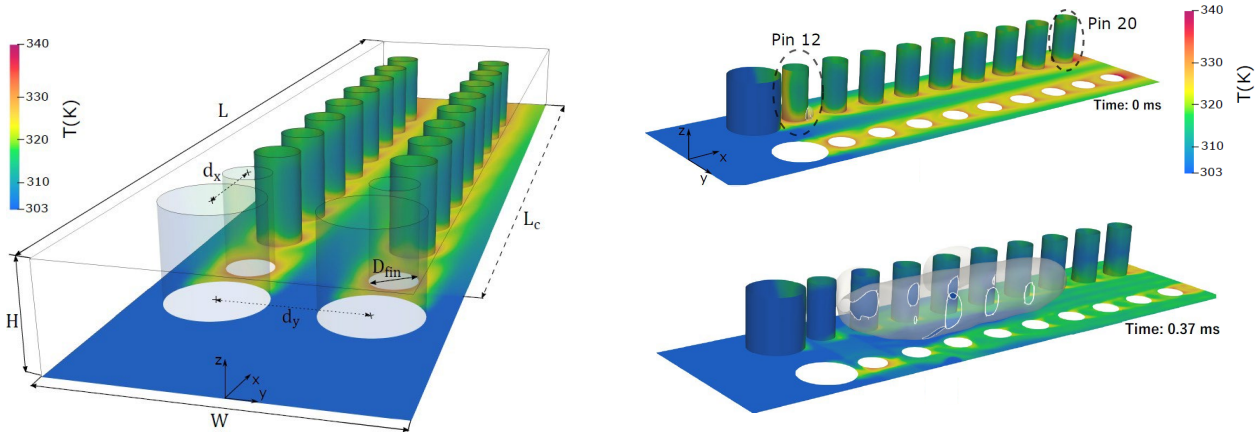


Figure 1: [left] Sketch of the geometry simulated showing two arrays of in-line pin fins; all walls are coloured with the single-phase steady-state temperature field. [right] Evolution of a vapour bubble nucleated at the feet of pin #12 and growing towards the exit. Conditions are heat flux 5 W/cm$^2$ and mass flux 1000 kg/m$^2$s.

The geometry is heated from the bottom surface with a constant heat flux of 5-10 W/cm$^2$. The operating fluid is R236fa. At the inlet, the fluid enters in saturated conditions at the temperature of 30 °C. Mass fluxes in the range 500-2500 kg/m$^2$s are considered. Hydrophilic walls are set for the two-phase simulations, with contact angles of 5 degrees.

## 3. Results

Single-phase simulations are first run until steady-state to obtain developed temperature and velocity profiles. Figure 1 shows examples of the steady temperature field, which presents local peaks in the wake of the cylinders where the fluid stagnates. These locations are potential nucleation points due to the high temperatures achieved. A two-phase simulation starts by seeding a small vapour bubble at the feet of cylinder #12, see Fig. 1 [right]. The superheated liquid causes a quick growth of the vapour bubble, which quickly fills the entire cross-section of the channels and grows downstream. As the channels are not separate, fractions of vapour may enter neighbour channels. The evaporation process cools down the walls over which the contact line is passing, resulting in efficient cooling of the surfaces. Additional simulations are run for different heat fluxes, flow rates and levels of subcooling also allowing for condensation where the local fluid temperature falls below saturation and will be presented at the conference.

## References

[1] Kosar, A., Peles, Y., 2006, Convective flow of refrigerant (R-123) across a bank of micro pin fins, Int. J. Heat Mass Transf. 49, 3142– 3155.

[2] Ricci, R., Montelpare, S., 2006, An experimental IR thermographic method for the evaluation of the heat transfer coefficient of liquid-cooled short pin fins arranged in line, Exp. Therm. Fluid Sci. 30, 381–391.

[3] Wan, W., Deng, D., Huang, Q., Zeng, T., Huang, Y., 2017, Experimental study and optimization of pin fin shapes in flow boiling of micro pin fin heat sinks, Appl. Therm. Eng. 114, 436–449.

[4] Zhao, J., Huang, S., Gong, L., Huang, Z., 2016, Numerical study and optimizing on micro square pin-fin heat sink for electronic cooling, Appl. Therm. Eng. 93, 1347–1359.

[5] Falsetti, C., Jafarpoorchekab, H., Magnini, M., Borhani, N., Thome, J. R., 2017, Two- phase operational maps, pressure drop, and heat transfer for flow boiling of R236fa in a micro- pin fin evaporator, Int. J. Heat Mass Transf. 107, 805–819.

[6] Municchi, F., El Mellas, I., Matar, O. K., Magnini, M., 2022, Conjugate heat transfer effects on flow boiling in microchannels, Int. J. Heat Mass Transf. 195, 123166.

[7] Carey, V. P., Liquid-Vapor Phase Change Phenomena, Taylor and Francis, 1992.

# Modelling Two-Phase Heat Transfer in Small-to-Micro Tubes Using Data-Driven Dimensional Analysis

Tullio TRAVERSO[1, 2,*], Francesco COLETTI[3, 4, *], Luca MAGRI[2, 1, *], Tassos G. KARAYIANNIS[5, *], Omar K. MATAR[6,1, *]

1: The Alan Turing Institute, British Library, 96 Euston Road, London NW1 2DB, UK
2: Department of Department of Aeronautics, Imperial College London, South Kensington Campus, London SW72AZ, UK
3: Department of Chemical Engineering, Brunel University London, Kingston Lane, Uxbridge, Middlesex UB8 3PH, UK
4: Hexxcell Ltd., Foundry Building, 77 Fulham Palace Rd., London, W6 8AF, UK
5: Department of Mechanical and Aerospace Engineering, Brunel University London, Kingston Lane, Uxbridge, Middlesex UB8 3PH, UK
6: Department of Chemical Engineering, Imperial College London, South Kensington Campus, London SW72AZ, UK

* Corresponding author: Email: ttraverso@turing.ac.uk; Francesco.Coletti@brunel.ac.uk; l.magri@imperial.ac.uk; tassos.karayiannis@brunel.ac.uk; o.matar@imperial.ac.uk

**Abstract:** Thermal design of electronic devices necessitates dissipating significant heat fluxes from small areas. This can be achieved through two-phase flow boiling in small-to-micro channels. Design of such compact heat exchangers requires accurate prediction of the two-phase heat transfer coefficient (HTC), based on geometry and operating conditions. Approaches to predict the HTC consist of empirical and semi-empirical correlations, and machine learning models, all of which involve performing complex nonlinear regressions on experimental data. In all cases, identifying optimal dimensionless groups for regressions is challenging due to intricate phase-changing flow interactions. To tackle this, we first parametrize the input using an arbitrary set of dimensionless groups. Second, we train a Gaussian process regression (GPR) model with experimental data from the Brunel Two-Phase Flow database. This provides a readily differentiable surrogate model of the HTC which is used to perform sensitivity-based data-driven dimensional analysis (DDDA), as proposed by Constantine et al. [1]. Via DDDA, we show (i) the most relevant dimensionless groups with respect to their impact on the HTC; (ii) that the predictive performance of the model does not depend on the choice of the dimensionless groups. Finally, we also demonstrate how GPR models handle noisy data while providing realistic estimates of the measurement noise.

## References

[1] Constantine, P. G., del Rosario, Z., & Iaccarino, G. (2017). Data-driven dimensional analysis: algorithms for unique and relevant dimensionless groups. *arXiv preprint arXiv:1708.04303*.

## Acknowledgements

We acknowledge funding from the Engineering and Physical Sciences Research Council, UK, through the grant Boiling Flows in Small and Microchannels (BONSAI): From Fundamentals to Design (EP/T03338X/1, EP/T033045/1); The Programme Grant PREMIERE (EP/T000414/1), and the Alan Turing Institute; L. Magri acknowledges financial support from the ERC Starting Grant PhyCo 949388.

# CFD analysis of a PCM-based TMS for a Li-Ion pouch cell

Dario GUARDA[1, *], Simone MANCIN[1], Stefano LANDINI[2]

1: Department of Management and Engineering, University of Padova, Vicenza, IT
2: School of Engineering, University of East Anglia, Norwich, UK

* Corresponding author: Tel.: +39 0444 998746; Email: dario.guarda@phd.unipd.it

**Abstract:** Organic Phase Change Materials (PCMs) such as paraffins, fatty acids, and esters present good properties to be used as Thermal Management System (TMS) for Li-Ion Batteries (LIB). The temperature of LIB cells should be ideally kept in the range of 25-35°C to maximise performances and minimise degradation. This represents a good opportunity to exploit the quasi-isothermal solid-liquid phase-change process of PCMs. Thanks to their high thermal energy densities, the use of PCMs limits the increment of TMS volume. Thus, by using PCMs in LIB TMS, it is possible to keep the LIB cells' temperature nearly constant (when the PCM is changing phase) both during charging and discharging cycles. In this study, a numerical model based on the enthalpy-porosity method implemented in Ansys Fluent was developed to investigate the PCM behaviour in a LIB pouch cell TMS. The model was validated against experimental data.

**Keywords:** Phase Change Material, Thermal Management System, Li-Ion Batteries, Thermal Storage, Cooling Device

## 1. Introduction

Compared to other energy storage systems, Li- Ion Batteries (LIB) present high energy densities, high peak power, and moderate ageing effect [1]. Nevertheless, these systems are highly sensitive to their operating temperature. The operating temperature of a LIB should be in the range of 25°C-35°C to avoid ageing and thermal runaway [1]. This results in the need to develop efficient, compact, and cost-effective LIB thermal management systems (TMS). One of the emerging technologies for LIB TMS is based on phase change materials (PCMs). In particular, Landini et al. [1] experimentally analysed the performances of four different LIB passive TMS based PCM.
This paper considers the model proposed in Guarda et al. [2]. Here, the validation of the aforementioned model based on measured PCM temperature is considered. The novelty and importance of this work are directly linked to the many complex parameters involved in the management of a PCM TMS for a LIB cell.

## 2. Model definition

Detailed information and a rigorous description of the model can be found in Guarda et al. [2]. For space constraint reasons, here it is reported a brief summary of the model. The computational fluid dynamics (CFD) software used is Ansys Fluent, where conservation of mass, momentum and energy equations are solved. The PCM considered is octadecane, an organic paraffin, melting at around 29°C with a latent heat of fusion of 217.8 kJ $kg^{-1}$. The solid-liquid phase change is modelled using the enthalpy porosity method [3]. The domain is assimilated to a porous media where the porosity is the liquid fraction, defined as a function of time. The simulations are transient with a time step of 0.1 s. The domain reported in Figure 1 represents a 2D section of the system analysed by Landini et al. [1]. It features an additive manufactured enclosure made in aluminium with three pockets. The PCM is located inside the external pockets while the LIB is located in the central pocket. The initial temperature of the system is considered to be a generic room temperature of 20°C.

The LIB heat generation rate, originally measured with a heat flux sensor [1], is assigned as time variant boundary condition. A natural convection boundary condition is assigned to the other walls of the domain (heat transfer coefficient of 10 W $m^{-2}$ $K^{-1}$ and a free stream temperature of 20°C).

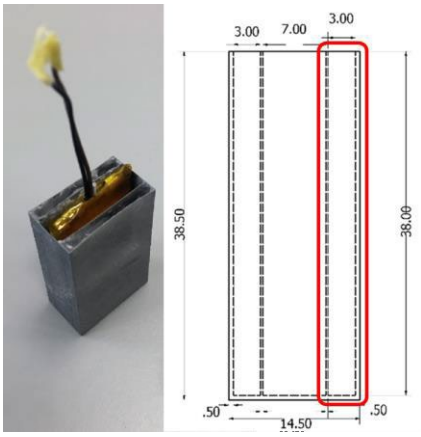


Figure 1. System modelled in the analysis: LIB pouch cell and its case (dimensions in mm) containing octadecane [1]. The 2D model considers the PCM section in red for symmetry reasons.

## 3. Results

The results of the transient simulations are reported with the depth of discharge (DOD) in the x-axis. DOD is defined as the ratio between the capacity discharged and the nominal capacity. It can be viewed as an dimensionless time to compare experiment with different time scale. For further details, please refer to [1].

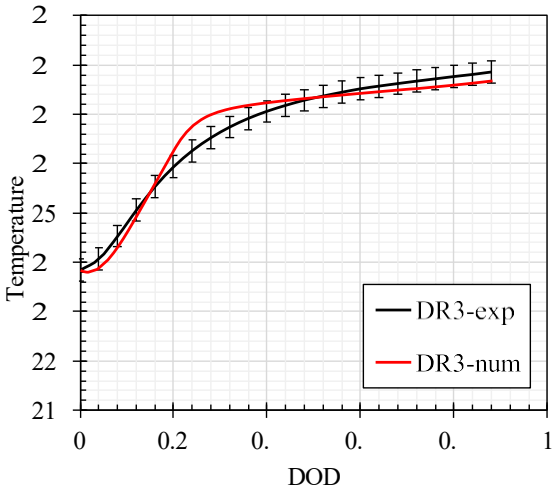


Figure 2. PCM temperature profiles for single discharge cycle with discharge rates of DR=3C.

In the present study, validation for single discharges cycles at discharge rates DR=3C, 5C, [1]) are presented in Figure 2 and 3. The root mean squared error is 0.22°C for the DR3 case and 0.30°C for the DR5 one.

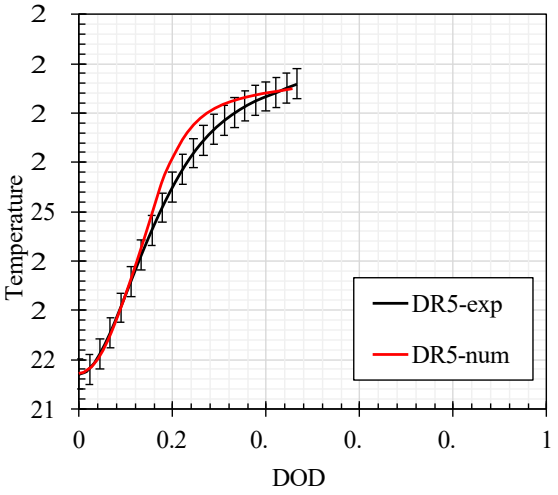


Figure 3. PCM temperature profiles for single discharge cycle with discharge rates of DR=3C.

## 3. Conclusions

A numerical model for the assessment of a PCM based TMS was successfully validated against experimental temperature data. In the future, it will be used to analyse and optimise the PCM TMS during battery cycling.

## Acknowledgements

The authors wish to acknowledge the support and the computational resources made available by the High-Performance Computing Lab at the Department of Management and Engineering (DTG), co-funded by the University of Padova in the framework of the program "Scientific research instrumentation 2015".

## References

[1] Landini, S., Waser, R., Stamatiou, A., Ravotti, R., Worlitschek, J., O'Donovan, T.S., 2020. Passive cooling of Li-Ion cells with direct-metal-laser-sintered aluminium heat exchangers filled with phase change materials. Appl. Therm. Eng. 173, 115238.
[2] Guarda, D., Calati, M., Delgado, W., Landini, S., Waser, R., Stamatiou, A., O'Donovan, T., Mancin, S., 2021. Numerical study of PCM based TMS for Li-Ion cells, in: 13th IIR Conference on Phase-Change Materials and Slurries for Refrigeration and Air Conditioning. Vicenza, Italy.
[3] Voller, V.R., Cross, M., Markatos, N.C., 1987. An Enthalpy Method for Convection/Diffusion Phase Change. Int. J. Numer. Methods Eng. 24, 271–284.

# Bubble in ordered porous electrodes for alkaline water electrolysis

Wu RUI [1], Zhihao HU[1,*]

1: Shanghai Jiao Tong University, Shanghai, China
* Corresponding author: Email: zhihaohu@sjtu.edu.cn

**Abstract**: Alkaline water electrolysis (AWE) is a widely-utilized method for producing green hydrogen through water electrolysis. Overcoming the performance bottleneck of OER is crucial for improving the system's efficiency. Bubble behavior can increase electrode resistance, transport resistance and reduce the electric active surface area. Currently, most industrial AWE systems utilize foamed metal electrodes, which have disordered pores leading to bubble plugging and negatively impact performance. To address this issue, we have fabricated nickel-based electrodes with ordered square cone hole (OSCH-Ni) by electrical discharge machining (EDM). Our experiments have shown that the disordered pores of traditional nickel foam electrodes are often blocked by gas bubbles. However, the OSCH-Ni significantly improves gas discharge by reducing the confinement of bubbles. The OSCH-Ni has shown excellent performance in AWE OER (1 M KOH electrolyte), with a current density of 34.4 mA cm-2 at a high potential of 0.77 V vs. Hg/Hg O, nearly three times the current density of 11.8 mA cm-2 of common industrial nickel foam electrodes. This work provides insight into the behavior of gas bubbles inside electrodes in alkaline electrolysis systems and how OSCH-Ni can improve electrolysis performance. It also supports a feasible solution for the industry's design of electrolytic water electrodes.

**Keywords:** Bubble behavior, Ordered porous electrodes, Alkaline water electrolysis

Alkaline water electrolysis (AWE) is a widely-utilized method for producing green hydrogen through the electrolysis of water. Overcoming the performance bottleneck of OER is crucial for improving the overall efficiency of the system. The behavior of bubbles during the OER process can significantly increase the resistance of the electrode in the electrolysis water reaction, resulting in increased transport resistance and reduced electrochemically active surface area of the electrode. This is particularly pronounced at high current densities, where the mass transfer and load transfer resistance of bubbles to the gas evolution reaction is greatly increased, ultimately affecting the overall electrochemical efficiency of the system. Currently, most industrial AWE systems utilize foamed metals as electrodes. While these materials have high specific surface areas, the disordered pore structure of metal foam can lead to bubble behavior such as bubble plugging, which negatively impacts electrochemical performance. To address this issue, we have fabricated a nickel-based electrode with ordered square cone holes (OSCH-Ni) using electrical discharge machining (EDM) as Fig.1. Our experiments have shown that the disordered pores of traditional nickel foam electrodes are often blocked, hindering gas discharge. However, the processed electrode with ordered square cone holes significantly improves gas discharge by reducing the confinement of bubbles during adhesion and expulsion.

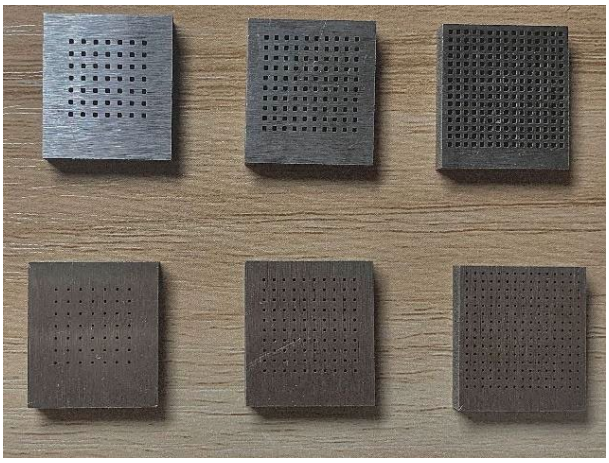

Fig.1 Nickel-based electrodes with ordered square cone holes

In addition, the structure electrode has shown excellent performance in alkaline water

electrolysis oxygen evolution (1 M KOH electrolyte), with a current density of 34.4 mA cm-2 at a high potential of 0.77 V vs. Hg/Hg O, nearly three times the current density of 11.8 mA cm-2 of common industrial nickel foam electrodes, as Fig.2. This work provides insight into the behavior of gas bubbles inside electrodes in alkaline electrolysis systems and how nickel-based ordered square cone electrodes can improve electrolysis performance. It also supports the bubble behavior model predicted by existing scientific research and provides an efficient and feasible solution for the design of electrolytic water electrodes in the industry.

# Critical Heat Flux Conditions in Flow Boiling in Microchannels

Ali H. AL-ZAIDI[1], Mohamed M. MAHMOUD[2], Atanas IVANOV[3], Tassos G. KARAYIANNIS[3, *]

1: University of Misan, Al-Amarah, Iraq
2: Faculty of Engineering, Zagazig University, Zagazig, Egypt
3: Department of Mechanical and Aerospace Engineering, Brunel University London, UK

*Corresponding author: Tel.: +44 (0) 1895 267132; Email: tassos.karayiannis@brunel.ac.uk

**Abstract:** An experimental study was carried out on flow boiling in a horizontal metallic microchannel heat exchanger that included assessment of critical heat flux conditions. The working fluid was HFE-7100. The critical heat flux results compared well with past correlations.

**Keywords:** Flow Boiling, Critical Heat Flux, Microchannels.

## 1. Introduction

Critical heat flux (CHF) is the maximum thermal limit that should be avoided in any thermal management system. A sudden jump in wall temperature and a reduction in heat transfer coefficient are the main consequences that can be catastrophic for the heat exchangers involved and the overall thermal process. Two-phase CHF in microchannels could occur due to flow reversal/instability, choking flow and dryout of the liquid film in annular flow [1]. Different models and correlations were proposed to identify this maximum limit. Some of these correlations were evaluated in the present study.

## 2. Experimental Facility

Fig. 1 shows the experimental rig that was used in the present study. HFE-7100 as a dielectric and eco-friendly refrigerant was examined at different operating conditions. The supplied heat to the test section was increased step-by-step until the critical heat flux was reached. The CHF was identified when the reading of the thermocouples inserted underneath the channels increased suddenly. A Phantom high-speed, high-resolution camera was used to capture the flow patterns. The test section was manufactured using a high precision micro-milling machine, see Fig. 2. It consisted of cover plate, housing, bottom plate, cartridge heaters, heating block and the heat sink. An oxygen free-copper heat sink including thirteen rectangular microchannels was fabricated. A set of thermocouples was used to measure the temperature variation along the flow direction. The present experiments were carried out at pressure 1 bar, inlet sub-cooling 5 K, mass flux range 100−300 kg/m$^2$s and wall heat flux up to 308 kW/m$^2$.

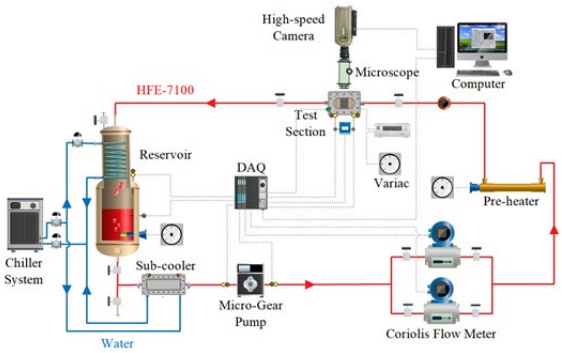


**Figure 1:** Schematic diagram of the experimental rig [2].

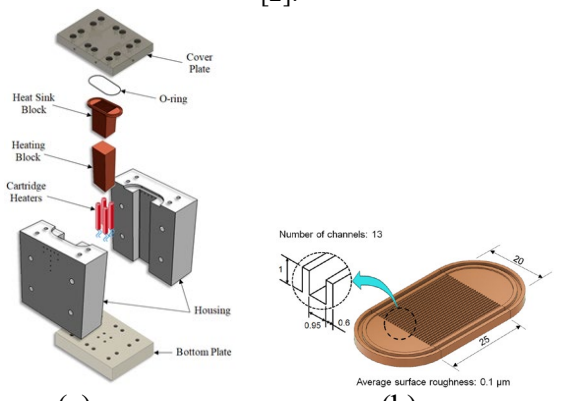


**Figure 2:** Test section: (a) Exploded drawing (b) Heat sink (dimensions in mm).

The wall heat flux was calculated from the vertical temperature gradient in the heating block and the channel wall heat transfer area. It

can also be calculated based on the heat sink base area (20 mm × 25 mm), see [2].

## 3. Results and Discussion

CHF was identified when there was a sudden unsteady increase in the channels bottom surface temperature. This was attributed to the dryout areas appearing during annular flow. Fig. 3 depicts that the wall heat flux increased with wall superheat before the occurrence of complete or mostly complete dryout of the liquid film in annular flow. After that, a sudden jump in the wall superheat occurred. The CHF was found to vary from 126 to 308 kW/m$^2$ for the current operating conditions.

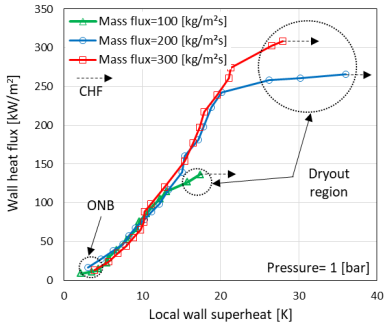


**Figure 3:** Boiling curve of HFE-7100 at heat sink middle.

Fig. 4 shows that the average two-phase heat transfer coefficient which increases with increasing heat flux and demonstrated a sudden decrease at the CHF conditions. The effect of mass flux is clear, i.e. the CHF depends strongly on the mass flux through the microchannel heat exchanger.

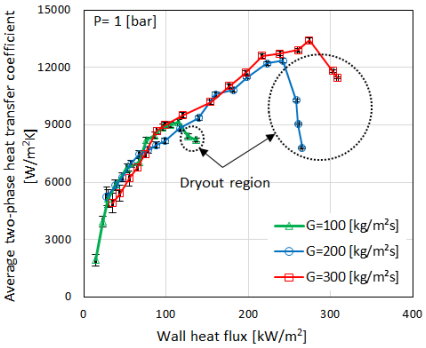


**Figure 4:** Two-phase heat transfer coefficient.

All the experimental data were compared with existing correlations, see Fig. 5. It can be seen in the figure that the correlations by Wojtan et al. [3] and Ong and Thome [4] predicted better the present CHF data. The correlation proposed in [3] was based on data for R134a and R245fa and micro-tubes of internal diameter 0.5 and 0.8 mm and heated lengths varying between 20 and 70 mm. The mass flux ranged covered was 400–1600 kg/m$^2$s. The correlation in [4] was developed based on data for flow boiling of R134a, R236fa and R245fa, for rectangular multi-channels and single tubes, hydraulic diameter 0.35–3 mm and mass flux 84–3736 kg/m$^2$s. The correlation proposed by [5] included data for water and R113 in rectangular multi-channels and single tubes with a diameter range of 0.34–2.5 mm at mass flux of 30–476 kg/m$^2$s.

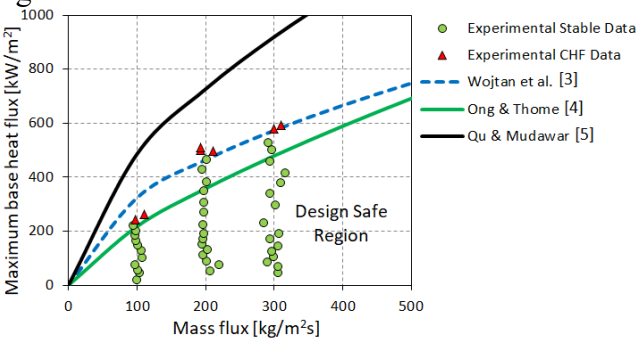


**Figure 5:** Design safe region.

## 4. Conclusions

The CHF of HFE-7100 in multi microchannels as a function of mass flux is reported in this study. It was found that CHF occurred due to dryout in annular flow. The correlations proposed by [3,4] demonstrated reasonable agreement with the present data. Further work is recommended to include different fluids, channel number and sizes, material of the heat exchanger and operating ranges to conclude on final recommendations for correlations predicting flow boiling CHF and safe operation in microchannels.

## References

[1] Kim SM, Mudawar I. Thermal design and operational limits of two-phase micro-channel heat sinks. IJHM. 2017, 861-76.
[2] Al-Zaidi AH, Mahmoud MM, Karayiannis TG. Flow boiling of HFE-7100 in microchannels: Experimental study and comparison with correlations. IJHMT. 2019, 100-28.
[3] Wojtan L, Revellin R, Thome JR. Investigation of saturated critical heat flux in a single, uniformly heated microchannel. ETFS. 2006, 765-74.
[4] Ong CL, Thome, JR. Macro-to-microchannel transition in two-phase flow: Part 2–Flow boiling heat transfer and critical heat flux. ETFS. 2011, 873-886.
[5] Qu W, Mudawar I. Measurement and correlation of critical heat flux in two-phase micro-channel heat sinks. IJHMT. 2004, 2045-59.

# Numerical study of mixed convection flow in a lid-driven enclosure filled water–aluminium oxide nanofluid

Wasaif ALRUWAELE[1,*], Jitesh GAJJAR[2]

1: Department of Management and Engineering, University of Hafr Al Batin, Al- Khafji, KSA
2: Department of Mathematics, University of Manchester, Manchester, UK

* Corresponding author: Tel.: +966137209526; Email: walruwaele@uhb.edu.sa

**Abstract**: The phenomena of mixed convection is widely employed in a variety of engineering processes such as the operation of solar collectors, heat exchangers, drying technologies, home ventilation, high-performance building insulation and lubrication technologies. Mixed convection is more difficult than other types of convection because of the interaction between the buoyancy force which caused by temperature difference and the shear force which caused by wall movement. Due to their low thermal conductivity, conventional heat-transfer fluids adopted in cooling systems such as water, oil, and silicone have limitations in their efficacy. There has been investigation on the possibility of using nanofluids in heat-transfer systems as a replacement for conventional fluids. In this work, a nanofluid was used to explore the heat transfer in an enclosed cavity. The nanofluid was water as the base fluid and aluminum oxide nanoparticles dispersed in it. This work considers the flow in a single lid-driven cavity. The impact of different viscosity models on the mixed convection heat transfer is examined in this numerical investigation. Numerical methods were used to obtain the solutions in parameter ranges where others have had difficulties, such as very large Rayleigh numbers.

**Keywords:** Nanofluid, Heat transfer, Viscosity, lid-driven cavity.

## 1. Introduction

The phenomena of mixed convection is widely employed in a variety of engineering processes such as the operation of solar collectors, heat exchangers, drying technologies, home ventilation, high-performance building insulation and lubrication technologies [3], [5] and [1]. Mixed convection is more difficult than other types of convection because of the interaction between the buoyancy force which is caused by temperature differences and the shear force which is caused by wall movement.

We investigate the steady Navier-Stokes equations for flow in a lid-driven cavity with two different dynamic viscosity formulas. Our aim is the investigation of the effect of nanofluid and dynamic viscosity in heat transfer enhancement.

## 2. Description and Formulation

This work considers two cases for the flow in the lid-driven square cavity with a width of W and a height of H. The first case, the top wall of the enclosure operates at an elevated temperature and the bottom wall of enclosure remains at lower constant temperature. The right and left of the enclosure wall are maintained at adiabatic condition.
The second case, the left wall of enclosure operates at elevated temperature and the right wall of enclosure remains at lower constant temperature the top and bottom of the enclosure wall are kept constant, with an adiabatic condition.
For the both, the nanofluid in the enclosed space is shown as a dilute solid-liquid fluid with uniform nanoparticles, such as water aluminum oxide, scattered inside a base fluid, such as

water.

## 3. Numerical Simulation

The Chebychev collocation method combined with Newton linearization have been used to discretize governing equations in the x and y-direction.

## 4. Conclusions

Two cases for mixed convective of nanofluid with different boundary conditions in double lid cavities were investigated. For the first case, the cavity's top and bottom walls were kept at fixed temperatures and the cavity's left and right walls were maintained insulated. The second case was designed so that the left and right walls were kept at fixed temperatures and the top and bottom walls were maintained insulated. In the double-lid cavity design, the top moved to the right as the bottom make a movement to the left at the same fixed speed. The Brinkman model [2] and the Pak correlation [4] are two viscosity models that are used to estimate the viscosity of nanofluids. A numerical investigation was done, and a group of results were presented and discussed to demonstrate the effect of nanoparticle presence and the Richardson number on flow and heat transfer behavior. The addition of nanoparticles was shown to significantly increase heat transfer, and this was considerably enhanced by raising the nanoparticle volume fractions for large Richardson numbers $Ri \geq .01$. In the first case, Nusselt numbers increases and the enhancement in Nusselt number was much greater when applying the Pak and Cho correlation than those referring to the Brinkman formula. However, the Pak and Cho correlation showed that the existence of nanoparticles would result in decreases in the Nusselt numbers for small Richardson number $Ri < .01$ in second case. In addition, the first case has a higher Nusselt numbers than that corresponding to the second case.

## References

[1] Boutra, A., Ragui, K., & Benkahla, Y. K. (2015). Numerical study of mixed convection heat transfer in a lid-driven cavity filled with a nanofluid. *Mechanics & Industry*, *16*(5), 505.

[2] Brinkman, H. C. (1952). The viscosity of concentrated suspensions and solutions. *The Journal of chemical physics*, *20*(4), 571-571

[3] Cha, C. K., & Jaluria, Y. (1984). Recirculating mixed convection flow for energy extraction. *International Journal of Heat and Mass Transfer*, *27*(10), 1801-1812.

[4] Pak, B. C., & Cho, Y. I. (1998). Hydrodynamic and heat transfer study of dispersed fluids with submicron metallic oxide particles. *Experimental Heat Transfer an International Journal*, *11*(2), 151-170.

[5] Pilkington, L. A. B. (1969). Review lecture: the float glass process. *Proceedings of the Royal Society of London. A. Mathematical and Physical Sciences*, *314*(1516), 1-25.

## SESSION 8b
## Multi-scale phase change processes
Chair: **G. Righetti**

# Analytical analysis of isothermal Pressure-driven Poiseuille flow using the extended OBurnett equations

Upendra YADAV[1,*], Anirudh JONNALAGADDA[2], Amit AGRAWAL[1]

1: Department of Mechanical Engineering, Indian Institute of Technology Bombay, Powai, Mumbai 400076, India
2: Department of Computational and Data Sciences, Indian Institute of Science, Bangalore, India

* Corresponding author: Tel.: +91 7042 961864; Email: upendra.yadav001@iitb.ac.in

**Abstract**: This work analyzes the plane pressure-driven Poiseuille flow problem in a two-dimensional isothermal gaseous flow in a long microchannel, employing the extended set of second-order accurate OBurnett equations. The newly proposed equations are closed by evaluating constitutive relationships for the stress tensor and the heat flux vector using a generalized additive-invariance-compliant and second-order accurate representation of the extended single-particle distribution function. Linear stability of the proposed macroscopic equations is found to be unconditionally stable for two-dimensional flows at all wave numbers. Closed-form solutions of both the pressure and velocity field have been presented for the first time using the proposed equations. The obtained results have been compared with the existing direct simulation Monte Carlo (DSMC) results and demonstrate good agreement, suggesting that the proposed equations may better describe flow physics for large Knudsen number. The significance of the present work lies in its ability to solve benchmark problems that have been hindered by the complexity of higher-order transport equations.

**Keywords:** Microchannel Flow, OBurnett Equations, Poiseuille Flow, Analytical, Pressure Driven

# Cherry-picking Nanoparticles from Surfaces Using Water Droplets

Sreehari PERUMANATH[1,*], Rohit PILLAI[2], Matthew K BORG[2]

1: Warwick Mathematics Institute, University of Warwick, Coventry CV4 7AL, UK
2: School of Engineering, University of Edinburgh, Edinburgh EH9 3FB, UK

* Corresponding author: Email: s.perumanath@warwick.ac.uk

**Abstract:** Many organisms in nature exploit the dynamics of condensing dew droplets to passively clean their bodies from different contaminants, such as pollen, atmospheric dust particles, and micro-organisms. For example, cicada wings have self-cleaning cababilities as the superhydophobicity of their surfaces enables neighbouring condensate water droplets to coalesce, jump away and take contaminants with them. However, the exact mechanism of this self-cleanning process, where nano-to-micrometre sized contaminants in the vicinity of a superhydrophobic surface interact with moving water droplets, is still elusive. Using molecular simulations, here we rationalise and theoretically explain this process and show, for the first time, that droplets can only remove certain types of contaminants from superhydrophobic surfaces. Those particles which are not removed during droplet coalescence are laterally relocated. Recent experiments conducted at micro-millimetre scales are also shown to fit well within our theory. This work signals the potential of droplet coalescence in enabling low-cost regulated transport of nanoparticles on superhydrophobic surfaces or in the design of miniature electronic devices and bio-sensors, where a nanoparticle's accurate placement is crucial.

**Keywords:** Cicada, Nanoparticle, Coalescence, Superhydrophobic surfaces, Self-cleaning

## 1. Introduction

Cicada wings and lotus leaves have a common feature that makes them excellent self-cleaning surfaces in nature. It is their ability to repel water – or their 'superhydrophobicity'. Dew condenses at nucleation sites on these surfaces, where water droplets will adopt a near-spherical shape with contact angle well above 150°. When two such neighbouring droplets coalesce on superhydrophobic surfaces, a part of their surface free energy that is released in the process is converted into the merged droplet's translational kinetic energy, and it will jump away from the underlying surface [1]. Cicadas utilize this *droplet jumping mode of self-cleaning* to remove individual contaminants at a time from their wings [2].

Alternatively, if the condensation occurs for longer periods on superhydrophobic surfaces so that the radii of the droplets become comparable to the liquid's capillary length (~1 mm for water), droplets can roll off inclined surfaces owing to the gravitational pull. This *droplet rolling mode of self-cleaning* is observed on lotus leaves, where many contaminants are removed at a time by droplets rolling down the leaves [3].

While these ubiquitous self-cleaning processes have substantial industrial promise – for example, in the design of automobile wind shields and solar panels [4], experiments have so far been unable to comprehend the underlying physics. This is primarily due to the challenge in exploring the nanoscale physics involved in these fast dynamic processes.

Here, the jumping mode of self-cleaning is studied in detail to reveal under what conditions water droplets are able to remove different nanoparticles on superhydrophobic surfaces.

## 2. Methodology

With the aid of molecular dynamics (MD) simulations, here we rationalise and theoretically explain different mechanisms of surface self-cleaning. Two spherical droplets are equilibrated on a superhydrophobic wall.

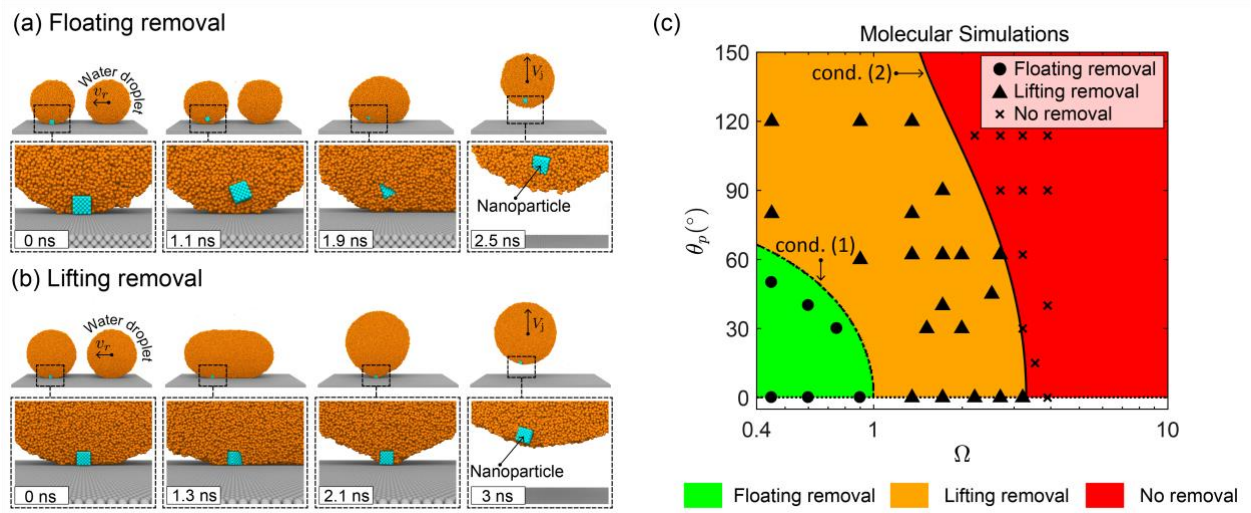


**Figure 1**: (a) Floating removal of a nanoparticle from a superhydrophobic surface, where the particle gets dislodged even before the droplets coalesce. (b) Lifting removal of a nanoparticle from a superhydrophobic surface. Here, the system assumes a hot-air balloon configuration (see the third panel) post-coalescence for the particle to get dislodged from the surface. In (a) and (b), the frontal half of both spherical droplets are not shown to enable better visualisation of the nanoparticle. (c) Phase diagram showing nanoparticle removal obtained from our MD simulations and their comparison with the new theory. Excellent agreement is observed between the theory and results of our MD simulations, as well as with previous experiments (not shown here). Here, $\Delta \approx 2$.

Underneath one of the droplets, a nanoparticle is kept to mimic a scenario where water vapour has condensed to form a droplet near a foreign particle that acts as a condensation nucleation site (see the first panels of Figs. 1(a,b)). After equilibration, one of the droplets is pushed towards the other with speed $v_r = 1\ m/s$ so that they will come in contact, coalesce, and jump off the superhydrophobic surface carrying the nanoparticle away from it.

## 3. Results

Two different types of particle removal mechanisms are exhibited by the droplet jumping mode of self-cleaning:

1. *Floating removal* occurs for relatively hydrophilic nanoparticles, where the intermolecular attraction from the enclosing droplet alone is enough to overcome its adhesion on the surface. Hence, the particle gets dislodged from the surface even before coalescence begins (see the second panel of Fig. 1(a)). It can be shown that, theoretically, this occurs when

$$cos\ \theta_p > \Omega, \qquad (1)$$

where $\theta_p$ is the contact angle between the condensing liquid and the nanoparticle, and $\Omega$ is the force of adhesion, $F_{adh}$, normalised with the surface tension force, $\gamma P$. Here, $\gamma$ is the condensing liquid's surface tension and $P$ is the nanoparticle's nominal perimeter. Notably, if condition (1) is satisfied, floating removal can occur on *any* surface irrespective of its interaction with the condensing liquid.

2. *Lifting removal* occurs for a relatively less hydrophilic nanoparticle, where its intermolecular attraction from the enclosing droplet alone is not large enough to overcome $F_{adh}$. However, only on superhydrophobic surfaces, when the merged droplet attains a hot-air balloon configuration after coalescence (see the third panel of Fig. 1(b)), an additional dislodging force appears in the system that aids the particle's removal from the surface. Theoretically, lifting removal occurs when:

$$cos\ \theta_p + \Delta > \Omega, \qquad (2)$$

where $\Delta$ is the additional dislodging force normalized with $\gamma P$. From Fig. 1(c), we note excellent agreement between the new theory and MD simulation results. Our results clearly indicate the potential of droplet dynamics in low-cost regulated transport of nanoparticles on various surfaces.

## References

[1] Perumanath, S. *et al.*, *Nanoscale* **12**, 20631–20637 (2020).
[2] Wisdom, K. M. *et al.*, *Proc. Natl. Acad. Sci. U. S. A.* **110**, 7992–7997 (2013).
[3] Barthlott, W. & Neinhuis, C., *Planta* **202**, 1–8 (1997).
[4] Yao, L. & He, J., *Prog Mater Sci* **61**, 94–143 (2014).

# The influence of cavity shapes on flow and heat transfer characteristics of curved microchannels

Murun LI [1,2], Xuan GAO [1,2], Haiwang LI [1,2], Jichang SANG [1,2], Weidong FANG [1,2] and Tiantong XU [1,2,*]

1: National Key Laboratory of Science and Technology on Aero-Engine Aero-Thermodynamics, Beihang University, Beijing, China
2: Research Institute of Aero-Engine, Beihang University, Beijing, China
* Corresponding author: Email: xutiantong@buaa.edu.cn

**Abstract:** This study investigates the flow and heat transfer characteristics of square curved microchannel heat sinks with wall cavities of various shapes and sizes. Two cavity shapes (rectangular and triangular) and two structural parameters (aspect ratio and incidence angle) were considered under Reynolds number (Re) = 0~800 conditions. The flow (Poiseuille number, Po), heat transfer (Nusselt number, Nu), and comprehensive heat transfer (Thermal Performance number, TP) characteristics were used to evaluate the microchannel. The results showed that the use of cavities reduced the flow resistance and improved the thermal performance of the microchannel within the investigated range. The study also found that the cavity shape has a significant impact on flow and heat transfer, with the triangular cavity outperforming the rectangular cavity. This difference is due to the more similar contour of the triangular cavity to the flow linear, which made it easier for the fluid to flow into its cavity. The thermal performance of triangular cavities increased by 86%, and rectangular cavities increased by 65%, without significant economic losses such as pressure drop.

**Keywords:** microchannel; microstructure; cavity; flow; heat transfer; curved

## 1. Introduction

Convective heat transfer in laminar flow is strongly affected by fluid mixing. In curved channels, centrifugal forces create pressure and velocity gradients that generate vortices and secondary flows, which promote fluid mixing. However, curved channels exhibit different heat transfer characteristics than straight channels, which makes it challenging to predict curved channel heat transfer based on straight channel data.

Cavities have emerged as an effective way to improve heat exchange by disrupting the flow and promoting mixing. Compared to other structures like fins, cavities do not necessarily increase flow resistance and their performance depends on specific working conditions and structures Therefore, optimizing cavity designs for different flow conditions and applications is important. However, existing studies have mostly focused on single structure size optimization or simple shape comparisons, lacking quantitative analysis and systematic research on cavity optimization.

This paper quantitatively analyzes the effects of cavity shape and size on flow and heat transfer characteristics in curved microchannels to improve heat transfer, reduce pressure drop, and fill the research blank of the coupling effect of these factors.

## 2. Methods

The microchannels with various cavities were designed as shown in Fig.1. The microchannel had closed top surfaces and adiabatic side surfaces, except for the solid-liquid contact and bottom heating surfaces. Silicon was used as the microchannel material, while deionized water was used as the fluid. A constant heat flux density was applied to the heating surface to raise the fluid's average temperature by 20 K. The Re range was set at 0-800.

The study was conducted under the following assumptions [1]: (1) laminar flow, (2) continuous medium hypothesis, (3) steady and incompressible flow, (4) constant solid thermophysical properties, and (5) ignored body force and radiation heat transfer.

The flow and heat transfer characteristics were

evaluated based on the Po and Nu, respectively, while the comprehensive thermal performance was assessed by the TP, which considers both flow and heat transfer. [1-2]

To ensure accuracy, the study's results were compared with those of previous studies. [3]

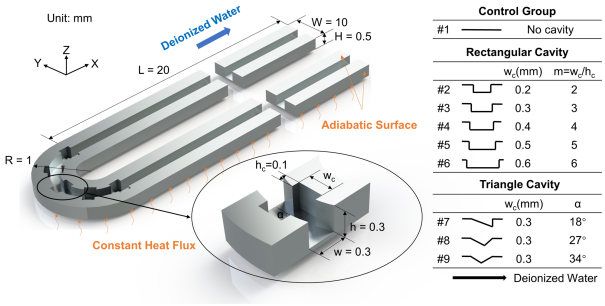


Fig.1 The schematic of the microchannel with cavities.

## 3. Results

The triangular cavity is taken as an example.

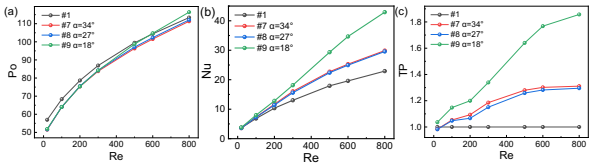


Fig.2 The flow and heat transfer characteristics of microchannels with triangular cavities, (a) Po versus Re, (b) Nu versus Re, (c) TP versus Re.

Fig.2 shows that the triangle cavity can simultaneously reduce flow resistance and improve thermal performance compared to the unstructured microchannel, regardless of the incidence angles. The TP of each microchannel gradually rises with increasing Re and then tends to stabilize. The optimal choice is the #9 microchannel with an incidence angle of 18°, which has a TP of up to 1.86.

To further explain these phenomena, flow diagrams and temperature cloud maps at Re = 20 and Re = 800 were examined. Slip occurs at the liquid-liquid interface between the main stream and the fluid in the cavity, and its resistance is less than that of the non-slip liquid-solid interface between the main stream and the solid wall, which reduces the flow resistance. This is independent of the incidence angle, leading to similar Po in each group. At low Re, there is little fluid entering the cavity, resulting in no significant difference in Nu among microchannels. At high Re, the main stream hits the cavity located outside the curved micro-channel and generates an impact vortex. The #9 microchannel with an incidence angle of 18° has no contraction section, causing the main stream to hit the cavity wall almost vertically. This leads to the destruction and re-development of the boundary layer, improving heat exchange. It can be seen that areas with a large vortex exhibit significantly lower temperatures than the surrounding areas.

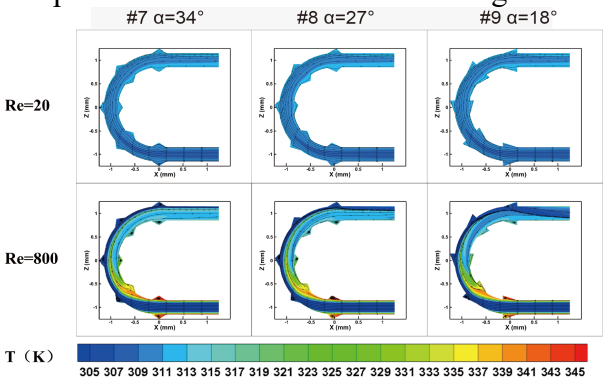


Fig.3 The flow diagrams and temperature cloud maps of microchannels with triangular cavities.

The triangular cavity has a more significant effect on the flow and heat transfer of microchannels than the rectangular cavity. This is due to the contour of the triangular cavity being more similar to the flow linear, allowing the fluid to flow more easily into the cavity.

## 4. Conclusion

This study investigated the influence of cavity shapes on flow and heat transfer characteristics of curved microchannels. Our findings show that the cavity shape has a significant impact on flow and heat transfer, with the triangular cavity outperforming the rectangular cavity. Specifically, the thermal performance of the microchannel with triangular cavities increased by 86%, and by 65% for rectangular cavities.

## 5. Reference

[1] Batchelor, C.K.; Batchelor, G.K. An Introduction to Fluid Dynamics, 1st ed.; Cambridge University Press: Cambridge, UK, 1967.

[2] Alfellag, M.A. et al. Optimal Hydrothermal Design of Microchannel Heat Sink Using Trapezoidal Cavities and Solid/Slotted Oval Pins. Appl. Therm. Eng. 2019, 158, 113765.

[3] Zhang, M, et al. The Calculation of Heat Transfer in Duct Flow by Unstructured Grids. J. Nanjing Inst. Technol. Nat. Sci. Ed. 2006, 4, 25.

# Microstructure and collective dynamics of externally driven deformable particle suspensions in strong confinement conditions

Sagnik SINGHA[1], Abilash R. MALIPPEDI[2], Mauricio ZURITA-GOTOR[3], Kausik SARKAR[2], Jerzy BLAWZDZIEWICZ[1,*]

1: Department of Mechanical Engineering, Texas Tech University, Lubbock, TX, USA
2: Department of Mechanical and Aerospace Engineering, George Washington University, Washington, DC, USA
3: Departmento de Ingeniería, Universidad Loyola Andalucía, Sevilla, Spain

* Corresponding author: Tel.: +1 806 834 0496; Email: jerzy.blawzdziewicz@ttu.edu

**Abstract:** We examine the dynamics and microstructure evolution of a strongly confined suspension of deformable drops subject to a combination of Poiseuille and Couette flows. Using both direct numerical simulations as well as an accurate quasi-2D numerical model, we show that sheared drop suspensions exhibit both stable and unstable diffusive dynamics which result from the symmetry of the leading order hydrodynamic interactions. When combined with the wave propagation behavior associated with pressure-driven flows, drop monolayers subject to simultaneous shear and pressure-driven flows exhibit a rich behavior, which includes the formation of a solitary propagation wave (soliton) that stabilizes any subsequent perturbation in drop particle number density.

**Keywords:** suspension microstructure, hydrodynamic interactions, confinement, collective particle dynamics

## 1. Introduction

Particle suspensions driven by external flows show complex collective behavior and can spontaneously self-assemble to form ordered structures. The underlying interparticle hydrodynamic coupling becomes especially pronounced for confined and deformable particle suspensions. Particle arrays in suspensions undergoing a Poiseuille flow exhibit wave-like dynamics, including longitudinal and transverse wave propagation, as well as development of shock-wave fronts. Monolayers of sheared and strongly confined drops self-organize into ordered, chain-like structures, aligned in the flow direction. Similar observations have been reported for red blood cells.

These behaviors can be explained using additive pairwise approximations to the velocity induced in each particle by the leading order contributions of the flow scattered by the remaining particles in the suspension. Scattered flow under confinement tends exponentially with distance to the form of a Hele-Shaw parabolic flow driven by a pressure gradient that can be expressed in terms of a 2D multipolar expansion.

In Poiseuille flow, collective dynamics of spherical particles are driven by the leading order dipolar term in the expansion. The antisymmetry of dipolar perturbations explains the wave-like dynamics of drop arrays. For deformable particles, quadrupolar terms for small but finite capillary numbers may also need to be considered to obtain correct collective dynamics [1].

On the other hand, we have shown [2] that the spontaneous self-assembly of sheared drop suspensions into arrays aligned with the flow direction is a result of two symmetric contributions: an attractive far-field behavior due to quadrupolar hydrodynamic interactions, and a near-field repulsive term due to interactions with the flow reflected by the walls (a transverse swapping contribution).

In this work we discuss the collective dynamics of strongly confined linear droplet arrays

subjected to an external flow with simultaneous symmetric (dipoles) and antisymmetric (quadrupoles and swapping) hydrodynamic interactions. Such a system could be physically observed in the Poiseuille flow of deformable drops, or for combined Poiseuille and Couette flows.

## 2. Discussion

Our direct numerical simulations based on the front-tracking method show that monolayers of unequally spaced droplet chains aligned in the flow direction exhibit either wave propagation dynamics, when subjected to Poiseuille flow, or diffusive behavior under simple shear.

Using a phenomenological continuum equation and a quasi-2D model, we show that this strikingly different behavior stems from the antisymmetry (pressure-driven suspensions) or symmetry (sheared suspensions) of hydrodynamic interactions in the system. In our quasi-2D model droplet $i$ velocity, $\mathbf{v}_i$, is obtained at each time step in a pairwise additive manner from the contributions $\mathbf{v}_{ij}$ due to interactions with remaining $j$ particles as

$$\mathbf{v}_i = \sum_j \mathbf{v}_{ij} = \alpha \mathbf{v}_{ij}^{d} + (1-\alpha)\mathbf{v}_{ij}^{qs}$$

where superscripts $d$ and $qs$ denote leading order antisymmetric (dipoles) and symmetric (quadrupoles and swapping) contributions, and $\alpha$ is a parameter representing the relative strength between antisymmetric and symmetric terms.

Fig. 1 shows numerical results of the evolution of drop suspension microstructure for either symmetric (left bottom panels) or antisymmetric interactions (right bottom panels). The initial drop positions are given by the top panel, where the inset provides a corresponding inverse droplet number density (a small harmonic perturbation of an equispaced uncompressed chain). Middle panels show instantaneous drop positions at increasing times, while bottom panels depict the evolution of the inverse number density (drop-to-drop distance). As seen, antisymmetric terms lead to wave propagation (right bottom panels), while symmetric terms (left bottom panels) lead to a diffusive instability and drop fragmentation.

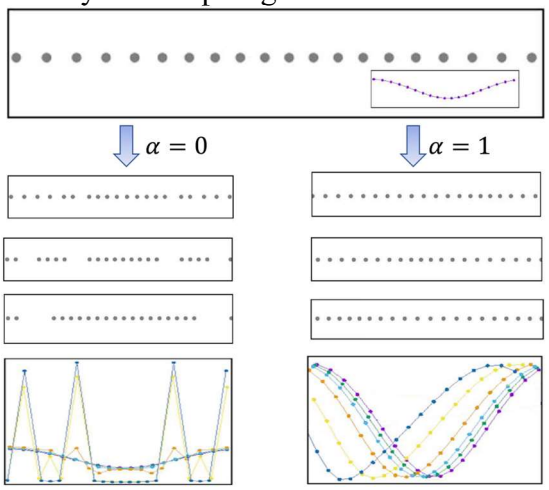


**Fig. 1**. Evolution of drop configuration in a linear array. Symmetric interactions (left panels) show unstable diffusive behavior, while antisymmetric interactions (right panels) show wave dynamics.

A combination of symmetric and antisymmetric contributions in the same system leads to a novel intriguing behavior. For example, Fig. 2 shows the development of a solitary propagating wave (soliton). Furthermore, our simulations show that solitons stabilize any subsequent perturbations in the drop particle number density.

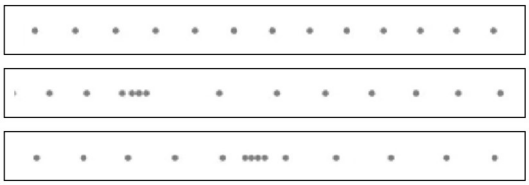

**Fig. 2**. Instantaneous drop positions for increasing times (top to bottom) of a system with combined symmetric and antisymmetric interactions. As shown, an initial equispaced and unstable drop array can develop a solitary propagation wave (soliton).

## References

[1] Janssen, P.J.A, Baron, M.D, Anderson, P.D., Blawzdziewicz, J., Loewenberg, M, Wajnryb, E. 2012. Collective dynamics of confined rigid spheres and deformable drops, Soft Matter 8, 7495-7506.

[2] Singha, S., Malipeddi, A.R., Zurita-Gotor, M., Sarkar, K., Shen, K., Loewenberg, M., Migler, K., Blawzdziewicz, J. 2019. Mechanisms of spontaneous chain formation and subsequent microstructural evolution in shear-driven strongly confined drop monolayers, Soft Matter 15, 4873-4889.

# Dislodging nanoparticles using surface acoustic waves

Rohit PILLAI[1], Matthew K. BORG[1], Saikat DATTA[1*]

1:School of Engineering, University of Edinburgh, Edinburgh EH9 3FB, United Kingdom

* Corresponding author: Email: Saikat.Datta@ed.ac.uk

**Abstract:** The removal of contaminants from engineered surfaces is an important issue, with applications to a range of areas such as semiconductor fabrication, single-molecule biophysics and bio-sensing. Due to the predominance of intermolecular forces, it is particularly challenging to remove nanoscale-sized contaminants, i.e., nanoparticles. Depending on the application, nanoparticles may need to be removed or relocated with extreme precision. Ultrasonic surface vibration at a high frequency could be an effective way to remove nanoparticles from surfaces, but the underlying mechanism is still unexplored. In this work, we employ Molecular Dynamics simulations to study the viability of surface vibrations to dislodge a nanoparticle that is attached to a surface. We find that the optimum energy requirement for particle detachment can be characterized by the maximum velocity of the surface during vibration. Furthermore, the study also reveals that the optimum energy needed for particle detachment follows a scaling law, which can conveniently be used for larger-sized nanoparticles (i.e., ~50-500 nm) that are beyond the computational limitations of molecular simulations. This work unravels the decisive factors to better design a process of decontamination of surfaces with nanoscale precision.

**Keywords:** Surface acoustic wave, Nanoparticle, Vibration, Surface contamination, Molecular Dynamics

## 1. Introduction

Surface contamination is an important problem in several engineering and clinical applications. Surface cleaning and decontamination, like oxides removal from steel surfaces [1], cleaning of particle-fouled ceramic membranes [2], and particle removal from semiconductors [3], are routinely used in industry. However, recent nanotechnology-based applications, such as electronic chip manufacturing [4], and biosensor development [5], require precise and smaller-scale decontamination techniques as to deal with nanoscale features and nanoparticles. Nanoparticle decontamination is technically challenging compared to its larger-scale counterparts due to the predominance of intermolecular forces. Therefore, an approach that exploits intermolecular forces for removing nanoparticles could be a practical way to deal with such size-dependent physics. Nanoscale surface vibrations produced by state-of-the-art surface acoustic wave devices (SAW) can produce localised mechanical work by harnessing intermolecular forces. This could provide an effective, energy-efficient, and less damaging method for nanoparticle removal compared to existing techniques. However, a deeper understanding of the underpinning physics of vibration-driven nanoparticle removal is yet to be unraveled. This is the first work to investigate nanoparticle removal using high-frequency surface vibrations.

## 2. Result and discussion

We perform Molecular Dynamics (MD) simulations to understand how SAWs can remove nano-sized particle from solid surfaces. The simulation domain consists of a cuboid-shaped nanoparticle resting on a solid substrate (Figure 1). The surface represents a small spanwise portion of a SAW device, therefore its motion is approximated by a sinusoidal vertical motion. Both the substrate and particle are composed of a face-centered cubic lattice with a lattice constant of 3.92 Å, and interactions between them are modelled by the Lennard-Jones (LJ) potential. We vary the SAW amplitude and frequency, and the LJ interactions potential (ε) to analyze their effect

on the vibration-driven particle removal.

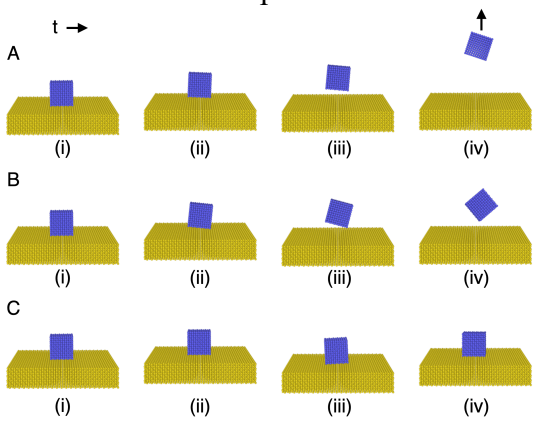


Fig. 1. Regimes of nanoparticle liftoff; A(i)-(iv) liftoff, B(i)-(iv) borderline liftoff, C(i)-(iv) non-liftoff.

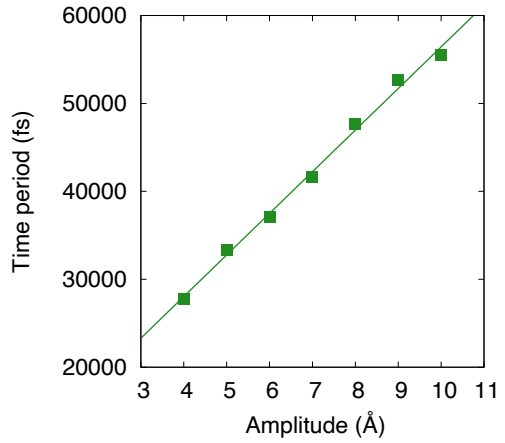


Fig. 2. The variation of the time-period of the oscillation for the borderline liftoff cases with the vibrational amplitude; ε = 0.5.

When subjected to vibration, the particle-substrate system behaves in three different modes: 1) *Liftoff,* where the particle moves away from the substrate with high velocity overcoming the work of adhesion due to the excess energy supplied upon vibration (see Figs. 1A(i)-(iv)); 2) *Borderline liftoff,* where the vibration energy is sufficient to overcome the work of adhesion, but the particle does not possess considerable kinetic energy (see Figs. 1B(i)-(iv)); and 3) *Non-liftoff* where the vibrational energy does not suffice to remove the particle from the surface (see Figs. 1C(i)-(iv)). In this study we are interested in the borderline liftoff cases as these demarcate between liftoff and non-liftoff regimes, denoting the minimum energy requirement for particle removal.

Figure 2 depicts the variation of the time-period of the oscillation for the borderline liftoff cases as a function of the vibrational amplitude, showing a strong linear correlation, such that

$$\frac{a}{T} = a\omega = V_{\max} = \text{Constant}, \qquad (1)$$

where $a$ is the amplitude, $T$ is the time period of the surface oscillation, and $\omega$ is the angular frequency of vibration. Equation (1) implies that the optimum liftoff of a particle depends on the maximum velocity ($V_{\max}$) of the vibrating surface (note that frequency and amplitude are not independent parameters). This finding is significant since, given a material and particle size, the magnitude of the constant obtained from these MD simulations can be utilized to determine the acoustic parameters for optimum liftoff of a vast range of SAW devices. These devices can have operational frequency and amplitude limit far beyond the nanoscale. Moreover, analysis of the nanoparticle energy reveals that vibration-driven removal follows a scaling law, determined by the kinetic energy of the particle and intermolecular forces. Therefore, the result obtained from this study can readily be used to design the procedures of this new avenue of nanoparticle removal for an extensive spectrum of particle sizes that are commonly encountered in different engineering and biomedical applications at diverse operating conditions.

## References

[1] Goode, B. J., Jones, R. D., Howells, J.N.H., 1998. Ultrasonic pickling of steel strip. Ultrasonics, 36 (1-5), 79-88.

[2] Lamminen, M.O., Walker, H.W., Weavers, L.K., 2004. Mechanisms and factors influencing the ultrasonic cleaning of particle-fouled ceramic membranes. J. Membr. Sci., 237 (1-2), 213-223.

[3] Kuehn, T.H., Kittelson, D.B., Wu, Y., Gouk, R., 1996. Particle removal from semiconductor wafers by megasonic cleaning. J. Aerosol Sci., 27(Suppl 1), S427-S428.

[4] Hoefflinger, B. ed., 2012. Chips 2020: a guide to the future of nanoelectronics. Berlin: Springer.

[5] Kang, H., Wang, L., O'Donoghue, M., Cao, Y.C., Tan, W., 2008. Nanoparticles for biosensors. In Optical Biosensors (583-621). Elsevier.

## SESSION 8c
## Fluid Flow in Micro and Nano systems
Chair: **F. Coletti**

# Effect of Corner Roundedness in Biomimetic Micropillars for Thin-Film Evaporation

Anand S[1], Chander Shekhar SHARMA[1,*]

1: Thermofluidics Research Lab, Department of Mechanical Engineering, IIT Ropar, Rupnagar-140001, India

* Corresponding author: Tel.: +91 1881 232358; Email: chander.sharma@iitrpr.ac.in

**Abstract:** Microprocessor development is a rapidly evolving technology that is accompanied by thermal management challenges. Heat transfer devices working on the principle of thin-film evaporation have shown tremendous potential in terms of thermal performance. Enhanced performance of such devices can be achieved by the diligent design of the wick microstructure. The biomimetic micropillar wick known as wedged micropillars inspired from the peristome of Nepenthes alata has the potential to show significant enhancement in the dryout heat flux due to high capillary pumping and permeability of flow due to their inherent sharp corners. Since the standard microfabrication techniques are limited by the resolution of the optical system it can lead to rounding off the sharp corners of the wedged micropillars. In this work, we explore the effect of rounded corners in the dryout heat flux prediction of the wedged micropillars. The model predicts that rounding off the corners can decrease the dryout heat flux significantly compared to wedged micropillars with sharp corners.

**Keywords:** thermal management, thin-film evaporation, capillarity

## 1. Introduction

The advancement of microprocessor technology accentuates the need for improved cooling options. Thin-film evaporation is a liquid-vapour phase change method that when aided by capillary pumping can promote significant heat dissipation frugally as demonstrated in the past. The thermal performance of the wick can be enhanced through the meticulous design and optimization of the wick microstructures[1,2]. Among the various kinds of wick micropillars, a nature-inspired design of the micropillar, as shown in Fig 1a, demonstrates significant enhancement in the dryout heat flux as reported by Anand and Sharma[3]. This is attributed to the high capillary pumping and permeability of flow of the wedge micropillars due to the inherent sharp corners. Due to the constraints in the lithography-based deep reactive ion etching process, the sharp corners can get rounded off with a finite radius of curvature as shown in Fig. 1b.

So, the objective of the present work is to understand the effect of corner roundedness on the dryout heat flux using a validated numerical model.

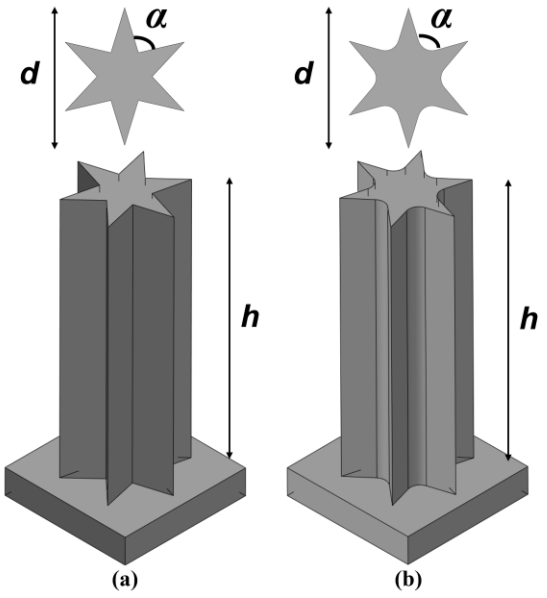


**Fig.1.** Schematic representation of biomimetic wedged micropillar with (a) sharp corner and (b) rounded corner of 2μm radius of curvature showing the geometrical parameters such as nominal diameter *d,* height *h*, and wedge corner angle *α.*

## 2. Numerical Model

The dryout heat flux is predicted using a 1D finite volume method of unit cell and device

level model[3,4]. The moment of dryout is captured by the receding contact angle criterion, where the meniscus curvature tends to maximum corresponding to minimum Laplace pressure. The modeling involves (a) generation of equilibrium meniscus shape for any given unit cell using the energy minimization algorithm of Surface Evolver, (b) fluid flow simulation to obtain the velocity field corresponding to the applied pressure gradient for the unit cell, and (c) linking unit cells based on the mass, and enthalpy conservation (Eq. (1)) to predict the dryout heat flux.

$$\rho(A_{i-1}U_{i-1} - A_iU_i)h_{fg} = q''l^2 \quad (1)$$

Here $\rho$, $A_i$, $U_i$, $h_{fg}$, and $q''$ are the density, midplane area and average velocity of the unit cell, latent heat of vaporization, and input heat flux respectively.

## 3. Results and Discussion

Thermal performance in terms of dryout heat flux of the biomimetic wedge micropillar with sharp corner and rounded corner is compared for a particular geometry of micropillar array with d=20µm, l=50µm, h=50µm, and L=5mm. The numerical model predicts the dryout at a maximum heat flux value of 218.7 W/cm$^2$ for the rounded corner wedge micropillar whereas the sharp corner wedge micropillar dissipates 688.2 W/cm$^2$. The rounded corner of the wedge micropillar has resulted in a reduction of the dryout heat flux by ~ 68%. This is due to the reduced Laplace pressure gradient as shown in Fig. 2, which results in less capillary pumping of liquid within the micropillar array.

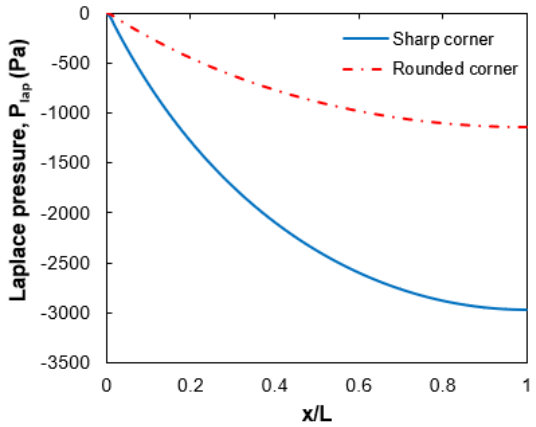


**Fig.2.** Variation of Laplace pressure along the flow direction for sharp and rounded corner wedge micropillar

## 4. Conclusions

This study highlights the effect of the rounded corner of the wedge micropillar which is an after-effect of the microfabrication technique involving lithography and deep reactive ion etching. We infer from the numerical modeling results that the rounded corner of the wedge leads to lower capillary pumping pressure which results in the reduced dryout heat flux for the given geometry of the micropillar array.

## Acknowledgments

The authors gratefully acknowledge the funding provided for this work by SERB, DST, Government of India under the Core Research Grant (CRG/2018/004539).

## References

[1] R. Ranjan, A. Patel, S. V. Garimella, J.Y. Murthy, Wicking and thermal characteristics of micropillared structures for use in passive heat spreaders, Int. J. Heat Mass Transf. 55 (2012) 586–596. https://doi.org/10.1016/j.ijheatmasstransfer.2011.10.053.

[2] T. Liu, M. Asheghi, K.E. Goodson, Multiobjective Optimization of Graded, Hybrid Micropillar Wicks for Capillary- Fed Evaporation, Langmuir. (2021). https://doi.org/10.1021/acs.langmuir.1c 02429.

[3] S. Anand, C.S. Sharma, Biomimetic Micropillar Wick for Enhanced Thin- Film Evaporation, ArXiv:2302.04573. (2023).

[4] Y. Zhu, D.S. Antao, Z. Lu, S. Somasundaram, T. Zhang, E.N. Wang, Prediction and Characterization of Dry- out Heat Flux in Micropillar Wick Structures, Langmuir. 32 (2016) 1920–1927. https://doi.org/10.1021/acs.langmuir.5b 04502.

# Cavity-based inertial microfluidic device for the separation of rare cells with different size: a computational study

Panagiotis SKALTSOUNIS[1,2,*], George KOKKORIS[3], Angeliki TSEREPI[1]

1: Institute of Nanoscience and Nanotechnology, NCSR "Demokritos", Patriarchou Gregoriou & 27 Neapoleos str., 153 41 Aghia Paraskevi, GR
2: School of Medicine, National and Kapodistrian University of Athens, 75 Mikras Asias str., 115 27 Athens, GR
3: School of Chemical Engineering, National Technical University of Athens, Zografou, 157 80 Athens, GR

* Corresponding author: Tel.: +30 210 650 3237; Email: p.skaltsounis@inn.demokritos.gr

**Abstract:** There are two main categories of microfluidic devices for the separation of rare cells. Active devices use external forces, while passive separation devices exploit the geometric and/or physical characteristics of cells. The focus of this study is on the passive cavity-based inertial microfluidic devices which have recently gained attention for their ability to separate rare cells from billions of blood cells and concentrate them in a small volume. In particular, a parametric computational study is conducted to investigate the effect of the geometric characteristics of both the microchannel and the cavity, and the Reynolds number on particle trapping efficiency in rounded cavities. The modeling framework consists of continuity and Navier-Stokes equations and a particle tracing model. Three-dimensional simulations are performed to study the generation of vortices in the cavities for different flow rates and the effect of these vortices on particles of various sizes. The optimum geometry and flow rate for particles of different size is extracted. This study provides insights into the design and optimization of rounded cavity-based microdevices for cell separation applications.

**Keywords:** Particle trapping, Cell separation, Sample preparation, Vortices, Round Cavities, Computational Study, Lab on Chip

## 1. Introduction

A critical operation in sample preparation modules of Lab on Chip (LoC) systems serving molecular diagnostics is the separation of usually rare (less than 1000 in a one milliliter sample) cells from the sample, e.g., cancer or bacteria cells from blood. There are two main categories of microdevices used for this purpose. The first is active microdevices, which, although usually showing good results, often use external components, which can significantly increase their complexity [1]. The second category is passive separation microdevices, which achieve separation by exploiting the geometric and/or physical characteristics of the particles.

Cavity-based inertial microfluidic devices are passive separation devices that have been developed considerably over the past decade. They consist of microchannels with periodic cavity expansions, i.e., periodic cavities at the sides of the main microchannel. They were introduced in 2011 by Hur et al. [2] and can separate rare cells from billions of blood cells and concentrate them in a very small volume. Compared to other separation methods, this approach has several advantages, such as simple structure, ease of fabrication and operation, and possibility to use several cavities in parallel or in series, thus enhancing the throughput or the separation efficiency, respectively. Several studies have addressed the design and improvement of, usually square shaped, cavities [2–5]. Shen et al. however, tried to use circularly shaped cavities which they found to show better results [1].

In the present work, a parametric computational study on rare cell separation in microchannels with rounded (not necessarily circular) cavities is performed. The aim is the optimization of the cell separation efficiency by changing the geometric characteristics of the rounded cavities, as well as the operating conditions (fluid flow). A variety of cell diameters is examined to cover different scenarios of cell separation, from bacteria to circulating tumor cells (CTCs).

## 2. Results and Discussion

### 2.1 Vortices generation

Initially, the relationship between the volumetric flow rate and the creation of vortices in the cavities is investigated; a relation between the extent of vortices and the cell trapping was pointed in previous studies [1]. To this end, a three-dimensional computational study is performed. In particular, the continuity and Navier-Stokes equations are numerically solved at steady state with a commercial code (Comsol Multiphysics 5.0).

Figure 1 shows the creation of vortices for volumetric flow rates corresponding to Reynolds numbers (Re) of 10, 100, and 300. Both the position and the extent of vortices changes with Re. It appears that Re = 10 (left) is not sufficient for the creation of vortices that can lead to efficient particle trapping. For Re = 100 (middle) and Re = 300 (right), vortices are formed in the center of the cavities. The study will be extended by examining the effect of different geometries on the formation of vortices.

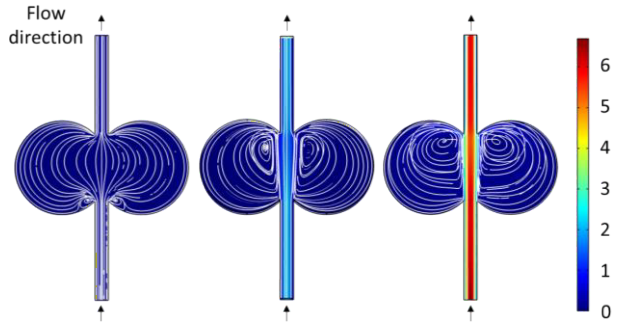


Fig. 1. Vortices generation (white colored lines) inside the rounded cavities, at a slice at the middle of the microchannel, for flow rates corresponding to Reynolds numbers of 10 (left), 100 (middle), and 300 (right). The colored contours show the velocity magnitude in m/s. The width, height, and length of the microchannel are 80 μm, 110 μm, and 1.6 mm respectively, while the cavities are circular with a radius equal to 240 μm.

### 2.2 Particle tracing

The effect of the aforementioned vortices on particles of different sizes was subsequently studied, so as to check whether and under what conditions the trapping of particles in the cavities is maximized. This method is used to evaluate the particle trapping mechanism and comes as a continuation of the method applied by Shen et al. [1] where the trapping efficiency was examined through the volume of the vortices formed. For this part of the computational study, Newton equations for particles of different diameters, resembling cells, are numerically solved with a commercial code (Comsol Multiphysics 5.0). The force field depends on the flow field and the size of the particle.

Figure 2 shows the percentage of the particles that are trapped inside a single rounded cavity in relation to Re of the flow inside the microchannel. Stokes and Schiller-Naumann force models were used to calculate the force exerted on the particles. Particles of different size, covering the whole size range from the small bacteria to big CTCs, are examined to investigate when the trapping efficiency is optimized. It seems that there is a maximum for each diameter. The location of this maximum (Re) depends on the diameter of the particle. For small sized particles (2 to 10 μm), the maximum trapping takes place at Re = 300. On the other side, larger particles (30 and 40 μm) get maximum trapping at Re = 100.

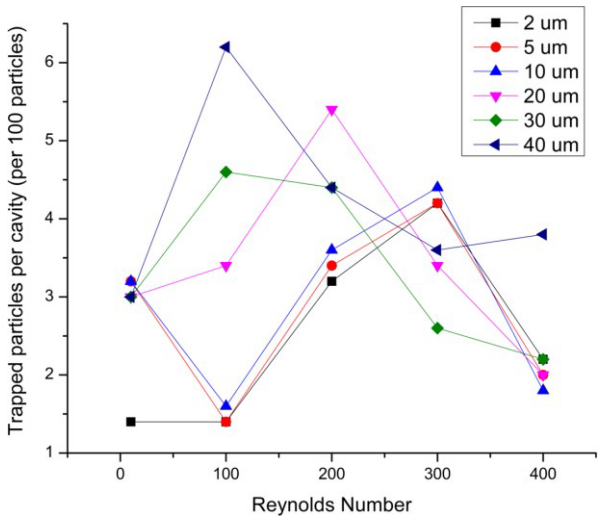


Fig. 2. Percentage of trapped particles vs Reynolds number of the flow inside the microchannel, for different sized particles.

[1] Shen, F. et *al.*, Round cavity-based vortex sorting of particles with enhanced holding capacity. *Phys. Fluids* 2021, 33, 082002.
[2] Hur, S.C. et *al.*, High-throughput size-based rare cell enrichment using microscale vortices. *Biomicrofluidics* 2011, 5, 022206.
[3] Mach, A.J. et *al.*, Automated cellular sample preparation using a Centrifuge-on-a-Chip. *Lab Chip* 2011, 11, 2827.
[4] Rastogi, N. et *al.*, Vortex chip incorporating an orthogonal turn for size-based isolation of circulating cells. *Anal. Chim. Acta*. 2021, 1159, 338423.

# Methodology for measurement of force during coalescence induced droplet jumping on superhydrophobic surface

Gopal Chandra PAL[1], Siddhartha SS[1], Manish AGRAWAL[1,*], Chander Shekhar SHARMA[1,#]

1: Thermofluidics Research Lab, Department of Mechanical Engineering, IIT Ropar, Rupnagar-140001, India

* Corresponding author: Tel.: +91 1881242379; Email: manish.agrawal@iitrpr.ac.in
# Corresponding author: Tel.: +91 1881 232358; Email: chander.sharma@iitrpr.ac.in

**Abstract:** Coalescence induced droplet jumping on superhydrophobic surfaces is a promising way to renew the surface rapidly during condensation due to its gravity-independent nature. Coalescing droplets jump from superhydrophobic surfaces when the reaction from the substrate can overcome the minimal capillary adhesion with the substrate. In order to study the droplet dynamics during coalescence, force analysis can therefore be an alternate approach to energy analysis. In the present work, we report a new method for measuring the transient force that the substrate exerts on the droplet during coalescence.

**Keywords:** superhydrophobic surface, Displacement, Force

## 1. Introduction

Coalescence-induced droplet jumping phenomena is one of the mechanisms by which droplets are removed from superhydrophobic surfaces during condensation [1]. However, the low efficiency of the process, which is measured as the ratio of upward kinetic energy at the time of droplet detachment to the excess surface energy during coalescence, draws a lot of researchers to study fluid dynamics involved in the process. When the reaction from the substrate can outweigh the weak capillary adhesion with the substrate, coalescing droplets detach from superhydrophobic surfaces. This force exerted by the coalescing droplets can be measurd as shown by Moutrade et al. [2]. In the current work, we develop a method to measure this force by using a flexible substrate. The force is determined based on the transient displacement profile of substrate which is obtained optically using a high-speed imaging.

## 2. Methodology

For the experiment, we prepare super-hydrophobic nanotextured surfaces on thin copper film (dimension = 40 x 4 x 0.01 $mm^3$) by spray coating commercially available silanized silica nanoparticles (Glaco). The apparent average advancing contact angle and contact angle hysteresis for the surface is $163 \pm 1.2^0$ and is $3.8 \pm 1.3^0$ respectively. After placing two droplets, coalescence is triggered by carefully moving one drop toward the other. Using a high-speed camera, the images are recorded at 10000 frames per second. As shown in the schematic diagram in the figure, we are able to determine the displacement beneath the droplet with respect to time through image analysis.

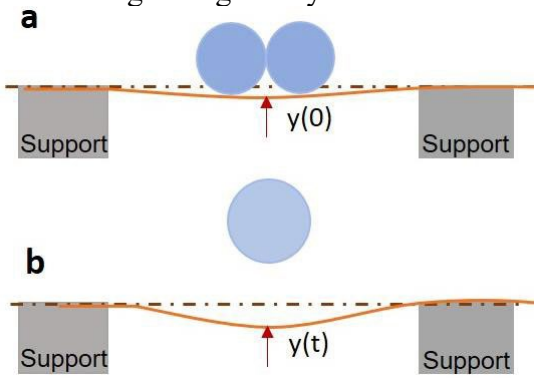


**Fig.1.** Schematic representation coalescence induced droplet jumping on flexible superhydrophobic at the (a) initial time with y(0) as static deflection (b) time t with displacement, y(t).

The initial point y(0) represents the substrate's position right before coalescence (the substrate initially deforms as a result of the weight of the droplets), and the point y(t) represents the point at which the coalesced droplet detaches from the substrate as a result of the reaction force exerted on the droplet by the substrate. The force is obtained using transient displacement data from the experiment with the help of numerical analysis using ANSYS Mechanical software. The substrate is modeled with 1d beam elements and a fixed-fixed boundary condition as shown in Figure 2(3D figure is

shown for the representation). To determine the force, we solve the equation (1) taking transient displacement data as input at the center. The probe is positioned in ANSYS at the center to capture the coalescence force as the output.

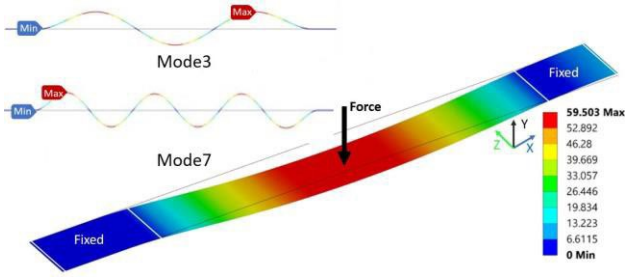


**Fig.2.** Boundary condition for the modeled geometry. Inset figures show the mode shape obtained from modal analysis

$$[\boldsymbol{M}]\{\ddot{y}\} + [\boldsymbol{C}]\{\dot{y}\} + [\boldsymbol{K}]\{y\} = \{\, f(t) \,\} \quad (1)$$

Here, $[M]$ is the mass matrix, $[C]$ is the damping matrix, and $[K]$is the stiffness matrix of substrate. $y$, $\dot{y}$, $\ddot{y}$ represent the displacement, velocity and acceleration of the substarte respectively, and f(t) is the coalescence force.We have performed a linear transient analysis. In the analysis the intial static deflection shown as y(0) in Figure 1 is considered to be zero. We have performed a grid independence study and based on it 100 µm element size has been chosen to descretize the substrate. For choosing an efficient time step we have performed a modal analysis. The time step of the simulation is taken as one-twentieth of the time period corresponding to the natural frequency of the highest mode($19^{th}$ mode) considered in the analysis. For verifying our model we performed a reverse analysis, where we have considered $f(t)$ from the transient analysis as input and displacement as output. The displacement obtained from the analysis is validated with the measured displacement data from experiment. For validation of transient analysis, the stiffness and mass value is taken from the modal analysis.

## 3. Results and Discussion

We have shown a qualitative comparison of force obtained from the transient structural analysis and force obtained by Mouterde et al. is shown in figure 3. The details of the setup is given in the methodology section. From the figure, it is clear that there is a good qualitative agreement between the two forces. However, there is significant noise in the obtained force profile. In future work, we will endevaour to improve this force measurement by improving the optical resolution for measuring the substarte displacement.

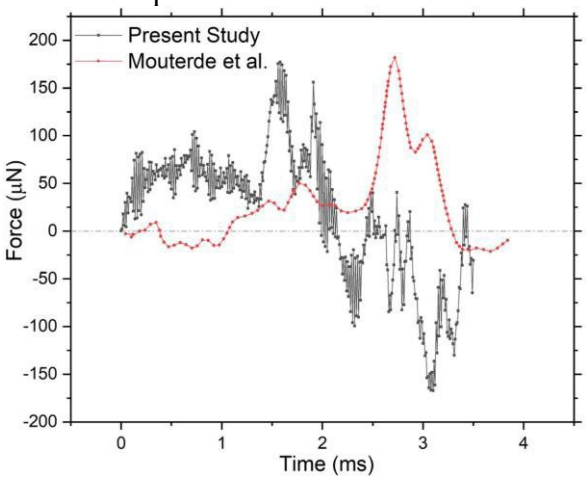


**Fig.3.** Comparison of transient force between the present study and Mouterde et al. [2]

## 4. Conclusions

A method to measure the force exerted by coalescing drops on a superhydrophobic surface has been developed. It involves droplet coalescence on a flexible substrate and optical measurement its dispalcement profile. The force derived from the current methodology displays good qualitative agreement with the literature[1]. However, higher optical resolution is required to reduce the noise in the measured force profile.

## Acknowledgments

The authors gratefully acknowledge facility and funding provided for this work by IIT Ropar under the ISIRD (Grant No.9-388/2018/IITRPR/3335 ).

## References

[1] N. Miljkovic, R.Enright, Y. Nam, K. Lopez, N. Dou, J. Sack, E. N. Wang, Jumping droplet enhanced condensation on scalable superhydrophobic nanostructured surfaces. Nano letters(2013), 13(1), pp.179-187.

[2] T. Mouterde, T.V. Nguyen, H.Takahashi, C. Clanet, I. Shimoyama, D. Quéré, How merging droplets jump off a superhydrophobic surface: Measurements and model. Physical Review Fluids. (2017) 2(11), p.112001. 586–596.

# Mixing and reaction efficiency in T-, X-, and arrow-shaped microreactors

Sara TOMASI MASONI[1], Alessandro MARIOTTI[1], Elisabetta BRUNAZZI[1], Maria Vittoria SALVETTI[1], Chiara GALLETTI[1,*]

1: Dipartimento di Ingegneria Civile ed Industriale, Università di Pisa, Pisa, IT

* Corresponding author: Tel.: +39 0502217897 Email: chiara.galletti@unipi.it

**Abstract:** Numerical simulations of liquid reactive flows are carried out to investigate the mixing behavior and reaction efficiency in T-, X-, and arrow-shaped microreactors operating in steady regimes. The microdevices are compared for the same inlet flow rates. The most promising flow pattern is the one with a single vortex in the center of the mixing channel that occurs in both the X- and arrow-shaped devices. At low flow rates, the X-device shows a higher mixing degree and reaction yield since it exhibits a single stronger central vortex in the mixing channels. Conversely, at higher Reynolds numbers, mixing and reaction efficiency becomes better for the arrow-reactor because this geometry presents a higher cross-section compared to the X-reactor. The worst performance is achieved by T-reactor, which shows two co-rotating vortices in the engulfment regime.

**Keywords:** Microfluidics, microreactors, CFD simulations, reaction yield, mixing efficiency

## 1. Introduction

Micromixers and microreactors are widely studied as they ensure continuous operation and a high surface-to-volume ratio [1]. It is well known that the flow inside these devices is laminar, thus is necessary to provide geometries that increase mixing. Among the passive devices, T-, X-, and arrow-shaped devices have been largely studied when fed with water-water [2-4]. The flow regimes inside T- and X-microreactors in presence of a test reaction are characterized in [5, 6]. Instead, no investigation is reported so far on the reactive flow regimes in an arrow-shaped device. Hence, this work aims to characterize steady flow regimes in an arrow-shaped device fed with reactive streams and then compare the performance of the three geometries in terms of mixing efficiency and reaction yield.

## 2. Test cases and numerical method

The T- and arrow-microdevices consist of two identical inlet channels with a square cross-section (1mm x 1mm) and the mixing channel with 2:1 aspect ratio. The X-microdevice has four channels, two inlets and two outlets, with a square cross-section (1mm x 1mm).

The test reaction is the reduction of methylene blue ($MB^+$) to the colorless leucomethylene blue ($LMB^+$) using ascorbic acid (AsA); such reaction is catalyzed by hydrogen chloride (HCl) and presents a pseudo-first-order kinetic. The reaction also produces dehydroascorbic acid (DA). An aqueous solution with $[MB^+] = 5.31 \cdot 10^{-5}$ mol/L and [HCl] = 2.19 mol/L is fed into one inlet channel, while an aqueous solution with [AsA] = 1.7 mol/L is fed into the other. The kinetic constant is $k_r = 21.43$ $s^{-1}$ [6].

Regarding the numerical model, steady Navier-Stokes equations, and transport/reaction equations for $MB^+$, $LMB^+$, AsA, HCl, and DA are solved in isothermal conditions using the finite volume code ANSYS Fluent v.19. More details on the computational grid (and its adaption to capture the mixing of reactants), fluid properties and numerical parameters are provided in Mariotti et al. [4, 5] and Tomasi Masoni et al. [6].

## 3. Results

The steady flow regimes inside the arrow-shaped microreactor, in presence of a reaction, indicated: a stratified pattern for Reynolds number Re<100 due to the higher density of the

AsA solution; an engulfment regime for 100<Re≤200 presenting two co-rotating vortices in the mixing channel; an engulfment regime with one single vortex for Re>200.
The three geometries are compared in terms of mixing degree and the reaction yield for the same inlet flow rates, thus for the same Reynolds number evaluated at the inlet, $Re_i$. In the stratified regime, the three geometries present a low mixing and reaction yield. At $Re_i$=50, the X-microreactor exhibits a single central vortex that enhances both the mixing and the yield.
X- and arrow-geometries achieve similar mixing performance in the engulfment regime as they both have a single vortical structure. However, the arrow-microdevice exhibits a higher reaction yield compared to X-geometry. The two smaller vortical structures exhibited by the T-reactor in the engulfment regime, do not allow the achievement of high values of mixing and reaction yield.

## 4. Conclusions

Comparing to the well-known T-shaped microreactor, X- and arrow-shaped devices are found to provide superior mixing and reaction yield, in steady flow regimes, thanks to their ability to promote a single strong vortex that occupies all the mixing channel.

## 5. References

[1] K. Elvira, X. C. I Solvas, R. C. Wootton, and A. J. Demello, *The past, present and potential for microfluidic reactor technology in chemical synthesis*. Nature Chemistry, 5:905-915, 2013.
[2] N. Ait-Mouheb, D. Malsch, A. Montillet, C. Solliec, and T. Henkel, *Numerical and experimental investigations of mixing in T- shaped and cross-shaped micromixers*. Chemical Engineering Science, 68(1):278-289, 2012.
[3] J. W. Zhang, W. F. Li, X. L. Xu, H. F. Liu, and F. C.Wang, *Experimental investigation of three-dimensional ow regimes in a cross shaped reactor*. Physics of Fluids, 31(3):034105, 2019.
[4] A. Mariotti, C. Galletti, E. Brunazzi, and M. V. Salvetti, *Steady regimes and mixing performance in arrow-shaped micro-mixers*. Phys. Rev. Fluids, 4:034201, 2019.
[5] A. Mariotti, M. Antognoli, C. Galletti, R. Mauri, M. V. Salvetti, E. Brunazzi, *The role of flow features and chemical kinetics on the reaction yield in a T-shaped micro-reactor*. Chemical Engineering Journal, 396:125223, 2020.
[6] S. Tomasi Masoni, M. Antognoli, A. Mariotti, R. Mauri, M.V. Salvetti, C. Galletti, E. Brunazzi, *Flow regimes, mixing and reaction yield of a mixture in an X-microreactor*. Chemical Engineering Journal, 437:135113, 2022.

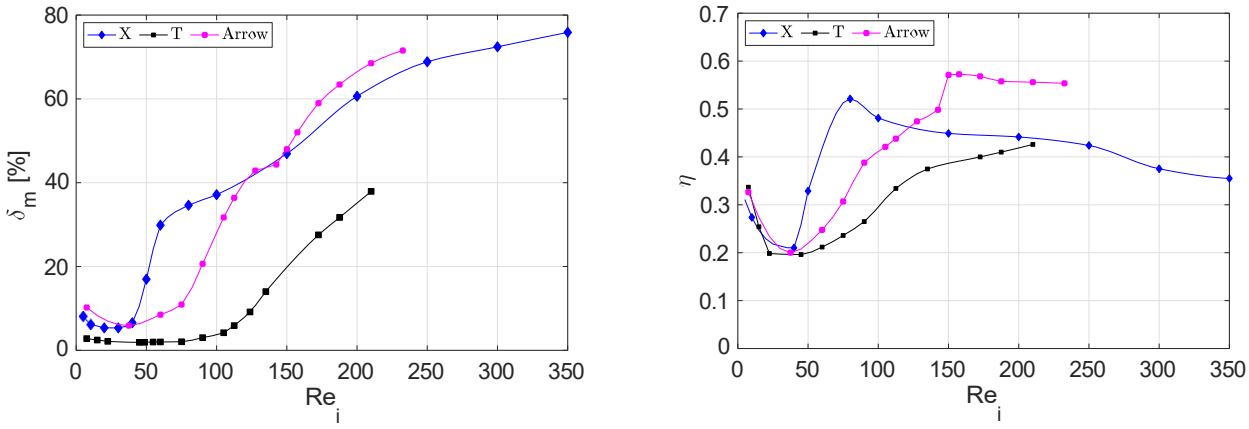


**(a)** **(b)**

**Figure 1:** Mixing degree (a) and reaction yield (b) of the T-, X-, and arrow-shaped microreactors evaluated at the Y=25 cross-section as a function of the inlet Reynolds number.

# High-frequency AC electrokinetic trapping of nanoparticles in a microchannel

Ahmed ABDELGHANY[1, *], Yoshiyasu ICHIKAWA[1,2], Masahiro MOTOSUKE[1,2]

1: Department of Mechanical Engineering, Tokyo University of Science, 6-3-1 Niijuku, Katsushika, Tokyo 125-8585, Japan.
2: Water Frontier Research Center, Research Institute for Science and Technology, Tokyo University of Science, Kagurazaka, Shinjuku, Tokyo 162-8601, Japan

* Corresponding author: Tel.: +81 03-5876-1718; Email: 452170@ed.tus.ac.jp

**Abstract:** Trapping of nanoparticles in a microfluidic device is a promising technique for preconcentrating low-concentration species in a sample. In this study, we demonstrate an effective method for trapping polystyrene nanoparticles (PsNPs) in a microchannel using coplanar electrodes with a gap under an AC electric field oscillating at a high frequency range of 50-150 kHz. We systematically study the concentration performance by varying the applied voltage and find that increasing the field strength leads to an enhanced concentration factor, exceeding ten times the initial concentration of the sample. We present a concentration map that shows the local concentration distribution of the trapped nanoparticles. Our results indicated that the concentration enhancement is field strength-dependent, with the maximum concentration occurring in the electrode gap. We also observed that the accumulation position and performance differ from those seen at low frequencies in previous studies (Abdelghany et al., 2022), where particles are accumulated at two separated positions far from the gap of the electrodes. Our study highlights the potential of high-frequency AC electrokinetic trapping as a powerful tool for preconcentrating low-concentration species in a sample, with a field strength-dependent concentration enhancement and a high concentration factor.

**Keywords:** Nanoparticles, AC electrokinetic, Microfluidics, Particle Trapping

## 1. Introduction

Microfluidic-based analytical techniques have gained significant interest in recent years due to their advantages such as rapid reaction, cost-effectiveness, portability, and multi-functional integration. However, the analyze of low-concentration species in a sample with microfluidics can be challenging, and a preconcentration step is often required to achieve high sensitivity. Various particle trapping techniques have been investigated, including electric forces (Oh et al., 2009). In this study, we focus on high-frequency AC electrokinetic trapping of nanoparticles in a microfluidic device using single-gap coplanar electrodes. We demonstrate an effective method for preconcentrating polystyrene nanoparticles and study the concentration performance systematically. Our results highlight the potential of the high-frequency AC electrokinetic trapping as a powerful tool for preconcentrating low-concentration species in a sample, with a field strength-dependent concentration enhancement and a high concentration factor.

## 2. Microfluidic Device

Figure 1. shows an example of rotational fluid motion and trapping position under the AC electric field in a cross-sectional view of the microchannel. The microfluidic device used for trapping nanoparticles consists of a microchannel and a glass substrate with coplanar symmetric electrodes. The microchannel is fabricated from PDMS and is bonded onto a glass substrate with a thickness of 0.7 mm and coated with a 150 nm-thick transparent ITO film, which serves as an electrode. The electrode consists of two parallel ITO strips separated by a 40-μm gap. The working fluid is an aqueous solution of fluorescent polystyrene nanoparticles (PsNPs)

with a diameter of 100 nm. The electrical conductivity of the solution was adjusted to $10^{-4}$ S/m, and the particles were dispersed in ultrapure water at a volume percentage of 0.02% to avoid particle-particle interaction.

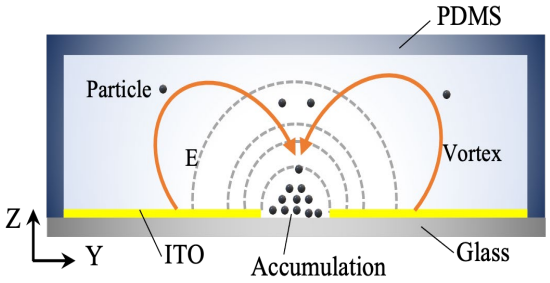


**Fig. 1.** Cross-sectional view of microchannel indicates electrokinetic flow pattern (orange arrows) and particle trapping position.

## 3. Results

Figure 2 presents the concentration factor (CF) distribution of PsNPs in the device under several electric field strengths at 50 kHz. Increasing the electric field strength (E) by increasing the applied voltage led to an improvement in the CF, with a maximum value of 16.3 at 3.5 x $10^6$ V/m. The peak of accumulation was observed to be inside the gap between the electrodes for all (E) values. This suggests that increasing the voltage leads to an increase in the CF under the same frequency. To gain further insights into the particle trapping performance in the microfluidic device, a mapping of the local CF values was performed. Color map of the accumulation performance at 150 kHz is shown in Figure 3. It was observed that a single high CF spot formed inside the gap between the electrodes, with a CF value that reached up to 30 times the initial concentration. The low CF region, where particles move away from this region, expanded to about 200 µm on each side of the electrode surface, as well as in the bulk with a height of around 150 µm. Additionally, the formation of AC electrokinetic vortices in this regime was observed, which transport particles toward the gap region, leading to the accumulation of particles in the center of the gap.

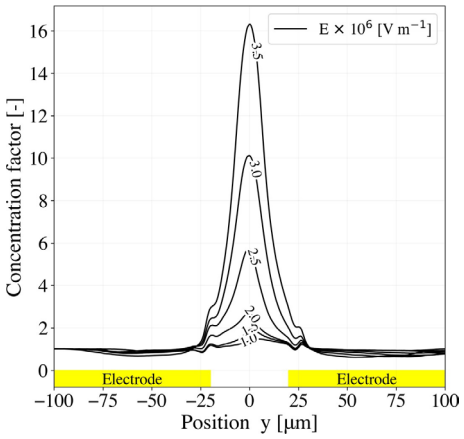


**Fig. 2.** Concentration factor distribution of 100 nm PsNPs in the device at different electric field strengths (E) oscillating at 50 kHz.

These results suggest that increasing the electric field strength can enhance the particle accumulation performance in the microfluidic device. Furthermore, the formation of AC electrokinetic vortices at high-frequency operation leads to the accumulation of particles in the center of the gap.

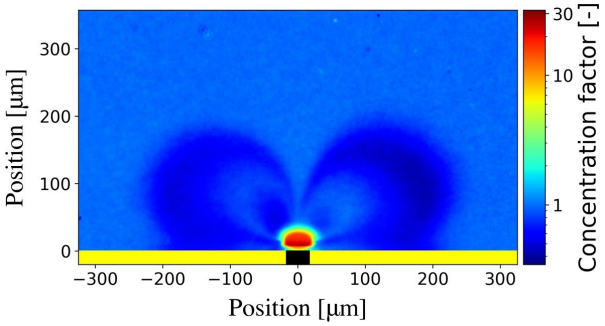


**Fig. 3.** Color map indicates the local concentration factor.

## References

Abdelghany, A., Yamasaki, K., Ichikawa, Y., Motosuke, M., 2022. Efficient nanoparticle focusing utilizing cascade AC electroosmotic flow. Electrophoresis 43, 1755–1764.

Oh, J., Hart, R., Capurro, J., Noh, H., 2009. Comprehensive analysis of particle motion under non-uniform AC electric fields in a microchannel. Lab Chip 9, 62– 78.